FAKULTÄT FÜR MATHEMATIK UND NATURWISSENSCHAFTEN
FACHGRUPPE PHYSIK
BERGISCHE UNIVERSITÄT WUPPERTAL

MEASUREMENT OF THE FIDUCIAL AND TOTAL SINGLE TOP-QUARK t-CHANNEL PRODUCTION CROSS-SECTIONS WITH THE ATLAS DETECTOR AT $\sqrt{s} = 8$ TeV

Die Dissertation kann wie folgt zitiert werden:

Für Denise und Nils

Introduction

The aspiration of elementary particle physics is to explain and describe the nature of the constituents of matter. The Standard Model of particle physics is a highly successful theoretical framework, that describes the fundamental particles and interactions at small distance scales around 1 fm. The Standard Model is a relativistic quantum field theory, that includes the fundamental particles, six quarks and six leptons, as well as the strong, weak and electromagnetic interactions.

In order to test predictions of the Standard Model, particles like protons or electrons are brought to collision, studying emerging particles in the process. The scale at which the structure of matter can be probed is inverse proportional to the center-of-mass energy of the colliding particles. Several particle collider experiments have been devised in the past, which exceeded the capabilities of their predecessors. The European Organization for Nuclear Research (CERN) hosts the **L**arge **H**adron **C**ollider (LHC) [1], which operates at a center-of-mass energy of $\sqrt{s}$ = 13 TeV, which is the highest currently available. The LHC is a circular collider in which protons are brought to collision at four interaction points. Four main particle detectors are located at the interaction points, where the ATLAS (**A T**oroidal **LHC A**paratu**S**) experiment [2], is one of the multipurpose detectors.

The heaviest known quark is also the one which eluded observation longer than the remaining five quarks. The discovery of the top quark was achieved in 1995 at the Tevatron in proton–antiproton-collisions at $\sqrt{s}$ = 1.8 TeV by the CDF and D0 experiments [3, 4], which was about 18 years after the bottom quark was discovered. Within the Standard Model of particle physics, the importance of top-quark production evolved from its discovery to one of the standard-candle processes in particle physics. The top quark is mainly produced in two distinct modes, where the top-quark pair production proceeds via the strong interaction and singly produced top-quarks involve the weak interaction. The t-channel single top-quark production yields the highest rate of singly produced top quarks, which renders it the most accessible production mode at the LHC. The top-quark mass (m_t) is currently known at high accuracy to be m_t = 173.34 ± 0.76 GeV [5], which is the world average obtained in 2014. The uncertainty on the top-quark mass measurement corresponds to 0.4 % relative total uncertainty.

The precise measurement of the single top-quark cross-section facilitate tests of Standard Model predictions. In particular the W-t-b vertex of the weak interaction is directly involved in the t-channel single top-quark production. The measured cross-section is proportional to the quark-mixing matrix-element $|V_{tb}|^2$, which is close to unity in the Standard Model. The constraint on $|V_{tb}|$ in the Standard Model is performed

with the assumption of the unitarity of the mixing matrix, which requires the number of quark generations to be three. The determination of $|V_{tb}|$ from the t-channel single top-quark cross-section alleviates the constraint on the number of quark generations.

Previous analyses [6, 7, 8] established the t-channel single top-quark production at the LHC at 7 and 8 TeV center-of-mass energies. This analysis is published, together with the differential t-channel single top-quark production cross-sections, in [9]. Beyond the observation of the t-channel production, more extensive measurements have been performed, which were enabled by improved data statistics. With the completion of the 2012 data-taking in the LHC run 1 operation, the full available dataset at a center-of-mass energy $\sqrt{s} = 8$ TeV is analysed within the scope of this theses. The unprecedented size of the dataset and a very sophisticated set of detector calibrations and MC simulation tunes, lay the basis for the most precise measurement of the t-channel single top-quark production cross-section.

The signature of the t-channel single top-quark production in terms of observable final-state particles, is characterised by the decay products of the top quark and an additional light-quark jet. The decay products of the top quark are a W boson and a b-quark, at nearly 100 % probability. Decays of the W boson into $e\nu$ or $\mu\nu$ leptons are considered in this analysis. Electrons or muons from the W-boson decay via a τ lepton are also included. The charged leptons from the W-boson decay are isolated and have large transverse momentum, while the corresponding neutrinos are not directly detectable, but are reconstructed as missing transverse momentum in the detector. Exactly one of the two selected jets is required to contain a b-quark, which corresponds to the top-quark decay. The single top-quark in an event is accompanied by an additional light-quark jet, which is scattered in the forward region of the detector and is one of the main features that enable the distinction from background processes.

The main challenge for this analysis is to separate signal events from background events. The primary background processes are the $t\bar{t}$ production and the W-boson production with additional jets. The $t\bar{t}$ production has a higher cross-section than t-channel single top-quark production, and the presence of top quarks in the event renders this background hard to separate from the signal. The W + jets production has a substantially larger cross-section compared to t-channel single top-quark production, and the similarity of the final state particles results in a significant contribution to the background. The analysis employs a neural network in order to improve the sensitivity to the signal process by combining kinematic observables that discriminate between signal and background processes into one single discriminant. Neural networks also reduce the dependency on systematic uncertainties compared to a singular discriminating observable. The presented analysis will study the configuration of the neural network, to reduce the required number of input observables, while preserving the sensitivity of the discriminant.

II

The measurement of the cross-section is performed separately for top quarks and top antiquarks in a visible part of the phase space, referred to as fiducial volume. The advantage of the measurement of a fiducial cross-section, is the separation of extrapolation effects associated to theoretical uncertainties from experimental uncertainties. Consecutively, the total cross-sections are obtained by extrapolation of the measured fiducial cross-sections. The cross-section ratio of the total cross-sections is determined, which yields a reduced systematic uncertainty due to cancellations. The measured cross-section ratio is sensitive to the u/d quark ratio in parton-distribution-functions, and can be used to test several predictions from parton-distribution-function sets. The $|V_{tb}|$ element of the quark-mixing matrix is extracted using the combined total cross-section, which is the sum of the extrapolated total cross-sections.

The presented analysis is based on previous ATLAS results with $5.8\,\mathrm{fb}^{-1}$ of $8\,\mathrm{TeV}$ collision data [10] and subsequently on [8] using $20.3\,\mathrm{fb}^{-1}$. The same technique was also used in the first measurement of the top quark-antiquark cross-section ratio in t-channel single top-quark events [7] using $7\,\mathrm{TeV}$ ATLAS data. The presented analysis aims to improve the preceding analyses and extend their scope.

The structure of this thesis is as follows. First the main concepts of the Standard Model of particle physics are introduced. The discussion is focused on methods important to the measurement of the t-channel single top-quark production cross-section. In the next chapter, the ATLAS experiment as part of the LHC particle accelerator at CERN is presented, followed by the introduction of the Monte Carlo simulation techniques and the definition of the involved physics objects. The event selection and background estimation introduce crucial aspects of the measurement as well as details on the employed neural network. Finally, the measurement technique and the treatment of systematic uncertainties are introduced followed by the measurement results and conclusions.

Contents

The Top-Quark within the Standard Model of Particle Physics

The theoretical aspects of this thesis involve fundamental particles and interactions at very small distance scales up to 1 fm. The Standard Model of fundamental particle physics (SM) describes the distance and energy regime, that is in focus in this thesis. Four distinct forces are known to explain the interactions between fundamental particles, namely the strong, weak, electromagnetic and gravitational interaction. With the exception of gravitation, which is described by general relativity, the remaining interactions are incorporated in the SM. The observed strength of gravity in our macroscopic world is only attained by vast accumulations of mass, and at distance scales around 1 fm gravity becomes a negligible contributor to the interactions of fundamental particles, compared to the three remaining forces, which allows gravity to be ignored in the SM. Since the inception of the SM, it was subject to numerous experimental tests, which exhibited very good agreement with the predictions of the SM.

All particles described by the SM are distinguished by their spin into fermions, which have half-integer spin, and bosons, which have integer spin. Figure 1.1 contains a summary of the SM particles, both fermions and bosons, as well as indicating the type of interaction the fermions are subjected to. This Section gives a overview of the main concepts of the SM. A more detailed introduction can be found in text books [11].
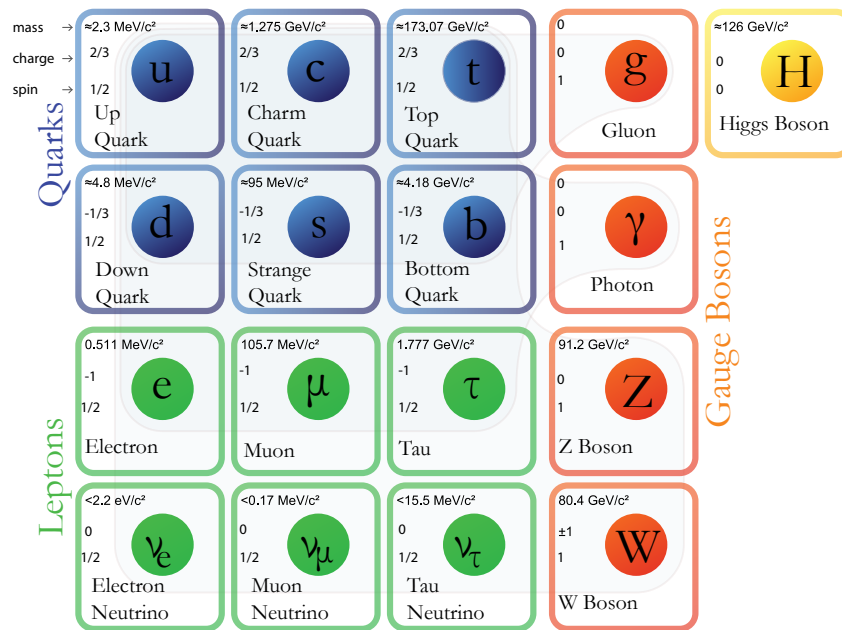
Figure 1.1.: Summary of the Standard Model of particle physics. On the left-hand side all fermions are specified, subdivided into quarks and leptons. The right-hand side shows the bosons of the SM, which mediate the weak, strong and electromagnetic interactions as well as the Higgs boson. The mass, charge and spin of all particles is given in the respective box. The generations of fermions are grouped vertically.[12, 13]

1.1. Fermions

Fermions are the constituents of visible matter in the universe. Fermions can be sub-divided into two groups, where the fermions of one group carry colour charge, and fermions of the other group do not. The fermions that carry colour charge are called quarks and the fermions that do not carry colour charge are called leptons.

The introduced types of fermions also occur in three generations which exhibit a strong mass hierarchy, while the structure of the generations itself is still one of the open questions in particle physics. The ordinary stable matter in the Universe is entirely composed of fermions of the first generation, while fermions of the second and third generation are unstable and decay ultimately into those of the first generation. Fermions of the second and third generation are only produced in high energy interactions All fermions have an weak isospin $T = 1/2$ and its third component T_3 is either $+1/2$ or $-1/2$.

Leptons

Leptons are occurring in three different so-called flavours, electron (e), muon (μ) and tau (τ) as well as their corresponding electron-neutrino (ν_e), muon-neutrino (ν_μ) and tau-neutrino (ν_τ). Electron, muon and tau leptons have $T_3 = -1/2$, while neutrinos carry $T_3 = +1/2$. While due to their electric charge, the former interact also via the electromagnetic interaction, neutrinos are exclusively interacting via the weak interaction.

Quarks

Quarks are the constituents of hadrons. The most common hadrons are protons and neutrons. Protons consist of two up-quarks (u) and one down-quark (d) while neutrons are comprised of two down-quarks and one up-quark. Including the three generations of fermions in the SM, six quarks are distinguished by their mass as well as their flavour quantum number. Quarks carry fractional electric charge, depending on the quark being of up- or down-type. Up-type quarks comprise u, charm- (c) and top-quark (t), while down-type quarks refer to d, strange- (s) and bottom-quarks (b). In case of up-type quarks the electric charge is $+2/3 Q_e$ and $T_3 = +1/2$, where for down-type quarks the electric charge is $-1/3 Q_e$ and $T_3 = -1/2$. In addition to the electric charge, quarks carry colour charge. The colour charge of quarks and antiquarks is three-fold, (anti-)blue, (anti-)green and (anti-)red.
Quarks are subject to the strong and electroweak interactions.

1.2. Fundamental Forces and Gauge Bosons

Mathematically the SM is a quantum field theory (QFT), which is a theoretical framework adopting a Lagrangian formalism to describe the dynamics of the theory. The SM Lagrangian is invariant under the $SU(3)_C \times SU(2)_L \times U(1)_Y$ symmetry group, while the $SU(3)_C$ group corresponds to the strong interaction and $SU(2)_L \times U(1)_Y$ corresponds to the unified electroweak interaction. The quantum fields correspond to fundamental particles. The electromagnetic, weak and strong force are mediated by gauge bosons which have integer spin and carry discrete amounts of energy between fundamental particles as they participate in the respective interactions.

Fundamental Interactions

Each interaction couples to a distinct charge property. The electric charge is the most easy perceivable of them, due to its impact on the macroscopic regime, its value is provided in units of the electron charge e. The electromagnetic force has an infinite range and is mediated by photons (γ). The range of the electromagnetic force is founded in the masslessness of the mediating photon. A special feature of the electromagnetic force is that it can be repulsive as well as attractive, depending on the sign of the electric charge. The strength of the electromagnetic interaction is indicated by the coupling constant α_{em} also referred to as the fine structure constant $\alpha_{em} \approx 1/137$. While the value of α_{em} depends on the energy scale, the change of its magnitude remains very small.

The weak force is mediated by three gauge bosons, the $W^\pm$-bosons which have either positive or negative electric charge, while the Z^0-boson has no electric charge. The masses of the two bosons are with $m_W = 80.385 \pm 0.015$ GeV [14] and $m_Z = 91.1876 \pm 0.0021$ GeV [14] the only non-zero masses of the three interactions. The masses of the bosons render the interaction short ranged with respect to the electromagnetic interaction. The weak interaction couples to the third component of the weak isospin T_3. Some features of the weak interaction are unique compared to the other interactions.

- Flavour transitions of quarks are possible by the exchange of a $W^\pm$-boson. The flavour transition is not limited by the generation of the quark, and thereby the reason that the 2nd and 3rd quark generation are not stable.

- The weak interaction is parity violating which is accounted for in the theory by a vector–axial-vector (V − A) structure. Therefore, $W^\pm$-bosons only interact with left-handed particles and right-handed antiparticles, whereas the Z^0-boson interacts with either chirality, although with different strengths.

The strong interaction couples to the colour charge, and it is mediated by eight gluons (g). The strong interaction is described by quantum chromodynamics (QCD). The coupling strength of the strong interaction is α_s which is close to one at low energies, and

around $\alpha_s(m_Z) = 0.118$ at the high energy scales at the Z-Boson mass. The strong force has the unique feature of increasing its strength with growing distance. That infers that the energy required to separate two colour-charged particles would quickly exceed the energy required to create a new pair of particles which will result in two pairs of colour-neutral hadrons. This effect is referred to as confinement. Hence no quark can be observed individually, but only jointly with other quarks in colour-neutral bound states. Several configurations of hadronic states have been observed. A meson is a pair of a quark and an antiquark, whereas a baryon comprises three quarks. Also more complex configurations are possible, for instance five quarks bound in a pentaquark which was theorised in Gellman [15] and Zweig [16] and recently observed at the LHCb experiment [17].

Figure 1.2 illustrates the fermions and bosons of the SM with regard to which interaction they are subjected. In the cases of the $W^\pm$- and Z^0-boson, gluon and Higgs-boson the self interaction are indicated.
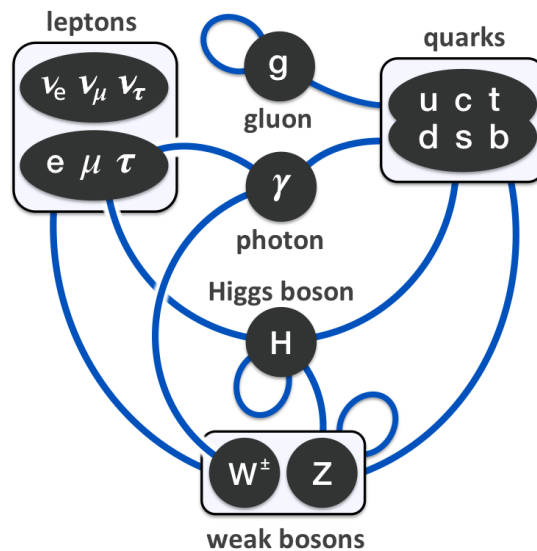
Figure 1.2.: Summary of the Standard Model interactions [18].

The Electroweak Unification and the Mass of Particles

Although the electromagnetic and weak interactions manifest differently at low energies, it was found that at the electroweak scale $\Lambda_{EW} \approx 246\,\text{GeV}$ both interactions can be described by a single theoretical model. In the 1970s, the electromagnetic and the weak interaction were successfully joined to a unified theory called the Glashow-Weinberg-Salam [19] (GWS) model. Mathematically the GWS model is described by a $SU(2)_L \times U(1)_Y$ gauge group, where the $SU(2)_L$ gauge group corresponds to three gauge bosons

$W^{1,2,3}$ and the $U(1)_Y$ gauge group has the gauge boson B. These four gauge bosons couple to the linear combination Y of the weak isospin and the electric charge, where Y is called hypercharge, which is defined as $Y = 2(Q - T_3)$.

The observed $\gamma, W^{\pm}$ and Z^0 bosons of the weak interaction however, are a mixture of the gauge bosons in the electroweak model. The weak mixing angle Θ_w relates the B^0 and W_3 gauge bosons to the physical states γ and Z^0. The $W^{\pm}$ bosons are linear combinations of $W_{1,2}$, c.f. Equations 1.1 and 1.2.

$$\begin{pmatrix} \gamma \\ Z^0 \end{pmatrix} = \begin{pmatrix} \cos \Theta_w & \sin \Theta_w \\ -\sin \Theta_w & \cos \Theta_w \end{pmatrix} \begin{pmatrix} B^0 \\ W_3 \end{pmatrix} \tag{1.1}$$

and

$$\begin{pmatrix} W^+ \\ W^- \end{pmatrix} = \frac{1}{\sqrt{2}} \begin{pmatrix} 1 & -i \\ 1 & i \end{pmatrix} \begin{pmatrix} W_1 \\ W_2 \end{pmatrix}. \tag{1.2}$$

The weak mixing angle depends on the mass ratio of the weak gauge bosons and is defined as:

$$\cos \Theta_w = \frac{m_{W^{\pm}}}{m_{Z^0}}, \tag{1.3}$$

which is not predicted by the SM but has to be determined from measurements. Currently, the mixing angle is known to be $\Theta_w = 28.74°$ [14].

In the GWS model, all four bosons are massless, and in order to introduce mass-terms of bosons of the weak interaction the spontaneous symmetry breaking was introduced. The Brout-Englert-Higgs (BEH) mechanism, was introduced in 1964 [20, 21, 22] to accommodate massive gauge bosons in the SM. The scalar Higgs field is introduced, which is accompanied by an observable fundamental particle called the Higgs boson. In 2012, a boson which is compatible with the Higgs boson has been observed by the ATLAS [23] and CMS [24] collaborations.

While the spontaneous symmetry breaking mechanism is leading to the mass of the gauge bosons of the weak interaction, the masses of quarks and charged leptons are described by a Yukawa coupling [25]. The coupling exists for all massive fermions and its strength is proportional to the mass of the fermion. Therefore, the top quark, as the heaviest fermion, is expected to have the largest coupling to the Higgs field. The non-zero masses of neutrinos however, are not introduced by this mechanism and indicate the presence of physics beyond the SM.

Quark Mixing and the CKM Mixing Matrix

The mass eigenstates of quarks are different from the weak eigenstates and their relation has been introduced by Cabbibo, Kobayashi and Maskawa in the form of a mixing matrix [26]. The Cabbibo-Kobayashi-Maskawa (CKM) matrix gives the transformation of the mass eigenstates (d,s,b) and the weak eigenstates (d',s',b'). The CKM matrix is

a unitary 3×3 matrix, assuming three quark generations:

$$\begin{pmatrix} d' \\ s' \\ b' \end{pmatrix} = \begin{pmatrix} V_{ud} & V_{us} & V_{ub} \\ V_{cd} & V_{cs} & V_{cb} \\ V_{td} & V_{ts} & V_{tb} \end{pmatrix} \begin{pmatrix} d \\ s \\ b \end{pmatrix} \tag{1.4}$$

Since the total probability of all transitions for each state is unity, the CKM matrix is unitary. The values of the CKM matrix are not predicted by the SM and are required to be measured experimentally. Equation 1.5 [27] gives the current state of knowledge of the values of the CKM matrix.

$$V = \begin{pmatrix} 0.97427 \pm 0.00014 & 0.22536 \pm 0.00061 & 0.00355 \pm 0.00015 \\ 0.22522 \pm 0.00061 & 0.97343 \pm 0.00015 & 0.0414 \pm 0.0012 \\ 0.00886^{+0.00033}_{-0.00032} & 0.0405^{+0.0011}_{-0.0012} & 0.99914 \pm 0.00005 \end{pmatrix}. \tag{1.5}$$

The CKM matrix is diagonally dominant, reflecting the fact that inter-generation flavour changing decays are strongly suppressed. The strength of the weak interaction of two quarks i and j is proportional to the respective CKM matrix-element $|V_{ij}|^2$. While the transition across generations has a magnitude of some percentage points for the first and second quark generation, $|V_{tb}|^2$ is much larger than $|V_{ts}|^2$ and $|V_{td}|^2$, and therefore top-quarks are almost exclusively decaying into bottom-quarks.

1.3. Hadronic Substructure

Protons that are brought to collision at the LHC, are compound objects which mainly consist, as mentioned before, of two up quarks and one down quark (uud), this however is only true at low energies. At high energies more sub-structure emerges which are called sea-quarks and gluons. The actual collision of two protons is taking place between two specific partons of each proton. The parton distribution functions (PDFs) provide the probability density to find the parton i with the fractional momentum x_i[1] of the proton, at a given energy-scale Q^2.

Theoretical predictions of PDFs cannot be derived from perturbative QCD due to non-perturbative effects in QCD bound states. This is the reason why the knowledge about the PDF is mainly obtained in deep inelastic scattering (DIS) experiments. In more recent PDF sets, LHC collision data is also included.

In order to extrapolate the obtained PDFs at low energies to higher energy scales, the DGLAP evolution equations [28, 29] were devised. The DGLAP evolution equations

---

[1] x refers to the Bjorken scale variable

are expressed in terms of so-called splitting functions or splitting kernels. The splitting functions correspond to four configurations. The production of a quark-gluon pair originating from a quark is described by P_{qq} and P_{gq}. The splitting function P_{qg} describes the production of a quark-antiquark pair originating from a gluon. The splitting function P_{gg} describes the production of a gluon-gluon pair also originating from a gluon. A scale-dependent expression of the probability that the corresponding particle is radiated and carries a certain momentum fraction x is derived. While the extrapolation for massless partons performs well, the DGLAP evolution is not able to incorporate massive partons, and additional methods have to be employed.

Several PDF sets are available by various groups, which each use different assumptions and data to provide precise predictions. The main differences arise from the value of $\alpha_s(m_Z)$, the value of the quark masses and the treatment of the heavy quark masses. The main PDF groups that are considered in this analysis are CTEQ [30, 31], JR [32], ABM [33], MSTW2008 [34]/MMHT14 [35], NNPDF 2.3/ 3.0 [36, 37], and HERAPDF [38, 39].

Figure 1.3 shows the PDFs of several partons which are obtained from NNPDF 3.0 at NLO and $\alpha_s(m_Z) = 0.118$. The distributions of the valence quarks u and d are shown with the $b, \bar{b}$ sea-quarks and the gluon. The gluon PDF is scaled by 0.05. The $Q^2 = m_t^2 = (172.5\,\text{GeV})^2$ is chosen for (a) and $Q^2 = (m_t/4\,\text{GeV})^2$ in (b). The two choices of Q^2 correspond to two distinct calculation schemes of t-channel single top-quark production, that will be introduced in Section 1.5.2.

Table 1.1 contains the PDF sets that are evaluated in the scope of this thesis, including the respective value of $\alpha_s(m_Z)$ and a summary of involved experimental data in their determination. Most used values of $\alpha_s(m_Z)$ are very similar except for the ABM11 PDF set.
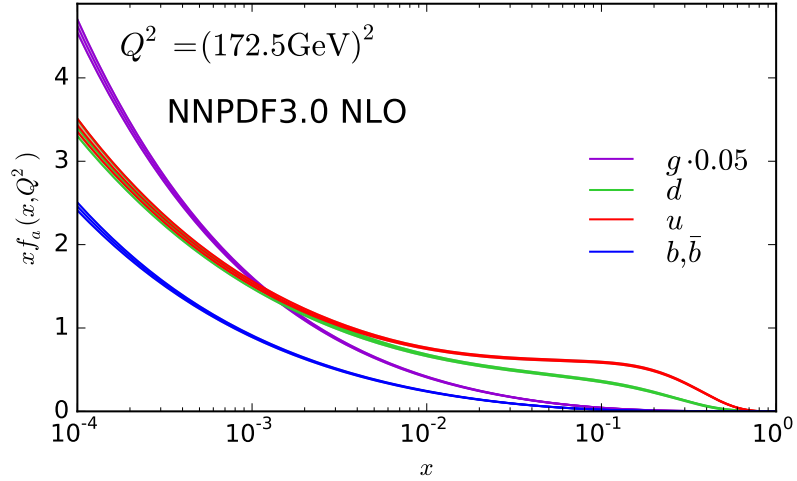
(a)
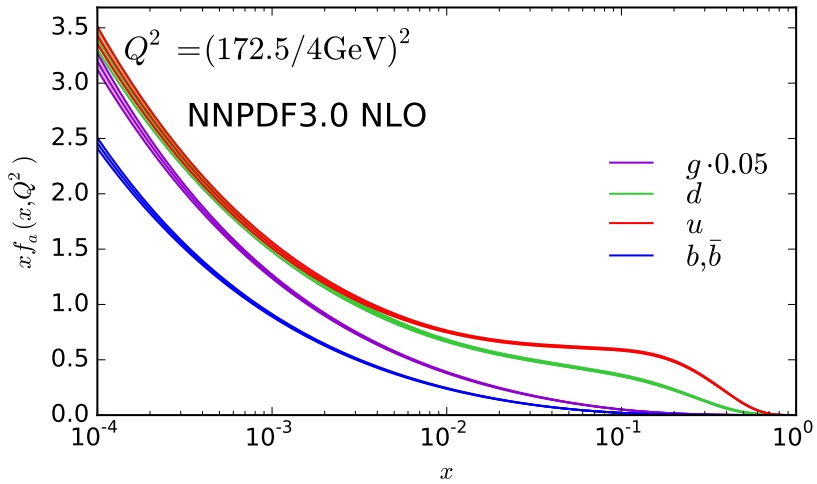
(b)

Figure 1.3.: Parton distribution functions of $\mathrm{NNPDF}\ 3.0$ at NLO and $\alpha_s(m_{\underline{Z}}) = 0.118$. The distributions of the valence quarks u and d are shown with the $b, \bar{b}$ sea-quarks and the gluon. The gluon PDF is scaled by 0.05. The $Q^2 = m_t^2 = (172.5\ \mathrm{GeV})^2$ is chosen for (a) and $Q^2 = (m_t/4\ \mathrm{GeV})^2$ in (b).

Table 1.1.: List of PDF sets together with their used α_s value and the list the experiments from which data are used.

PDF set	$\alpha_s(m_Z)$	Experiments
CT10	0.118	HERA, Fixed target, Tevatron
CT14	0.118	Combined HERA, Fixed target, Tevatron, LHC
ABM11	0.109	Combined HERA, Fixed target
MSTW2008	0.120	HERA, Fixed target, Tevatron
MMHT14	0.120	Combined HERA, Fixed target, Tevatron, LHC
NNPDF 2.3	0.118	Combined HERA, Fixed target, Tevatron, LHC
NNPDF 3.0	0.118	Combined HERA, Fixed target, Tevatron, LHC
JR14	0.116	HERA, Fixed target, Tevatron
HERAPDF 1.5	0.118	Combined HERA
HERAPDF 2.0	0.118	Combined HERA
ATLAS (epWZ12)	0.118	Combined HERA, ATLAS W, Z

1.4. Predictions of the SM

The cross-section calculation in pp collisions can be separated into partonic cross-section $\hat{\sigma}_{a,b}$ of the hard scattering, and the PDFs, as stated by the factorisation theorem [40]:

$$\sigma = \sum_{ab} \int dx_a dx_b f_{a/A}(x_a, Q^2) f_{b/B}(x_b, Q^2) \hat{\sigma}_{a,b} , \qquad (1.6)$$

where x_a and x_b are the fractions of momentum of the protons and $f_{a/A}(x_a, Q^2)$ and $f_{b/B}(x_b, Q^2)$ are the PDFs of the partons a and b, respectively.

In order to calculate the cross-section of particle collisions using the formalism of the SM, approximations need to be employed. Perturbation theory is a mathematical formalism used to obtain approximate results. The perturbative expansion is performed in terms of the coupling constants of the SM Lagrangian. While due to the strength of α_s, the QCD contribution is the largest, the electroweak perturbative expansion in terms of α_W can also give significant contributions, c.f. Ref. [41].

The partonic cross-section $\hat{\sigma}_{a,b}$ can be calculated with perturbative QCD, given that the process involves a high momentum transfer Q^2, corresponding to a sufficiently small α_s, such that the perturbative expansion is valid.

In order to evaluate the expression of the partonic cross-section one needs to choose the renormalisation scale (μ_r) and factorisation scales (μ_f) [42]. The factorisation scale is employed to separate the low-energetic soft regime from the high-energetic hard interaction, while the renormalisation scale controls the absorption of loop divergences into the strong coupling constant.

There is no principle to derive the correct $\mu_{r,f}$ scales, yet the range of them can be limited, see Ref. [42]. This ambiguity is accounted for as a dedicated scale uncertainty. The uncertainty in the scale choice is estimated using a prescription referred to as independent restricted scale variations, proposed in Ref. [43]. In this procedure the renormalisation (μ_r) and factorisation (μ_f) scales are varied independently by a factor of two w.r.t. the nominal scale. The scale variations are restricted since the combinations $\mu_r = 2 \cdot \mu_r^{nom}, \mu_f = 0.5 \cdot \mu_f^{nom}$ and $\mu_f = 2 \cdot \mu_f^{nom}, \mu_r = 0.5 \cdot \mu_r^{nom}$ are excluded to prevent overestimation of the effect.

The order of perturbative expansion that is considered by a calculation is denoted leading order (LO), for the lowest order approximation and next-to-leading order (NLO) refers to an additional power of (α_s), and so forth.

In addition to the accuracy provided by the order of perturbative expansion that is considered, additionally soft-gluon effects can be included to improve the precision of the estimate. The so-called soft-gluon resummation [44, 45], hereby enables to resum contributions of gluons that are not considered due to the choice of μ_f, into α_s. These

soft-gluon contributions lead to logarithms, which are divergent in the calculation of the fixed-order perturbation theory and are therefore truncated at the μ_f scale. The soft-gluon resummation however adds these contributions to the fixed-order calculation and are denoted in terms of the order of the considered logarithm, thereby leading-logarithm (LL) and next-to-leading-logarithm (NLL) are differentiated.

While the higher-order contributions of the fixed-order perturbative calculation can entail cancellation effects and can have negative magnitude, the magnitude of the soft-gluon resummation is always positive.

1.5. Top-Quarks

The top-quark (t) has the highest mass of all known fundamental particles. The mass of the top-quark is not predicted by the SM and has to be determined in experiments.

The decay width of the top-quark decay $\Gamma_t = 1.35\,\text{GeV}$ at NLO [27], assuming $m_t = 173.3\,\text{GeV}$, which corresponds to a average lifetime of $\tau_t \approx 0.5 \cdot 10^{-24}$ s [46]. The lifetime of the top-quark is smaller than the timescale on which the strong force acts $1/\Lambda_{QCD} \approx 10^{-23}$ s [47]. Therefore, top-quarks decay before they can form hadrons, fully retaining the spin-information of the top-quark and enables its study as a bare quark.

The top-quark decay is almost entirely dominated by the $t \to Wb$ mode. The origin of this is that the CKM-matrix element $|V_{tb}|^2$, which corresponds to the transition probability of a t quark into a b quark, is close to unity. The W boson consecutively decays into either leptons or quarks. While the branching fraction of the W boson into quarks is exceeding those of the leptonic decay modes, the hadronic decay modes suffer from a large background, which renders the leptonic W-boson decay modes the preferred one for this thesis.

1.5.1. Production of Top-Quarks

The production of top-quarks at the LHC occurs in two major modes, producing either a top-quark–top-antiquark ($t\bar{t}$) pair or a single top-quark or a single top-antiquark. The main production mode is induced by the strong interaction, where a $t\bar{t}$ pair is emerging, while single top-quarks are produced by means of the weak interaction, leading to a reduced production rate of the latter.

Top-Quark–Top-Antiquark Pair Production

Top-quark pair production is dominated by the gluon-fusion channel at the LHC which is supplemented by quark-antiquark annihilation. Both modes are represented in Figure 1.4. The total cross-section for $t\bar{t}$ is calculated at next-to-next-to leading order (NNLO) in fixed-order perturbative QCD, including soft-gluon resummation at next-to-next-to leading logarithm (NNLL) to be $\sigma(t\bar{t}) = 253^{+13}_{-15}$ pb [48] at $\sqrt{s} = 8\,\text{TeV}$. The cross-section calculation assumes a top-quark mass of 172.5 GeV.
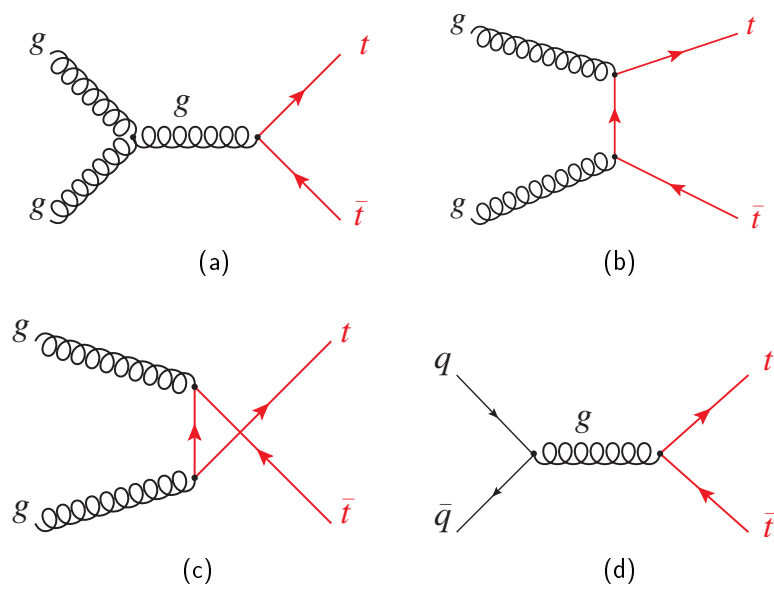
Figure 1.4.: Feynman diagrams of the dominant $t\bar{t}$ production modes. (a)-(c) are gluon fusion induced processes, while (d) shows the production via $q\bar{q}$ annihilation.

Single Top-Quark Production

Single top-quark production is occurring in three distinct production modes, which are distinguished by the virtuality of the exchanged W-boson. The t-channel mode is the most dominant production which is the focus of this thesis. Figure 1.5(a) shows the LO-signature of the t-channel production in the 5 FS. The top quark is produced by the weak interaction of a b-quark with a light-quark via a W-boson exchange. The initial light-quark is originating from the incoming proton, while the b-quark emerges from a gluon-splitting in the 4 FS, which will be introduced in the following Section 1.5.2. The initial light-quark changes its flavour in the process and is scattered into the forward region of the detector. The t-channel production can involve a top quark as well as a top-antiquark, which are denoted tq and $\bar{t}q$ respectively. Due to charge conservation the initial light-quark of the tq and $\bar{t}q$ are different. In case of the tq production the initial light-quarks can be either up-type quarks or down-type antiquarks, while for $\bar{t}q$ vice versa, down-type quarks and up-type antiquarks. Since a valence quark is involved in the production of top-quarks and top-antiquarks, a preliminary conclusion on the cross-section ratio can be drawn. The ratio of u- over d-quarks in the proton is exactly two, which directly relates to the roughly estimated cross-section ratio. This estimate does not account for the relative contributions of the other light-quarks mentioned.

The top-quark produced in the t-channel configuration is 100 % polarised in the direction of the light quark. As mentioned before, the top-quark decays before hadronisation, thereby transferring the spin information to the W boson and subsequently the lepton. The single top-quark t-channel production was measured for the first time at the Tevatron at $\sqrt{s} = 1.96$ TeV [49, 50]. At the LHC, measurements of the t-channel single top-quark cross-section at $\sqrt{s} = 7$ TeV have been performed by the ATLAS Collaboration [51, 52] as well as by the CMS Collaboration [53]. At a center-of-mass energy of $\sqrt{s} = 8$ TeV the CMS Collaboration measured the t-channel cross-sections and the cross-section ratio, R_t [54].

The other production modes are the associated production of a W boson and a top quark (Wt), as well as the s-channel ($t\bar{b}$). The LO representations are shown in Figure 1.5(b) for the Wt-channel and in Figure 1.5(c) for the s-channel.

1.5.2. Number flavour Schemes

The t-channel single top-quark MC event generation can be performed by means of two distinct theoretical calculation methods, which offer several contrasting features. The calculation methods are referred to as four-flavour scheme (4 FS) and five-flavour scheme (5 FS), which correspond to the treatment of heavy-quarks in PDFs. Since the DGLAP evolution is not valid for massive quarks, a dedicated treatment is required to properly account for heavy-quark contributions, see Ref. [55]. To alleviate the $m_b = 0$
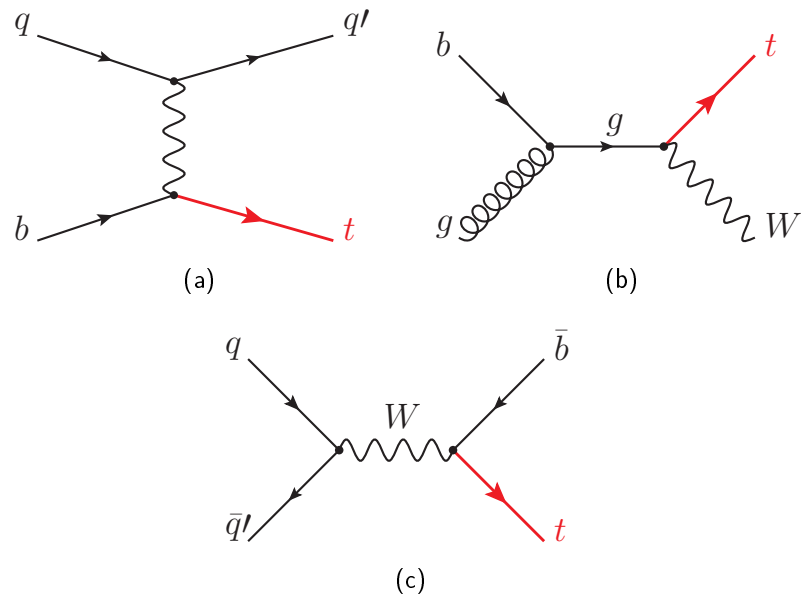
Figure 1.5.: Feynman diagrams of the dominant single top-quark production modes. The t-channel production is shown in (a) at the LO representation in the 5 FS. The Wt-channel and s-channel LO representations are shown in (b) and (c), respectively.

approximation used in the DGLAP evolution, initial state b-quarks can be systematically replaced by gluon-splittings.

Figure 1.6 displays the LO representations of the t-channel single top-quark production in the 5 FS (a) and 4 FS (b).
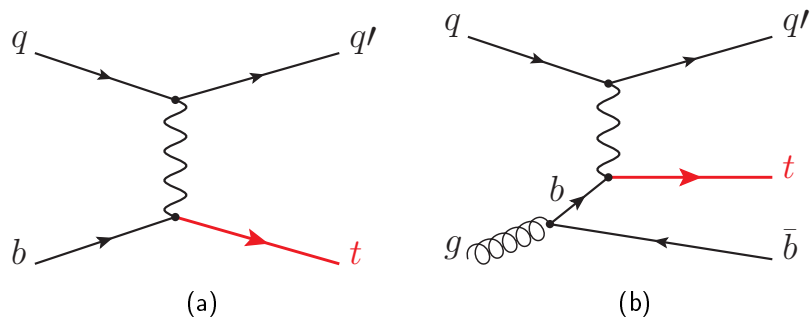
Figure 1.6.: Feynman diagrams of the t-channel single top-quark production modes in the 5 FS (a) and the 4 FS (b).

In the 4 FS, the initial b-quark is not introduced from the PDFs but from gluon-splitting and therefore generated in the matrix elements. In the 5 FS the initial b-quarks mass

needs to be neglected in the matrix element calculation to remain valid in terms of factorisation. The cross-section depends on the b-quark mass only implicitly in the 5 FS, but it is explicitly contained in the matrix elements in the 4 FS, see Ref. [56]. Another difference of both schemes becomes visible upon evaluating the scale uncertainty, as the scale dependence of the 4 FS representation is stronger than that of the 5 FS representation, due to the additional factor of α_S in the ME, see Ref. [57].

The 2nd b-quark enters only at NLO in the 5 FS ME and is therefore modelled at LO accuracy for current NLO MC ME-generators, or at LL accuracy if the 2nd b-quark is added by the PS MC generator. In the 4 FS ME the 2nd b-quark is already included at LO and thus has an improved accuracy with recent MC generators. Therefore, quantities involving the 2nd b-quark are better modeled in the 4 FS.

While in the 5 FS logarithms of the form $\log(\mu_f^2/m_b^2)$ of the PDF evolution are resummed, which leads to a more precise total rate calculation at NLO, this effect almost vanishes for the 4 FS. The effects of this resummation however are mild, according to Ref. [58].

A useful choice of the $\mu_{r,f}$ scales in the 5 FS is $\mu_{r,f} = m_t$ as well as $\mu_{r,f} = m_t/4$ in the 4 FS. Indications for the difference of scale choice for the 5 FS and 4 FS are presented in Ref. [56]. In the case of a dynamic scale choice in the 4 FS of $\mu_r = \mu_f = 4 \cdot \sqrt{m_b^2 + p_{T,b}^2}$, it was found in Ref. [56], that $\mu_{r,f} = m_t/4$ correspond to the average scale in the bulk of MC events.

In summary, the 5 FS provides the most accurate estimate of the total cross-section, while the 4 FS is the better choice when differential distributions are compared, especially involving the 2nd b-quark kinematics. In the limit in perturbation theory, when all orders are considered, both 4 FS and 5 FS are exactly equivalent in terms of the total production cross-section.

The ATLAS Experiment at the Large Hadron Collider

The aspiration of experimental physics is to devise experiments that can test theoretical predictions as well as explore and discover new physics. The SM has been subject of rigorous inspection by many experiments over the last decades. The most important improvement over time is the energy scale at which particles are brought to collision. Besides the energy scale, the luminosity of a collider is an important metric, which indicate the expected performance in terms of expected particle collisions per time-interval and collision area. Higher collision energies and high luminosities enable to probe rare particle productions at the frontier of our understanding. Various designs of particle colliders have been developed, where proton synchrotron colliders provide the currently highest center-of-mass energy of $\sqrt{s} = 13\,\text{TeV}$.

2.1. The Large Hadron Collider

The LHC at CERN, near Geneva is the currently most powerful particle accelerator in the world. It is the largest ring at the CERN accelerator complex depicted in Figure 2.1, which is between 45 m and 170 m underground. At the LHC either protons or lead ions are accelerated and brought to collision at four interaction points, which host the main experiments. Protons are boosted in large packages, which are called bunches, by a chain of smaller accelerators to reach the full energy. Table 2.1 shows an overview

of the performance reached by the LHC in 2012, compared to the design parameters. In many terms the LHC has nearly reached its potential, and in some even surpassed it.
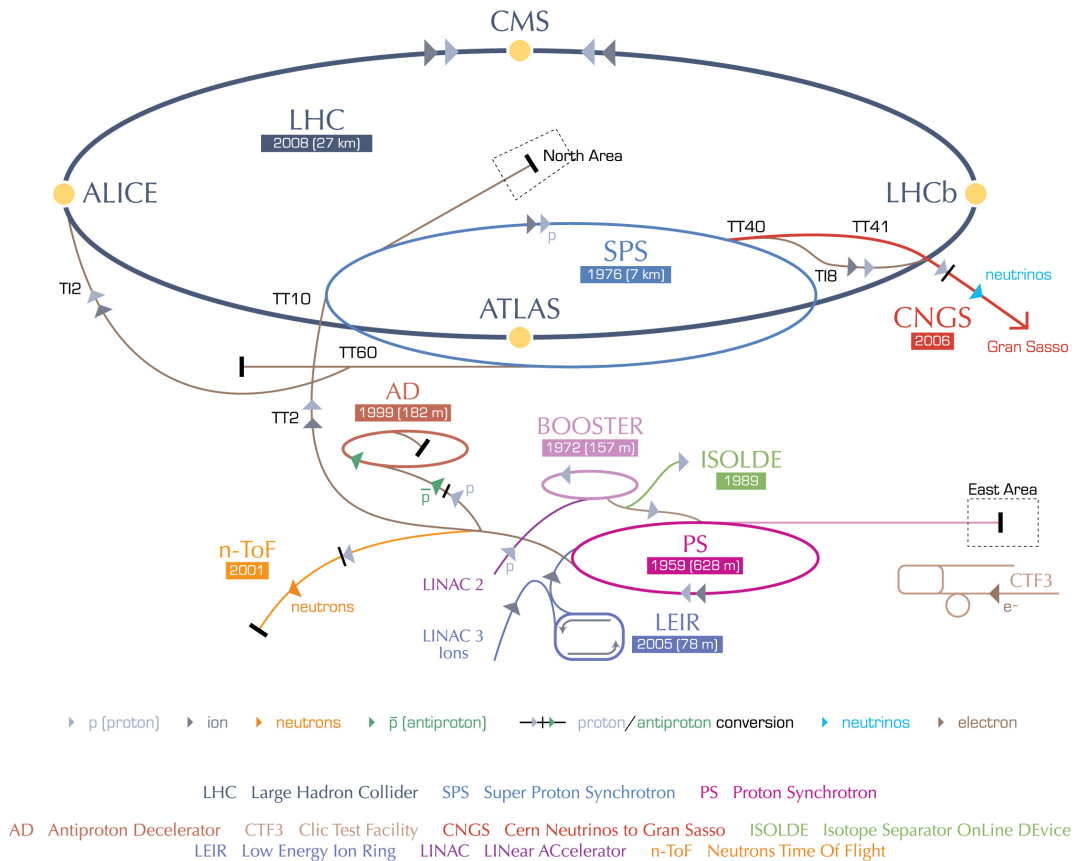
Figure 2.1.: The CERN accelerator complex [59]. The largest ring contains the LHC accelerator, which is supplied with high energetic protons from a chain of smaller accelerators.

ATLAS is a multi-purpose detector designed to cover a large fraction of physics processes at high energies anticipated to occur. Among the already known SM physics, the detector is designed to enable the exploration of unprecedented physics regimes. The search focus for new physics was initially dominated by the Higgs-boson, which culminated in the discovery of the Higgs-boson in 2012 [60]. The search focus shifted towards Super Symmetry and other theoretical models, for which sensitivity might be in reach.

CMS (**C**ompact **M**uon **S**olenoid) [61] is the other multi-purpose detector which covers nearly the same physics as ATLAS. Both experiments are also built with similar focus, in order to validate or refute observations made by the other. This principle was beau-

tifully demonstrated in the observation of the Higgs boson [62], which is compatible with the discovery made by ATLAS.

ALICE (**A L**arge **I**on **C**ollider **E**xperiment) [63] utilises the capability of the LHC to collide lead ions, to inspect the quark-gluon plasma state. This state of matter is similar to the state of the Universe moments after the big bang, enabling the study of QCD confinement.

The LHCb (LHC beauty) [64] experiment is specialised to detect hadron decays, where the hadron contains *b*-quarks, to inspect the imbalance of matter versus antimatter in the universe, known as CP-violation. In 2015 LHCb observed a resonance consistent with a pentaquark state [17], which has been predicted by theory.

Besides the four main experiments at the LHC there are three highly specialised detectors. LHCf (LHC forward) [65] is designed to investigate π^0 mesons, which are produced in a small angle with respect to the beam pipe. The aim is to improve the understanding of cosmic rays and their theoretical modelling. TOTEM (**TOT**al **E**lastic and diffractive cross-section **M**easurement) [66], measures the total cross-section of proton-proton collisions, with regard to elastic and diffractive scattering. MoEDAL (**Mo**nopol and **E**xotics **D**etector **A**t the **L**HC) [67] is specialised to search for magnetic monopoles and massive pseudo-stable charged particles.

2.2. Luminosity

The luminosity of the LHC is one of the most important features of a particle accelerator, as it determines the performance in terms of expected particle collisions per time-interval and collision area.

The definition of the luminosity L is given by:

$$L = \frac{N_{\text{bunches}} \cdot f_{\text{rev}} \cdot N_1 \cdot N_2}{A},$$

(2.1)

where f_{rev} is the revolution frequency and $N_{1,2}$ is the number of colliding particles in the bunches of beam 1 and beam 2. The area A corresponds to the effective collision area, given at a beam width of two standard deviations; and N_{bunches} is the number of bunches. The area A in Equation 2.1 is given by:

$$A = 4\pi \epsilon \beta^* = 4\pi \frac{\epsilon^*}{\beta\gamma} \cdot \beta^*,$$

(2.2)

with ϵ being the physical emittance of the beam. It is related to the normalised emittance ϵ^* by $\epsilon^* = \beta\gamma \cdot \epsilon$, β being the relativistic velocity v/c and γ being the relativistic γ-factor. The value of the betatron function β at the point of the collision is denoted

Table 2.1.: LHC performance in 2012 compared to the design parameters [68].

Parameter	2012	Design
Beam Energy [TeV]	4	7
β^* [m] in ATLAS	0.6	0.55
Bunch spacing [ns]	50	25
N_p per bunch	$1.6 - 1.7 \cdot 10^{11}$	$1.15 \cdot 10^{11}$
N_{bunches}	1374	2808
$L_{\text{max}}[\text{cm}^{-2}\,\text{s}^{-1}]$	$7.7 \cdot 10^{33}$	$1 \cdot 10^{34}$

β^*. Thus, the luminosity at the LHC can be expressed as:

$$L = \frac{f \cdot N_p^2 \cdot N_{\text{bunches}} \cdot F \cdot \beta\gamma}{4 \cdot \pi \cdot \epsilon^* \cdot \beta^*}, \tag{2.3}$$

assuming that the bunches in beam 1 and beam 2 contain the same number of protons N_p. The additional factor F accounts for the geometrical reduction due to the overlap of the two ellipses of the colliding bunches, determined by the crossing angle between them and their individual geometric parameters. Details can be found in Ref. [1].

Table 2.1 shows several LHC parameters as they were used for the 2012 data-taking period compared to the design parameters.

2.3. The ATLAS Detector

The ATLAS detector is located at interaction point 1 (IP1) approximately 100 m underground. Following the design of a multi-purpose detector, ATLAS is constructed to cover most of the solid angle. While the performance focus of ATLAS is towards measuring particles that are produced transverse to the beam axis, the barrel layout of ATLAS also provides decent precision at small angles to the beam axis. The particles that are produced in the proton collision have different physical observables, which can be individually measured by sub-detectors. The sub-detectors are constructed in a concentric layered pattern, around the beam axis, from the inside out, shown in Figure 2.2. The sub-detector closest to the collision point is the inner detector (ID). The IDs main purpose is to measure charged particle trajectories. In the next sub-detector layer, the energy measurement of charged and neutral particles is performed by the calorimeter system. These sub-detectors are surrounded by the muon system, forming the outermost part of ATLAS. The muon system measures the momentum of muons and provides trigger information. This Section introduces the ATLAS detector as is was for the 2012 data-taking period.

The ATLAS coordinate system has its origin at the nominal interaction point, while the z-axis is defined alongside the beam direction. The x–y-plane is defined transverse to the z-axis where the positive x-axis is pointing to the center of the LHC ring and the positive y-axis points upwards. Because of the cylindrical layout of ATLAS it is convenient to define the polar angle θ with respect to the beam, as well as the azimuthal angle ϕ around the beam axis. The transverse component of the momentum, is defined as the magnitude of the momentum in the x–y-plane:

$$p_{\mathrm{T}} = \sqrt{p_x^2 + p_y^2}. \tag{2.4}$$

For physics reasons the rapidity, y, is used instead of θ:

$$y = \frac{1}{2} \ln \left(\frac{E + p_z}{E - p_z} \right), \tag{2.5}$$

or the pseudorapidity is defined as:

$$\eta = -\ln \tan \left(\frac{\theta}{2} \right), \tag{2.6}$$

which is identical to y for massless particles. The distance between two objects is expressed in the η–ϕ-plane:

$$\Delta R = \sqrt{(\Delta \eta)^2 + (\Delta \phi)^2} \tag{2.7}$$

The transverse component of the energy is:

$$E_{\mathrm{T}} = E \cdot \sin\theta = \sqrt{m^2 + p_{\mathrm{T}}^2}. \tag{2.8}$$
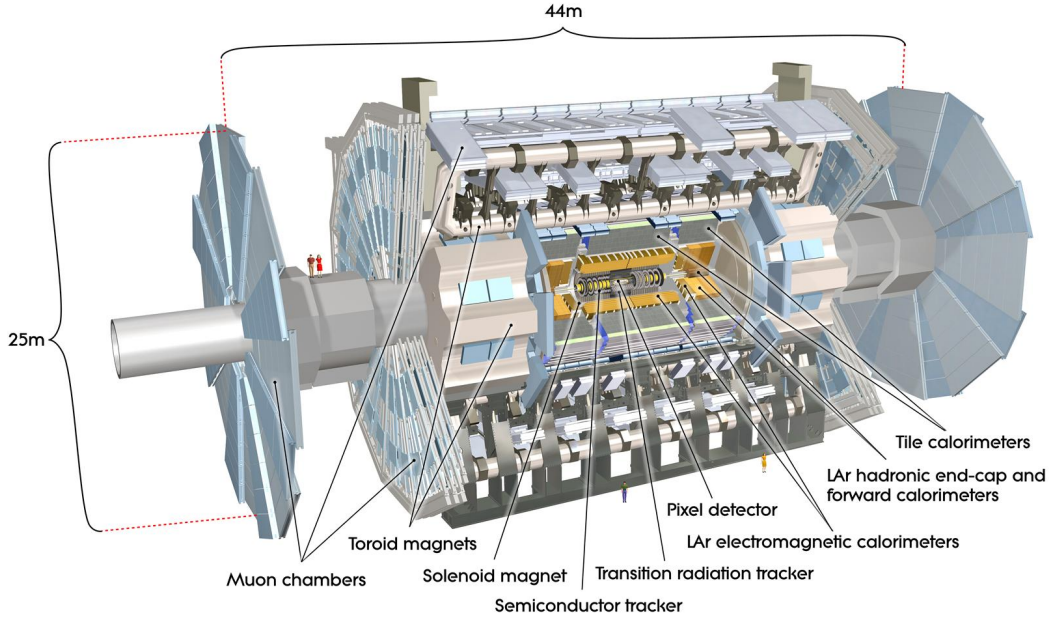
Figure 2.2.: Cut-away view of the ATLAS detector. The dimensions of the detector are 25 m in height and 44 m in length [2].

2.3.1. The Inner Detector

The ID [69] is built to identify the trajectories of charged particles produced in the proton collision, promptly after they emerge. This task is best performed in direct vicinity to the particle production. The momentum of charged particles is measured by immersing the ID in a 2 T solenoidal magnetic field.

In addition, the ID is operating in a very dense environment, since about 1000 particles are created in each proton collision. Additionally, the collision rate of 40 MHz places great demands on the read-out system.

The ID is build from three complementary sub-detectors which contribute to the determination of particle trajectories within $|\eta| < 2.5$.

Figure 2.3 illustrates the sub-detector layout of the ID. The layout of the barrel region and the endcap region are shown in (a) and (b), respectively.

- The pixel detector extends from 50.5 to 122.5 mm from the beam axis. The pixel detector consists of 1744 silicon pixel modules layered in three levels in the barrel region and three discs in the endcap region. The Pixel detector is contributing three space points to the track determination with a resolution of $10 \times 115\,\mu m$ in $R - \phi \times z$.

- The semiconductor tracker (SCT) [70] is the second ID sub-detector consisting of 4088 modules of silicon microstrip sensors. The modules are layered in four levels in the barrel region and nine discs in the endcap region. Two identical pairs of modules are glued back-to-back, with a stereo angle of 40 mrad between them to improve the resolution in the z-direction. The SCT sub-detector contributes typically eight strip-measurements which corresponds to four space points with a resolution of $17 \times 580\,\mu m$ in $R - \phi \times z$ to the ID track determination.

- The transition radiation tracker (TRT) [71] is the outer-most sub-detector of the ID. The TRT performs two complementary measurements, one is the track determination, and the other is the electron identification. Proportional drift-tubes (straws) contain a xenon-based gas-mixture, which is ionised by traversing charged particles. The electrons are accelerated by a strong electric field towards a sense wire in the center of each straw, which produces a measurable signal. The straws are arranged in cylindrical layers in the barrel region and radially oriented in the endcap region. Between the straws two different materials with highly varying indices of refraction are placed. The difference in the refractive indices cause ultra-relativistic particles to emit transition radiation, which lead to distinct signals in the straws. The transition radiation is a good discriminator to distinguish electrons from charged pions. The TRT sub-detector typically provides 35 space points with a resolution of $130\,\mu m$ to the ID track determination.

Table 2.2 summarises the main characteristics of the ID sub-detectors.

Table 2.2.: Summary of the main characteristics of the ID sub-detectors. The individual size and resolution of the sensor elements are compared amongst the sub-detectors, as well as the number of track space-points provided to the overall track determination [72].

Sub-detector	Radius [mm]	Element size $R - \phi \times z$	Resolution $R - \phi \times z$	Track space-points
Pixel	$50.5 - 122.5$	$50 \times 400\,\mu m$	$10 \times 115\,\mu m$	3
SCT	$299 - 560$	$80\,\mu m$	$17 \times 580\,\mu m$	4
TRT	$563 - 1066$	$4\,mm$	$130\,\mu m$	35
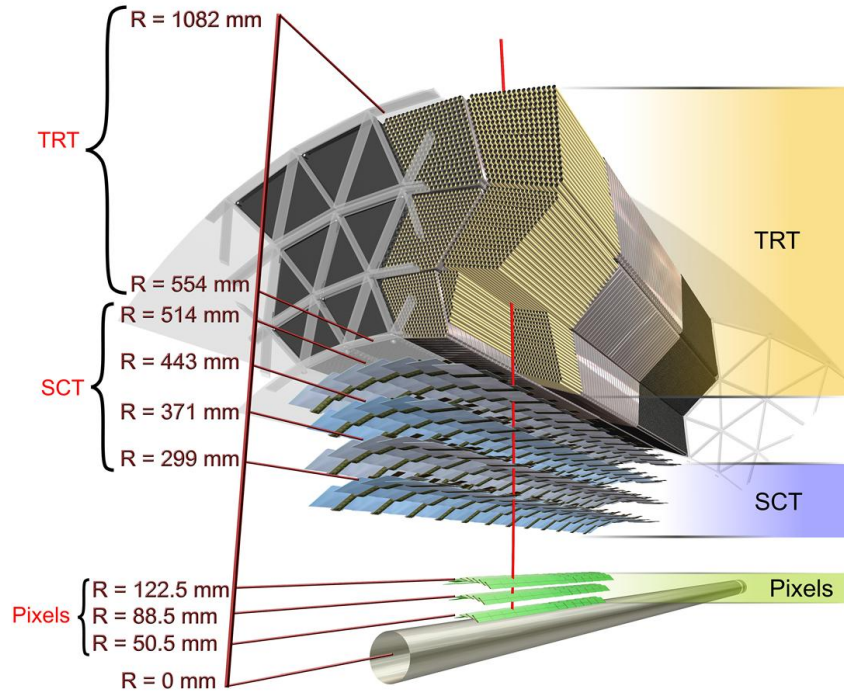
(a) ID barrel region
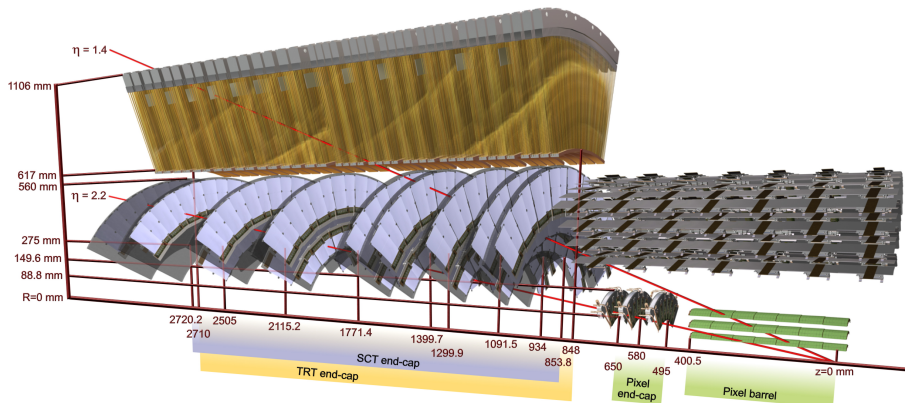
(b) ID endcap region

Figure 2.3.: Illustration of the ID and its components with focus on the barrel region in (a), and the endcap region in (b). The red lines in (b) indicate a particle passing the ID at $\eta = 1.4$ and $\eta = 2.2$. [73].

2.3.2. The Calorimeter System

The ATLAS calorimeter system [74] provides the particle energy determination capability to the ATLAS experiment. The calorimeter is forming the second sub-detector beyond the ID with a full ϕ coverage and $|\eta| < 4.9$, see Figure 2.2. In order to measure the energy of a particle, its energy is absorbed in the calorimeter system. The calorimeter system follows the sampling calorimeter design, which uses alternating layers of absorber material and active material. The sampling calorimeter design enables a precise measurement of the energy, deposited in the active material, while reducing the transverse dimensions of the calorimeter system. The absorber material promotes the decay of the incident particles into a particle shower, which is detected in the active material. The individual absorber material and active material are different for separate parts of the calorimeter system. Since the energy of both light particles and also hadrons needs to be determined at high precision, the calorimeter is sub-divided into the electromagnetic (EM) calorimeter and the hadronic calorimeter. The calorimeter system is non-compensating, which implies that the calorimeter response to EM particles and hadrons is not identical, and must be calibrated accordingly.

- The EM calorimeter is specialised in the energy determination of electrons and photons. Electrons radiate their energy in form of bremsstrahlung when entering the absorber material. A large fraction of photons produced by this process convert to electron–positron pairs. This effect is called pair production. Bremsstrahlung and subsequent pair production lead to showers of EM particles. The extension of the EM calorimeter can be expressed in terms of radiation length X_0, where the barrel region provides the least coverage of 22 X_0 which is increased to over 30 X_0 in the endcap region, ensuring that most electrons are captured.[1] The barrel region of the EM calorimeter is defined within $|\eta| < 1.5$, the endcap region within $1.5 < |\eta| < 3.2$ and the forward region within $3.1 < |\eta| < 4.9$. Liquid Argon (LAr) is used as active material, while the absorber material is lead in the barrel and endcap calorimeters as well as copper in the forward calorimeter. The barrel calorimeter is constructed in a accordion layout, which provides a full ϕ coverage without cracks.

- The hadronic calorimeter is placed beyond the EM calorimeter to capture particles which did not deposit all their energy in the EM calorimeter. The main purpose of the hadronic calorimeter is to determine the energy of hadrons. The hadronic calorimeter consists of four segments, the barrel region $|\eta| < 1.0$, the extended barrel $0.8 < |\eta| < 1.7$, the endcap $1.5 < |\eta| < 3.2$ and the forward calorimeter $3.1 < |\eta| < 4.9$. Three different components cover the complete range in η, the tile calorimeter (TileCal) in the barrel and extended barrel regions, the LAr hadronic endcap calorimeter (HEC), as well as the LAr forward calorimeter (FCal). The TileCal is composed of steel as absorber material as well as scintillating tiles

---

[1] Mean distance over which the energy of a high-energetic electron is reduced to $1/e$ via bremsstrahlung.

for the active material. In the HEC copper is utilised as absorber material, while tungsten is used for FCal. The depth of the hadronic calorimeter can, similar to the EM calorimeter, be expressed via the interaction length λ.[2] The hadronic calorimeter provides at least 10 λ over most of the η range, up to 14 − 18 λ in the barrel and endcap regions.

2.3.3. Muon Spectrometer

The **m**uon **s**pectrometer (MS) [75] forms the outer-most part of ATLAS. The first main objective of the MS is the determination of muon trajectories and momentum. As the interaction of muons with matter is much weaker than for electrons, muons pass the ID and the calorimeter system. Within the pseudorapidity of $|\eta|$ < 2.7 the MS provides trajectory and momentum determination of muons, as well as trigger capability up to $|\eta|$ < 2.4, which is the second main objective. In order to access the muon momentum, the MS is immersed in a toroidal magnetic field, generated by three separate superconducting magnets. The magnetic field is designed to be mostly orthogonal with respect to the muon trajectories, thus maximising the bending of the trajectories, while minimising the degradation of resolution due to multiple scattering. The field strength in the barrel region is 0.5 T, which is increased to 1.0 T for the end-cap region.

Four different technologies are employed to fulfil the MS objectives under different circumstances. The **m**onitored **d**rift **t**ubes (MDTs) perform the most precise measurement of the muon momentum within the MS. The MDTs are drift chambers in the form of aluminium tubes with a diameter of 3 cm and variable length. The MDT tubes contain a argon-based gas mixture which is ionised by traversing muons. The MDT resolution is 80 μm for a individual tube and 35 μm in the z-direction. The MDTs are arranged in three cylindrical layers at 5 m, 7.5 m and 10 m from the beam axis.

Due to higher background rates in close proximity to the beams, **c**athode **s**trip **c**hambers (CSCs) are replacing the functionality of the MDTs in the forward region between 2.0 < $|\eta|$ < 2.7 and close to the interaction point. CSCs are multiwire proportional chambers where the readout is performed using cathode strips, which are perpendicular to the wires. To improve the spatial resolution the cathode strips are segmented in addition to allow for charge interpolation between adjacent wires. CSCs provide higher granularity compared to the MDTs.

Resistive **p**late **c**hambers (RPCs) are gaseous detectors placed on both sides of MDTs to provide trigger information in the barrel region within the pseudorapidity range $|\eta|$ < 1.05. **T**hin **g**ap **c**hambers (TGCs) serve a similar function as the RPCs but

---

[2]Mean distance over which the numbers of relativistic charged particles is reduced to 1/e via nuclear interaction.

in the end-cap region $1.05 < |\eta| < 2.7$. The TGCs are placed on both sides of the MDTs or CSCs, respectively. In addition to the trigger capability, both RPCs and TGCs add complementary coordinate measurement w.r.t. MDTs and CSCs, to the track determination.

A typical muon track traversing the MS has about 20 associated space points, which reach 35 μm spatial resolution [76]. The momentum resolution at low p_T is still dominated by the ID, while above 100 GeV the MS dominates the combined momentum resolution for muons.

2.3.4. Data Acquisition and Trigger System

The ATLAS trigger system [2, 77, 78] performs a fast analysis of the data collected to reduce the amount of events that will be stored. The storage of the all measured events is not possible by current technology, hence only predefined categories of events pass the trigger system in order to be stored for analyses. The trigger system is designed in a three stage approach, where each stage refines the decision of its predecessor. The level-1 trigger (L1) is hardware-based and provides a response in 2.5 μs at maximum. The consecutive level-2 trigger (L2) and event-filter (EF) are software based and ensure 40 ms for the L2 and 4 s in case of the EF. Figure 2.4 shows an illustration of the ATLAS trigger system, including the trigger stages and the technical infrastructure. Approximate requirements on the event rates are also indicated.

- The hardware-based L1 is capable to reduce the event rate from 20 MHz to maximal 70 kHz in the 2012 data taking. The L1-trigger decision incorporates coarse information about electrons, photons, muons, jets, and τ-leptons decaying into hadrons, as well as scalar sums of transverse energy. All information is obtained from the calorimeter system at reduced granularity and the muon system.

- The L2 trigger improves the coarse L1-trigger decision by invoking object reconstruction in regions-of-interest (RoIs) seeded by the L1. The L2 trigger has the entire information of the all detector components in the RoIs at its disposal.

- The EF invokes a full event reconstruction adopted from the offline reconstruction to apply pattern recognition in order to further reduce the event rate to approximately 700 Hz on average and 1000 Hz at peak.

Given the post-trigger event rate of 700 Hz and an average size of the event information that needs to be stored of approximately 1.5 Mb, this yields 1050 Mb/s of data to store for further processing.
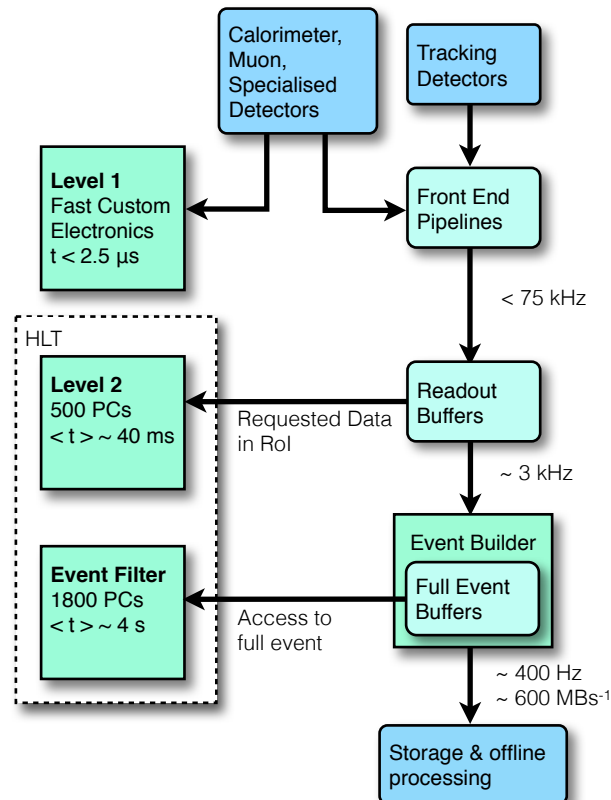
Figure 2.4.: Illustration of the ATLAS trigger system [79]. The individual trigger stages and the technical infrastructure are indicated with the approximate event rate demands. The displayed rates correspond to the 2011 data-taking period.

ATLAS Data and Monte Carlo Simulation

It is imperative for this analysis to have theoretical models which are able to describe the collective physics processes that comprise the selected sample. The modelling of the t-channel single top-quark process is most important, as it directly relates to the capability to extract the process cross-section at high precision. As the background processes carry a significant fraction of the selected data events, their precise modelling is important as well. Almost the entire set of included processes rely on Monte Carlo (MC) event generation to mimic the underlying physics.

This chapter introduces the observed data sample that is analysed as well as the primary features of the MC simulation. A detailed list of used MC samples is provided.

3.1. Observed Data

The collected data obtained with the ATLAS detector in the Run 1 2012 data taking period is analysed in this thesis. The data have been collected from 5$^\text{th}$ April 2012 until 6$^\text{th}$ December, accumulating $\mathcal{L}_\text{int}$ = 20.2 ± 0.4 fb^{-1} of integrated luminosity of pp collisions. Figure 3.1(a) shows the accumulation of luminosity over time in 2012. The determination of the luminosity is performed in Ref. [80]. The beam energy was set to 4 TeV resulting in 8 TeV center-of-mass energy at the interaction point.

In order to maximise the delivered integrated luminosity, the LHC used a dense pattern of proton bunches where the bunch spacing was set to be 50 ns, which results in a high
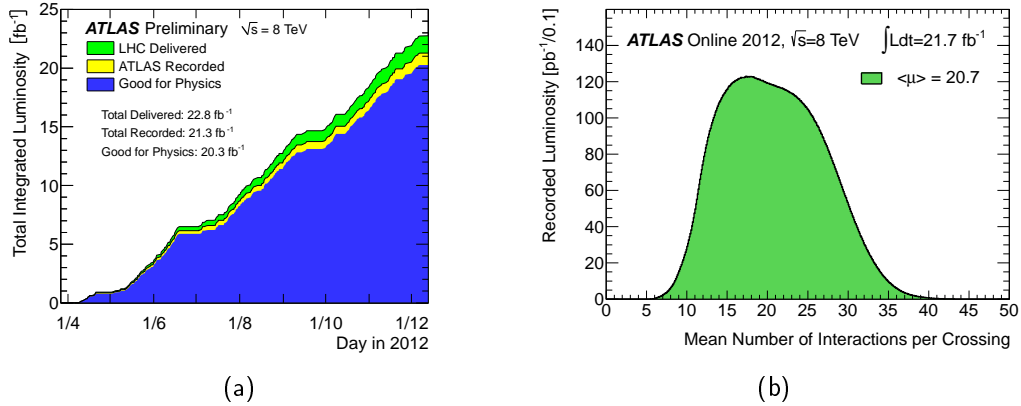
Figure 3.1.: Delivered LHC luminosity and ATLAS recorded in 2012 shown in (a) and average interactions per bunch-crossing for the 2012 dataset in (b). [81]

number of additional interactions.

These additional interactions are referred to as pile-up events. The average interaction per bunch-crossing is shown in Figure 3.1(b), for the 2012 dataset. The pile-up activity is very high with 20.7 average interactions per bunch-crossing.

The event selection on trigger level employs two triggers to select potential electron events (`EF_e24vhi_medium1`, `EF_e60_medium`) as well as two triggers to select potential muon events (`EF_mu36_tight`, `EF_mu24i_tight`).

Electron Trigger

The three stage trigger system, which is introduced in Section 2.3.4, provides the basis selection of electron candidates. Events are selected at L1 trigger stage, that have $E_T > 30\,\text{GeV}$ or $E_T > 18\,\text{GeV}$ if the electron is isolated. In the EF trigger stage, the L1 calorimeter cluster is matched to a track and is required to have $E_T > 60\,\text{GeV}$ (`EF_e60_medium`) [82] or $E_T > 24\,\text{GeV}$ (`EF_e24vhi_medium1`) [82] in case of the electron candidate being isolated.

Muon Trigger

This analysis uses two separate single-muon triggers, which at L1 require a muon trigger-chamber track with a $p_T > 15\,\text{GeV}$-threshold. At the EF the transverse momentum must be higher than $p_T > 36\,\text{GeV}$ (`EF_mu36_tight`) [77] or $p_T > 24\,\text{GeV}$ (`EF_mu24i_tight`) [77] in case of the object being isolated.

3.2. Monte Carlo Simulation

Monte Carlo simulation is the means by which current event generators and parton showers create realistic artificial particle physics interactions and the decays. The main premise of the MC method is the sampling of highly complex phase space, which is not possible in an analytic approach.
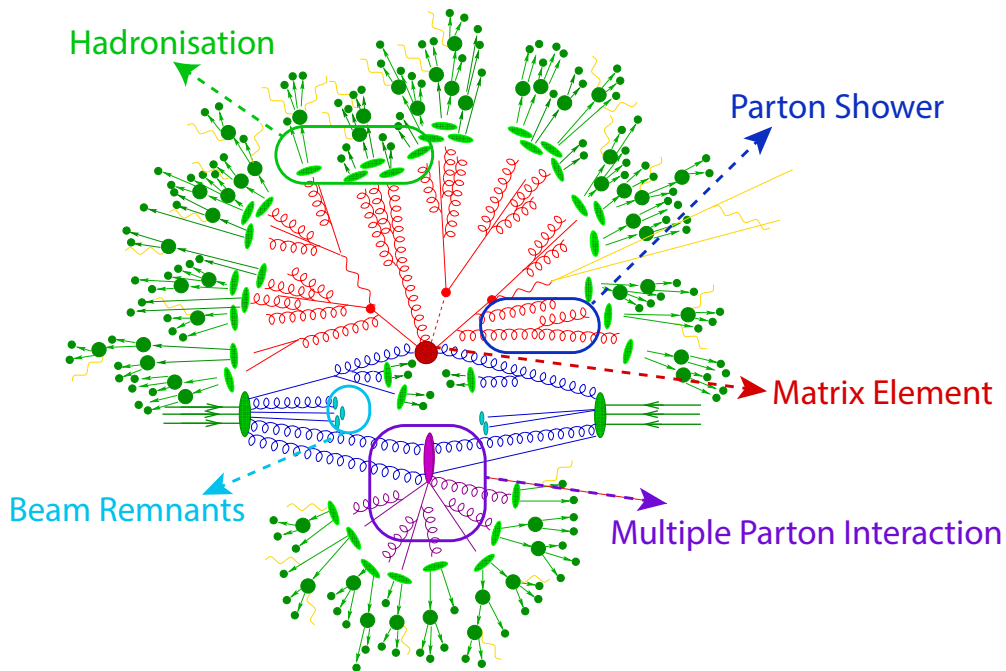
Figure 3.2.: Sketch of a hadron-hadron collision as simulated by a Monte-Carlo event generator. The generation of a Higgs boson in association with a $t\bar{t}$ pair (tth) and the subsequent decay is illustrated. The red big circle indicates the hard process simulated by the ME part of the simulation, including initial/final state gluon radiation, indicated in red. The parton shower (PS) generator part of the simulation is indicated by the blue box, followed by the hadronisation exemplary shown in the green box. Parton-to-hadron transitions are indicated in light green, while soft photon radiation is represented in yellow. In addition, the beam remnants are indicated with the cyan box, and the purple box shows an example of multi parton interaction (MPI). [83]

Figure 3.2 illustrates the various parts of a simulated events realised by separate stages of MC generators. The central part of an event is the hard collision represented by the big red circle. The generation of a Higgs boson in association with a $t\bar{t}$ pair (tth) and the subsequent decay is illustrated. The hard collision is simulated by matrix element (ME) event generators, while the parton shower (PS) performs the decay and hadronisation

of the particles produced. All particles emerging from the smaller three red circles are typically generated by the PS while these smaller red circles are still simulated by the ME event generator. The process indicated by the purple box shows a so-called underlying event, which can occur simultaneously as the primary interaction but involves other partons from the same colliding protons.

The simulated event has to be folded with the detector geometry in terms of interactions as well as the extraction of the detector response for a given particle. The simulation of the ATLAS detector is realised using the GEANT4 framework [84, 85]. The detector simulation is able to perform the evaluation in two different modes, one invokes the full-depth simulation at maximum precision. The second mode invokes a fast simulation rendering of the effects of particle shower evolution, which significantly reduces the per-event time consumption of the simulation. The fast particle shower model relies on template-based evaluation of set topologies instead of re-evaluating similar patterns many times. This analysis utilises the simplified simulation mode named 'ATLFAST-II', which offers improved MC statistics compared to the fully detector simulated MC samples produced by ATLAS.

3.2.1. MC Event Generation and Parton Shower

The full simulation of events is separated into several phases. A ME generator is employed to evaluate the part of the process which has the largest momentum transfer and is therefore predictable in terms of perturbative QCD. At low momentum transfers below 1 GeV perturbative QCD is not able to describe the interactions between particles anymore and thus PS MC generators rely on phenomenological models [42]. While the hard and soft energy regime are clearly defined, the intermediate regime is populated by scale evolution of the hard process. The scale evolution gives rise to many additional partons which eventually be subsumed in the resulting hadrons at lower scales, which interconnects the hard and soft scales modelling further.

The QCD factorisation theorem [40] enables that the hard process can be treated independently from the non-perturbative regime.

ME generators and PS MC generators are often separate programs which serve a partial purpose of simulating the phases of the event generation.

Due to the inherent overlap of the phase space generated at the ME generation phase and the PS phase, methods have been devised to remove this overlap from the final generated phase space.

The $\mu_{r,f}$ scale choice is typically expressed with the momentum transfer (Q) of the hard process, $\mu_r = \mu_f = Q$. In s-channel type resonances, the mass of the produced particle is corresponding to Q thereby setting the $\mu_{r,f}$ scales accordingly to $\mu_r = \mu_f = m$. In case of massless particle-pair production the transverse momentum p_T is typically used

to express the $\mu_{\mathrm{r,f}}$ scales, $\mu_{\mathrm{r}} = \mu_{\mathrm{f}} = p_{\mathrm{T}}$. In addition the starting shower-scale, at which the PS commences the shower generation, is also set to the value of the $\mu_{\mathrm{r,f}}$ used in the ME generation.

As proposed in Ref. [56], the choice of the $\mu_{\mathrm{r,f}}$ scales in the 4 FS is defined in terms of the spectator b-quark jet properties on an event-by-event basis:

$$\mu_{\mathrm{r}} = \mu_{\mathrm{f}} = 4 \cdot \sqrt{m_b^2 + p_{\mathrm{T},b}^2}. \tag{3.1}$$

The $\mu_{\mathrm{r,f}}$ scale choice, introduced in Equation 3.1, is also referred to as *dynamic scale*, as it is a function of the event kinematics, while for the 5 FS choice, $\mu_{\mathrm{r,f}} = m_t$ is used.

MC@NLO

The MC@NLO method [86] is an ME generator capable to provide predictions accurate at NLO. Since the MC@NLO program only involves the ME generation one is required to account for double counting of the overlapping contributions emerging in the PS. The main principle of the MC@NLO method is to remove the emission from the NLO generation that will be added by the PS program. The removal of the overlapping contributions is achieved by a modification of the subtraction terms in the NLO calculation. The PS can be performed by the Herwig program.

Powheg-Box

The Powheg method [86] is an NLO accurate ME generator. The main principle is to generate the hardest real emission in an event at NLO accuracy and pass the remaining event generation to a subsequent PS program. This emission therefore must be removed in the PS generation, which is achieved differently in both types of shower-ordering in current PS programs. While in transverse-momentum ordered showers, the removal is simply the omission of the first emission in the PS program, for angular-ordered PS the removal is less trivial. In angular-ordered PS the hardest emission is not necessarily the first one, where the so-called 'truncated shower' approach is used to define a lower scale at which the shower evolution is terminated [87].

The Powheg-Box is a framework that facilitates the Powheg method in an automatised manner for a given matrix element. Powheg-Box includes the ME generation for several processes at NLO accuracy. Powheg-Box achieves the NLO accurate calculation by a scheme of reweighting the Born-level expression of the inclusive cross-section with NLO contributions [42].

MadGraph 5_aMC@NLO

The MadGraph 5_aMC@NLO projects incorporates the MC@NLO method in a fully automated NLO event generator, which also includes one-loop corrections provided by MadLoop [88].

Sherpa

Sherpa general-purpose event generator is capable of ME generation as well as a full hadronisation, parton shower and underlying event simulation. Sherpa provides NLO accurate predictions for several processes. The PS that is integrated in Sherpa is based on the Catani–Seymore dipole subtraction [89].

The CKKW method [87] is implemented to purge the overlapping configurations that arise in the ME and PS generations.

AcerMC

The AcerMC program [90] is a ME generator that provides LO accurate predictions. In the case of t-channel single top-quark production, AcerMC includes both 4 FS and 5 FS generated events, which are matched using the ACOT method [91], to remove kinematic overlap.

Pythia

Pythia [92, 93] is a multi-purpose event generator that is capable of ME simulation at LO accuracy as well as PS simulation. The simulation of hadronisation and underlying event is also an integral part of the Pythia event generator. Pythia employs the Lund string-hadronisation model [94]. The PS simulation follows a p_T-ordered paradigm [95], which proceeds with the initial-state and final-state radiation of the highest p_T object first.

Two major releases of the Pythia program are currently employed, the first being the Pythia 6 event generator, which was developed for several decades and extensively tested and tuned. The more recent release of the Pythia family is Pythia 8, which is an entirely new developed version, designed as a successor to Pythia 6. One of the prominent changes is the migration from Fortran to C++.

Herwig

The Herwig program [96, 97, 98] is a multi-purpose event generator which has similar capabilities as the Pythia event generators. While Herwig is able to simulate the hadronisation and parton shower internally, the underlying event simulation is performed by the Jimmy multi-parton interaction generator.

The cluster hadronisation model [99] is employed in Herwig, which is one of the key differences with respect to Pythia in terms of methodology. The PS simulation performs the radiation in a angular-ordered paradigm, which enables the inclusion of colour coherence effects, as adjacent radiation is simulated first.

Three major releases of the Herwig generator are used in this analysis, the first being Herwig, which was developed for several decades, similar to Pythia 6. The successors of Herwig are Herwig++ and even more recently Herwig 7.

All event generators of the Herwig family are employed to perform the PS and hadronisation simulation interfaced with an NLO ME generator.

3.3. Signal and Background Processes Modelling

The signal and most of the background processes are simulated using different MC generators and configurations.

3.3.1. Signal Modelling

The contribution of t-channel single top-quark events is modelled using the POWHEG-BOX ME generator (r2556) [56] for the hard process and PYTHIA 6 performs the PS simulation. The 4 FS is employed as described in Section 1.5.2. The parton densities are provided by the CT10f4 [30] PDF-set in the 4 FS. The mass of the top-quark is set to be m_t = 172.5 GeV. POWHEG-BOX provides an NLO-accurate description of the $qg \rightarrow q't\bar{b}$ process in perturbative QCD. The choice of renormalisation and factorisation scales are parametrised in terms of the second b-quark p_T, proposed in Ref. [56] and given in Section 1.5.2. The decay of top-quarks is modelled at LO using MADSPIN [100], which preserves all spin correlations. The parton shower is performed by PYTHIA 6 (v6.428) using the set of tuned parameters according to Perugia2012 (P2012) [101]. In addition, PYTHIA 6 simulates the effects of underlying events and hadronisation.

In order to estimate the systematic effects of t-channel single top-quark event generation, different ME generators and PS as well as their parameter choices are employed. In case of the ME generator, MADGRAPH 5_aMC@NLO (v2.2.2) [102] is replacing POWHEG-BOX to assess the effect of the different NLO-matching methods implemented in both ME generators. The PS generator is interchanged with HERWIG (v6.5.20) [96], where mainly the string-fragmentation model in combination with the p_T-ordered shower of PYTHIA 6 is compared to the cluster-model in combination with a angular-ordered shower employed in HERWIG. The underlying event simulation is realised using JIMMY (v4.31) [103], and the parameter-tune set AUET2 [104] is applied.

The approach of independent-restricted-scale-variations, introduced in Section 1.4, is used to estimate the dependence of the signal modelling on the choice of μ_r and μ_f. Two sets of MC samples are produced, which correspond to the maximum deviation found in the independent-restricted-scale-variations approach. These samples use the nominal POWHEG-BOX + PYTHIA 6 combination. The first variation refers to $\mu_r = \mu_f = 2 \cdot \mu_{r,f}^{nom}$ and the second variation refers to $\mu_r = \mu_f = 0.5 \cdot \mu_{r,f}^{nom}$. In addition to the change of $\mu_{r,f}$, the parameter tune-set of the PS is also varied, in terms of α_s, to reflect the change in QCD activity in the ME generator and fully propagate the effect of the $\mu_{r,f}$ variation. In the case that $\mu_{r,f}$ is doubled, the corresponding P2012radLo parameter

tune-set incorporates reduced strength of α_s used in the nominal case. The scale at which α_s is evaluated is scaled by a factor of two, see Ref. [101]. The second $\mu_{r,f}$ variation is using the P2012radHi PS tune-set, which incorporates an increased strength of α_s.

Table 3.1 contains a detailed summary of the ME generators and PS generators employed to simulate t-channel single top-quark events.

Table 3.1.: Details of the generator settings used to calculate the fiducial cross section. The dynamic scale (dyn.) is defined as $\mu = 4 \cdot \sqrt{m_b^2 + p_{T,b}^2}$. All parton shower tunes use the $\mathrm{CTEQ6L1}$ PDF set apart from A14 which uses NNPDF 2.3 LO.

ME Generator	Shower MC	method	scale	ME PDF	PS tune
MG5_aMC@NLO	HERWIG (v6.5.20)	4FS(NLO)	dyn.	CT10f4	AUET2 [104]
MG5_aMC@NLO	HERWIG++(v2.7.1)	4FS(NLO)	dyn.	CT10f4	UE-EE-5 [105]
POWHEG-BOX	PYTHIA 6 (v6.427)	4FS(NLO)	dyn.	CT10f4	Perugia2012 [101]
POWHEG-BOX	PYTHIA 8 (v8.2xx)	4FS(NLO)	dyn.	CT10f4	A14 [106]
POWHEG-BOX	HERWIG (v6.5.20)	4FS(NLO)	dyn.	CT10f4	AUET2 [104]
ACERMC	PYTHIA 6 (v6.426)	matched(LO)	115 GeV	CTEQ6L1	Perugia2011C [101]
MG5_aMC@NLO	HERWIG++(v2.7.1)	5FS(NLO)	m_t	CT10	UE-EE-5
POWHEG-BOX	PYTHIA 6 (v6.427)	5FS(NLO)	m_t	CT10	Perugia2012
POWHEG-BOX	PYTHIA 8 (v8.2xx)	5FS(NLO)	m_t	CT10	A14

3.3.2. Momentum Fractions and Parton Distributions

The PDFs introduced in Sec. 1.3, provide the probability density to find the parton i with the fractional momentum x_i of the proton. While the PDFs are generic by construction, it is instructive to investigate the fractional momentum involved in the production of t-channel single top-quarks, as well as the flavour of the initial light-quark. The flavour fractions of the initial light-quark and the x-distribution in selected MC events are determined.

MC-simulated events are produced using AcerMC + Pythia 6 ($\mu_{r,f} = 115\,\text{GeV}$)[1], since the required information is not available with Powheg-Box + Pythia 6.

Figure 3.3 shows the flavour fractions of initial light quarks for top-quark production in (a) and top-antiquark production in (b). In top-quark production, u quarks contribute 80 % to all selected top-quark events, top-antiquark production only involves about 62 % d quarks in the initial state. The main discrepancy of u and d contributions correspond to the ratio of u and d valence quarks in the proton.

Figure 3.4(a) displays the distribution of the momentum fraction x of t-channel single top-quark events for all involved initial quarks ($u, c, \bar{d}, \bar{s}$). Figure 3.4(b) contains the distribution of the momentum fraction x for top-antiquark production for the involved initial-quarks ($d, s, \bar{u}, \bar{c}$).

---

[1]The $\mu_{r,f}$ scales are optimised to match the acceptance of NLO ME generators studied in Ref. [8]

(a) top-quark production   (b) top-antiquark production
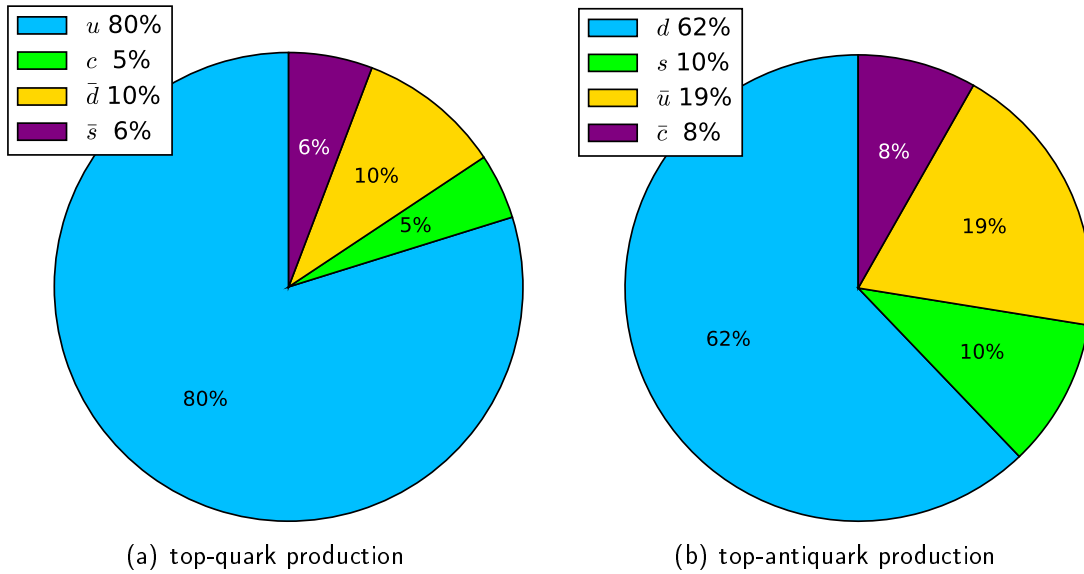
Figure 3.3.: Flavour fractions of initial light quarks in t-channel single top-quark production as determined by MC events generated with AcerMC + Pythia 6. (a) shows the flavour fractions in top-quark production, which is dominated by 80 % of u quarks. (b) shows the corresponding fractions of the top-antiquark production. In case of the fractions of initial light quarks in top-antiquark production initial d-quarks are only dominating by 62 %.

(a) top-quark production   (b) top-antiquark production
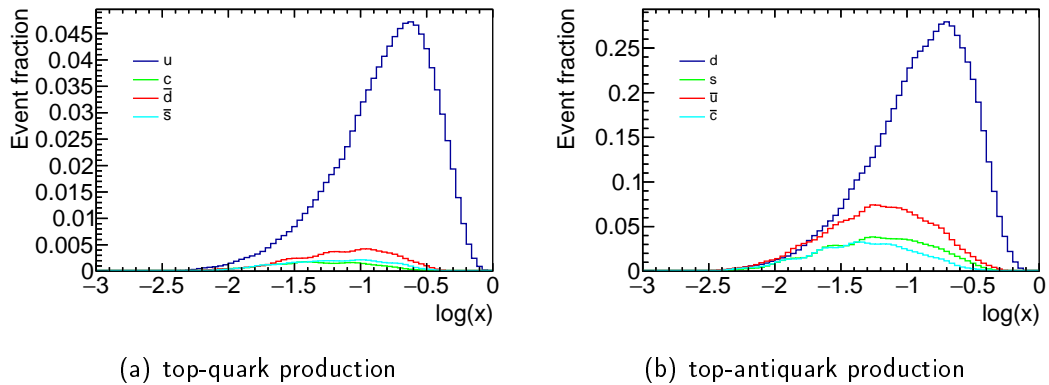
Figure 3.4.: Distribution of the momentum fraction x of the partons in t-channel single top-quark events in (a), for all involved initial quarks $(u, c, \bar{d}, \bar{s})$, and for the top-antiquark production in (b) for the involved initial quarks $(d, s, \bar{u}, \bar{c})$.

3.3.3. Top Quark Backgrounds

Besides the signal process, three other backgrounds involve the production of top-quarks. While $t\bar{t}$ production yields the highest contribution to the top-quark backgrounds, single top-quark production via the Wt and the s-channel have sizable yield in the signal region. The Powheg-Box (r2819, r3026) [107, 108, 109, 110] ME generator is employed for the simulation of all three processes, utilising the CT10 PDF set. In the case of $t\bar{t}$ production the so-called h_{damp} parameter of the Powheg-Box ME generator is set to $m_t = 172.5\,\mathrm{GeV}$. The h_{damp} parameter controls the p_{T} of the first, and typically hardest, emission which is radiated beyond the Born configuration of the $t\bar{t}$ process. The renormalisation and factorisation scales are implemented in Powheg-Box. In order to simulate the parton shower, underlying event and hadronisation Pythia 6 is employed, while the Perugia2011C (P2011C) set of tuned parameters is used.

The mass of the top-quark is set to be $m_t = 172.5\,\mathrm{GeV}$. The exclusive decay of $t \to Wb$ is used to generate MC events, neglecting the very small contribution of $t \to Ws/d$ decays. In the case of $t\bar{t}$ production at least one produced W-boson is required to decay leptonically.

Systematic uncertainties related to MC generation of top-quark background events are estimated with similar methods as used for the signal process. For all three processes, MC@NLO is suitable to generate the ME part of MC events at NLO accuracy to evaluate the systematic effect of the NLO-matching methods. The comparison of Powheg-Box +Herwig and MC@NLO +Herwig is used to estimate the uncertainty of the NLO-matching method. The systematic effect of hadronisation is estimated by comparing Powheg-Box +Herwig to Powheg-Box +Pythia 6.

The estimation of the impact of the choice of $\mu_{\mathrm{r,f}}$ is obtained by MC samples with varied settings of these parameters. The procedure is almost identical to the one introduced for the signal process, with the exception of the $t\bar{t}$ production. In addition to the parameter variation of $\mu_{\mathrm{r,f}}$ and the PS tune-set, the h_{damp} parameter is modified to $h_{\mathrm{damp}} = 2 \cdot m_t$ in case of the $\mu_r = \mu_f = 2 \cdot \mu_{r,f}^{\mathrm{nom}}$ variation.

3.3.4. V+jets Backgrounds

The W + jets background processes comprise several production channels involving one W boson accompanied by additional jets of light quarks, c-quarks or b-quarks as well as a singular c-quark jet. Z + jets events are simulated where the Z-boson decays leptonically, and the accompanying jet can be of light-flavour or stem from c/b-quarks. In addition, the invariant mass of the lepton pair originating from the Z-boson decay must fulfill $m(\ell\ell) > 40\,\mathrm{GeV}$. The V + jets events are simulated using Sherpa (v1.4.1) [111] as the ME generator. Sherpa is capable of simulating the W +

jets process at LO accuracy, including up to four additional partons. In contrast to Powheg-Box or MadGraph5_aMC@NLO, Sherpa is not interfaced with a separate MC program to perform the PS but it is also employed to simulate the PS, hadronisation and underlying event. Additionally, b- and c- quarks are treated as massive in the MC simulation.

In order to remove the overlap that occurs between the $V + n$ parton configuration and associated heavy-quark pair production, the ME+PS merging algorithm [87] is employed.

3.3.5. VV Backgrounds

Diboson (VV) production is simulated with the Sherpa MC generator, similar to V + jets in terms of methodology. The simulated matrix elements comprise all diagrams involving four electroweak vertices. In case of 0 additional partons, Sherpa provides NLO accurate predictions and up to 3 additional partons with LO accuracy. Decays are considered where one boson decays leptonically and the other hadronically.

3.3.6. QCD Multijet Production

The QCD-multjet production is simulated with Pythia 8 using the CTEQ6L1 LO PDF-set. All events have at least two jets, one of which exceeds the transverse momentum threshold of $p_T > 17\,\text{GeV}$ and is contained within a pseudorapidity range of $|\eta(j)| < 2.7$. The sample of MC simulated events is denoted 'JF17'.

3.3.7. Samples of MC Simulated Events

Tables 3.2-3.4 contain all samples of MC simulated events used in the presented analysis. As introduced in Section 3.2, the simulation type 'ATLFAST-II' is employed in the generation of all samples.

Table 3.2.: Top quark event MC samples used for this analysis. The cross-section column includes k-factors and branching ratios. The k-factor is the ratio $\frac{\sigma_{NLO}}{\sigma_{LO}}$ of the production cross-sections for a given process. The symbol ℓ represents the sum of electron, muon and tau final states.

	σ [pb]	k-factor	Generator	$N_{\mathrm{MC}}/10^6$	dataset ID
$tq(\ell+\mathrm{jets})$	17.5	1.05	POWHEG-BOX +PYTHIA 6	5	110070
$\bar{t}q\ (\ell+\mathrm{jets})$	9.4	1.06	POWHEG-BOX +PYTHIA 6	5	110071
$tq\ (\ell+\mathrm{jets})$	17.5	1.05	POWHEG-BOX +HERWIG	5	110086
$\bar{t}q\ (\ell+\mathrm{jets})$	9.4	1.06	POWHEG-BOX +HERWIG	5	110087
$tq+\bar{t}q\ (\ell+\mathrm{jets})$	26.6	1.07	MG 5_aMC@NLO +HERWIG	10	110121
$tq+\bar{t}q\ (\ell+\mathrm{jets})$	28	1.04	MG 5_aMC@NLO +HERWIG++	1	110097
$t\bar{b}\ (\ell+\mathrm{jets})$	1.6	1.11	POWHEG-BOX +PYTHIA 6	6	110119
$t\bar{b}\ (e+\mathrm{jets})$	0.6	1.08	MC@NLO +HERWIG	1	108343
$t\bar{b}\ (\mu+\mathrm{jets})$	0.6	1.08	MC@NLO +HERWIG	1	108344
$t\bar{b}\ (\tau+\mathrm{jets})$	0.6	1.08	MC@NLO +HERWIG	1	108345
Wt all decays	20.5	1.09	POWHEG-BOX +PYTHIA 6	20	110140
Wt all decays	20.5	1.09	POWHEG-BOX +HERWIG	10	110144
Wt all decays	20.6	1.08	MC@NLO +HERWIG	5	108346
$t\bar{t}$ no all hadronic $h_{\mathrm{damp}}=m_t$	114	1.20	POWHEG-BOX +PYTHIA 6	100	110404
$t\bar{t}$ no all hadronic	114	1.20	POWHEG-BOX +PYTHIA 6	15	110401
$t\bar{t}$ lepton filter	115.6	1.19	POWHEG-BOX +HERWIG	30	105860
$t\bar{t}$ no all hadronic	112.9	1.22	MC@NLO +HERWIG	30	105200

Table 3.3.: Background MC samples used for the presented analysis. The cross-section column includes filter efficiencies and branching ratios. The k-factor is the ratio $\frac{\sigma_{NLO}}{\sigma_{LO}}$ of the production cross-sections for a given process.

	σ [pb]	k-factor	Generator	$N_{\mathrm{MC}}/10^6$	dataset ID
$W \to e\nu$	10295	1.10	SHERPA	50	167742
$W \to e\nu$ b-filtered	140	1.10	SHERPA	15	167740
$W \to e\nu$ c-filtered	538	1.10	SHERPA	10	167741
$W \to \mu\nu$	10368	1.10	SHERPA	50	167745
$W \to \mu\nu$ b-filtered	140	1.10	SHERPA	15	167741
$W \to \mu\nu$ c-filtered	466	1.10	SHERPA	10	167744
$W \to \tau\nu$	10327	1.10	SHERPA	50	167748
$W \to \tau\nu$ b-filtered	140	1.10	SHERPA	15	167742
$W \to \tau\nu$ c-filtered	506	1.10	SHERPA	10	167747
$Z \to e^+e^-$	764	1.12	SHERPA	1	167751
$Z \to e^+e^-$ b-filtered	31	1.12	SHERPA	4	167749
$Z \to e^+e^-$ c-filtered	314	1.12	SHERPA	3	167750
$Z \to \mu^+\mu^-$	764	1.12	SHERPA	1	167754
$Z \to \mu^+\mu^-$ b-filtered	31	1.12	SHERPA	4	167752
$Z \to \mu^+\mu^-$ c-filtered	314	1.12	SHERPA	3	167753
$Z \to \tau^+\tau^-$	764	1.12	SHERPA	1	167757
$Z \to \tau^+\tau^-$ b-filtered	31	1.12	SHERPA	4	167755
$Z \to \tau^+\tau^-$ c-filtered	314	1.12	SHERPA	3	167756
$WW \to e\nu q\bar{q}$	7	1.06	SHERPA	3.2	183734
$WW \to \mu\nu q\bar{q}$	7	1.06	SHERPA	3.2	183736
$WW \to \tau\nu q\bar{q}$	7	1.06	SHERPA	3.2	183738
$ZZ \to e^+e^- q\bar{q}$	0.2	1.00	SHERPA	0.12	183586
$ZZ \to \mu^+\mu^- q\bar{q}$	0.2	1.00	SHERPA	0.12	183588
$WZ \to e\nu q\bar{q}$	2	1.05	SHERPA	0.84	183735
$WZ \to \mu\nu q\bar{q}$	2	1.05	SHERPA	0.84	183737
$WZ \to \tau\nu q\bar{q}$	2	1.05	SHERPA	0.84	183739
$ZW \to e^+e^- q\bar{q}$	1.5	1.05	SHERPA	0.7	183585
$ZW \to \mu^+\mu^- q\bar{q}$	1.5	1.05	SHERPA	0.7	183587
Multijet production (JF17)	93,052,540	1.00	PYTHIA 8	110	129160

Table 3.4.: Top quark event MC samples used for this analysis with different top masses used during event generation. All samples are produced with Powheg-Box +Pythia 6. The cross-section column includes k-factors and branching ratios. The k-factor is the ratio $\frac{\sigma_{NLO}}{\sigma_{LO}}$ of the production cross-sections for a given process. The symbol ℓ represents the sum of electron, muon and tau final states.

	m_{top} [GeV]	σ [pb]	k-factor	$N_{\mathrm{MC}}/10^6$	dataset ID
tq (ℓ+jets)	165.0	19.1	—	3	110268
tq (ℓ+jets)	167.5	18.6	—	3	110270
tq (ℓ+jets)	170.0	18.2	—	3	110272
tq (ℓ+jets)	175.0	17.4	—	3	110274
tq (ℓ+jets)	177.5	17.0	—	3	110276
tq (ℓ+jets)	180.0	16.6	—	3	110278
$\bar{t}q$ (ℓ+jets)	165.0	10.4	—	3	110269
$\bar{t}q$ (ℓ+jets)	167.5	10.1	—	3	110271
$\bar{t}q$ (ℓ+jets)	170.0	9.9	—	3	110273
$\bar{t}q$ (ℓ+jets)	175.0	9.4	—	3	110275
$\bar{t}q$ (ℓ+jets)	177.5	9.2	—	3	110277
$\bar{t}q$ (ℓ+jets)	180.0	9.0	—	3	110279
Wt all decays	165.0	23.4	1.09	3	110124
Wt all decays	167.5	22.4	1.09	3	110126
Wt all decays	170.0	21.5	1.09	3	110128
Wt all decays	175.0	19.7	1.09	3	110130
Wt all decays	177.5	18.9	1.09	3	110132
Wt all decays	180.0	18.2	1.09	3	110134
$t\bar{b}$ (ℓ+jets)	165.0	2.0	1.1	0.5	110123
$t\bar{b}$ (ℓ+jets)	167.5	1.9	1.1	0.5	110125
$t\bar{b}$ (ℓ+jets)	170.0	1.8	1.1	0.5	110127
$t\bar{b}$ (ℓ+jets)	175.0	1.6	1.1	0.5	110129
$t\bar{b}$ (ℓ+jets)	177.5	1.5	1.1	0.5	110131
$t\bar{b}$ (ℓ+jets)	180.0	1.4	1.1	0.5	110133
$t\bar{t}$ no all had.	165.0	120.6	1.2	4	117836
$t\bar{t}$ no all had.	167.5	111.7	1.2	4	117838
$t\bar{t}$ no all had.	170.0	103.7	1.2	4	117840
$t\bar{t}$ no all had.	175.0	89.5	1.2	4	117842
$t\bar{t}$ no all had.	177.5	83.3	1.2	4	117844
$t\bar{t}$ no all had.	180.0	77.6	1.2	4	117846

Object Definition

In the attempt to access the small scale interactions, the produced particles and the subsequent decay products, signals from the detector are combined to form proxies of physical objects. This Chapter provides details of physics objects crucial for single top-quark analysis final states, which contain charged leptons, jets and $E_{\mathrm{T}}^{\mathrm{miss}}$. The identification of jets from b-quark decays is also presented, as it is of high importance for this analysis. In order to facilitate the measurement of the fiducial cross-sections, particle-level object definitions are introduced in this chapter that follow the same signature of the t-channel single top-quark process.

4.1. Object Definition at Reconstruction Level

The reconstruction of events that have been recorded with the ATLAS detector is of key importance for this analysis. In order to reconstruct the objects that are involved in the signature of t-channel single top-quark events, the proxies for the physical objects are defined.

Charged particles leave hits in the ID, which can be reconstructed to form tracks. Using the calorimeter system the energy of particles can be determined. Figure 4.1

shows an exemplary t-channel single top-quark event candidate[1] in the electron channel [112]. The x–y projection at $z = 0$ is shown. The collision takes place in the center and the hits in the TRT of the detectable particles are seen as white dots. The orange lines show the reconstructed tracks and the yellow towers show the combined energy deposition in the calorimeter system. The blue line indicates the direction of the selected electron. The yellow and blue cones illustrate the reconstructed jets in the event.
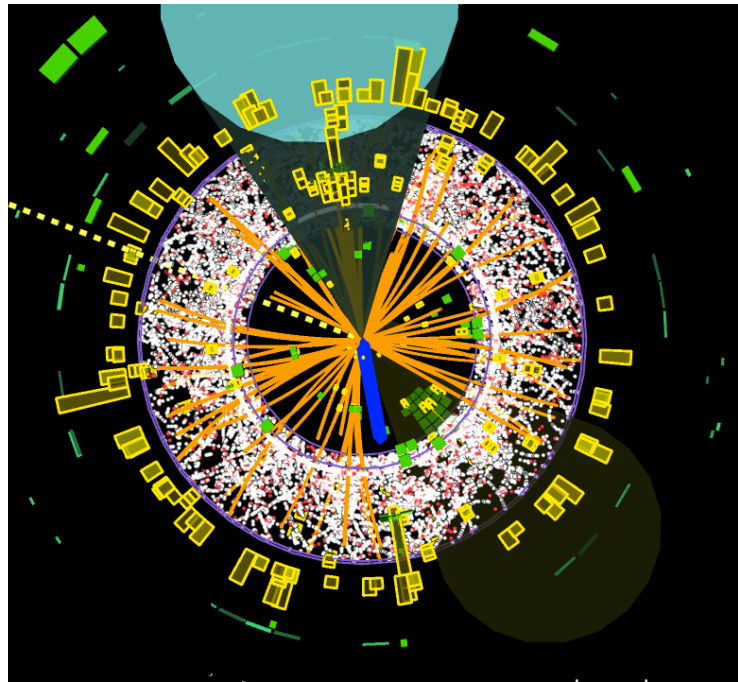
Figure 4.1.: Exemplary event display of a t-channel single top-quark event candidate in the electron channel [112]. The x–y projection at $z = 0$ is shown. The collision takes place in the center and the hits of the detectable particles in the TRT are seen as white dots. The orange lines show the reconstructed tracks and the yellow towers show the combined energy deposition in the calorimeter system. The blue line indicates the direction of the selected electron. The yellow and blue cones illustrate the reconstructed jets in the event.

---

[1]Event run number is 209109 and the event number is 14178406. The event was recorded on 8th June 2012.

4.1.1. Track and Vertex Reconstruction

As introduced in Section 2.3.1, the track determination is one of the key features in order to identify charged particles and measure their momentum. Since the interactions between particles are localised in a vertex, the reconstruction of these is a powerful aid to rebuild the event topology [113]. Tracks are defined by requiring multiple signals, so-called hits, in different sub-detectors of the tracking system. The more hits can be associated to a track, the higher its quality. The track reconstruction follows the 'inside-out' strategy, which exploits the high granularity of the pixel and SCT detectors, and extrapolates the track to the TRT. Track candidates are seeded by three hits in the pixel- and SCT-detectors, if the track exceeds $p_\text{T} > 500\,\text{MeV}$, and their trajectory is projected into the TRT. A Kalman-filter [114] is employed as pattern recognition technique, to estimate the correct association of hits to a track candidate.

If two of more tracks point to the same origin, a vertex is formed. Three types of vertices are distinguished, the primary vertex is defined as the vertex where the sum of p_T^2 of all associated tracks to the vertex is maximal. The vertex is only considered if five tracks can be associated to it, where each track has $p_\text{T} > 400\,\text{MeV}$ [115]. The second vertex type is denoted pile-up vertex, which corresponds to additional proton-proton collisions in the same proton bunch-crossing, where only the sum of p_T^2 of all associated tracks is lower than that of the primary vertex. Secondary vertices stem from subsequent decays of particles emerging from the primary vertex. In most cases the particles produced in the primary interaction travel only a microscopic distance, so that no secondary vertex can be associated, given the limited resolution of the detector. However, a few particle species have a long lifetime, such that a reconstruction of a secondary decay vertex is possible. The tracks associated to secondary vertices typically have large impact parameter with respect to the primary vertex.

4.1.2. Electron Candidates

Electrons are the first class of leptons which are important for this analysis. We define electron candidates as proxies of the physical leptons which are produced in the hard interaction and the subsequent decays.

Due to the layout of the ATLAS detector and the properties of electrons, their identi-fication relies on the ID introduced in Section 2.3.1, as well as the EM calorimeter in which electrons deposit their energy, forming so-called clusters. The electron recon-struction consists of three stages. In the first stage a sliding window algorithm [116] is used to locate clustered energy deposits in the LAr EM calorimeter. The size of the sliding window depends on the part of the ID that is scanned. In the barrel part, the sliding window has the dimensions 3×7 cells in $\eta \times \phi$, 5×5 cells in the endcap calor-imeter. Electron candidates are built from tracks from the ID and clusters in the LAr

EM calorimeter. The quality requirements on the tracks is very stringent [117, 118]. Three different cut-based selections of electron identification are defined by ATLAS, where the selections *loose*, *medium* and *tight* are differentiated. The name of each selection refers to the background rejection capability, where *tight* offers the highest electron purity, that means the highest probability that electron candidates originate from true electrons. In this analysis only electron candidates fulfilling the *tight* electron identification cuts [119] are considered in the event selection. The electron identification cut sets *loose* and *medium* are employed to reject events containing additional leptons, which will be discussed in Section 5. The analysis-specific p_T-requirement of electron candidates is set to be $p_T > 25$ GeV, and it has to be detected within $|\eta_{\mathrm{clus}}| < 2.47$, where η_{clus} refers to the pseudorapidity of the reconstructed cluster in the EM calorimeter. Electrons in the pseudorapidity range $1.37 < |\eta_{\mathrm{clus}}| < 1.52$ are vetoed, due to inactive material in the overlap region of the barrel and endcap part of the detector. Additional requirements are that the electron candidate has to be isolated and it must be matched to a trigger-level object within $\Delta R = 0.15$.

The quality requirements on the tracks [117] comprise demands on the ID subsystems, which are defined as:

- $n_{\mathrm{pixel}} \geq 1$
- $n_{\mathrm{pixel}} + n_{\mathrm{SCT}} \geq 7$
- $|d_0| < 1$ mm
- $n_{b-\mathrm{layer}} \geq 1$.

Where, "pixel" and "SCT" refer to the ID subsystems and the term *b*-layer refers to the innermost layer of the pixel detector. The requirements on associated tracks ensure that they are well-measured, and increase the likelihood that they originate from the primary vertex.

Electron Isolation The isolation criterion represents a cone of inactivity in the EM calorimeter around the selected signal, which is characteristic for electrons originating from *W*-boson decays. Three major types of background processes for electron production can be suppressed by requiring electron isolation, the first being hadronic jets faking an electron, as well as photon conversion or electrons from heavy-flavour decays. Two separate isolation requirements are invoked including EM calorimeter isolation and track isolation. For the purpose of the isolation requirements, a cone with a specific radius parameter ΔR is defined.

The isolation requirements [119] of electrons are optimised to provide a uniform selection efficiency of 90 % in E_T and η_{clus}. The EM calorimeter isolation of $\Delta R = 0.2$ with 90 % efficiency (`EtCone20@90`), corresponds to the scalar sum of the transverse momenta of calorimeter energy deposits within the cone. The track isolation of $\Delta R = 0.3$ with 90 % efficiency (`PtCone30@90`), which corresponds to the scalar sum of track transverse momenta within the cone. In either isolation criterion, the

calorimeter energy deposits or track associated to the electron candidate are omitted.

An additional isolation requirement is that within a cone of $\Delta R = 0.3$ no tracks with p_{T} in the range $0.9\,\mathrm{GeV}$ to $2.5\,\mathrm{GeV}$ are found, omitting the tracks belonging to the electron candidate.

Electron Reconstruction Performance

The reconstruction and identification efficiency is corrected in simulation by comparing well-known resonances in $Z \rightarrow e^+e^-$ and $J/\Psi \rightarrow e^+e^-$ events in simulation and collision data [120, 119].

The calibration of the electron energy scale and resolution was performed by using the electron decay modes of well-known resonances in $Z \rightarrow e^+e^-$ and $J/\Psi \rightarrow e^+e^-$ events. In addition, studies on the E/p, that is the ratio of the energy measured by the EM calorimeter and the momentum that was determined in the ID, improved the precision of the electron energy scale determination [117].

Corresponding scale factors are derived to correct the performance in simulation to the observation in collision data. The deviation in resolution between simulation and data is corrected by smearing in simulation.

4.1.3. Muon Candidates

Muon candidates are similarly defined as electron candidates, for their main difference arises from the detector response, and not from the kinematic properties induced by their production. Since muons are losing far less energy in material than electrons, the crucial identification of muons is obtained by the muon system, which was introduced in Section 2.3.3.

The reconstruction of muon candidates employs tracks in the MS and match them with tracks in the ID [121], so-called combined (CB) muon. The analysis-specific p_{T}-requirement of muon candidates is set to be $p_{\mathrm{T}} > 25\,\mathrm{GeV}$. The muon candidate is required to be detected within $|\eta| < 2.5$. Additional requirements are that the muon candidate has to be isolated and it must be matched to a trigger object.

Further requirements are placed on the ID tracks used to reconstruct muons to ensure that the ID tracks are well-measured.

- $n_{\mathrm{pixel}} \geq 1$
- $n_{\mathrm{SCT}} \geq 5$
- $n_{\mathrm{TRT}} \geq 9$, if $0.1 < |\eta| < 1.9$
- Maximum two active pixels or SCT sensors which are traversed by a track, but no hits are recorded.

Muon Isolation

The importance of the muon isolation has the same reason as for the electron candidates, to suppress contributions from heavy-flavour decays. In the case of muons, the cone radius is not fixed, but is rather a function of the lepton p_T, which reduces the dependence on the pileup environment. The so-called mini-isolation [122] I_iso is defined as the scalar sum of all transverse momenta of the tracks which are within the dynamic cone radius and are not associated to the muon candidate. Only tracks above $p_\mathrm{T} > 1\,\mathrm{GeV}$ are considered. The cone radius is defined as:

$$R_\mathrm{iso} = \frac{10\,\mathrm{GeV}}{p_\mathrm{T}(\mu)}, \tag{4.1}$$

and the isolation requirement

$$\frac{I_\mathrm{iso}}{p_\mathrm{T}(\mu)} < 0.05 \tag{4.2}$$

The muon candidate has to pass the isolation requirement.

Muon Reconstruction Performance

In order to correct the muon reconstruction and identification efficiency in simulation to match collision data, well-known resonances in $Z \rightarrow \mu^+\mu^-$, $J/\Psi \rightarrow \mu^+\mu^-$ and $\Upsilon \rightarrow \mu^+\mu^-$ events are used [123, 124, 125]. The muon reconstruction efficiency is above 96 %. The agreement with MC predictions better than 1 %. The energy scale and resolution of muons is determined in the mass spectrum of $Z \rightarrow \mu^+\mu^-$ events.

4.1.4. Jet Candidates

As quarks and gluons are produced in the hard collision, hadrons are quickly formed, due to the QCD confinement. Most of the hadrons are only short-lived and their decays leads to the subsequent formation of additional hadrons, which share the energy of the initial quark. The emerging bundles of hadrons, called jets, are detected as energy depositions in the calorimeter system. The jets retain the approximate direction of motion of the initial quark and have typically a circular shape in the η–ϕ-plane. The parametrisation of the jet candidate, which is the proxy of the physical jet, is defined by a cone-shape with the radius parameter R. The definition exploits the circular shape in the η–ϕ-plane and the cone size is chosen such that the cone contains most of the energy of the associated initial quark. An additional consideration is that, as the cone size is increased, the probability that the found energy deposition does not belong to a single quark rises.

The energy deposits in the calorimeter are clustered, using the topological cluster algorithm [116, 126], which is initially seeded by large energy deposits and iteratively joins energy deposits in adjacent calorimeter cells. The joining is only performed if the cell contains significant energy w.r.t. the expected noise level. To prevent the formation of very large clusters, which can occur mainly in the forward region of the detector, found clusters are split according to separate local energy maxima in the previously determined clusters.

A jet is reconstructed by application of the anti-k_t algorithm [127] on topological clusters. The algorithms uses a radius parameter of 0.4. The anti-k_t algorithm offers collinear- and infrared safety, which means that the algorithm is robust against the inclusion of many very small contributions, as well as collinear configurations that mainly originate in radiation effects.

As the ATLAS calorimeter system is non-compensating, the responses for electrons (electromagnetic scale) and hadrons (hadronic scale), are not equal. A calibration of the energy deposits in both parts of the calorimeter must be performed. The calibration of the topological clusters is performed with the local cluster weighting (LCW) method [126, 128]. The LCW calibration classifies the topological cluster into 'em-like', 'hadron-like' or noise by comparing the shape and location of the cluster. Due to a lower response of the calorimeter to hadronic clusters the 'hadron-like' clusters are subject to larger corrections than the 'em-like' clusters.

The analysis-specific requirements on the transverse momentum of jets are $p_T > 30\,\text{GeV}$ within a pseudorapidity range of $|\eta| < 4.5$. Due to observed discrepancies between simulated W + jets events and data in the transition region of the calorimeter, the minimum jet p_T is raised to $35\,\text{GeV}$ within $2.7 < |\eta| < 3.5$.

The reconstruction of jets suffers from pathological noise bursts, which obfuscate the anti-k_t algorithm and thereby rendering the jet unusable. The origin of these noise bursts has been studied in detail in Ref. [129]. In order to minimise the contamination of events containing incorrectly reconstructed jets, these events are rejected, provided that the transverse momentum of the jet is $p_T > 20\,\text{GeV}$. Jets are tagged as 'bad' in the electromagnetic calorimeter if they satisfy $|f_{\text{quality}}| > 0.8$ and $f_{\text{EM}} > 0.95$, where f_{quality} indicates the fraction of energy of a jet, associated to bad-quality calorimeter cells. The quantity f_{EM} is the fraction of energy deposited in the EM calorimeter. This event-cleaning requirement rejects about 0.01 % of events as mentioned in Ref. [129], with similar jet requirements as this analysis.

Jets are not considered if they overlap with an identified electron candidate, as the likelihood of them corresponding to the same object, is very high. The jet and electron overlap is considered if their distance in the η–ϕ plane is smaller than $\Delta R(j, e) < 0.2$, where the positions in η and ϕ refer to the detector coordinates of the jet prior to any correction.

Due to the technique of clustering energy deposits, jet reconstruction suffers from en-

ergy deposits that originate from pile-up events, thereby contaminating the reconstructed jet. The jet vertex fraction (JVF) [130] is defined as the fraction of tracks associated to the jet which originate from the primary vertex and the sum of all tracks of the jet. To reject jets that originate from pile-up events, the absolute value of the jet vertex fraction is required to be |JVF| > 0.5 provided that the transverse momentum of the jet is p_T < 50 GeV. For jets with p_T ≥ 50 GeV, no JVF requirement is applied.

4.1.5. Missing Transverse Momentum

Particles, like neutrinos, which do not interact with the detector material, are not directly observed and escape direct detection. Due to the fact that the colliding protons do not carry transverse momentum, the indirect deduction of the transverse momentum of these particles is possible [131]. The missing transverse momentum $\vec{E}_{\text{Tmiss}}$ is reconstructed as the negative vector sum of the transverse momenta of all reconstructed objects. The considered reconstructed objects are electrons, photons, τ-leptons, muons and jets. In order to account for detector signals that are not associated to physics objects, a "soft term" is introduced.

$$E_{x(y)}^{\text{miss}} = E_{x(y)}^{\text{miss},e} + E_{x(y)}^{\text{miss},\gamma} + E_{x(y)}^{\text{miss},\tau} + E_{x(y)}^{\text{miss,jets}} + E_{x(y)}^{\text{miss},\mu} + E_{x(y)}^{\text{miss,soft}}, \tag{4.3}$$

where the individual terms are calculated as the negative vectorial sum of transverse momenta of all objects in each category.

The magnitude of the missing transverse momentum is calculated as:

$$E_{\text{T}}^{\text{miss}} = \sqrt{(E_x^{\text{miss}})^2 + (E_y^{\text{miss}})^2} \tag{4.4}$$

The analysis-specific requirements on the missing transverse momentum is $E_{\text{T}}^{\text{miss}}$ > 30 GeV.

4.1.6. b-Quark Jet Identification

The capability to distinguish jets which originate from b quarks or c quarks from those stemming from a light-quark, is of key importance for this analysis. As explained in Section 1.5, the top-quark decay is entirely dominated by the $t \to Wb$ mode, making b-quark jets a very important feature of the weak b-decay which is exploited by employing a b-tagging requirement. The most important feature of a b-jet arises from the average lifetime of the weakly decaying b-hadron, which is $\tau \approx 1.6$ ps [27]. This lifetime leads to an average distance of $\beta\gamma c\tau \approx 500$ μm that the b-hadron travels before it

decays. This macroscopic distance is sufficient to reconstruct the decay vertex, which is called secondary vertex shown schematically in Figure 4.2 [132].

ATLAS has developed several b-tagging algorithms [133] which exploit the properties of the b-hadron decay. These algorithms focus on either impact parameters of the charged-particle tracks from the b-hadron decay products, or reconstruct the secondary vertex. This analysis incorporates the MV1c tagger, which is a neural network based b-tagging algorithm. The inputs of three distinct b-tagging algorithms are used in combination, which improves the power of separating b-quark jets from light-quark jets.

The first input to the MV1c b-tagger is the IP3D algorithm [134, 135], which uses the transverse impact parameter significance $S(d_0)$ and the longitudinal impact parameter significance $S(z_0)$ of charged-particle tracks, including their correlation. All tracks associated to the secondary vertex are weighted by comparing distributions for b-quark and light-quark jets from simulation. The second b-tagger is the SV1 algorithm, which attempts to reconstruct a secondary vertex. Once the secondary vertex is reconstructed, several parameters of the reconstructed vertex can be used to increase the sensitivity of the b-quark jet identification. The main characteristics that are exploited are the signed decay length significance, the invariant mass of all tracks associated to the secondary vertex, the fraction of energy these tracks contribute to the total jet energy and the number of two-track vertices.

The third MV1c input is the JetFitter algorithm [135, 136]. The JetFitter is a sophisticated approach which exploits the topological structure of weak b- and c-hadron decays inside the jet. The JetFitter employs a Kalman filter, to find a common line, connecting the primary vertex to the b- and c-hadron vertices. The JetFitter aims to distinguish the vertices of b- and c-hadrons, which is enabled by the long lifetime of the c-hadron. The JetFitter provides weights which correspond to the probabilities for a jet originating from a b-, c- or light-quark, denoted P_b, P_c and P_u. The JetFitter uses a neural network to discriminate either b-, c- or light-quark hypothesis. The outputs of the NN are used with a likelihood-ratio technique to obtain the discriminant distribution, called JetFitterCOMBNN(c). The likelihood ratio $w = \log(P_b/P_c)$ is defined to maximise the separation of b-quark jets from c-quark jets.

Finally, the MV1c b-tagger employs an NN with uses the IP3D-, SV1- and JetFitter b-taggers as input variables. The input b-tagging algorithms provide complementary information about the features of b-hadrons. Specifically the input from the JetFitter contributes the most in terms of c-quark-jet rejection.

A calibration is performed to account for normalisation discrepancies of the b-tagging efficiency between the MC predictions and observed data. The calibration results are obtained by a combination of two methods [133]. One method (`system8`) is based on a sophisticated tag-and-probe technique and the second method uses a combinatorial likelihood approach which is applied to dileptonic $t\bar{t}$ events. In addition, the

b-tagging efficiency is determined for each parton shower MC employed in this analysis.
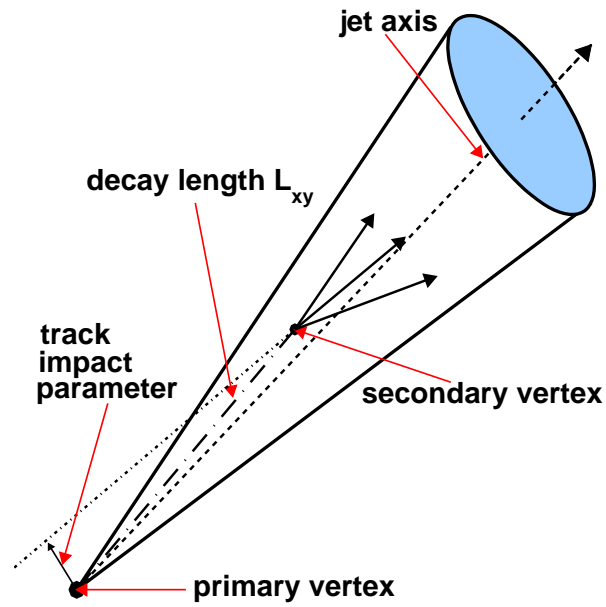
Figure 4.2.: A schematic of the *b*-hadron decay topology. The impact parameter and decay length are key features of a secondary vertex that indicate the presence of a long-lived particle within the jet [137].

4.2. Object Definition at Particle Level

The signature of t-channel single top-quark events at particle level is identical with the signature at reconstruction level. In addition to analysis objects defined on measured events, we need to define objects for particle-level events to enable the cross-section measurement in the fiducial volume. The so-called particle level hereby refers only to stable particles, with a mean lifetime $\hat{\tau} > 0.3 \cdot 10^{-10}$ s. The particle-level definition enables a description of the fiducial volume independent of the MC generator.

4.2.1. Leptons

Leptons are defined to originate from a W-boson decay. This however, is implemented as an indirect requirement since certain MC generators do not include W bosons in their event record. The indirect requirement is achieved by excluding leptons coming from hadronic decay-chains, directly, or via a τ decay. Electrons, muons or neutrinos from τ decays are accepted if the τ lepton does not originate from a hadron decay. The four-vectors of electrons and muons are combined with photons within a distance of $\Delta R < 0.1$. Figure 4.3 displays the resolutions in p_{T} and η for selected leptons. In case of the lepton p_{T}, only a small deviation from zero to smaller values is observed. The RMS of the residual distributions which provide a measure of the resolution of the respective quantities. The resolution of the lepton p_{T} is about 1.6 GeV and the resolution of the pseudorapidity of the lepton is $< 10^{-3}$.

4.2.2. Missing transverse momentum

The $E_{\mathrm{T}}^{\mathrm{miss,truth}}$ is defined as the magnitude of the vector sum of the p_{T} of all selected neutrinos, using the lepton definition already introduced. Figure 4.4 shows the resolution of the $E_{\mathrm{T}}^{\mathrm{miss}}$. The mean value of the residual distribution shows a 5 GeV shift to higher values for reconstructed $E_{\mathrm{T}}^{\mathrm{miss}}$, w.r.t. the true $E_{\mathrm{T}}^{\mathrm{miss,truth}}$. This shift hints to the exclusion of low energetic particles in the $E_{\mathrm{T}}^{\mathrm{miss}}$ definition in the reconstruction procedure. The RMS of the distribution corresponds to the resolution of the reconstructed $E_{\mathrm{T}}^{\mathrm{miss}}$, which is found to be about 14 GeV.

4.2.3. Jets

Jets are clustered from all stable particles, excluding selected e, μ and ν. The photons that are associated with e or μ are not included in the clustering. The clustering is
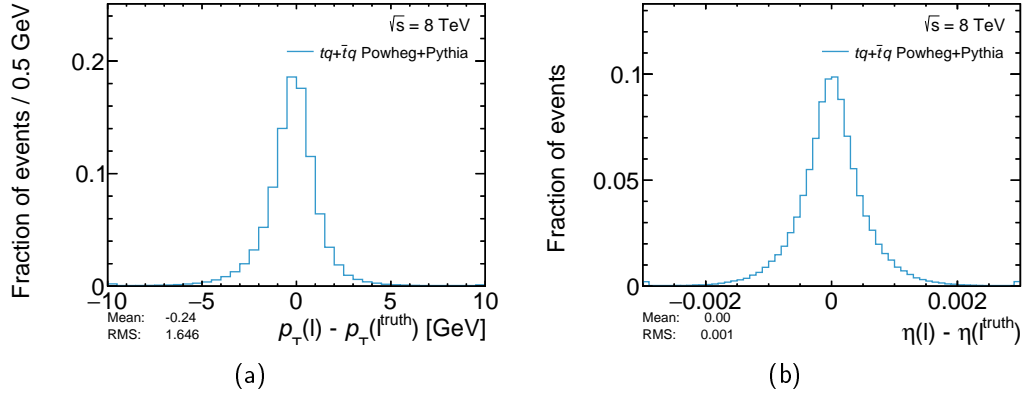
Figure 4.3.: Residual distributions of the lepton (ℓ) transverse momentum (a) and pseudorapidity (b) for selected leptons of t-channel single top-quark events. The mean values of the distributions correspond to a systematic bias in the reconstruction process. Values beyond the axis range are contained in the first and last bin.
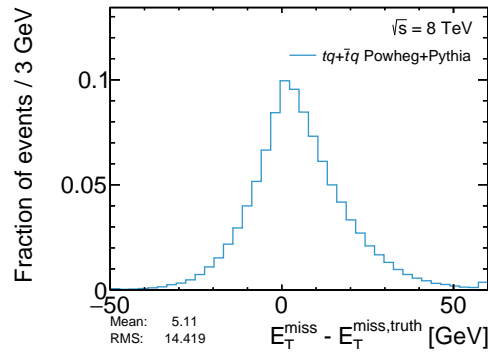
Figure 4.4.: The residual distribution of the reconstructed $E_{\mathrm{T}}^{\mathrm{miss}}$ for selected events. The mean value of the distribution corresponds to a systematic bias in the reconstruction process. Values beyond the axis range are contained in the first and last bin.

performed with the anti-k_t algorithm with a radius parameter of 0.4, implemented in the FastJet program at version 3.6 [138]. In order to associate b hadrons to jets, a technique known as ghost-matching is employed, by which the b hadrons energy is rescaled to essentially zero and inserted into the jet-clustering procedure, therefore the energy of the particle level jets is not biased. This provides the particle level equivalent of b tagging. Figure 4.5 shows the resolutions in p_{T} and η for selected tagged and untagged jets. The mean value of the distributions corresponds to a systematic bias in the respective quantity due to the reconstruction process. The mean value of the residual distribution of the untagged jet shows a shift of $0.9\,\text{GeV}$ to higher values for the reconstructed jet, w.r.t. the true jet p_{T}. In case of tagged jets the mean value is shifted by $3.9\,\text{GeV}$ to lower values of $p_{\text{T}}(b) - p_{\text{T}}(b^{\text{truth}})$. The RMS of the distribution corresponds to the resolution of the reconstructed jets, which is found to be about $8\,\text{GeV}$ and $12\,\text{GeV}$ for untagged and tagged jets, respectively.

(a) Untagged jet

(b) Untagged jet

(c) b-tagged jet
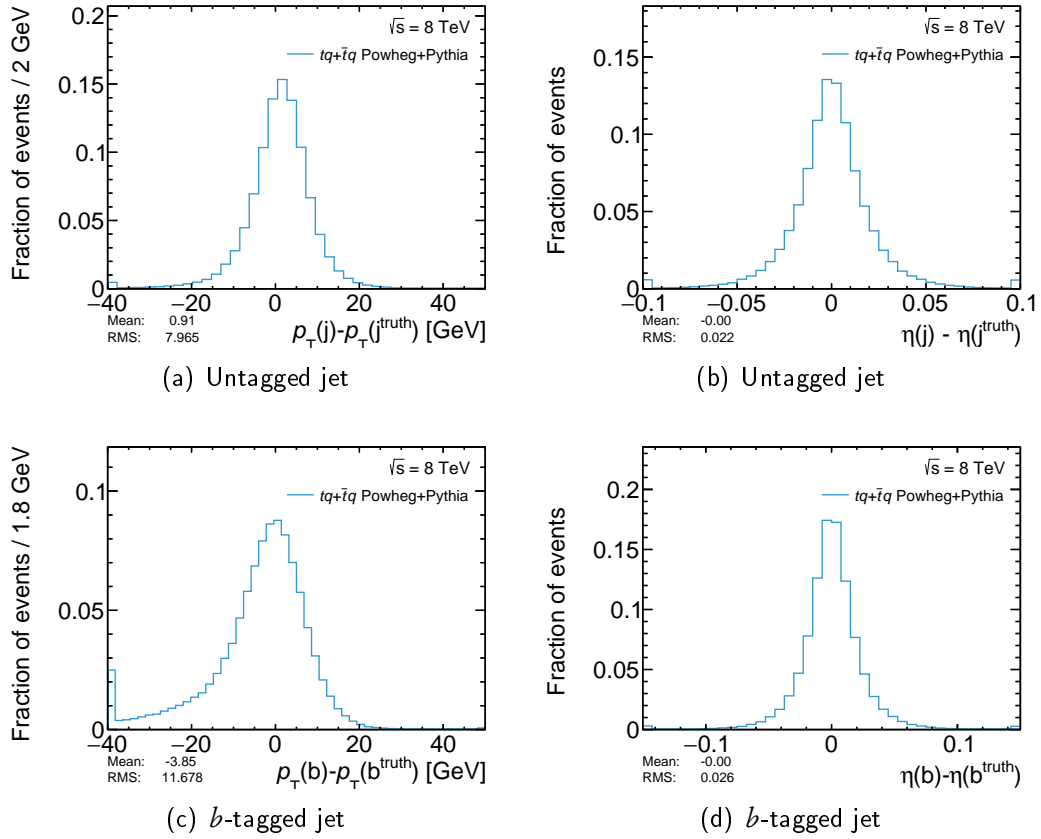
(d) b-tagged jet

Figure 4.5.: The residual distribution of reconstructed jets for selected leptons of t-channel single top-quark events. Figures (a) and (b) show the p_T and η distributions for the untagged jet, and Figures (c) and (d), show the same quantities for the tagged jet. Values beyond the axis range are contained in the first and last bin.

Event Selection and Background Estimation

The event selection exploits the signature of signal and background processes to enrich signal-like events. A metric of the quality of the event selection is the ratio of the number of signal events to the number of background events (S/B). Another important aspect of the event selection is to remove known modelling deficiencies and maintain a good agreement between data and the MC simulation.

The relevance of the background processes for this analysis arises from two different sources. The first being the physical background which results in the identical final state observed by the detector. Although the final state may be identical to the signal process, distinct differences in the process kinematics allow for discrimination between the two. The other kind of background arises from the instrumental limitation of the detector. Even though the fake rates for the utilised physics objects is small, high production cross-sections of instrumental backgrounds result in a sizable contribution to the number of events.

The description of the normalisation for several background processes is difficult to calculate accurately by theory for the phase space of interest, therefore the normalisation is obtained by a maximum-likelihood fit to Data, which is described in this Chapter.

The measured fiducial cross-sections refer to a subset of the total phase-space for single top-quark t-channel production, which is designed to be close to the detector acceptance in order to minimise extrapolation effects. This Chapter introduces the definition of the fiducial volume.

5.1. Event Selection

All events that are considered for the analysis must fulfill two different types of requirements. The first type are event-based criteria, e.g. number of jets, and the second type are object-based criteria, e.g. the p_T of the lepton, which are introduced in Chapter 4.

The leading-order signature of the t-channel single top-quark decay in the 4 FS is shown in Figure 5.1, where one b-quark jet, one lepton and missing transverse energy are the key features accompanied by an additional jet. While a second b-quark emerges from the initial gluon-splitting, it is not included in the event selection, since its transverse energy is typically relatively low and its pseudorapidity rather high, thereby escaping the acceptance of the detector.

Figure 5.2 shows the relative event yield of the ℓ^+ channel in (a) and the ℓ^- channel in (b) after the full selection is applied. In the ℓ^+ channel a $S/B = 27\,\%$ is achieved and in the ℓ^- channel $S/B = 17\,\%$.
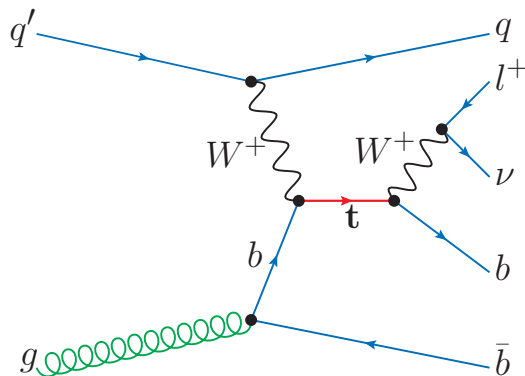
Figure 5.1.: Example Feynman diagram of the t-channel single top-quark production and semi-leptonic decay in the 4FS at LO QCD

5.1.1. Removal of the $m(\ell b)$-tail

Current MC generators do not include off-shell effects in the matrix-element calculation, since their contributions are missing in the so-called 'stable-top' approximation, therefore all events which have $m(\ell, b) > 160\,\text{GeV}$ are removed. The inclusion of off-shell top-quark production in current t-channel single top-quark MC event generators is subject to recent studies in Ref. [139].
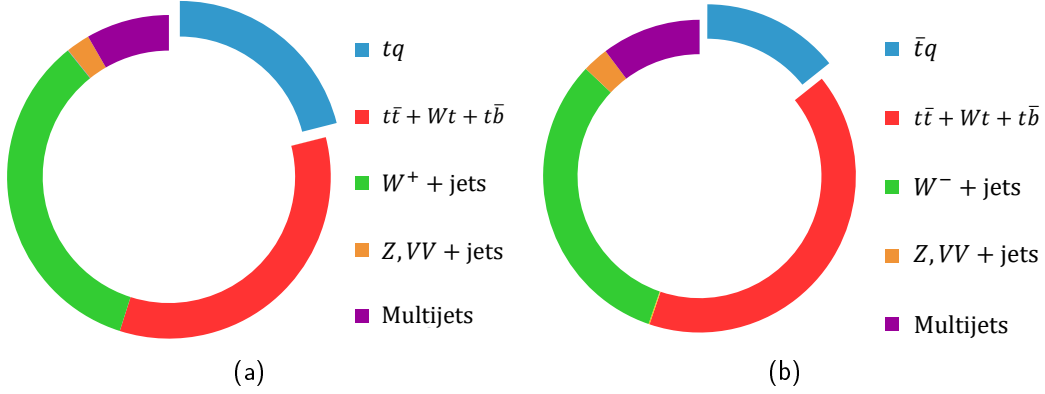
Figure 5.2.: Relative event yield of the ℓ^+ channel in (a) and the ℓ^- channel in (b) after the full selection is applied.

5.1.2. The Multijet Veto

Multijet events are rejected in three separate observables The main feature of multijet events compared to the signal process is that they do not contain W bosons. Since the source of neutrinos in multijet events is not related to on-shell W-boson decays, but from less energetic processes which populate the lower spectrum of the $E_\mathrm{T}^\mathrm{miss}$ distribution rendering it a discriminating variable for signal and multijet process. For the same reason the transverse mass of the W boson ($m_\mathrm{T}(\ell\nu)$), offers significant discrimination power of the signal and multijet process.

Events are required to fulfill $E_\mathrm{T}^\mathrm{miss} > 30\,\mathrm{GeV}$ and $m_\mathrm{T}(\ell\nu) > 50\,\mathrm{GeV}$ where

$$m_\mathrm{T}(\ell\nu) = \sqrt{2p_\mathrm{T}(\ell)E_\mathrm{T}^\mathrm{miss}\left(1 - \cos\Delta\phi\left(\ell, E_\mathrm{T}^\mathrm{miss}\right)\right)} \tag{5.1}$$

The third requirement to reduce multijet events is an additional isolation criterion for low p_T leptons $\Delta\phi\left(j_1, \ell\right)$:

$$p_\mathrm{T}\left(\ell\right) > 40\,\mathrm{GeV}\left(1 - \frac{\pi - |\Delta\phi\left(j_1, \ell\right)|}{\pi - 1}\right), \tag{5.2}$$

where j_1 is the highest p_T-jet. Figure 5.3 shows the requirement in the 2D-plane of the lepton-p_T and the $\Delta\phi\left(j_1, \ell\right)$, where all MC predictions are subtracted from collision data to highlight the regions of increased multijet contribution.
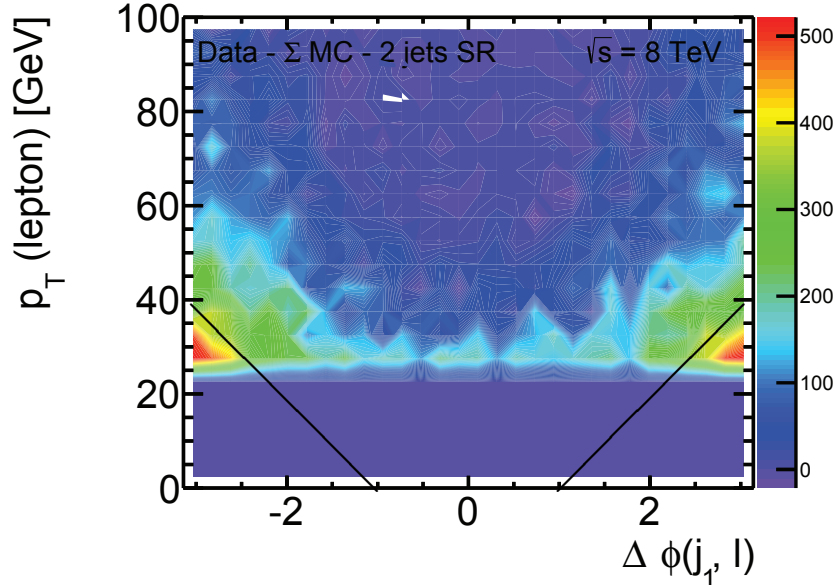
Figure 5.3.: The event rate dependence on the lepton p_T and the $\Delta\phi\,(j_1, \ell)$ for data after subtracting the MC predictions for all background processes.

5.1.3. The Dilepton Veto

The lepton requirements, especially the isolation criteria, allow for additional leptons in the event associated to Z-boson decays or $t\bar{t}$ dilepton final states. For the purpose of the dilepton veto, only additional leptons are considered if they have opposite electric charge to the primary lepton. The dilepton veto aims to reject events with additional leptons that do not pass the standard lepton requirements introduced in Chapter 4. Table 5.1 contains all requirements on additional leptons with respect to the standard lepton definition. The main feature of additional leptons is the lack of isolation and lower transverse momentum ($p_T(\ell_2) > 10\,\text{GeV}$) as well as the extended pseudorapidity range for electrons.

The electron quality requirement is separated between `loose` for central electrons within $|\eta(e_2)| < 2.47$ and forward electrons using `medium` within $2.47 < |\eta(e_2)| < 4.9$. Since the charge of forward electrons cannot be deduced from calorimeter measurements, forward electrons are always considered opposite charge to the primary lepton, for the purpose of the dilepton veto. Two separate vetoes are applied, depending on the flavour of the additional lepton with respect to the primary lepton. For additional leptons that have the same flavour as the primary selected lepton, an invariant mass criterion on the lepton pair is applied. Events with $80 < m(\ell_1, \ell_2) < 100\,\text{GeV}$, are rejected, which reduces the number events containing a leptonically decaying Z-boson. If an event has an additional lepton with different flavour as the primary lepton, the

event rejected, unless the additional lepton is within $\Delta R = 0.4$ to the selected b-jet. This requirement mainly reduces the number of $t\bar{t}$ events where both W-bosons decay leptonically.

In Tables 5.2 the efficiencies of the dilepton veto for all considered processes are given. The reduction of Z + jets events is 32.6 % in the μ-channel and 49.1 % in the e-channel. In events originating from $t\bar{t}+Wt+t\bar{b}$ processes, a reduction of 21.1 % in the e-channel and 20.8 % in the μ-channel is achieved. The number of signal events is only reduced by about 2.5 % in both channels, which is considered very small.

Table 5.1.: Requirements of additional leptons.

Requirement	Value
Transverse momentum	$p_{\mathrm{T}}(\ell_2) > 10\,\mathrm{GeV}$
Pseudorapidity range	$|\eta|(\mu_2) < 2.5$ $|\eta|(e_2) < 4.9$
Quality `loose` Quality `medium`	$|\eta(e_2)| < 2.47$ $|2.47 < \eta(e_2)| < 4.9$

Table 5.2.: Cut efficiency of the dilepton veto for events in the electron and muon channel.

	No Veto	Veto	rel. difference
Electrons			
Z + jets	2156	1097	-49.1%
W + jets	14249	14021	-1.6%
$t\bar{t}, Wt, t\bar{b}$	20752	16380	-21.1%
$tq, \bar{t}q$	8134	7935	-2.5%
Muons			
Z + jets	2076	1400	-32.6%
W + jets	19240	18936	-1.6%
$t\bar{t}, Wt, t\bar{b}$	25604	20275	-20.8%
$tq, \bar{t}q$	10190	9942	-2.4%

5.1.4. Definition of Signal and Control Regions

Three orthogonal selections are defined to enrich the signal and two main backgrounds in each region. The regions are only separated by different b-tagging requirements.

Signal Region   To enrich signal events in the signal region (SR) exactly one b-tagged jet is required with a MV1c weight higher than $w_{\mathrm{MV1c}} > 0.9195$, which corresponds to 50 % b-tagging efficiency. The choice of the specific b-tagging algorithm is founded in the optimised c-jet rejection to suppress the $W + c$-jet production background. The second jet is therefore required to be untagged.

W + jets Validation Region   The W + jets validation region (W + jets VR) is defined by requiring exactly one b-tagged jet with a MV1c weight higher than $w_{\mathrm{MV1c}} > 0.4051$, which corresponds to 80 % b-tagging efficiency. Events in the SR are rejected. In addition all events with a MV1c weight in the range $0.9195 < w_{\mathrm{MV1c}} < 0.8641$ are removed to reduce the signal contribution in the W + jets VR.

$t\bar{t}$ Validation Region   The $t\bar{t}$ validation region ($t\bar{t}$ VR) is defined by requiring exactly two b-tagged jets with the same criterion used in the SR. Since the resulting selection does not contain untagged jets, the notation b_1 and b_2 are introduced by comparing the pseudorapidity of them: $|\eta(b_1)| < |\eta(b_2)|$. This enables to define all observables that include the untagged jet in the SR to the $t\bar{t}$ VR, e.g. $|\eta(j)|$ in the SR becomes $|\eta(b_2)|$ in the $t\bar{t}$ VR.

5.2. Background Estimation

The estimation of the background contribution to the selected events is very important to validate the prediction of MC simulation in the SR. With the exception of the QCD multijet background this analysis relies on MC simulated events. The special case of the QCD multijet background arises from the contribution of so-called fake leptons which are misidentified jets. Even though the fake rate of leptons is very small, due to the high cross-section of the QCD multijet background processes the resulting contribution to the selected events is sizable. This circumstance makes this process also very inefficient to simulate using MC methods, because one would need to generate vast amounts of events to produce sufficient statistics in the final selection.

5.2.1. QCD Multijet Models

To obtain the contribution of the QCD multijet process this analysis relies on two different models to describe the kinematics of these events. The main sources of QCD multijet events are semileptonic b-quark decays and long-lived particles which decay via the weak interaction like $\pi^{\pm}$ or K mesons. In addition, misidentified electrons are contributed by π^0 particles which decay into two photons, where the required

tracks for the electron reconstruction are falsely associated to the energy cluster in the electromagnetic calorimeter.

In the electron channel the Jet-Lepton model is used, which employs a specialised selection on MC simulated events, while in the muon channel a selection on measured data events is used.

Jet-Lepton Model

The Jet-Lepton selection [140] is applied on MC simulated events to enrich the number of events containing a jet which are likely to be mis-identified in the detector as a lepton. The MC simulation is based on PYTHIA 8 and provides a sample containing at least two jets, one of which must have $E_T(\text{jet}) > 17\,\text{GeV}$ and $|\eta| < 2.7$. A selected event must contain exactly one 'jet-lepton' candidate, which fulfils the requirements given in Table (5.3). The criteria already incorporates the electron kinematic requirements introduced in Section 4.1.2. The fraction of energy deposited in the EM calorimeter system (EM fraction) is required to be in the range $0.8 < f_{EM} < 0.95$, to improve the likelihood of the jet to be mis-identified. The 'jet-lepton' candidate replaces the electron in the SR selection to match the lepton + two jet signature.

Table 5.3.: Applied cuts to define a 'jet-lepton' sample.

Variable	Cut
Transverse energy of jet	$E_T > 25\,\text{GeV}$
η of jet	$|\eta| < 2.47$
EM fraction	$0.8 < f_{EM} < 0.95$

Anti-Muon Model

While the Jet-Lepton model relies on MC simulation to construct a QCD multijet background template, the Anti-Muon model [140] uses collision data to achieve that. In order to select events which contain a jet likely to be mis-identified as a muon, the muon identification criteria are inverted, see Table 5.4. The resulting set of events contain only a small fraction of signal muons from W-boson and Z-boson decays, by vetoing events with additional leptons.

Matrix Method

The Matrix Method [140] is a complementary procedure to estimate the multijet contribution for a given event selection. Similar to the Jet-Lepton and Anti-Muon methods, the Matrix Method employs a specific selection, called loose selection, to enrich fake-lepton events. In the context of the Matrix Method, mis-identified leptons are called "fake" leptons, and correctly identified leptons are called "real" leptons. In addition to the loose selection, a tight selection is defined, which corresponds to the standard lepton selections employed in this analysis, introduced in Sections 4.1.2 and 4.1.3. The

Table 5.4.: Selection criteria that are different from the nominal requirements in the antimuon sample.

Variable	Cut
Impact parameter z_0	no cut
Isolation	Etcone20$/p_T(\mu) > 0.03, I_{iso}/p_T(\mu) < 0.1$
Energy loss type	energyLossType == 1, (Not Isolated)
Energy loss	energyLoss < 6 GeV

loose selection includes a loose lepton definition, for which the isolation requirement on the leptons is removed. Both selections result in two samples of events with different compositions of real and fake leptons. As these selections are applied on the same dataset, one can trace events which are selected by either selection. The number of events that pass both selections can be expressed as a linear combination of the number of events that contain either a real or a fake lepton. This system of equations can be solved to determine the number of fake-lepton (multijet) events in the SR. The Matrix Method provides predictions for the kinematics of multijet events, as well as the normalisation. The Matrix Method is employed in this analysis to estimate the systematic uncertainty on the modeling of the multijet process. More information is presented in Ref. [140].

5.2.2. Estimation of the QCD-Multijet Background

In order to estimate the contribution of the multijet background, a binned maximum-likelihood (ML) fit on the E_T^{miss} distribution is performed. In the following the multijet process refers to the process template obtained with the Jet-Lepton model in the electron channel and the Anti-Muon model in the muon channel. The fit is performed in the three respective selection regions including events which have $0 < E_T^{miss} \leq 30$, to increase sensitivity to the multijet process. The multijet normalisation obtained from the fit is then applied to the respective selection region excluding the low-E_T^{miss} region.

In each region six separate channels are differentiated, the electron channel is split into two pseudorapidity regions, to overcome a modeling deficiency of the Jet-Lepton model. The modeling deficiency refers to an observed discrepancy between the size of the multijet contribution in the barrel pseudorapidity region $|\eta| < 1.5$ and the endcap pseudorapidity region $1.5 < |\eta| < 2.5$. The origin of the modeling deficiency is probably founded in the characteristics of the utilised dijet MC-sample. Since generator-level cuts on the number of jets and the jet p_T are applied on the dijet MC-sample, the selected Jet-Lepton model sample is incomplete. This, however, can be partially remedied by

a simultaneous fit in the two regions. Barrel electrons are defined in the pseudorapidity region $|\eta| < 1.5$, while endcap electrons are corresponding to $1.5 < |\eta| < 2.5$. Therefore three lepton channels are constructed for which the respective lepton charge is distinguished, resulting in six channels.

Figure 5.4 shows the different process templates in the $E_\mathrm{T}^\mathrm{miss}$ distribution. The significant difference of the process template of the multijet contribution compared to the W + jets and top-quark contributions enable the determination of the multijet normalisation in this observable distribution. Both multijet and Z + jets processes exhibit comparably low values of $E_\mathrm{T}^\mathrm{miss}$, due to the lack of neutrinos originating from a W boson in these processes. The similarity of the Z + jets processes to the multijet contribution results in virtually no sensitivity to obtain the normalisation of both at the same time, thus the former contribution remains fixed to its prediction based on the theoretical cross-section.

The multijet processes are assumed to produce the same number of events containing positive and negative charged leptons, therefore the fit performed constrains the multijet normalisation in the ℓ^+ channel and ℓ^- channel simultaneously. The performed fit includes the normalisation of the multijet, top-quark and W + jets processes in each of the three channels separately. In case of the two validation regions, the remaining backgrounds are highly depleted and are not included in the fit, hence only the multijet normalisation is obtained together with W + jets in the W + jets VR and $t\bar{t}$ in the $t\bar{t}$ VR.

A systematic uncertainty on the normalisation and modeling of the multijet estimation is assigned. The modeling component in the electron channel of the SR is defined by the comparison of the Jet-Lepton model to the Matrix Method prediction, while in the muon channel, the Anti-Muon model is compared to the Matrix Method prediction. The normalisation uncertainty is derived by the comparison of the multijet estimate obtained by the ML fit and the prediction of the Matrix Method. In the validation regions however only a normalisation uncertainty of 50 % is assigned. The estimate on the normalisation uncertainty was mainly studied in Ref. [6, 7, 140], while the estimate was found to be valid for this analysis as well.

Table 5.5 contains the fit results for all channels in the three selection regions.

The corresponding $E_\mathrm{T}^\mathrm{miss}$ distributions leading to these results are shown in Figures 5.5 and 5.6 for the electron channel and in Figures 5.7 and 5.8 for the muon channel and separated by the lepton charge.
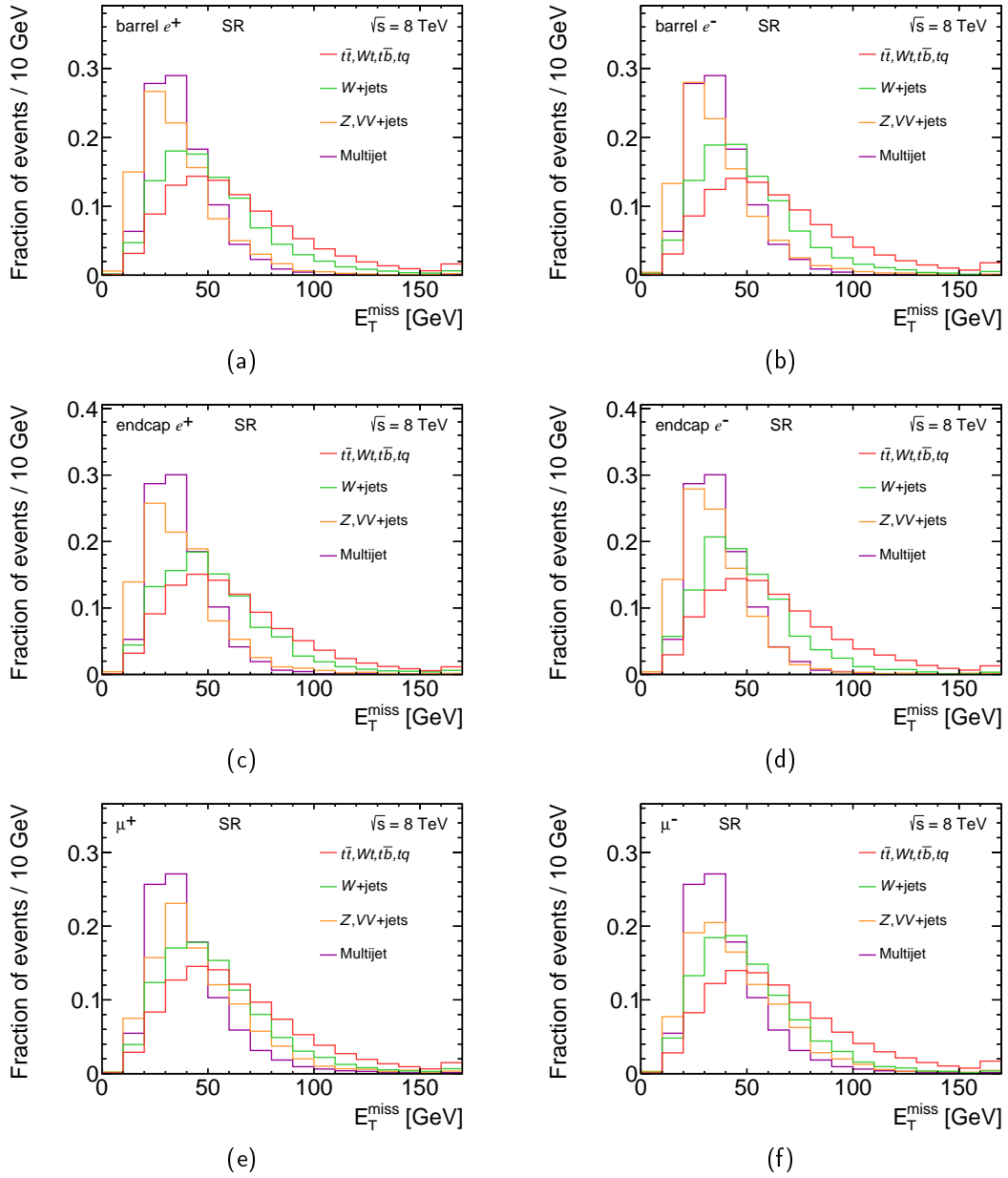
Figure 5.4.: Template E_T^{miss} distributions in the signal region. All distributions are normalised to unit area.

Table 5.5.: Estimate of the multijet background in the signal and control regions using the binned maximum-likelihood fit in the $E_{\mathrm{T}}^{\mathrm{miss}}$ distribution. The quoted numbers are the expected number of events in each region together with the scale factors of the simultaneously fitted backgrounds. The uncertainties on the scale factor β, the number of multijet events predicted by the Matrix Method and the multijet estimate are statistical only.

Channel	events fitted	events Matrix Method	fraction	$\beta(\mathrm{top})$	$\beta(W+\mathrm{jets})$
		signal region			
barrel e^+	850 ± 200	807 ± 28	5.0 %	0.98 ± 0.03	1.11 ± 0.08
barrel e^-	850 ± 200	831 ± 29	6.0 %	0.99 ± 0.03	1.07 ± 0.08
endcap e^+	721 ± 86	592 ± 24	15.5 %	0.97 ± 0.07	1.09 ± 0.08
endcap e^-	721 ± 86	597 ± 24	21.2 %	0.96 ± 0.06	1.11 ± 0.09
μ^+	2950 ± 280	2463 ± 50	10.4 %	0.98 ± 0.03	1.08 ± 0.06
μ^-	2950 ± 280	2381 ± 49	13.4 %	0.98 ± 0.03	1.06 ± 0.06
		$W+$ jets VR			
barrel e^+	3210 ± 240	-	9.6 %	fixed	1.07 ± 0.01
barrel e^-	3210 ± 240	-	11.3 %	fixed	1.04 ± 0.01
endcap e^+	2680 ± 150	-	21.2 %	fixed	1.09 ± 0.02
endcap e^-	2680 ± 150	-	23.6 %	fixed	1.09 ± 0.02
μ^+	6100 ± 410	-	9.8 %	fixed	1.08 ± 0.01
μ^-	6100 ± 410	-	12.7 %	fixed	1.05 ± 0.01
		$t\bar{t}$ VR			
barrel e^+	47 ± 24	-	3.4 %	1.03 ± 0.03	fixed
barrel e^-	47 ± 24	-	3.9%	1.06 ± 0.03	fixed
endcap e^+	30 ± 11	-	11.0 %	1.06 ± 0.07	fixed
endcap e^-	30 ± 11	-	12.5 %	0.99 ± 0.07	fixed
μ^+	138 ± 40	-	6.7 %	1.02 ± 0.03	fixed
μ^-	138 ± 40	-	7.6 %	1.02 ± 0.03	fixed
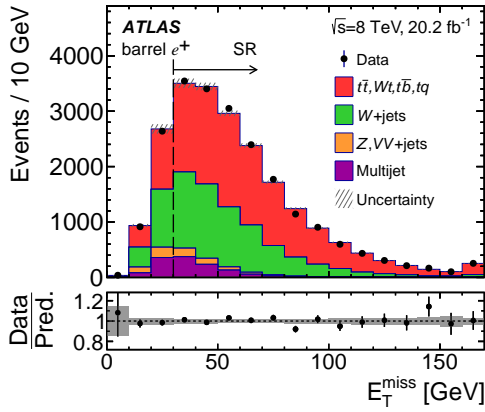
(a) Barrel electron channel in the SR.
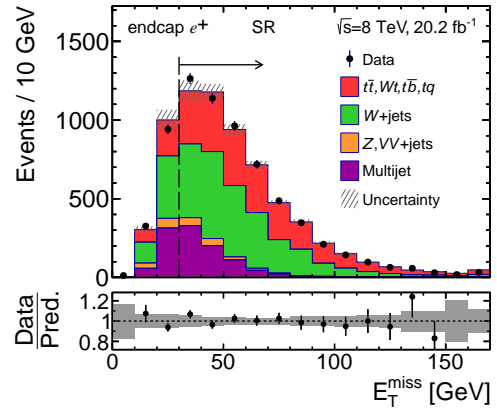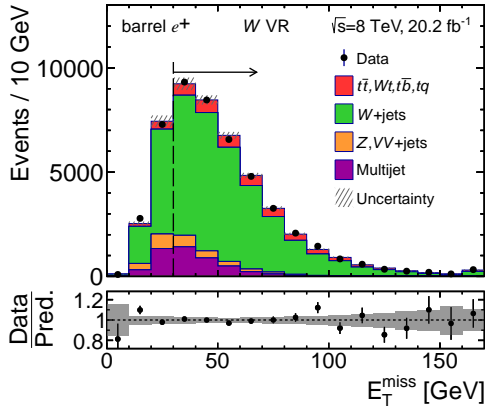
(b) Endcap electron channel in the SR.

(c) Barrel electron channel in the W + jets VR.
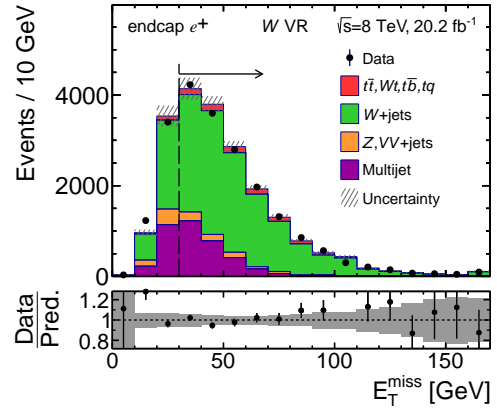
(d) Endcap electron channel in the W + jets VR.
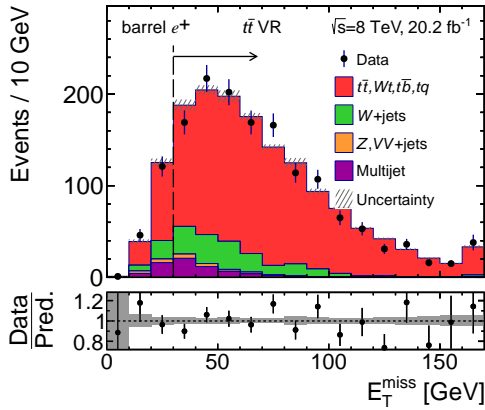
(e) Barrel electron channel in the $t\bar{t}$ VR.
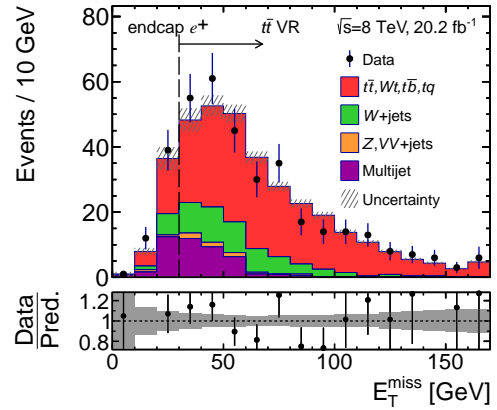
(f) Endcap electron channel in the $t\bar{t}$ VR.

Figure 5.5.: Result of the binned maximum-likelihood fit to the $E_{\mathrm{T}}^{\mathrm{miss}}$ distributions for the SR ((a),(b)), the W + jets VR ((c),(d)), and the $t\bar{t}$ VR ((e),(f)) for electrons with positive charge in the barrel (left) and endcap (right) regions, respectively. The dashed vertical line indicates the threshold of the respective selection region. The ratio between the observed and expected (Pred.) number of events in each bin is shown in the lower panel.
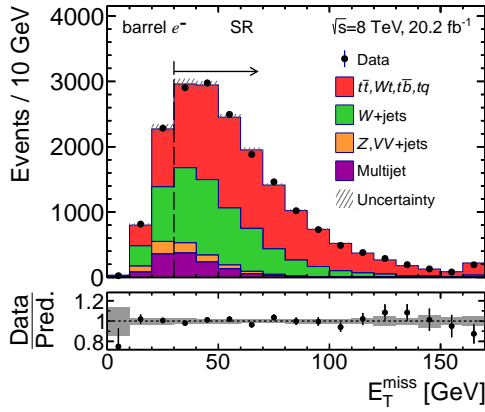
(a) Barrel electron channel in the SR.
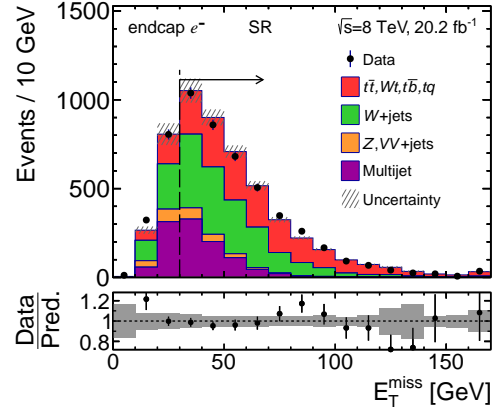
(b) Endcap electron channel in the SR.

(c) Barrel electron channel in the W + jets VR.

(d) Endcap electron channel in the W +jets VR.

(e) Barrel electron channel in the $t\bar{t}$ VR.

(f) Endcap electron channel in the $t\bar{t}$ VR.

Figure 5.6.: Result of the binned maximum-likelihood fit to the E_T^{miss} distributions for the SR ((a),(b)), the W + jets VR ((c),(d)), and the $t\bar{t}$ VR ((e),(f)) for electrons with negative charge in the barrel (left) and endcap (right) regions, respectively. The dashed vertical line indicates the threshold of the respective selection region. The ratio of observed to predicted (Pred.) number of events in each bin is shown in the lower panel.
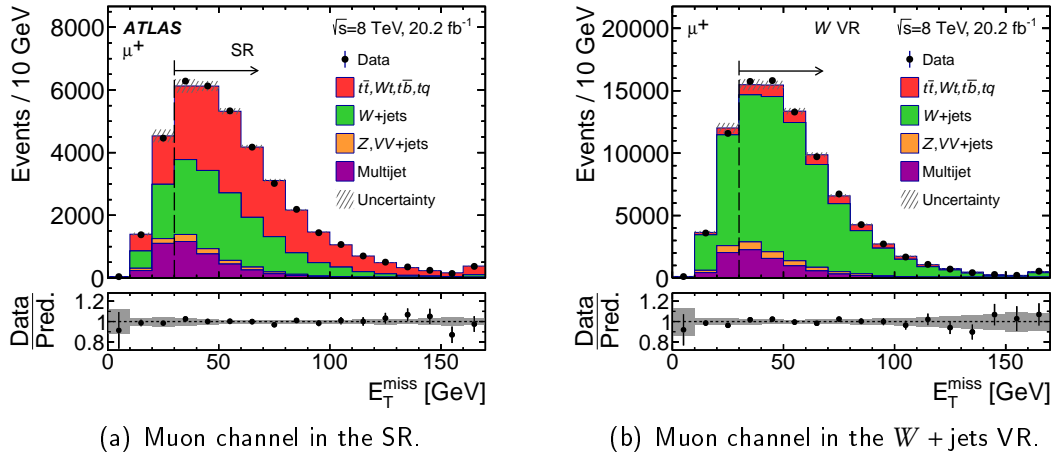
(a) Muon channel in the SR.

(b) Muon channel in the W + jets VR.
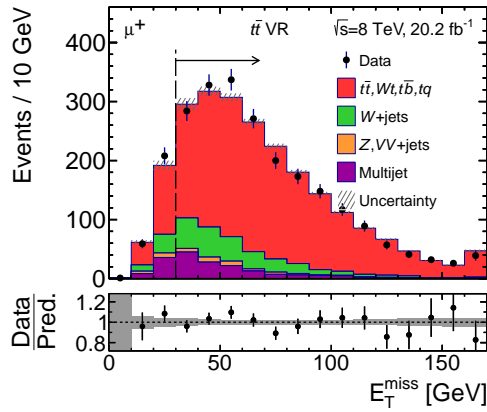
(c) Muon channel in the $t\bar{t}$ VR.

Figure 5.7.: Result of the binned maximum-likelihood fit to the $E_{\mathrm{T}}^{\mathrm{miss}}$ distributions for the SR (a), the W + jets VR (b), and the $t\bar{t}$ VR (c) for the muon channel with positive charge. The dashed vertical line indicates the threshold of the respective selection region. The ratio of observed to predicted (Pred.) number of events in each bin is shown in the lower panel.

(a) Muon channel in the SR.

(b) Muon channel in the W + jets VR.

(c) Muon channel in the $t\bar{t}$ VR.
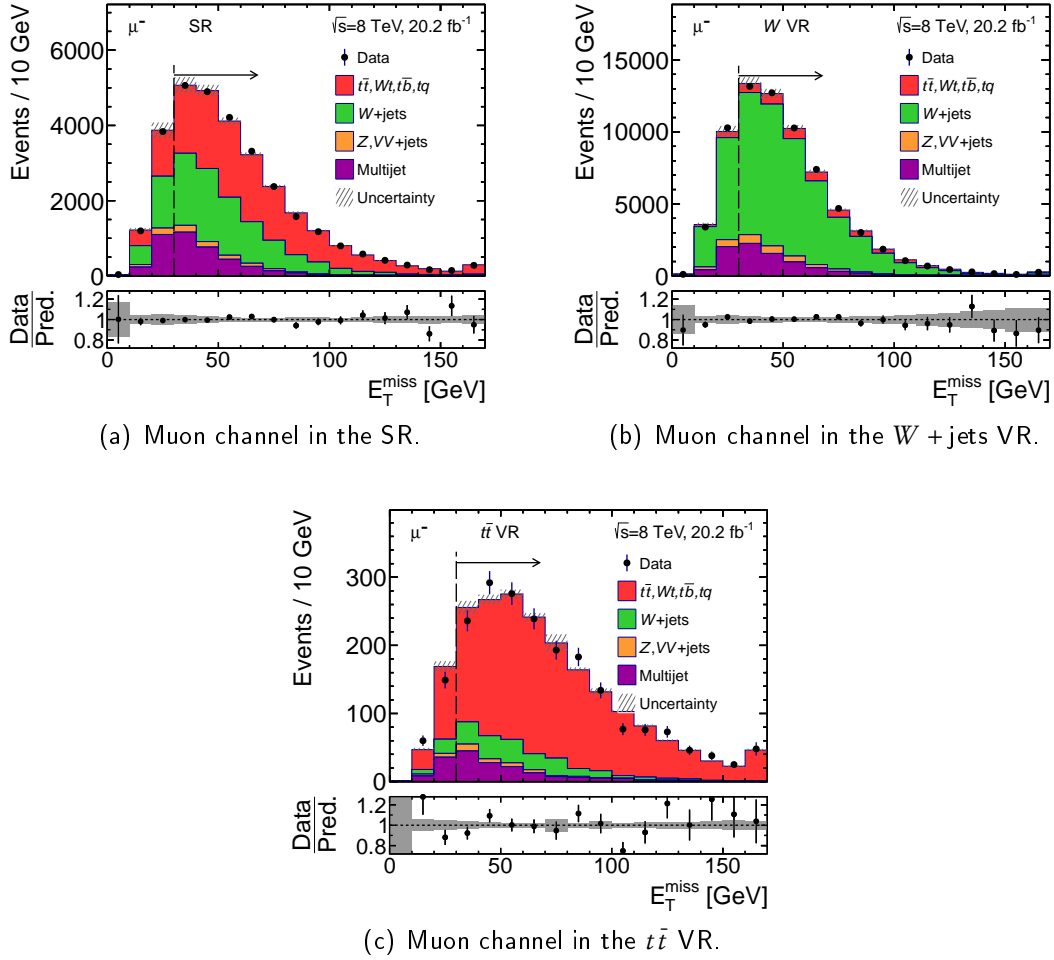
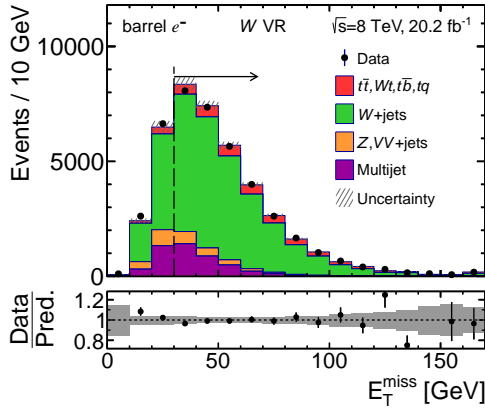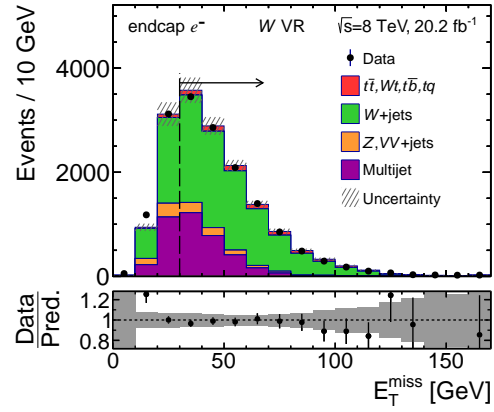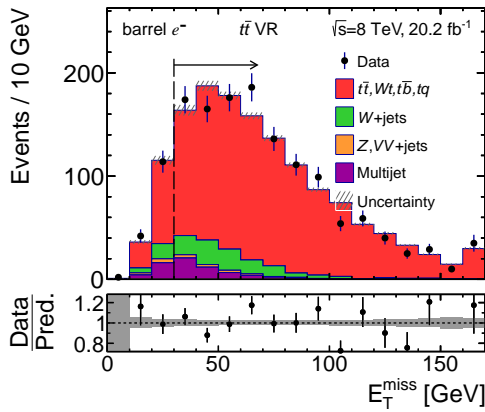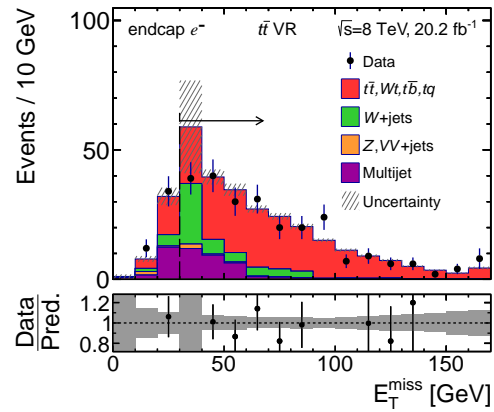**Figure 5.8.:** Result of the binned maximum-likelihood fit to the E_T^{miss} distributions for the signal region (a), the W + jets VR (b), and $t\bar{t}$ VR (c) for the muon channel with negative charge. The dashed vertical line indicates the threshold of the respective selection region. The ratio of observed to predicted (Pred.) number of events in each bin is shown in the lower panel.

5.2.3. Kinematic Modelling

In order to validate the estimated yield of the multijet contribution, the kinematic modelling of the charged lepton and the jets in the W + jets VR and $t\bar{t}$ VR is inspected. Figures 5.9 - 5.12 show the distribution in the W + jets VR, while Figures 5.13 - 5.15 show the same distributions in the $t\bar{t}$ VR. In both VRs the ℓ^+ channel and ℓ^- channel are shown separately. The estimates of the barrel- and endcap-region of the electron are merged, as they are in the main analysis. The processes are scaled to the result of the fit to the $E_{\mathrm{T}}^{\mathrm{miss}}$ distribution in the respective selection region. The fit results are given in Table 5.5. For the W + jets and the top-quark background processes the fit result is given as scale factors w.r.t. the theoretical cross sections.

In case of the multijet contribution, the obtained template shape is normalised to the obtained estimate in the fit. The scale factors obtained for the W + jets and top processes are only used to validate the kinematic modelling of the MC simulated processes and the multijet contribution with collision data and the scale factors are not used in the main analysis.

The overall agreement that is observed in the two validation regions is very good. The general absence of slopes in any ratio of collision data and MC simulation indicates the absence systematic mis-modelling of the multijet process.
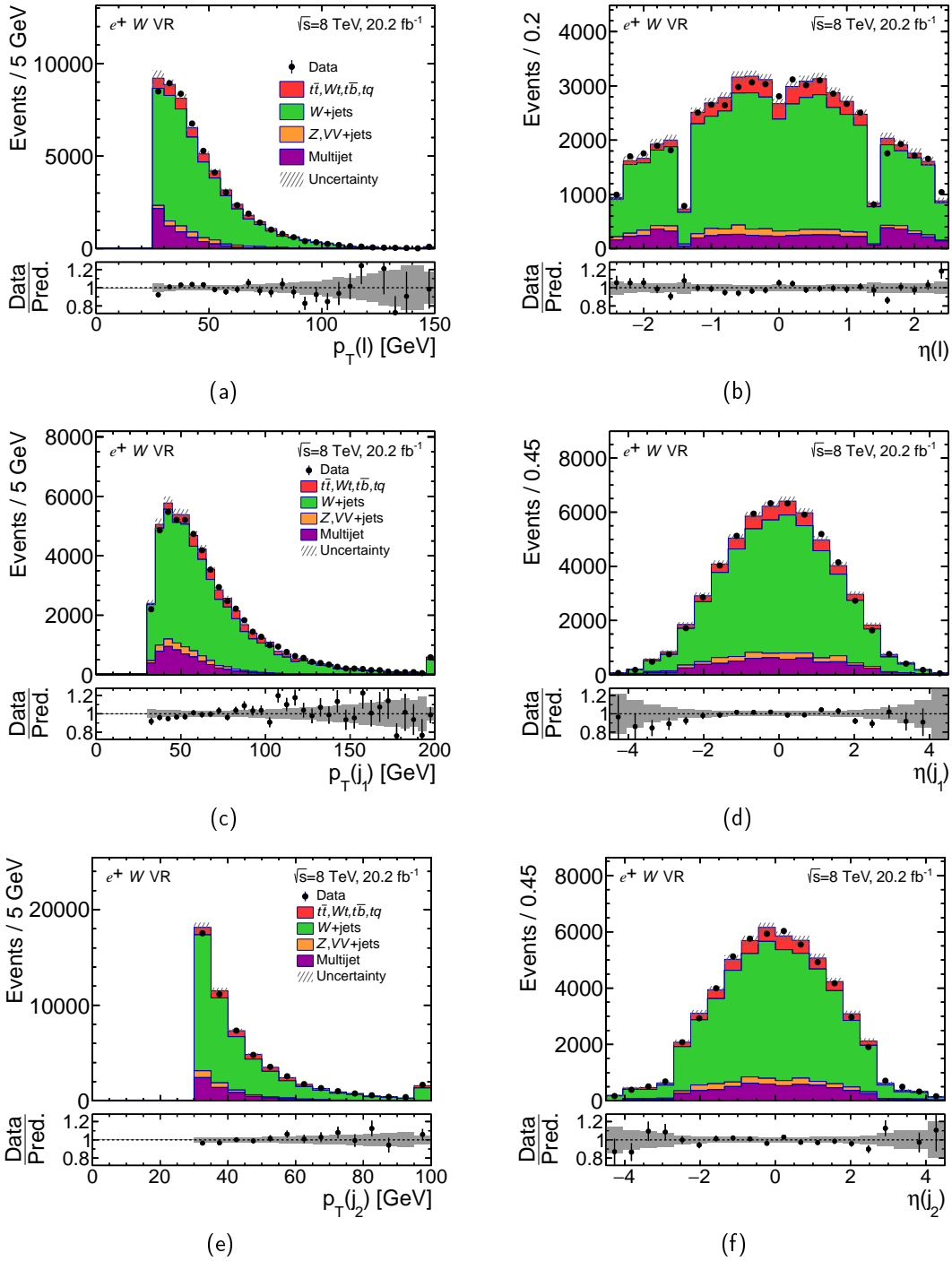
Figure 5.9.: Kinematic distributions in the W + jets VR for the e^+ channel. (a) p_T and (b) η of the electron, (c) p_T and (d) η of the leading jet and, (e) p_T and (f) η of the sub-leading jet. The hatched error band represents the uncertainty on the multijet rate as well as the MC statistical uncertainty. The ratio of observed to predicted (Pred.) number of events in each bin is shown in the lower panel. Events beyond the axis range are included in the last bin.

(a)

(b)

(c)

(d)

(e)

(f)
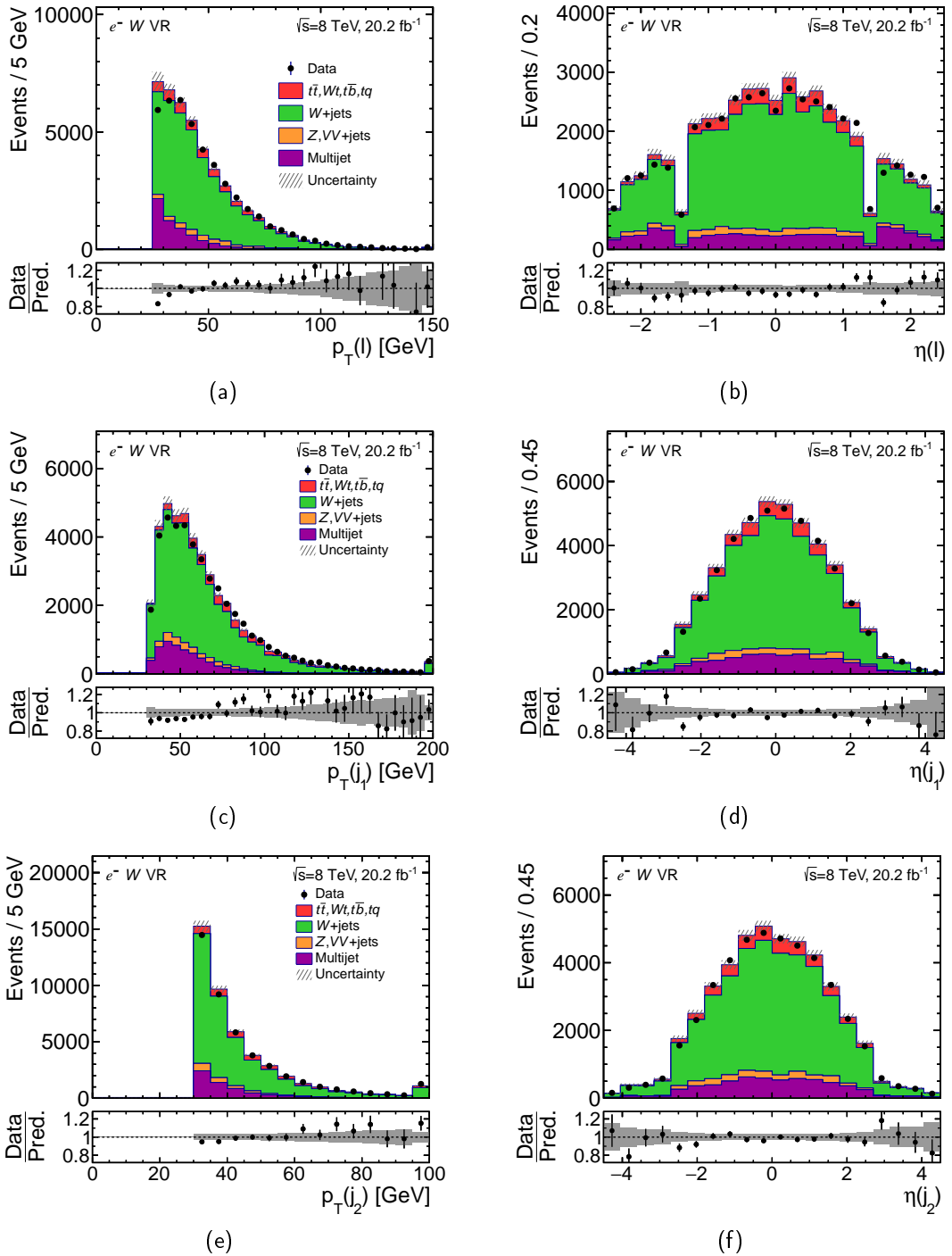
Figure 5.10.: Kinematic distributions in the W + jets VR for the e^- channel. (a) p_T and (b) η of the electron, (c) p_T and (d) η of the leading jet and, (e) p_T and (f) η of the sub-leading jet. The hatched error band represents the uncertainty on the multijet rate as well as the MC statistical uncertainty. The ratio of observed to predicted (Pred.) number of events in each bin is shown in the lower panel. Events beyond the axis range are included in the last bin.
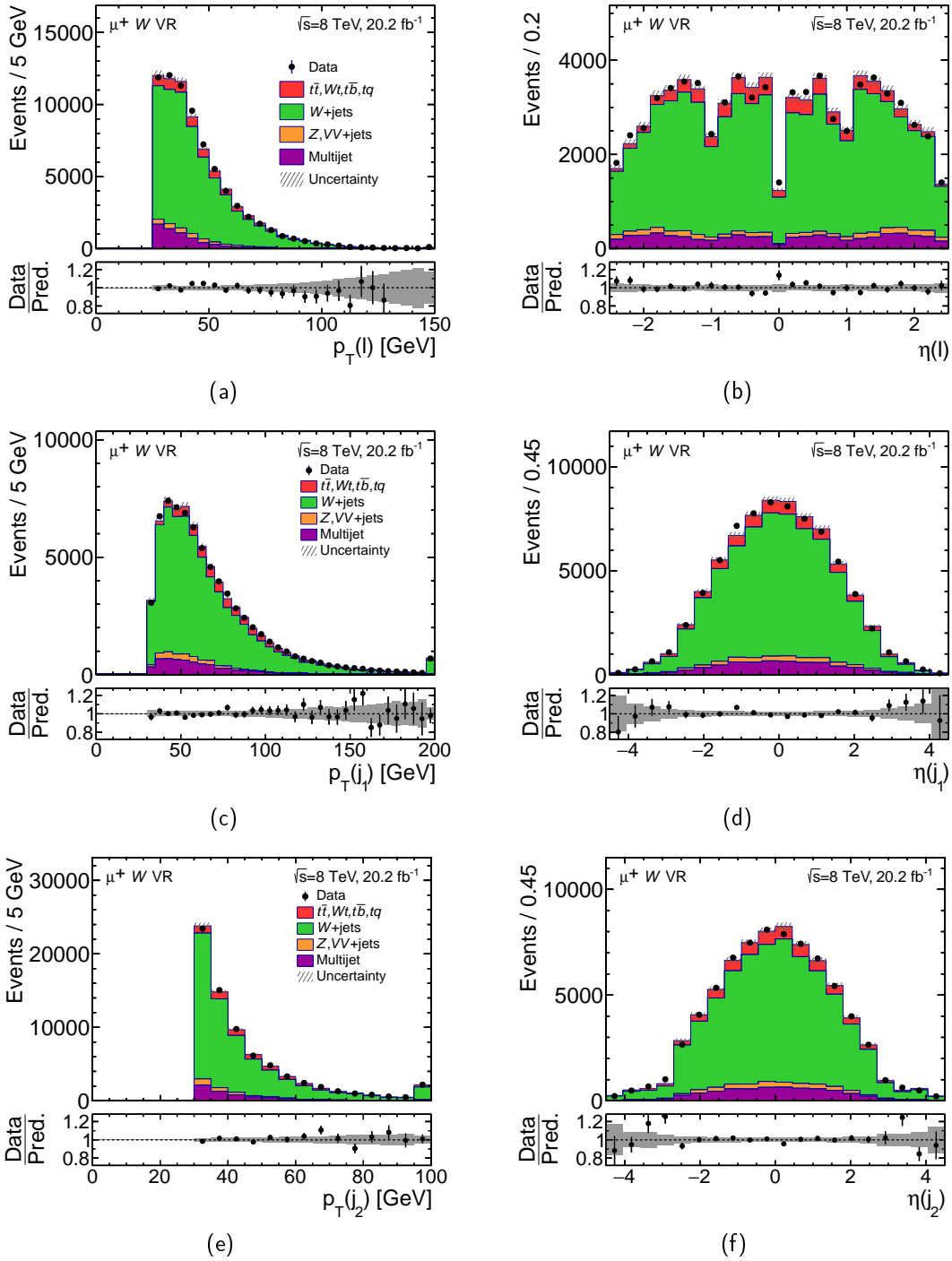
Figure 5.11.: Kinematic distributions in the W + jets VR for the μ^+ channel. (a) p_T and (b) η of the muon, (c) p_T and (d) η of the leading jet and, (e) p_T and (f) η of the sub-leading jet. The hatched error band represents the uncertainty on the multijet rate as well as the MC statistical uncertainty. The ratio of observed to predicted (Pred.) number of events in each bin is shown in the lower panel. Events beyond the axis range are included in the last bin.

Figure 5.12.: Kinematic distributions in the W + jets VR for the μ^- channel. (a) p_T and (b) η of the muon, (c) p_T and (d) η of the leading jet and, (e) p_T and (f) η of the sub-leading jet. The hatched error band represents the uncertainty on the multijet rate as well as the MC statistical uncertainty. The ratio of observed to predicted (Pred.) number of events in each bin is shown in the lower panel. Events beyond the axis range are included in the last bin.
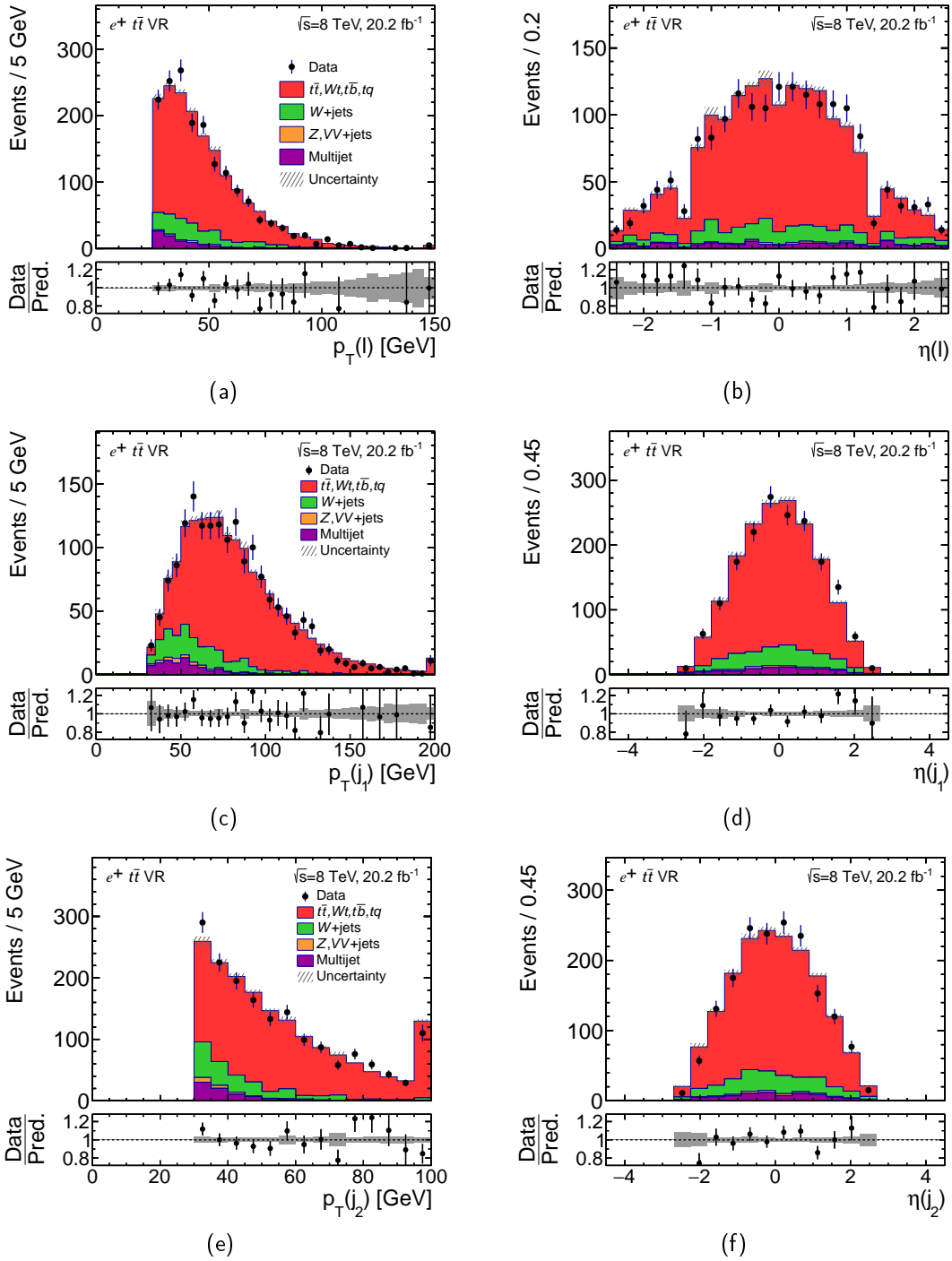
Figure 5.13.: Kinematic distributions in the $t\bar{t}$ VR for the e^+ channel. (a) p_T and (b) η of the electron, (c) p_T and (d) η of the leading jet and, (e) p_T and (f) η of the sub-leading jet. The hatched error band represents the uncertainty on the multijet rate as well as the MC statistical uncertainty. The ratio of observed to predicted (Pred.) number of events in each bin is shown in the lower panel. Events beyond the axis range are included in the last bin.
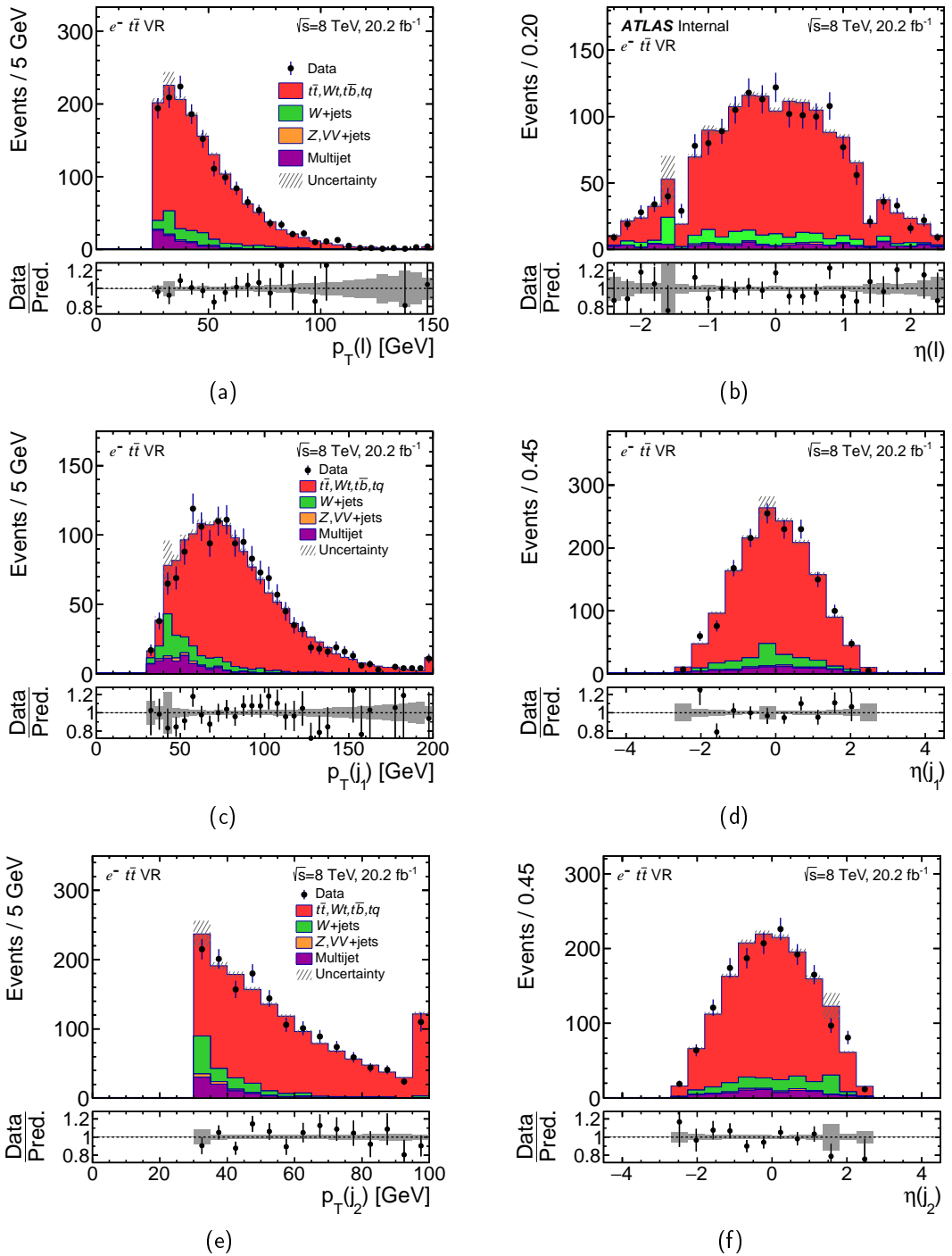
Figure 5.14.: Kinematic distributions in the $t\bar{t}$ VR for the e^- channel. (a) p_T and (b) η of the electron, (c) p_T and (d) η of the leading jet and, (e) p_T and (f) η of the subleading jet. The hatched error band represents the uncertainty on the multijet rate as well as the MC statistical uncertainty. The ratio of observed to predicted (Pred.) number of events in each bin is shown in the lower panel. Events beyond the axis range are included in the last bin.
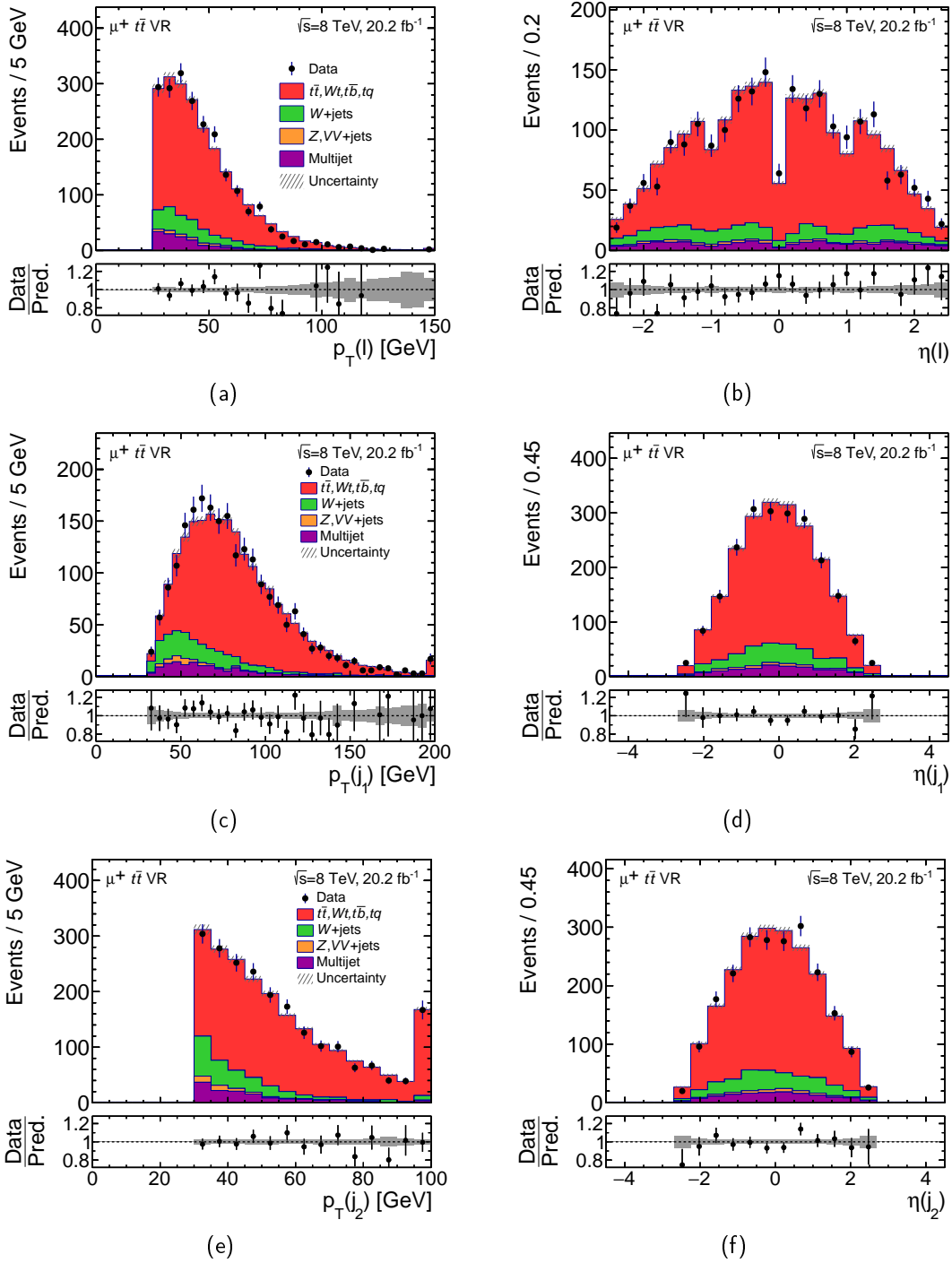
Figure 5.15.: Kinematic distributions in the $t\bar{t}$ VR for the μ^+ channel. (a) p_T and (b) η of the muon, (c) p_T and (d) η of the leading jet and, (e) p_T and (f) η of the sub-leading jet. The hatched error band represents the uncertainty on the multijet rate as well as the MC statistical uncertainty. The ratio of observed to predicted (Pred.) number of events in each bin is shown in the lower panel. Events beyond the axis range are included in the last bin.
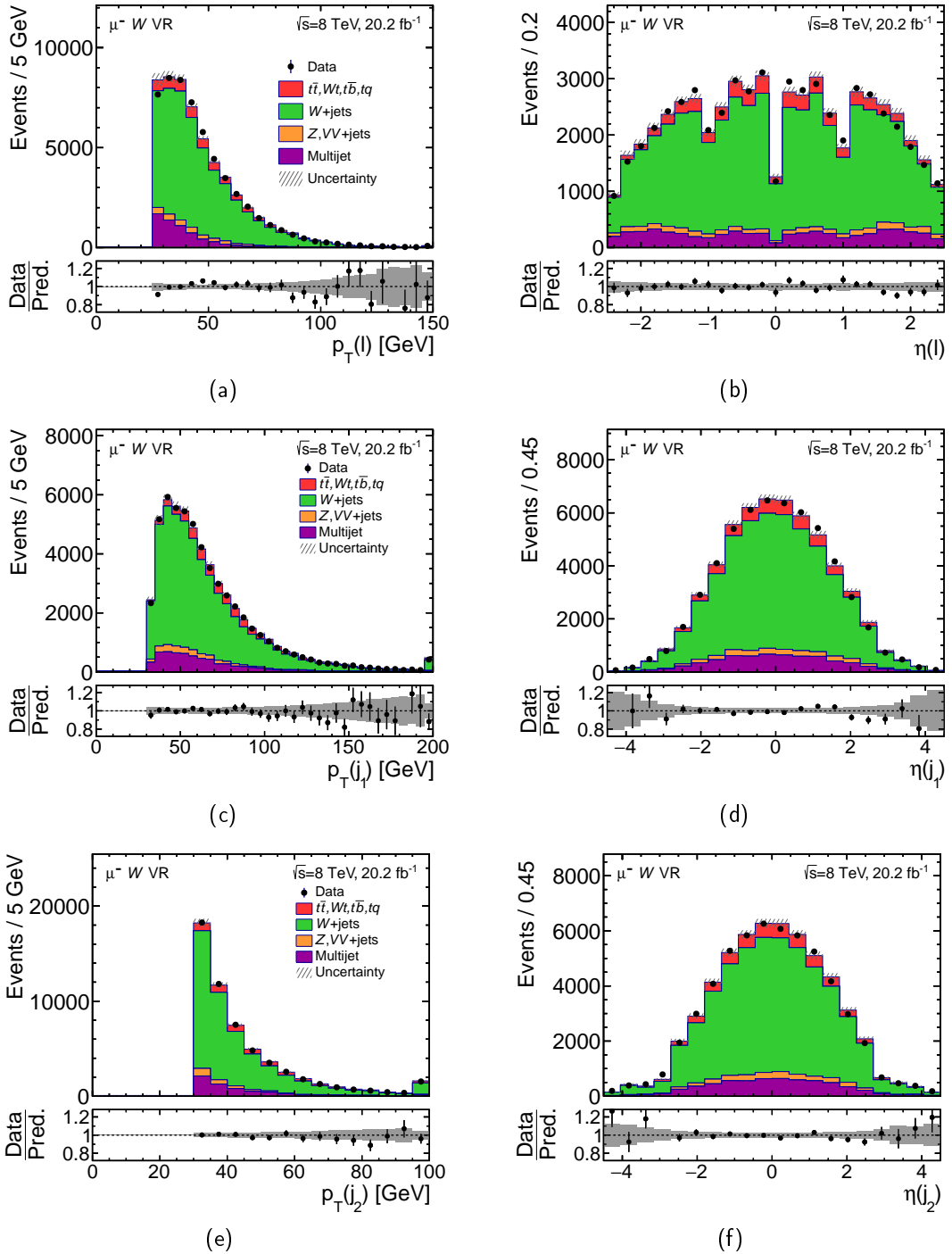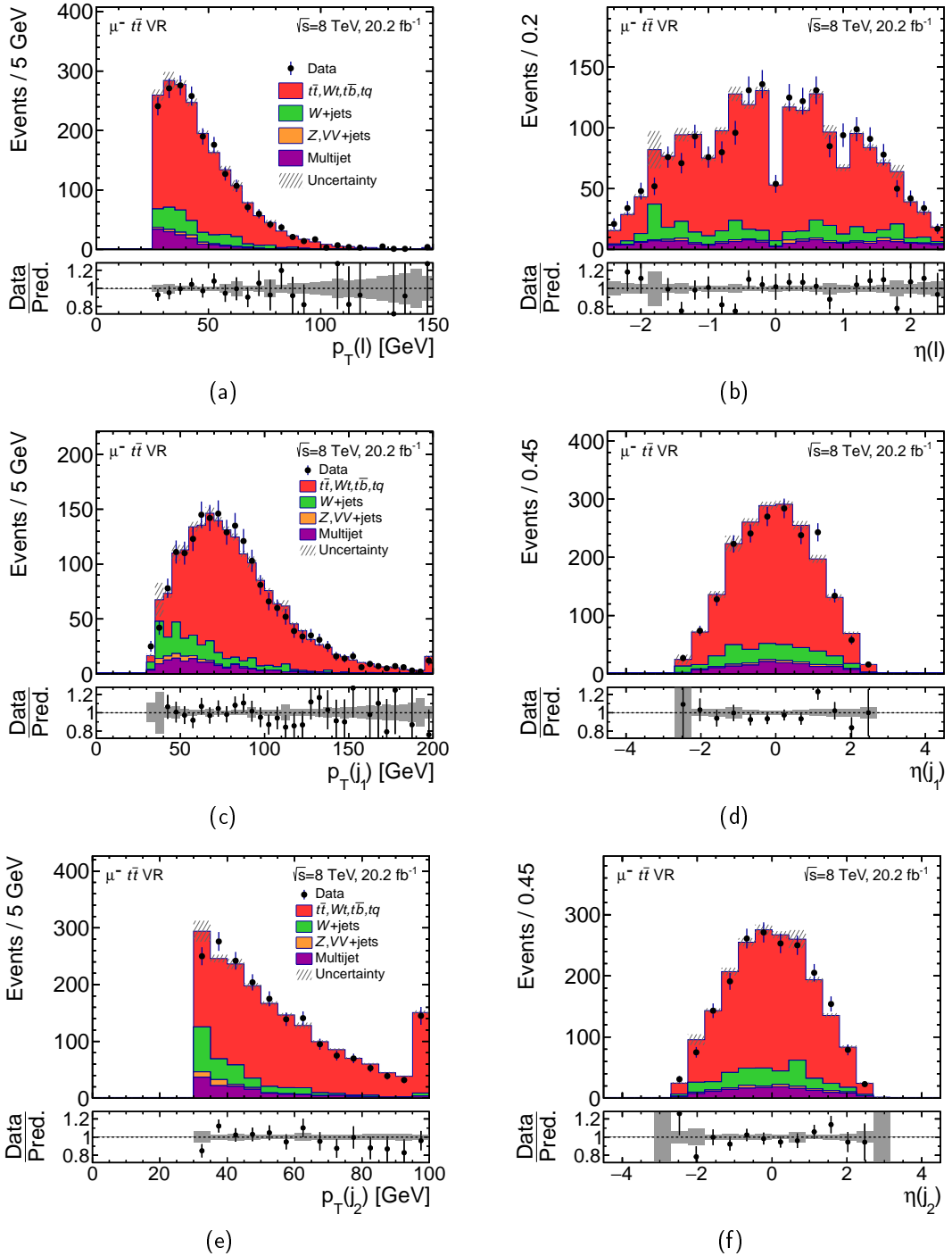
Figure 5.16.: Kinematic distributions in the $t\bar{t}$ VR for the μ^- channel. (a) p_T and (b) η of the muon, (c) p_T and (d) η of the leading jet and, (e) p_T and (f) η of the subleading jet. The hatched error band represents the uncertainty on the multijet rate as well as the MC statistical uncertainty. The ratio of observed to predicted (Pred.) number of events in each bin is shown in the lower panel. Events beyond the axis range are included in the last bin.

5.3. Composition of the Processes

The processes are grouped together for the plots and the binned likelihood fit as follows:

- Top: Background processes that include the production of top quarks. These processes are $t\bar{t}$ production and single top-quark production in the $Wt, t\bar{b}$ and $tq/\bar{t}q$.

- W+jets: Production of a real W boson in association with light-quark or heavy-quark jets.

- Z+jets, VV: Production of a Z boson associated with jets and the production of WW, ZZ and WZ.

- Multijet: Events with a fake lepton originating from multijet production. In the electron channel, the shape of the model is derived with the jet-lepton model and in the muon channel from the anti-muon method.

5.4. Event yields and Control Distributions

The number of expected and observed events in the signal region in the ℓ^+ channel and ℓ^- channel are displayed in Tables 5.6 and 5.7 respectively. Tables 5.8 and 5.9 summarises the respective event yields in the W + jets VR. For the $t\bar{t}$ VR, Tables 5.10 and 5.11 summarise the respective event yields.

The event yields are derived by the acceptance of the MC samples for the respective process contribution normalised to their theoretical cross sections. In case of the multijet process, the normalisation is obtained via the ML fit of the $E_{\mathrm{T}}^{\mathrm{miss}}$ distribution introduced in Section 5.2. The uncertainties on the event yields reflect the MC statistical uncertainty, and the multijet normalisation uncertainty defined in Section 5.2.

Table 5.6.: Number of observed and expected events for both lepton channels with positive charge in the signal region. The normalisation is given by the MC-prediction. The given uncertainties are due to the limited size of the simulated samples, and the multijet estimate for the multijet process.

Process	electron channel barrel	electron channel endcap	electron channel total	muon channel total
tq	4159 ± 64	870 ± 29	5030 ± 71	6428 ± 80
$\bar{t}q$	3 ± 2	7 ± 3	10 ± 3	0 ± 0
$t\bar{t}$	5776 ± 76	1176 ± 34	6952 ± 83	8681 ± 93
$t\bar{b}$	208 ± 14	73 ± 9	281 ± 17	381 ± 20
Wt	802 ± 28	147 ± 12	949 ± 31	1182 ± 34
$W^+ +$ light jets	345 ± 19	138 ± 12	483 ± 22	717 ± 27
$W^- +$ light jets	0 ± 0	0 ± 0	0 ± 0	0 ± 0
$W^+ + bb$ jets	3000 ± 55	1382 ± 37	4382 ± 66	6082 ± 78
$W^- + bb$ jets	2 ± 2	15 ± 4	18 ± 4	0 ± 0
$W^+ + c(c)$ jets	2271 ± 48	698 ± 26	2969 ± 54	4064 ± 64
$W^- + c(c)$ jets	2 ± 1	5 ± 2	7 ± 3	0 ± 0
$Z + bb$ jets	258 ± 16	82 ± 9	340 ± 18	401 ± 20
$Z + cc$ jets	36 ± 6	11 ± 3	47 ± 7	110 ± 10
$Z +$ light jets	12 ± 3	11 ± 3	23 ± 5	22 ± 5
VV	97 ± 10	39 ± 6	136 ± 12	211 ± 15
Multijet	850 ± 130	720 ± 110	1570 ± 240	2950 ± 440
Total expected	$17\,820 \pm 180$	5380 ± 130	$23\,200 \pm 280$	$31\,230 \pm 470$
Data	$18\,283$	5571	$23\,854$	$31\,946$

Table 5.7.: Number of observed and expected events for both lepton channels with negative charge in the signal region. The normalisation is given by the MC-prediction. The given uncertainties are due to the limited size of the simulated samples, and the multijet estimate for the multijet process.

	electron channel		muon channel	
Process	barrel	endcap	total	total
tq	3 ± 2	14 ± 4	17 ± 4	0 ± 0
$\bar{t}q$	2397 ± 49	420 ± 20	2817 ± 53	3482 ± 59
$t\bar{t}$	5829 ± 76	1158 ± 34	6987 ± 84	8579 ± 93
$t\bar{b}$	130 ± 11	38 ± 6	168 ± 13	218 ± 15
Wt	791 ± 28	149 ± 12	940 ± 31	1174 ± 34
$W^{+}+$light jets	0 ± 0	2 ± 1	2 ± 1	0 ± 0
$W^{-}+$light jets	268 ± 16	173 ± 13	441 ± 21	566 ± 24
$W^{+}+bb$ jets	4 ± 2	25 ± 5	28 ± 5	0 ± 1
$W^{-}+bb$ jets	2187 ± 47	754 ± 27	2942 ± 54	3965 ± 63
$W^{+}+c(c)$ jets	5 ± 2	12 ± 3	17 ± 4	0 ± 0
$W^{-}+c(c)$ jets	2112 ± 46	515 ± 23	2628 ± 51	3495 ± 59
$Z+bb$ jets	261 ± 16	84 ± 9	345 ± 19	370 ± 19
$Z+cc$ jets	44 ± 7	18 ± 4	62 ± 8	107 ± 10
$Z+$light jets	1 ± 1	19 ± 4	20 ± 4	8 ± 3
VV	94 ± 10	26 ± 5	120 ± 11	162 ± 13
Multijet	850 ± 130	720 ± 110	1570 ± 240	2950 ± 440
Total expected	$14\,970 \pm 170$	4130 ± 120	$19\,100 \pm 270$	$25\,080 \pm 470$
Data	$16\,208$	4420	$20\,628$	$25\,443$

Table 5.8.: Number of observed and expected events for both lepton channels with positive charge in the W + jets VR. The normalisation is given by the MC-prediction. The given uncertainties are due to the limited size of the simulated samples, and the multijet estimate for the multijet process.

Process	electron channel barrel		electron channel endcap		electron channel total		muon channel total	
tq	1460 ±	38	337 ±	18	1797 ±	42	2292 ±	48
$\bar{t}q$	1 ±	1	2 ±	2	3 ±	2	0 ±	0
$t\bar{t}$	1820 ±	43	410 ±	20	2230 ±	47	2780 ±	53
$t\bar{b}$	45 ±	7	22 ±	5	67 ±	8	94 ±	10
Wt	322 ±	18	66 ±	8	387 ±	20	488 ±	22
W^{+}+light jets	13 390 ±	120	6029 ±	78	19 420 ±	140	27 540 ±	170
W^{-}+light jets	6 ±	2	48 ±	7	53 ±	7	0 ±	0
$W^{+}+b\bar{b}$ jets	1987 ±	45	959 ±	31	2946 ±	54	4108 ±	64
$W^{-}+b\bar{b}$ jets	2 ±	1	11 ±	3	13 ±	4	0 ±	0
$W^{+}+c(\bar{c})$ jets	13 000 ±	110	4115 ±	64	17 120 ±	130	22 830 ±	150
$W^{-}+c(\bar{c})$ jets	21 ±	5	54 ±	7	75 ±	9	0 ±	0
$Z+b\bar{b}$ jets	145 ±	12	53 ±	7	198 ±	14	215 ±	15
$Z+c\bar{c}$ jets	468 ±	22	185 ±	14	652 ±	26	701 ±	26
Z+light jets	417 ±	20	203 ±	14	620 ±	25	663 ±	26
VV	411 ±	20	157 ±	13	567 ±	24	785 ±	28
Multijet	3200 ±	1600	2700 ±	1300	5900 ±	2900	6100 ±	3100
Total expected	36 700 ±	1600	15 300 ±	1300	52 000 ±	3000	68 600 ±	3100
Data	38 566		16 261		54 827		73 218	

Table 5.9.: Number of observed and expected events for both lepton channels with negative charge in the W + jets VR. The normalisation is given by the MC-prediction. The given uncertainties are due to the limited size of the simulated samples, and the multijet estimate for the multijet process.

Process	electron channel			muon channel
	barrel	endcap	total	total
tq	1 ± 1	4 ± 2	6 ± 2	0 ± 0
$\bar{t}q$	841 ± 29	157 ± 13	998 ± 32	1233 ± 35
$t\bar{t}$	1822 ± 43	399 ± 20	2221 ± 47	2790 ± 53
$t\bar{b}$	27 ± 5	10 ± 3	38 ± 6	52 ± 7
Wt	327 ± 18	68 ± 8	395 ± 20	486 ± 22
W^{+} +light jets	7 ± 3	152 ± 12	159 ± 13	0 ± 0
W^{-} +light jets	10 220 ± 100	3708 ± 61	13 930 ± 120	18 690 ± 140
W^{+} +bb jets	2 ± 1	18 ± 4	20 ± 4	0 ± 0
W^{-} +bb jets	1494 ± 39	544 ± 23	2038 ± 45	2817 ± 53
W^{+} +$c(c)$ jets	18 ± 4	79 ± 9	98 ± 10	0 ± 0
W^{-} +$c(c)$ jets	12 270 ± 110	3078 ± 55	15 350 ± 120	19 700 ± 140
$Z + bb$ jets	139 ± 12	60 ± 8	200 ± 14	220 ± 15
$Z + cc$ jets	438 ± 21	193 ± 14	631 ± 25	653 ± 26
Z +light jets	411 ± 20	169 ± 13	580 ± 24	642 ± 25
VV	389 ± 20	124 ± 11	513 ± 23	651 ± 26
Multijet	3200 ± 1600	2700 ± 1300	5900 ± 2900	6100 ± 3100
Total expected	31 600 ± 1600	11 400 ± 1300	43 100 ± 3000	54 000 ± 3100
Data	32 330	11 887	44 217	56 120

Table 5.10.: Number of observed and expected events for both lepton channels with positive charge in the $t\bar{t}$ VR. The normalisation is given by the MC-prediction. The given uncertainties are due to the limited size of the simulated samples, and the multijet estimate for the multijet process.

	electron channel			muon channel
Process	barrel	endcap	total	total
tq	145 ± 12	27 ± 5	172 ± 13	218 ± 15
$\bar{t}q$	0 ± 0	0 ± 0	0 ± 0	0 ± 0
$t\bar{t}$	911 ± 30	161 ± 13	1072 ± 33	1328 ± 36
$t\bar{b}$	112 ± 11	28 ± 5	140 ± 12	187 ± 14
Wt	23 ± 5	4 ± 2	27 ± 5	33 ± 6
$W^+ +$light jets	5 ± 2	0 ± 0	5 ± 2	0 ± 0
$W^- +$light jets	0 ± 0	0 ± 0	0 ± 0	0 ± 0
$W^+ + b\bar{b}$ jets	135 ± 12	50 ± 7	185 ± 14	234 ± 15
$W^- + b\bar{b}$ jets	0 ± 0	0 ± 0	0 ± 0	0 ± 0
$W^+ + c(c)$ jets	16 ± 4	0 ± 0	16 ± 4	9 ± 3
$W^- + c(c)$ jets	0 ± 0	0 ± 0	0 ± 0	0 ± 0
$Z + b\bar{b}$ jets	5 ± 2	1 ± 1	6 ± 2	16 ± 4
$Z + c\bar{c}$ jets	0 ± 0	0 ± 0	0 ± 0	0 ± 0
$Z +$light jets	0 ± 0	0 ± 0	0 ± 0	0 ± 0
VV	10 ± 3	5 ± 2	14 ± 4	19 ± 4
Multijet	47 ± 23	30 ± 15	77 ± 39	138 ± 69
Total expected	1409 ± 44	305 ± 22	1714 ± 56	2183 ± 82
Data	1398	314	1712	2142

Table 5.11.: Number of observed and expected events for both lepton channels with negative charge in the $t\bar{t}$ VR. The normalisation is given by the MC-prediction. The given uncertainties are due to the limited size of the simulated samples, and the multijet estimate for the multijet process.

Process	electron channel barrel	electron channel endcap	electron channel total	muon channel total
tq	0 ± 0	1 ± 1	1 ± 1	0 ± 0
$\bar{t}q$	90 ± 10	14 ± 4	104 ± 10	138 ± 12
$t\bar{t}$	920 ± 30	161 ± 13	1081 ± 33	1314 ± 36
$t\bar{b}$	68 ± 8	15 ± 4	83 ± 9	106 ± 10
Wt	24 ± 5	4 ± 2	28 ± 5	34 ± 6
$W^+ +$light jets	0 ± 0	0 ± 0	0 ± 0	0 ± 0
$W^- +$light jets	0 ± 0	17 ± 4	17 ± 4	0 ± 0
$W^+ + b\bar{b}$ jets	0 ± 0	1 ± 1	1 ± 1	0 ± 1
$W^- + b\bar{b}$ jets	99 ± 10	25 ± 5	124 ± 11	163 ± 13
$W^+ + c(c)$ jets	0 ± 0	0 ± 0	0 ± 0	0 ± 0
$W^- + c(c)$ jets	2 ± 2	0 ± 0	2 ± 2	25 ± 5
$Z + b\bar{b}$ jets	4 ± 2	1 ± 1	6 ± 2	18 ± 4
$Z + c\bar{c}$ jets	0 ± 0	0 ± 0	0 ± 0	0 ± 0
$Z +$light jets	0 ± 0	0 ± 0	0 ± 0	0 ± 0
VV	8 ± 3	2 ± 1	9 ± 3	12 ± 3
Multijet	47 ± 23	30 ± 15	77 ± 39	138 ± 69
Total expected	1262 ± 42	271 ± 22	1533 ± 54	1948 ± 81
Data	1299	246	1545	1936

Fiducial Volume and Cross-Section Predictions

6.1. Fiducial Volume Definition

The fiducial volume refers to a subset of the total phase space, defined by requirements on the particle-level objects and events. Figure 6.1 illustrates the relationship between the total, fiducial and reconstructed phase space. Both fiducial and reconstructed phase space are subsets of the total phase space. A large overlap between the two should enhance the cancellation of the extrapolation uncertainties.

The advantage of a fiducial cross-section measurement over a total cross-section measurement is, that extrapolation uncertainties can be reduced. The extrapolation uncertainties refer to the transition of the fiducial phase space to the full phase space. In addition a reinterpretation of the measurement is facilitated by a clear definition of the fiducial volume which can be adopted in calculations, MC simulations or generator studies.

The total cross-section is expressed as follows:

$$\sigma_{\text{tot}} = \frac{\hat{\nu}}{\epsilon \cdot \mathcal{L}_{\text{int}}} \quad \text{with} \quad \epsilon = \frac{N_{\text{sel}}}{N_{\text{total}}} \,, \tag{6.1}$$

where $\hat{\nu}$ is the measured expectation value of the number of signal events, N_{total} refers to the sum of event weights prior to any selection and N_{sel} refers to the sum of event
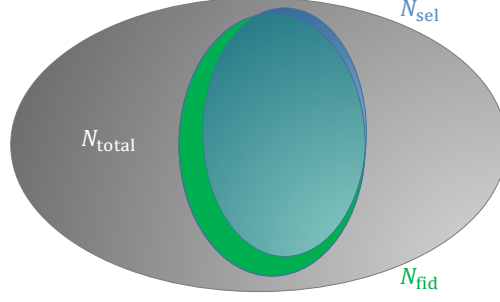
Figure 6.1.: Illustration of the relation of the total phase space (grey), the fiducial volume (green) and the reconstructed phase space (blue). The quantity N_{total} refers to the total number of expected events and N_{sel} refers to the number of expected events selected in the reconstructed phase space, as well as N_{fid} which refers to the number of expected events in the fiducial volume.

weights after all selection requirements have been applied. The quantity ϵ refers to the total event selection efficiency.

The fiducial acceptance gives the selection efficiency of the fiducial volume w.r.t. the total phase space:

$$A_{\text{fid}} = \frac{N_{\text{fid}}}{N_{\text{total}}} \tag{6.2}$$

where N_{fid} refers to the sum of event weights after the fiducial volume selection requirements are applied.

$$\sigma_{\text{tot}} = \frac{1}{\frac{N_{\text{sel}}}{N_{\text{total}}}} \cdot \frac{\hat{\nu}}{\mathcal{L}_{\text{int}}} = \frac{1}{\frac{N_{\text{sel}}}{N_{\text{fid}}} \cdot \frac{N_{\text{fid}}}{N_{\text{total}}}} \cdot \frac{\hat{\nu}}{\mathcal{L}_{\text{int}}} = \frac{1}{A_{\text{fid}}} \cdot \frac{N_{\text{fid}}}{N_{\text{sel}}} \cdot \frac{\hat{\nu}}{\mathcal{L}_{\text{int}}} \,, \tag{6.3}$$

leading to the definition of the fiducial cross-section:

$$\sigma_{\text{fid}} := \frac{N_{\text{fid}}}{N_{\text{sel}}} \cdot \frac{\hat{\nu}}{\mathcal{L}_{\text{int}}} \,. \tag{6.4}$$

In Equation (6.4) the ratio $\frac{N_{\text{sel}}}{N_{\text{fid}}}$ is affected by systematic uncertainties, some of which alter N_{fid} and N_{sel} very similarly therefore reducing the overall effect of them. In consequence, the extrapolation uncertainty of the chosen model is absorbed into the fiducial acceptance. Using the fiducial cross-section σ_{fid}, the total cross-section can be extrapolated to the full phase space as follows:

$$\sigma_{\text{tot}} = \frac{1}{A_{\text{fid}}} \cdot \sigma_{\text{fid}} \tag{6.5}$$

6.1.1. Particle Level Selection

Using the particle-level objects defined in Section 4.2, the particle-level selection is defined as follows:

- One electron or one muon with $p_T > 25$ GeV and $|\eta| < 2.5$.
- Exactly two jets with $p_T(j) > 30$ GeV and $|\eta| < 4.5$.
- $m(\ell, b) < 160$ GeV

In addition, the requirement on the pseudorapidity of the jet is reduced to $|\eta| < 2.5$ if the jet has an associated b-hadron. If a jet has an associated b-hadron and its pseudorapidity is in the range $2.5 < |\eta| < 4.5$ the jet is regarded un tagged, which is similar to the selection in the reconstructed phase space, as the b-tagging capability is limited to $|\eta| < 2.5$.

The cut on $m(\ell, b) < 160$ GeV is defined exactly as in the reconstructed phase space, due to limitations of the current MC event generators, see Chapter 5.

Table 6.1 contains the predicted quantities N_{total}, N_{fid} and the ratio $\frac{N_{\text{fid}}}{N_{\text{sel}}}$ obtained for several MC event generators and for top-quark and top-antiquark events respectively. The sum-of-weights of events selected in the fiducial volume is denoted N_{fid} and similarly for the full phase space N_{total}. The quantity N_{sel} corresponds to the sum-of-weights of events selected in the reconstructed phase space. The total cross-section, predicted by several MC generators is given in Table 6.2. In addition to the MC generator combinations, the total cross-sections are also predicted using the three PDF sets CT10, MSTW2008 and NNPDF 2.3. The fiducial acceptance for different MC event generators is given in Table 6.3 for the tq process and in Table 6.4 for the $\bar{t}q$ process.

In case of the POWHEG-BOX + PYTHIA 6, POWHEG-BOX + HERWIG and MADGRAPH 5_aMC@NLO + HERWIG the ratio $\frac{N_{\text{fid}}}{N_{\text{sel}}}$ is identical to sub-percent level (see Table 6.1), while the difference on the fiducial acceptance is over 2 % for POWHEG-BOX + PYTHIA 6 and MADGRAPH 5_aMC@NLO + HERWIG, see Table 6.3 and Table 6.4.

Table 6.1.: Sum-of-weights of selected events in the fiducial volume N_{fid} and sum-of-weights of selected events in the reconstructed volume N_{sel}, as well as their ratio, for different t-channel single top-quark samples.

ME Generator	Shower MC	$N_{\mathrm{total}}(tq)$	$N_{\mathrm{sel}}(tq)$	$N_{\mathrm{fid}}(tq)$	$\frac{N_{\mathrm{fid}}(tq)}{N_{\mathrm{sel}}(tq)}$
MG 5_aMC@NLO	Herwig	172021	5385.9	29967	5.53
MG 5_aMC@NLO	Herwig++	196281	5540.07	26620	4.78
Powheg-Box	Pythia 6	0.17420	0.00555	0.03096	5.55
Powheg-Box	Herwig	169868	5374.9	29965.8	5.54
AcerMC	Pythia 6	8736480	245427	1414690	5.73

ME Generator	Shower MC	$N_{\mathrm{total}}(\bar{t}q)$	$N_{\mathrm{sel}}(\bar{t}q)$	$N_{\mathrm{fid}}(\bar{t}q)$	$\frac{N_{\mathrm{fid}}(\bar{t}q)}{N_{\mathrm{sel}}(\bar{t}q)}$
MG 5_aMC@NLO	Herwig	90296.3	2860.63	15731.6	5.46
MG 5_aMC@NLO	Herwig++	105385	3222.5	14859.5	4.59
Powheg-Box	Pythia 6	0.09312	0.0030	0.01667	5.52
Powheg-Box	Herwig	46760.9	1477.75	8299.92	5.59
AcerMC	Pythia 6	4525700	132436	751193	5.65

Table 6.2.: Total cross sections for different event generators and the different PDFs. The scale uncertainties are defined as the envelope of the restricted independent scale variations and the quoted PDF uncertainties are the internal PDF uncertainties defined by the respective PDF group. Missing values are not being calculated due to the high CPU usage. [a] Calculated using CT10. [b] Calculation taken from Mad-Graph 5_aMC@NLO.

ME Generator	method	PDF	$\sigma(tq)$ [pb]	stat. unc. [pb]	scale unc. [pb]	PDF unc. [pb]
MG 5_aMC@NLO	4FS(NLO)	CT10	53.4	± 0.1	+5.8 / -6.5	+1.9 / -1.7
MG 5_aMC@NLO	4FS(NLO)	MSTW2008	51.8	± 0.4	+5.8 / -6.2	+0.6 / -0.7
MG 5_aMC@NLO	4FS(NLO)	NNPDF 2.3	51.4	± 0.5	+6.0 / -6.4	+0.6 / -0.6
Powheg-Box	4FS(NLO)	CT10	52.6	± 0.1	+5.6 / -6.6	+1.9 / -1.7[b]
Powheg-Box	4FS(NLO)	MSTW2008	51.2	± 0.1	+5.6 / -6.6[a]	+0.6 / -0.7[b]
Powheg-Box	4FS(NLO)	NNPDF2.3	50.9	± 0.1	+5.6 / -6.6[a]	+0.6 / -0.6[b]
AcerMC	matched(LO)	CTEQ6L1	55.7	± 1.5	+1.8 / -3.2	–
MG 5_aMC@NLO	5FS(NLO)	CT10	54.0	± 0.1	+3.0 / -2.3	+1.2 / -1.3
MG 5_aMC@NLO	5FS(NLO)	MSTW2008	55.7	± 0.1	+3.0 / -2.3	+0.6 / -0.6
MG 5_aMC@NLO	5FS(NLO)	NNPDF 2.3	55.1	± 0.1	+3.3 / -2.3	+0.6 / -0.6
Powheg-Box	5FS(NLO)	CT10	54.4	± 0.1	+3.0 / -2.0	+1.2 / -1.3[b]
Powheg-Box	5FS(NLO)	MSTW2008	55.9	± 0.1	+3.0 / -2.0[a]	+0.6 / -0.6[b]
Powheg-Box	5FS(NLO)	NNPDF2.3	55.8	± 0.1	+3.0 / -2.0[a]	+0.6 / -0.6[b]

ME Generator	method	PDF	$\sigma(\bar{t}q)$ [pb]	stat. unc. [pb]	scale unc. [pb]	PDF unc. [pb]
MG 5_aMC@NLO	4FS(NLO)	CT10	28.5	± 0.1	+4.9 / -6.1	+1.8 / -1.7
MG 5_aMC@NLO	4FS(NLO)	MSTW2008	27.9	± 0.3	+6.0 / -6.6	+1.0 / -1.1
MG 5_aMC@NLO	4FS(NLO)	NNPDF 2.3	28.2	± 0.3	+5.8 / -6.5	+0.9 / -0.9
Powheg-Box	4FS(NLO)	CT10	28.2	± 0.1	+6.5 / -7.0	+1.8 / -1.7[b]
Powheg-Box	4FS(NLO)	MSTW2008	28.0	± 0.1	+6.5 / -7.0[a]	+1.0 / -1.1[b]
Powheg-Box	4FS(NLO)	NNPDF 2.3	27.8	± 0.1	+6.5 / -7.0[a]	+0.9 / -0.9[b]
AcerMC	matched(LO)	CTEQ6L1	28.8	± 0.8	+0.9 / -1.7	—
MG 5_aMC@NLO	5FS(NLO)	CT10	28.8	± 0.1	+3.1 / -2.2	+1.9 / -1.7
MG 5_aMC@NLO	5FS(NLO)	MSTW2008	30.4	± 0.1	+3.0 / -2.2	+1.0 / -1.1
MG 5_aMC@NLO	5FS(NLO)	NNPDF 2.3	30.3	± 0.1	+3.3 / -2.3	+0.9 / -0.9
Powheg-Box	5FS(NLO)	CT10	29.0	± 0.1	+3.0 / -2.0	+1.9 / -1.7[b]
Powheg-Box	5FS(NLO)	MSTW2008	30.5	± 0.1	+3.0 / -2.0[a]	+1.0 / -1.1[b]
Powheg-Box	5FS(NLO)	NNPDF 2.3	30.4	± 0.1	+3.0 / -2.0[a]	+0.9 / -0.9[b]

Table 6.3.: Fiducial acceptance A_{fid} for different top quark t-channel single top-quark samples. [a] Calculated using AcerMC + Pythia 6. [b] Calculation taken from Powheg-Box + Pythia 6.

ME Generator	Shower MC	method	$A_{\mathrm{fid}}(tq)$ [%]	stat. unc. [%]	scale unc. [%]	PDF unc. [%]
MG 5_aMC@NLO	Herwig	4FS(NLO)	16.91	± 0.02	+0.5 / -0.2[b]	± 0.10[a]
MG 5_aMC@NLO	Herwig++	4FS(NLO)	15.5	± 0.10	+0.5 / -0.2[b]	± 0.10[a]
MG 5_aMC@NLO	Herwig 7	4FS(NLO)	18.4	± 0.10	+0.5 / -0.2[b]	± 0.10[a]
Powheg-Box	Pythia 6	4FS(NLO)	17.26	± 0.02	+0.5 / -0.2	± 0.10[a]
Powheg-Box	Pythia 8	4FS(NLO)	17.17	± 0.02	+0.5 / -0.2[b]	± 0.10[a]
Powheg-Box	Herwig	4FS(NLO)	17.13	± 0.02	+0.5 / -0.2[b]	± 0.10[a]
Powheg-Box	Herwig++	4FS(NLO)	15.7	± 0.10	+0.2 / -0.1	± 0.10[a]
Powheg-Box	Herwig 7	4FS(NLO)	15.7	± 0.10	+0.1 / -0.1	± 0.10[a]
AcerMC	Pythia 6	matched(LO)	15.68	± 0.01	± 3.1	± 0.10
MG 5_aMC@NLO	Herwig++	5FS(NLO)	16.1	± 0.10	+0.2 / -0.2	± 0.10[a]
MG 5_aMC@NLO	Herwig 7	5FS(NLO)	16.2	± 0.10	+0.3 / -0.3	± 0.10[a]
Powheg-Box	Pythia 6	5FS(NLO)	17.2	± 0.10	+0.9 / -0.2	± 0.10[a]
Powheg-Box	Pythia 8	5FS(NLO)	17.3	± 0.10	+0.5 / -0.3	± 0.10[a]

Table 6.4.: Fiducial acceptance A_{fid} for different top antiquark t-channel single top-quark samples. [a] Calculated using AcerMC + Pythia 6. [b] Calculation taken from Powheg-Box + Pythia 6.

ME Generator	Shower MC	method	$A_{\mathrm{fid}}(\bar{t}q)$ [%]	stat. unc. [%]	scale unc. [%]	PDF unc. [%]
MG5_aMC@NLO	Herwig	4FS(NLO)	17.07	±0.02	+0.2 / -0.4[b]	± 0.16[a]
MG5_aMC@NLO	Herwig++	4FS(NLO)	16.3	± 0.2	+0.2 / -0.4[b]	± 0.16[a]
MG5_aMC@NLO	Herwig 7	4FS(NLO)	18.3	± 0.2	+0.2 / -0.4[b]	± 0.16[a]
Powheg-Box	Pythia 6	4FS(NLO)	17.52	± 0.02	+0.2 / -0.4	± 0.16[a]
Powheg-Box	Pythia 8	4FS(NLO)	17.45	± 0.02	+0.2 / -0.4[b]	± 0.16[a]
Powheg-Box	Herwig	4FS(NLO)	17.36	± 0.02	+0.2 / -0.4[b]	± 0.16[a]
Powheg-Box	Herwig++	4FS(NLO)	15.9	± 0.2	+0.2 / -0.1[b]	± 0.16[a]
Powheg-Box	Herwig 7	4FS(NLO)	16.7	± 0.2	+0.1 / -0.1[b]	± 0.16[a]
AcerMC	Pythia 6	matched(LO)	16.26	± 0.01	± 2.7	± 0.16
MG5_aMC@NLO	Herwig++	5FS(NLO)	16.2	± 0.10	+0.2 / -0.2	± 0.16[a]
MG5_aMC@NLO	Herwig 7	5FS(NLO)	17.1	± 0.10	+0.4 / -0.3	± 0.16[a]
Powheg-Box	Pythia 6	5FS(NLO)	18.0	± 0.10	+0.1 / -0.2	± 0.16[a]
Powheg-Box	Pythia 8	5FS(NLO)	17.8	± 0.10	+0.2 / -0.3	± 0.16[a]

6.2. Prediction of the t-Channel Production Cross-Section at NLO

The measurement of the cross-section ratio R_t can be compared to predictions based on several different PDF sets at NLO. The calculation is performed with the HATHOR program [141] which includes the evaluation of the uncertainties on the choice of renormalisation and factorisation scales, the parametrisation of the given PDF set and the α_s dependence.

The cross-section calculation is performed using the following electroweak parameters, which are standard ATLAS prescriptions. The so-called G_F scheme, and the $\mu_{r,f} = m_t$ scales are employed.

- $m(W) = 80.403\,\text{GeV}$
- $m(Z) = 91.1876\,\text{GeV}$
- $m(t) = 172.5\,\text{GeV}$
- $G_F = 1.166\,37 \times 10^{-5}\,\text{GeV}^{-1}$

The evaluated PDF sets are provided at NLO precision, which generally should match the order of the associated ME calculation. The calculation uses the facilities provided by the LHAPDF program v6.1.5 [142]. The cross-section calculation is performed for the available main PDF sets, as well of sub-sets, including only parts of the experimental data used to derive them.

The uncertainty on the choice of $\mu_{r,f}$ is estimated by following the prescription of independent restricted scale variations, as introduced in Section 3.3.1. The intrinsic PDF uncertainty of each given set is evaluated. The evaluation of the uncertainties on R_t involves the correct treatment of the correlation between uncertainties on $\sigma_{\text{tot}}(tq)$ and $\sigma_{\text{tot}}(\bar{t}q)$. In order to account for the correlated effect the uncertainties have on $\sigma_{\text{tot}}(tq)$ and $\sigma_{\text{tot}}(\bar{t}q)$, the variation is applied simultaneously.

Table 6.5 gives the predicted cross-sections of t-channel single top-quark and top-antiquark production calculated at NLO with HATHOR. The production cross-sections calculated at NLO are compared to calculations at NLO+NNLL [143] and NNLO [144] orders of perturbative QCD. The PDF and scale uncertainties are provided for the NLO and NLO+NNLL calculations, whereas the NNLO calculation only quotes a scale uncertainty. The PDF uncertainty of the NLO calculation takes the three main PDF sets CT10, MSTW2008 and NNPDF 2.3 into account, where the central value of the prediction refers to the midpoint of these three PDF set predictions, and the uncertainty refers to the envelope w.r.t. the midpoint. The NLO+NNLL calculation uses the MSTW2008 PDF set and its intrisic PDF uncertainty, while accounting for a 90 % C.L. estimation.

The results of the R_t calculation, including all systematic uncertainties, are summarised in Table 6.6 and displayed in Figure 6.2. Figure 6.3 shows the predicted fiducial cross-sections for several NLO MC generators. The fiducial cross-sections are calculated using the total cross-section predicted by each MC generator and each fiducial acceptance A_{fid}, c.f. Tables 6.2, 6.3, 6.4. The uncertainties on the scale choice and PDF are considered as 100 % correlated between the predicted cross-sections and A_{fid}. The agreement of all considered MC generators is high. In particular the predictions involving the Herwig and Pythia 6 PS programs are in very high agreement. Predictions involving the Herwig 7 PS program deviate to smaller cross-sections compared to the predictions using Herwig and Pythia 6.

Table 6.5.: Inclusive cross section predictions calculated for different orders in perturbation theory. The PDF and scale uncertainties are provided for the NLO and NLO+NNLO calculations, as well as on which basis they are evaluated.

	NLO	NLO+NNLL	NNLO
PDF	CT10, MSTW2008, NNPDF 2.3	MSTW2008	MSTW2008
PDF unc.	PDF4LHC	MSTW2008 (90 % CL)	—
Scale unc.	independent var.	$\mu = 0.5 \cdot \mu_0, \mu = \mu_0 \cdot 2$	independent var.
$\sigma(tq)$ [pb]	54.9 pb	56.4 pb	54.4 pb
$\Delta\sigma(tq)$ - PDF	±1.6 pb	±1.1 pb	—
$\Delta\sigma(tq)$ - Scale	−1.1 pb / +1.6 pb	−0.3 pb / +2.1 pb	−0.2 pb / +0.4 pb
$\sigma(\bar{t}q)$ [pb]	29.7 pb	30.7 pb	29.8 pb
$\Delta\sigma(\bar{t}q)$ - PDF	±1.4 pb	−1.1 pb / +0.9 pb	—
$\Delta\sigma(\bar{t}q)$ - Scale	−0.6 pb / +0.9 pb	±0.7 pb	−0.2 pb / +0.1 pb

Table 6.6.: Calculated R_t values for different NLO PDF sets together with the uncertainty on the renormalisation and factorisation scale, the internal PDF uncertainty, and the uncertainty on α_s. The statistical uncertainty is negligible.

PDF set	R_t	scale unc.	PDF unc.	α_s
ABM11 (5 flav.)	1.98	0.1 % / -0.5 %	1.6 % / -1.6 %	-1.6 % / 1.6 %
ATLAS (epWZ12)	1.80	0.1 % / -0.5 %	3.7 % / -4.0 %	—
CT14	1.88	0.5 % / -0.2 %	3.5 % / -3.5 %	0.5 % / -0.6 %
CT10	1.87	0.4 % / -0.2 %	4.0 % / -4.0 %	0.3 % / -0.4 %
CT10 (+ D0 W asym.)	1.81	0.9 % / -0.4 %	2.6 % / -2.6 %	0.4 % / -0.4 %
HERAPDF 2.0	1.89	0.2 % / -0.5 %	3.2 % / -3.2 %	0.5 % / -0.6 %
HERAPDF 1.5	1.92	0.1 % / -0.5 %	3.3 % / -3.6 %	0.5 % / 0.4 %
JR14 (VF)	1.80	0.5 % / -0.2 %	0.6 % / -0.6 %	—
MMHT2014 (68% C.L.)	1.81	0.5 % / -0.3 %	2.3 % / -2.3 %	0.6 % / -0.6 %
MSTW2008 (68% C.L.)	1.83	0.3 % / -0.5 %	2.5 % / -2.0 %	
NNPDF 3.0	1.82	0.3 % / -0.3 %	3.4 % / - 3.4 %	0.4 % / -0.3 %
NNPDF 3.0 (no LHC)	1.83	0.1 % / -0.5 %	4.0 % / -4.0 %	< 0.1 % / -0.5 %
NNPDF 3.0 (no jet data)	1.82	0.3 % / -0.5 %	5.8 % / -5.8 %	< 0.1 % / -0.4 %
NNPDF 3.0 (only HERA)	1.87	0.1 % / -0.6 %	12.5 % / -12.5 %	-1.2 % / -2.9 %
NNPDF 3.0 (HERA + ATLAS)	1.89	0.3 % / -0.4 %	12.1 % / -12.1 %	-0.8 % / -2.4 %
NNPDF 3.0 (HERA + CMS)	1.87	0.1 % / -0.7 %	9.1 % / -9.1 %	1.3 % / 1.8 %
NNPDF 2.3	1.83	0.2 % / -0.5 %	2.0 % / -2.0 %	< 0.1 % / -1.0 %
NNPDF 2.3 (collider only)	1.80	0.2 % / -0.3 %	3.7 % / -3.7 %	-0.3 % / -0.2 %
NNPDF 2.3 (no LHC)	1.84	0.4 % / -0.3 %	2.7 % / -2.7 %	-0.1 % / -0.9 %
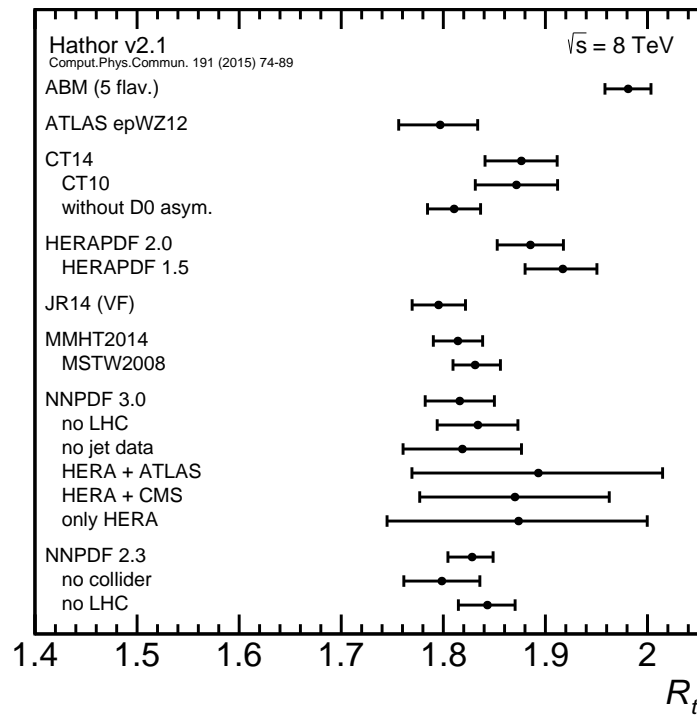
Figure 6.2.: Values of R_t calculated for different NLO PDF sets. The errors contain the uncertainty on the renormalisation and factorisation scale, the internal PDF uncertainty, and the uncertainty on α_s.
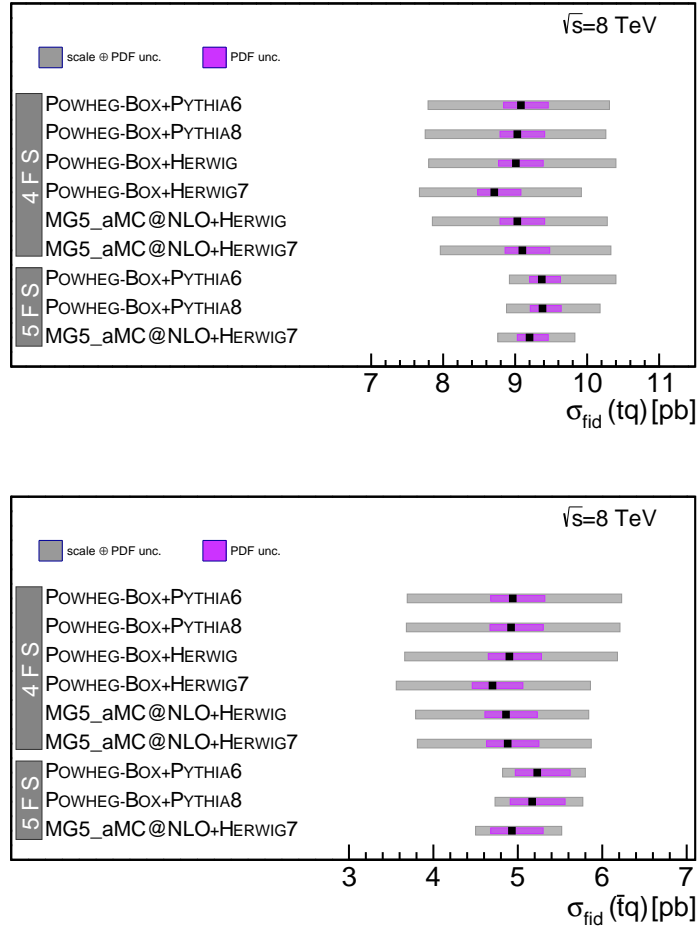
Figure 6.3.: Predicted *t*-channel single top-quark and top-antiquark fiducial cross-sections for different NLO MC generators. The uncertainty on the predictions consists of the scale uncertainty and the uncertainty on the PDFs.

Construction of Neural Network Discriminant

This analysis employs a neural network (NN) discriminant to improve the sensitivity to separate t-channel single top-quark events from background events. NNs combine the discriminating attributes of several observable distributions into a single discriminant. In order to define observable distributions the event kinematics needs to be fully reconstructed, which is described in the following section.

NNs provided by the NeuroBayes® package [145, 146], involve two main aspects. The first stage is the preprocessing, which ensures the generality of the input quantities. The second aspect is the training stage, which performs the computation of the individual weights leading to the final topology of the NN. Both stages are explained in the following sections.

7.1. Reconstruction of the W boson and top quark

In order to access the properties of the top quark it has to be reconstructed from its decay products. In the first step towards the reconstruction of the $\ell\nu b$ system, the W boson is formed as the four-momentum sum of the selected charged lepton and the neutrino, $p_W = p_\nu + p_{e,\mu}$. The charged lepton $p_{e,\mu}$ is measured at high accuracy. However, the neutrino is measured as missing transverse energy. Its z-component is not known a priori. Since the neutrino originates from an on-shell W-boson, the pole

mass of the W boson $m(W) = 80.4\,\text{GeV}$, can be imposed to constrain the z-component of the ν momentum ($p_{z,\nu}$). Therefore, $p_{z,\nu}$ can be calculated by solving the quadratic equation:

$$p_{z,\nu}^2 - 2 \cdot \frac{\mu \cdot p_{z,\ell}}{E_\ell^2 - p_{z,\ell}^2} \cdot p_{z,\nu} + \frac{E_\ell^2 \cdot p_{T,\nu}^2 - \mu^2}{E_\ell^2 - p_{z,\ell}^2} = 0\,, \tag{7.1}$$

$$\text{with} \quad \mu = \frac{m_W^2}{2} + \cos \Delta\Phi(E_T^{\text{miss}}, \ell) \cdot p_{T,\ell} \cdot p_{T,\nu}\,. \tag{7.2}$$

In case that two real solutions are found, the smaller solution of $p_{z,\nu}$ is chosen since that is closer to the measured E_T^{miss}, described in Ref. [147]. In the case that $m_T(\ell\nu)$ exceeds $m(W)$, the radicand becomes negative, leading to an imaginary solution for $p_{z,\nu}$. The origin of a complex solution is the finite resolution of the E_T^{miss} determination, or the neutrino did not originate from a W boson. However only a real solution of $p_{z,\nu}$ is physically valid. A valid solution is obtained by modifying E_T^{miss} such that the radicand assumes zero. Additional information can be found in Ref. [148].

In order to reconstruct the top quark, the four-momentum of the W boson is added to the four-momentum of the selected b-tagged jet.

7.2. Discriminating Variables

In order to construct an NN discriminant to separate the signal process and the background processes, observables that provide significant distinction between the signal process and the background processes are required to be identified.

Since the event topology has been reconstructed entirely, several observable quantities are derived. The set of considered observables contains the primary kinematic characteristics of an event, i.e. $\eta(j), p_T(\ell)$, as well as complex relations of angular and kinematic quantities, i.e. the difference of the transverse momentum between the $\ell\nu b$ system and the E_T^{miss} ($\Delta p_T(\ell\nu b, E_T^{\text{miss}})$) or the cosine of the angle θ^* between the charged lepton and the untagged jet in the rest frame of the reconstructed top quark ($\cos\Theta(\ell, j)$). The main prerequisite of input observables for the NN is that the employed models describe the observed data well. In order to validate that the models do describe the observed data in all respective observable distributions, they are verified in the two validation regions.

7.3. Variable Preprocessing

Prior to the training stage of the NN, NeuroBayes® invokes the preprocessing of all input variables. The preprocessing step is technically not required to formulate the final NN topology, yet the performance and robustness of the NN training is improved. A inherent nuisance of the NN training in general is over-training, which is the failure of incorporating only the generic characteristics of the training sample, but also include statistical aspects of the sample. Over-training leads to an overestimated performance of the NN, which does not hold for generic data.

The initial step of the variable preprocessing is the transformation of the range to the interval $[0, 1]$. In addition, the distribution is flattened, using variable bin widths, and finally the distribution of the purity is fitted using a spline function. By means of the spline function the distribution is converted to a Gaussian distribution with $\mu = 0$ and $\sigma = 1$. These steps reduce the impact of extreme outliers and dampen statistical fluctuations.

The other main objective of the preprocessing is to rank the input variables according to the sensitivity they contribute to the final NN discriminant. The ranking requires the knowledge about the degree of correlation amongst all input variables.

The global indicator of the separation power of the NN is given by the total correlation-to-target quantity. To calculate the total correlation-to-target the correlation-to-target matrix for all individual input variables is rotated such that only the singular quantity is determined. The correlation loss is defined as the reduction in total correlation to-target by the removal of one variable from the input set.

For the ranking, initially the correlation matrix $((N + 1) \times (N + 1))$ is determined for N input variables, plus one bias node. A key measure of the significance of an input variable is the correlation to the target function, which assumes 1 for the signal process and 0 for background processes.

The ranking procedure iteratively removes the least significant variable, recalculated in each iteration, until only the most significant variables remains.

In addition, the input variables are decorrelated to improve the training procedure. The decorrelation is performed by first calculating the covariance matrix of the pre-processed input variables, and than they are diagonalised by means of Jacobian rotations.

The significance, σ_i, is defined in terms of the correlation loss ,ρ_i, via the size of the corresponding sample (n): $\sigma_i = \rho_i \cdot \sqrt{n}$.

Only input variables contributing more than 2σ are considered in the NN training procedure.

7.4. Neural Network Training

Neural networks mimic the behaviour of biological neural networks, in terms of collating relevant information from several sources and providing a joint decision as output.

A three-layer feed-forward NN is implemented in the NeuroBayes® program. The first layer is the input layer that comprises $N + 1$ nodes, one each for N input variables, plus one bias node. The second layer is referred to as hidden layer, that consists of a variable number of hidden nodes. The choice of number of hidden nodes is almost arbitrary. While very small numbers of hidden nodes, can limit the learning capabilities of the NN, very large numbers only impair the performance of the learning process. For this analysis 15 hidden nodes are chosen for any network configuration that is presented.

The third layer is the output layer, which in case of the binary classification, consists of one node.

The entropy loss function is defined as:

$$E_{\mathrm{D}} = \sum_{k=1}^{n} \log \left(\frac{1}{2} (1 + t_k \cdot o_k + \epsilon) \right) , \qquad (7.3)$$

where t_k is the target value, o_k is the network output and ϵ is a regularisation constant. This parametrisation of the classification problem poses advantages over other approaches, since E_D assumes infinitely large values for completely wrong classifications $o_k = 1$ for $t_k = -1$. This behaviour makes it fast for the learning process to exclude these configurations.

The regularisation constant ϵ is introduced to avoid numerical problems occurring in the first iterations of the training procedure. The ϵ constant is decreasing per iteration and quickly assumes zero. In addition, a pruning strategy is applied to set very small weights to zero, which dampens statistical fluctuations and improves the learning speed.

The training input dataset comprises a mixture of events of the signal process and all background processes. The mixture of events is 50 % for background processes as well as 50 % for the signal process. While the respective mixture is artificial, it improves the learning capabilities of the network. In case of the background events, the individual relative contribution is proportional to the process cross-section. In case of the multijet process the contribution is derived from the multijet event fraction obtained in Section 5.2.

To validate the trained NN, the training input dataset is split into a training sample which accounts for 80 % of the input events, and a test sample including the remain-

ing 20 %. For consistency the test sample is not used in the training stage. Figure 7.1 shows the loss entropy function as a function of the number of training iterations for both the training sample and the test sample. The training is concluded when the change of the entropy loss function w.r.t it's value in the last iteration becomes smaller that a predefined threshold, which occurs after eight training iterations, in this case. The high similarity of both samples indicates that no over-training takes place.
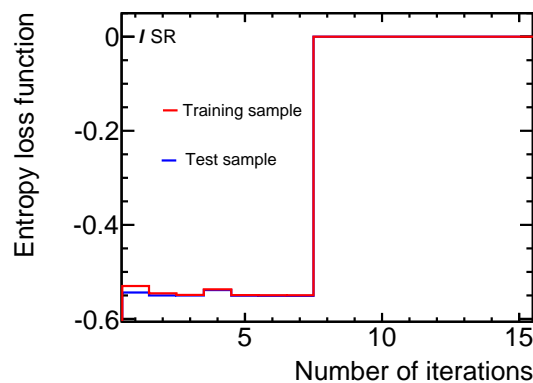
Figure 7.1.: Entropy loss function as a function of the number of training iterations. The training sample is shown in red, the test sample shown in blue.

7.5. Consolidation of Input Variable Set

While an NN could be formed using many input variables, a minimal set of input variables is regarded optimal, if it maintains the sensitivity provided by a maximal set of input variables. The sensitivity of the network can be approximated by the total correlation-to-target quantity provided by the training procedure.

To overcome the limitations of the approximation of the sensitivity using the total correlation-to-target, the expected total uncertainty of the cross-section measurement, including all systematic uncertainties is repeated for each configuration. The precision of this analysis is limited by systematic uncertainties, thus an optimization of the statistical uncertainty is not performed. The considered systematic uncertainties correspond to preliminary prescriptions in case of the JES uncertainty and the MC generator modeling uncertainties.

A set of 17 observable distributions have been identified that display excellent data MC agreement in both, the $t\bar{t}$ VR and the W + jets VR, which serve as the maximum set of

NN input variables under consideration. Table 7.1 gives the input variables that have been considered.

In order to determine the minimal set of input variables, an iterative strategy is applied, in which the least significant input variable is removed and a new NN is trained with the remaining variables. Finally, 17 NNs are obtained, each differing in the number of input variables. Figure 7.2 shows the total correlation-to-target as a function of the number of NN input variables. The total correlation-to-target of the set of input variables is increasingly degrading after retaining less than seven input variables.

Table 7.1.: Initial Neural Network input variables

n	Variable	Correlation Loss.
1	$m(jb)$	38.47
2	$|\eta(j)|$	22.89
3	$m(\ell\nu b)$	18.11
4	$m_T(\ell\nu)$	15.17
5	$|\Delta\eta(\ell\nu, b)|$	11.43
6	$m(\ell b)$	9.22
7	$\cos\theta^*(\ell, j)$	7.83
8	E_T^{miss}	4.71
9	$|\Delta p_T(\ell, j)|$	3.85
10	$\Delta\eta(\ell, j)$	3.56
11	$\cos\Theta(\ell, j)$	2.48
12	$\eta(\ell)$	3.77
13	$|\Delta p_T(E_T^{\text{miss}}, b)|$	3.26
14	$|\Delta p_T(\ell\nu, \ell)|$	2.83
15	$|\Delta p_T(\ell\nu b, \ell)|$	2.87
16	$|\Delta p_T(b, j)|$	2.82
17	$|\Delta p_T(\ell\nu b, E_T^{\text{miss}})|$	2.03

Figure 7.3 shows the total systematic uncertainty for $\sigma_{\text{fid}}(tq), \sigma_{\text{fid}}(\bar{t}q)$ and R_t, as a function of number of NN input variables. The treatment of systematic uncertainties is introduced in Section 8.2. The relative precision is 0.1 percentage points, which corresponds to 10^6 pseudo experiments. The total uncertainty steeply increases after removing 12 input variables for all three measured quantities. A minimal set of input variables is chosen to contain the seven most significant input variables from Table 7.1. This configuration retains the same total systematic uncertainties as any larger input-variable set.

Another interesting feature can be seen from inspecting the slight decrease in total systematic uncertainty from eight to seven input variables. This decrease is mostly visible
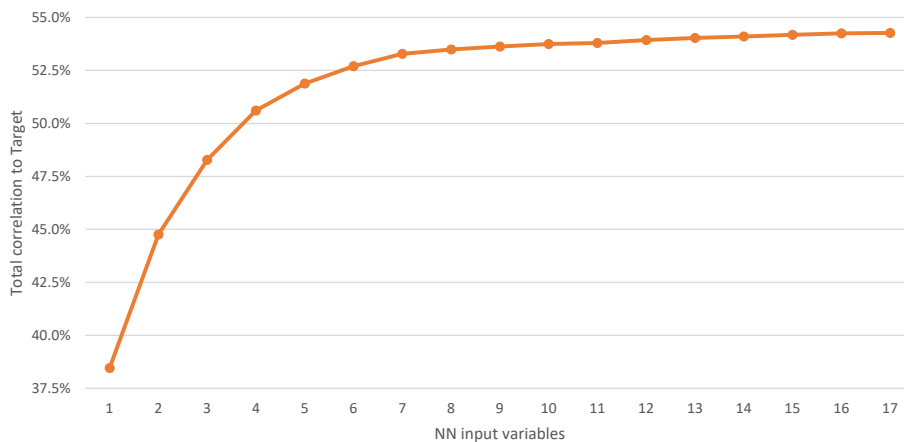
Figure 7.2.: The total correlation-to-target quantity as a function of the number of NN input variables.

for the $\sigma_{\mathrm{fid}}(\bar{t}q)$ and R_t quantities and hint to the fact that excluding $E_{\mathrm{T}}^{\mathrm{miss}}$ from the set of input variables is beneficial for the overall performance. As introduced in Section 8.2, a shape uncertainty is assigned to $E_{\mathrm{T}}^{\mathrm{miss}}$ which has non negligible influence on the total systematic uncertainty. By removing the $E_{\mathrm{T}}^{\mathrm{miss}}$ from the set of input variables, the NN discriminant becomes independent of the individual shape uncertainty associated to the $E_{\mathrm{T}}^{\mathrm{miss}}$. A similar effect is indicated between the networks containing two and one input variables, as the $|\eta(j)|$ is removed. Several systematic uncertainties, i.e. JES η-calibration and NLO-matching method, introduce a strong shape uncertainty at large $|\eta(j)|$, where the signal sensitivity reaches maximum. Especially in the case of the $|\eta(j)|$ input variable, which is a key feature of the signal, a removal is contra-indicated.

This, however, also indicates an alternative optimisation of the NN input variables, which has not been investigated in the scope of this thesis. One could estimate the individual dependence of the total uncertainty for each input variable. Instead of several input variables, only one input variable can be used for the NN training. In case that an input variable is particularly sensitive to one systematic uncertainty, its resulting total systematic uncertainty is higher compared to that of other input variables.
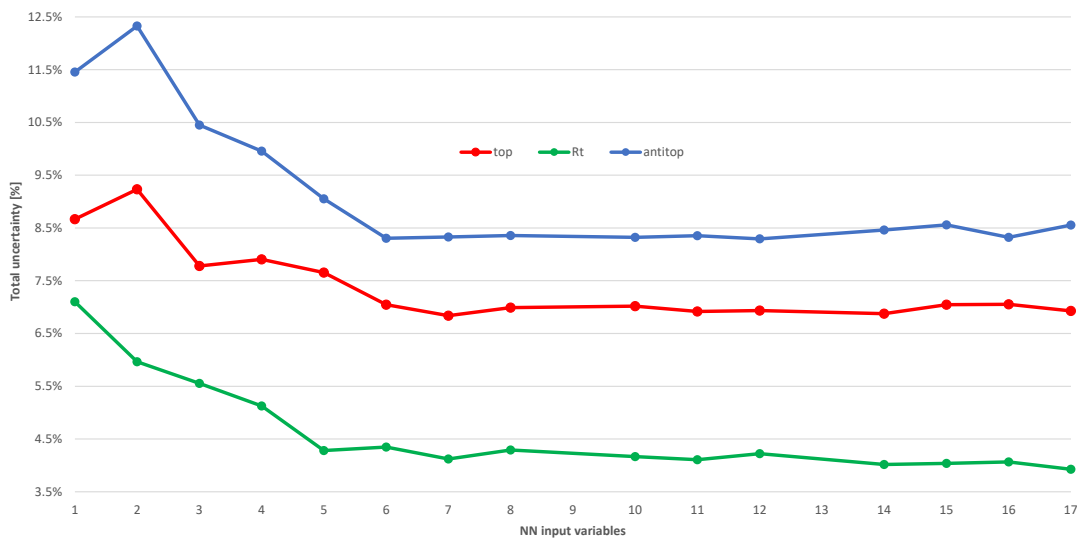
Figure 7.3.: Total systematic uncertainties as a function of the number of NN input variables. The total systematic uncertainty on the fiducial cross-section of top-quark production, top-antiquark production and the cross-section ratio R_t is shown.

Table 7.2.: The 7 variables which are used in the training of the neural network ordered by their importance. The correlation loss of each variable is the loss of correlation to the target by removing the n-th variable.

| Variable	Corr. loss	Definition
$m(jb)$	38.4 %	The invariant mass of the untagged jet (j) and the b-tagged jet (b).
$\|\eta(j)\|$	22.9 %	The absolute value of the pseudorapidity of the untagged jet.
$m(\ell\nu b)$	18.6 %	Top-quark mass reconstructed from the charged lepton, the neutrino (ν) and the b-quark jet.
$m_{\mathrm{T}}(\ell E_{\mathrm{T}}^{\mathrm{miss}})$	13.5 %	Transverse mass of the reconstructed W boson.
$\|\Delta\eta(\ell\nu, b)\|$	11.8 %	The absolute value of $\Delta\eta$ of the reconstructed W boson and the b-tagged jet.
$m(\ell b)$	9.4 %	The invariant mass of the charged lepton (ℓ) and the b-tagged jet.
$\cos\theta^*(\ell, j)$	8.1 %	The cosine of the angle θ^* between the charged lepton and the untagged jet in the rest frame of the reconstructed top quark.

7.6. Final NN Discriminant Characteristics

After we established the dedicated observable distributions that are used to perform the NN training, the agreement of observed data and the MC simulated events need to be validated in detail in the two validation regions.

Table 7.2 lists the observables which are used as input variables for the NN training. The variables are given in order of their importance determined by the NN preprocessing procedure. The correlation loss and the definition of all variables is provided.

Figure 7.4 illustrates the topology of the NN, where the edges are coloured corresponding to their weight assigned by the NN training. In addition one can see that several of the hidden nodes are not connected to the output node, since they were subject to the pruning feature and were removed to improve the learning speed. This also shows that even if the number of hidden nodes is chosen to be large, the NN training removes unnecessary nodes itself.

Figures 7.5-7.7 show all input variables in the order of their importance for the NN training for the ℓ^+ channel on the left and ℓ^- channel on the right. Figure 7.8 shows the O_{NN} distribution for the signal and background processes normalised to unit area.
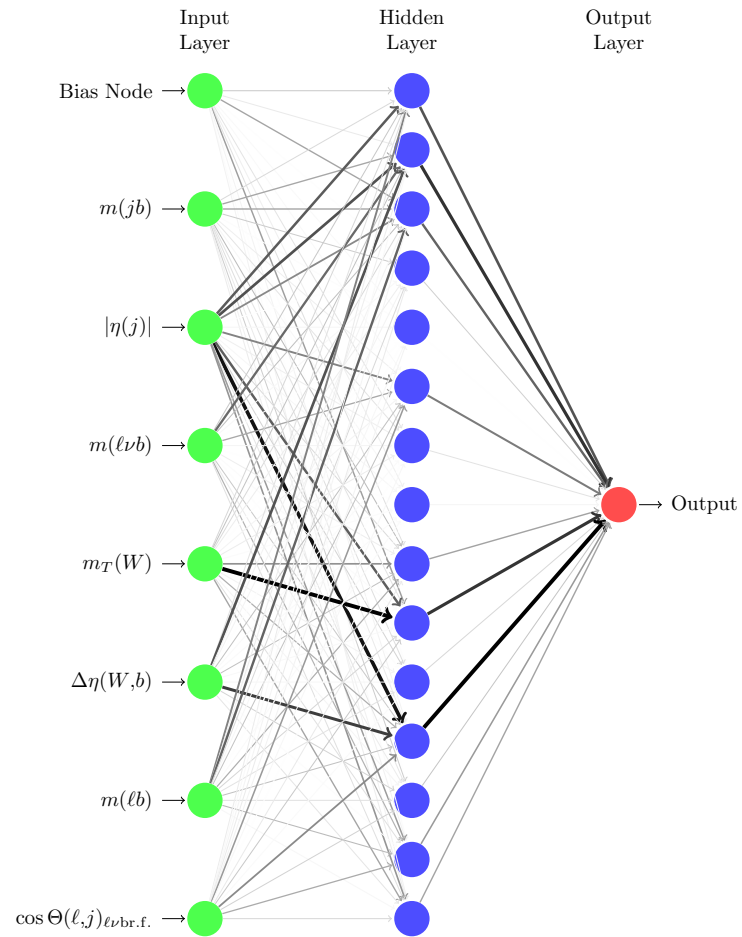
Figure 7.4.: Final network configuration. The width of the lines correspond to the weights between the nodes.
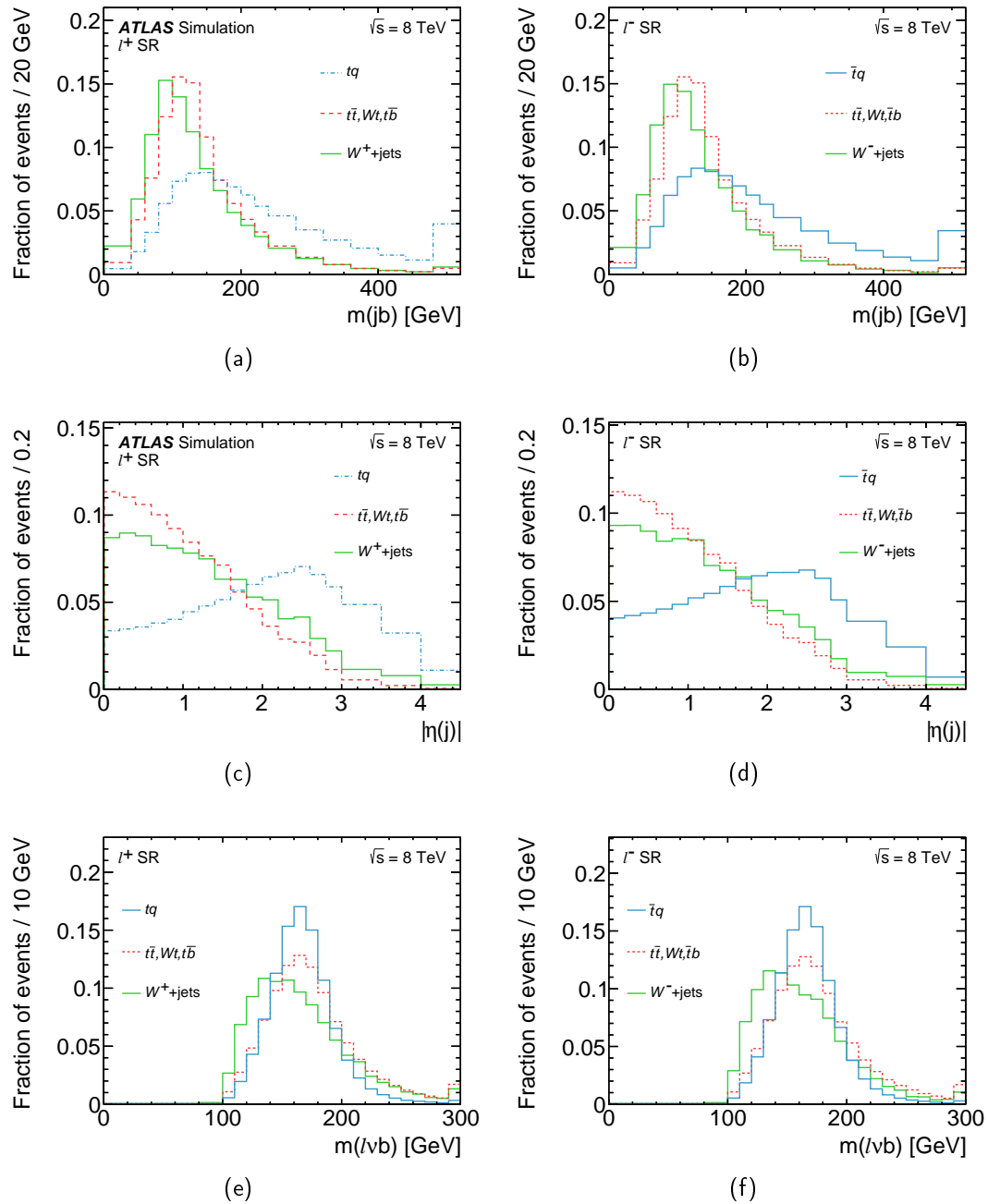
Figure 7.5.: Distributions normalised to unit area of the discriminating variables $m(jb)$, $|\eta(j)|$ and $m(\ell\nu b)$ for the ℓ^+ channel (left) and ℓ^- channel (right) in the SR.
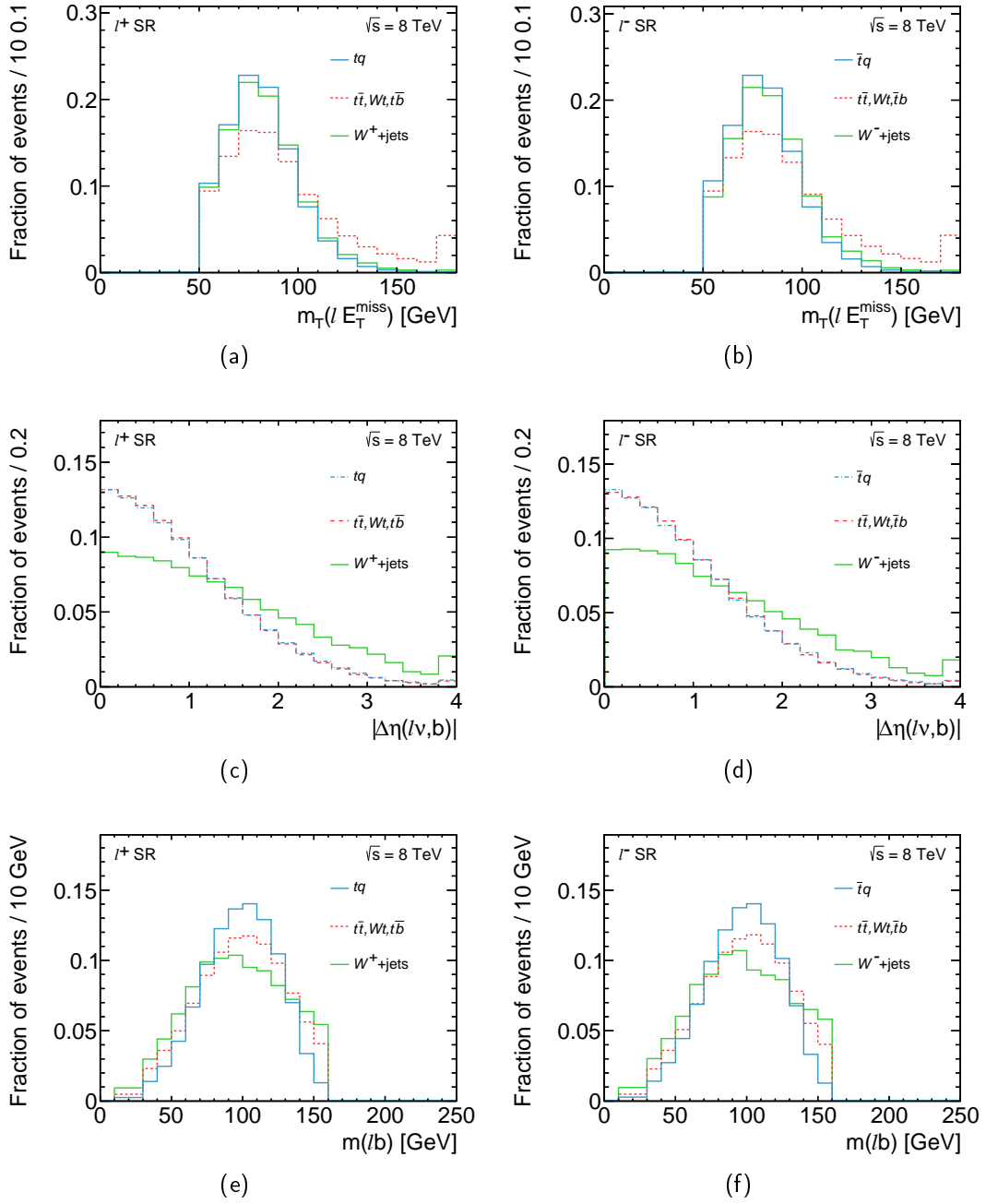
Figure 7.6.: Distributions normalised to unit area of the discriminating variables $m_\mathrm{T}(\ell E_\mathrm{T}^\mathrm{miss})$, $|\Delta\eta(\ell\nu, b)|$ and $m(\ell b)$ for the ℓ^+ channel (left) and ℓ^- channel (right) in the SR.
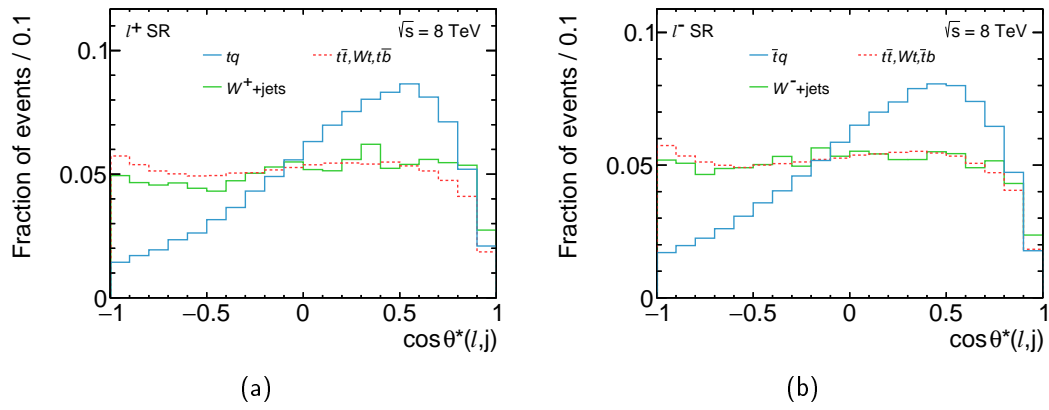
Figure 7.7.: Distributions normalised to unit area of the discriminating variable $\cos\theta^*(\ell, j)$ for the ℓ^+ channel (left) and ℓ^- channel (right) in the SR.

(a)
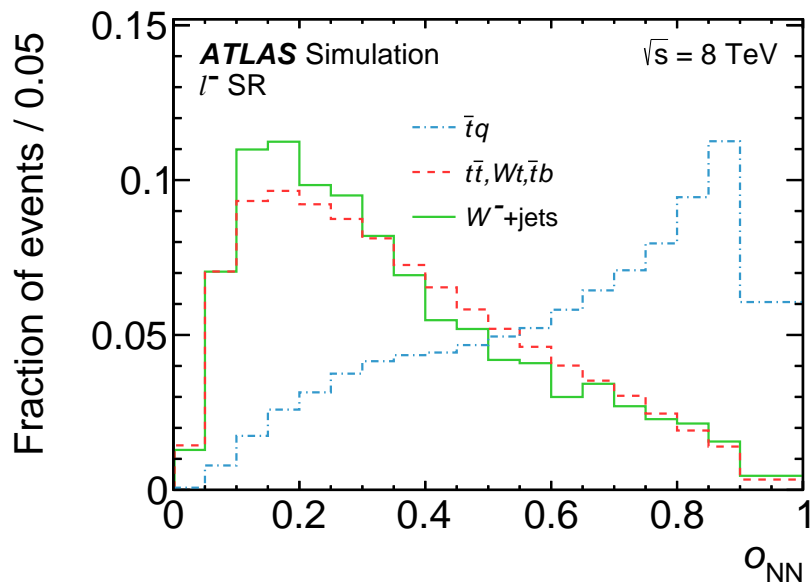
(b)

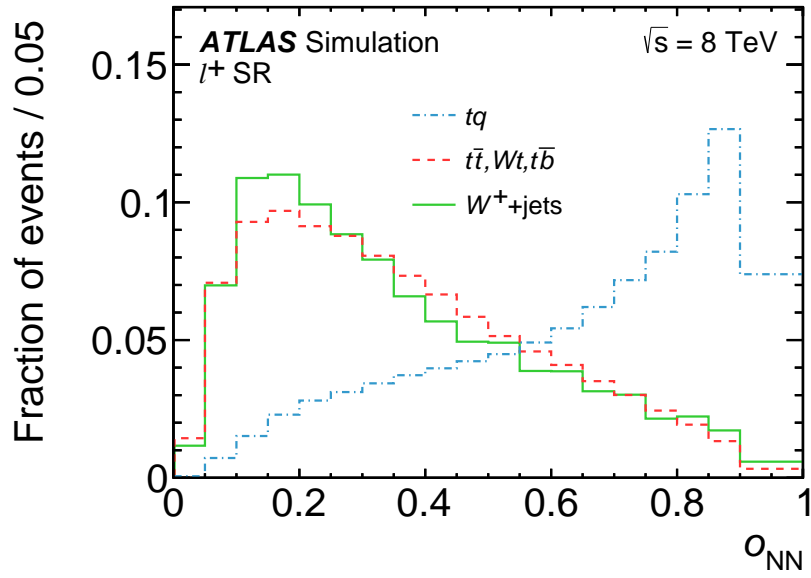**Figure 7.8.:** Signal and background O_{NN} distributions normalised to unit area for the ℓ^+ channel (top) and the ℓ^- channel (bottom).

7.6.1. Neural Network Discriminant in the Validation Regions

In order to validate the modeling of the NN input variables of the main background processes all input variables are inspected in both the W + jets VR and $t\bar{t}$ VR. The individual inspection in the W + jets VR and $t\bar{t}$ VR, enables the modeling of the W + jets and $t\bar{t}$ backgrounds to be isolated. Distributions of all input variables in the W + jets VR are shown in Figures 7.9-7.11 and in the $t\bar{t}$ VR in Figures 7.12-7.14.

The distributions are normalised to the number of expected events and compared to the observed data in the respective distributions. The uncertainty bands represent the uncertainty in the pre-fit process cross-sections and the bin-by-bin MC statistical uncertainty, added in quadrature. The level of agreement between MC simulation and observed data is very high for all of the NN input variables in both the W + jets VR and $t\bar{t}$ VR. In case of the $m(jb)$ distribution in the W + jets VR, Figures 7.9(a) and 7.9(b), two bins at low $m(jb)$ exhibit a discrepancy between MC simulation and data. The deviation probably originates from MC generator level cuts in the W + jets SHERPA MC simulation. The discrepancy have been studied and a $m(jb) > 60\,\mathrm{GeV}$ requirement was tested, which had no significant impact on the O_{NN} distribution. Therefore the discrepancy is neglected.

Figure 7.15 shows the O_{NN} distributions in the W + jets VR (top) and $t\bar{t}$ VR (bottom), in the ℓ^+ channel (left) and ℓ^- channel (right). The agreement of MC simulation with data is excellent.
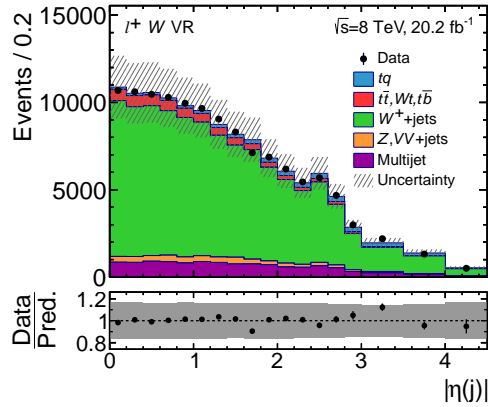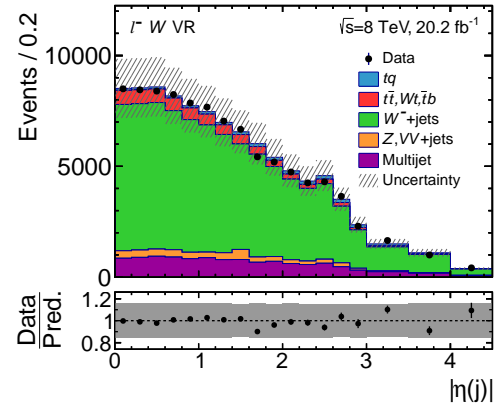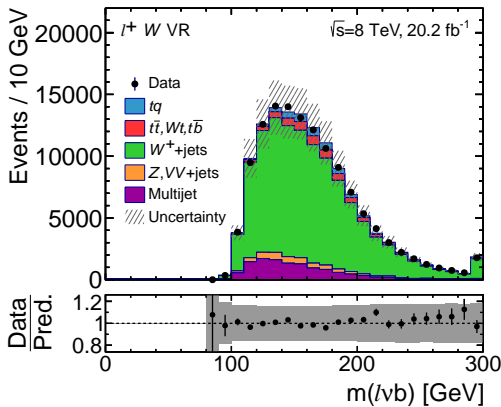
Figure 7.9.: Distributions normalised to the number of expected events of the discriminating variables $m(jb)$, $|\eta(j)|$ and $m(\ell\nu b)$ for the ℓ^+ channel (left) and ℓ^- channel (right) in the W + je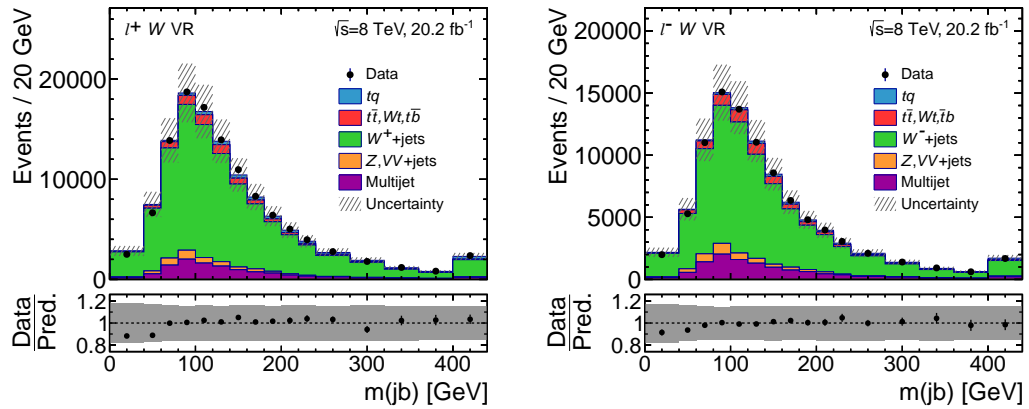ts VR. The hatched uncertainty band represents the uncertainty in the pre-fit process cross-sections and the bin-by-bin MC statistical uncertainty, added in quadrature. The ratio of observed to predicted (Pred.) number of events in each bin is shown in the lower panel. Events beyond the axis range are included in the last bin.

Figure 7.10.: Distributions normalised to the number of expected events of the discriminating variables $m_T(\ell E_T^{miss})$, $|\Delta\eta(\ell\nu, b)|$ and $m(\ell b)$ for the ℓ^+ channel (left) and ℓ^- channel (right) in the W + jets VR. The hatched uncertainty band represents the uncertainty in the pre-fit process cross-sections and the bin-by-bin MC statistical uncertainty, added in quadrature. The ratio of observed to predicted (Pred.) number of events in each bin is shown in the lower panel. Events beyond the axis range are included in the last bin.

(a)   (b)
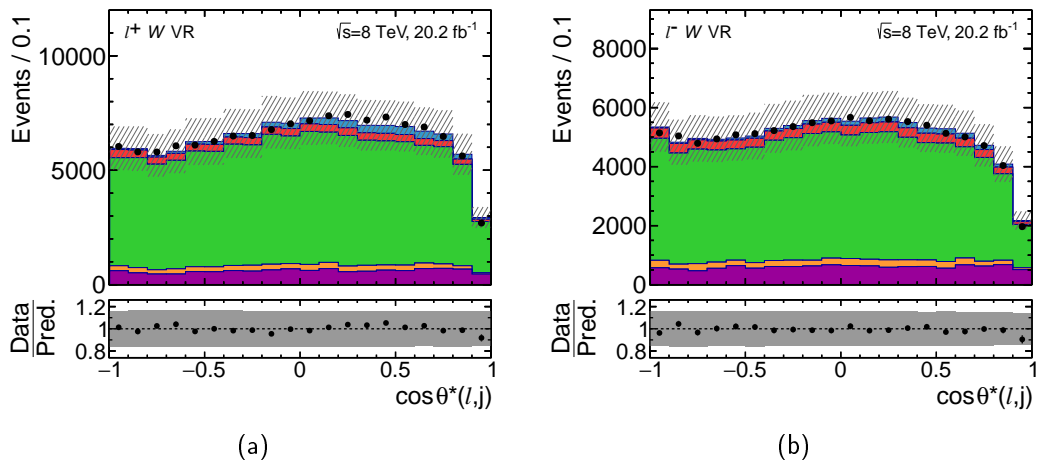
Figure 7.11.: Distributions normalised to the number of expected events of the discriminating variable $\cos\theta^*(\ell, j)$ for the ℓ^+ channel (left) and ℓ^- channel (right) in the W + jets VR. The hatched uncertainty band represents the uncertainty in the pre-fit process cross-sections and the bin-by-bin MC statistical uncertainty, added in quadrature. The ratio of observed to predicted (Pred.) number of events in each bin is shown in the lower panel.
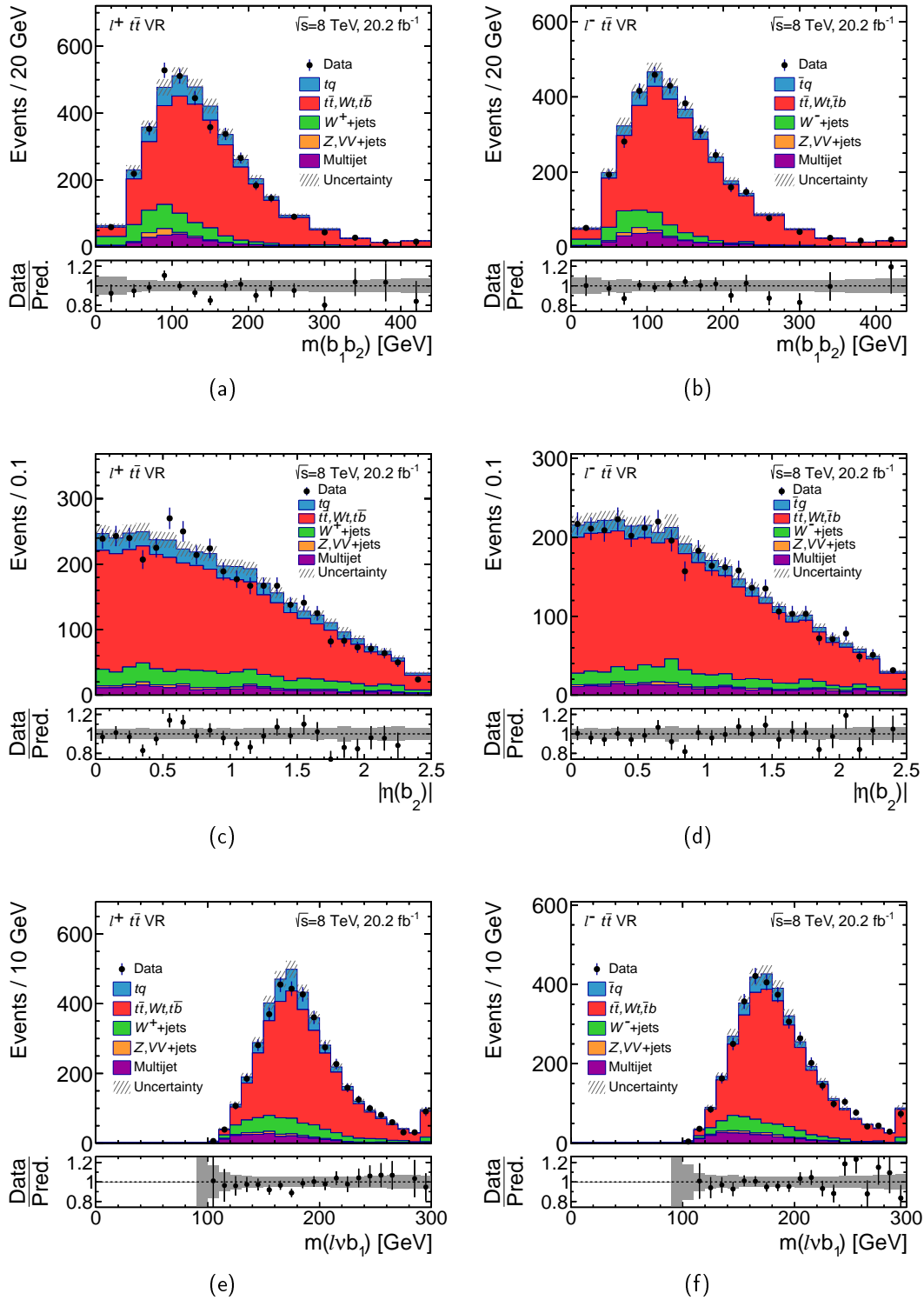
Figure 7.12.: Distributions normalised to the number of expected events of the discriminating variables $m(jb)$, $|\eta(j)|$ and $m(\ell\nu b)$ for the ℓ^+ channel (left) and ℓ^- channel (right) in the $t\bar{t}$ VR. The hatched uncertainty band represents the uncertainty in the pre-fit process cross-sections and the bin-by-bin MC statistical uncertainty, added in quadrature. The ratio of observed to predicted (Pred.) number of events in each bin is shown in the lower panel. Events beyond the axis range are included in the last bin.
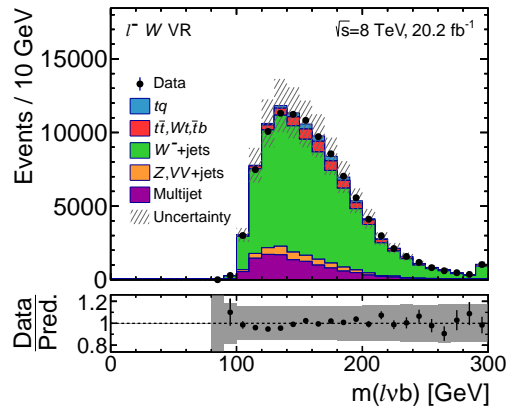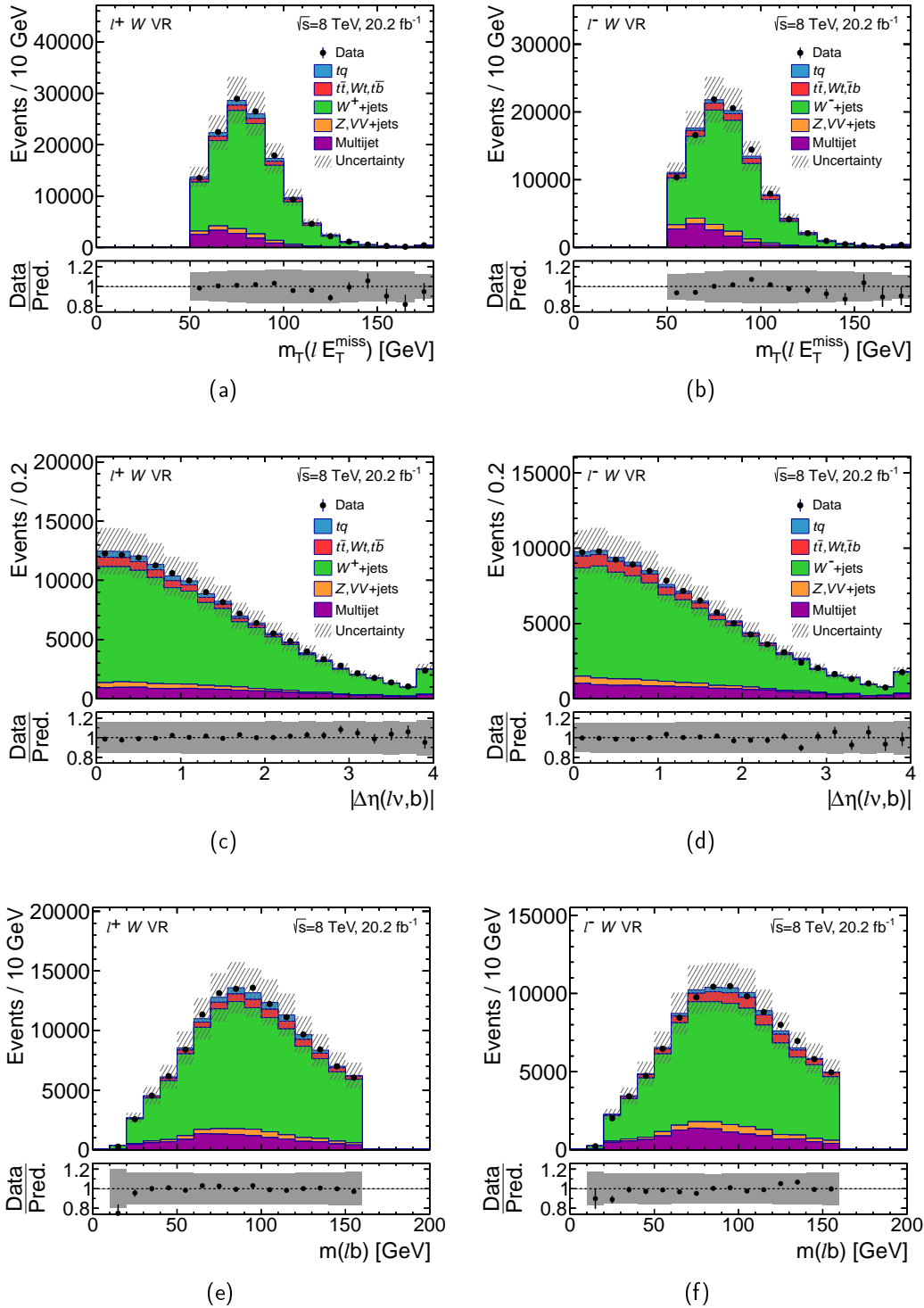
Figure 7.13.: Distributions normalised to the number of expected events of the discriminating variables $m_{\mathrm{T}}(\ell E_{\mathrm{T}}^{\mathrm{miss}})$, $|\Delta\eta(\ell\nu, b)|$ and $m(\ell b)$ for the ℓ^+ channel (left) and ℓ^- channel (right) in the $t\bar{t}$ VR. The hatched uncertainty band represents the uncertainty in the pre-fit process cross-sections and the bin-by-bin MC statistical uncertainty, added in quadrature. The ratio of observed to predicted (Pred.) number of events in each bin is shown in the lower panel. Events beyond the axis range are included in the last bin.
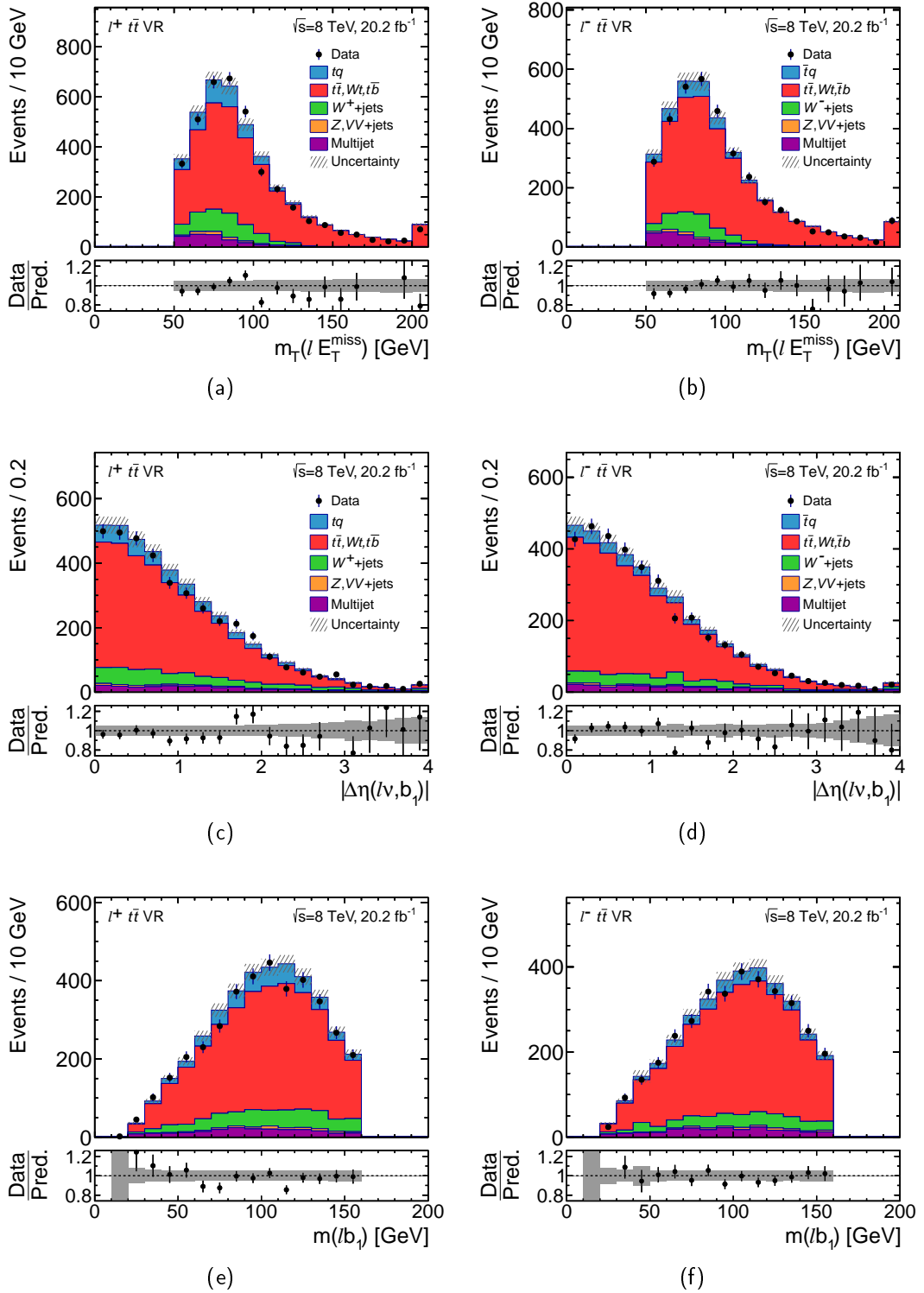
(a)   (b)

Figure 7.14.: Distributions normalised to the number of expected events of the discriminating variable $\cos\theta^*(\ell, j)$ for the ℓ^+ channel (left) and ℓ^- channel (right) in the $t\bar{t}$ VR. The hatched uncertainty band represents the uncertainty in the pre-fit process cross-sections and the bin-by-bin MC statistical uncertainty, added in quadrature. The ratio of observed to predicted (Pred.) number of events in each bin is shown in the lower panel.
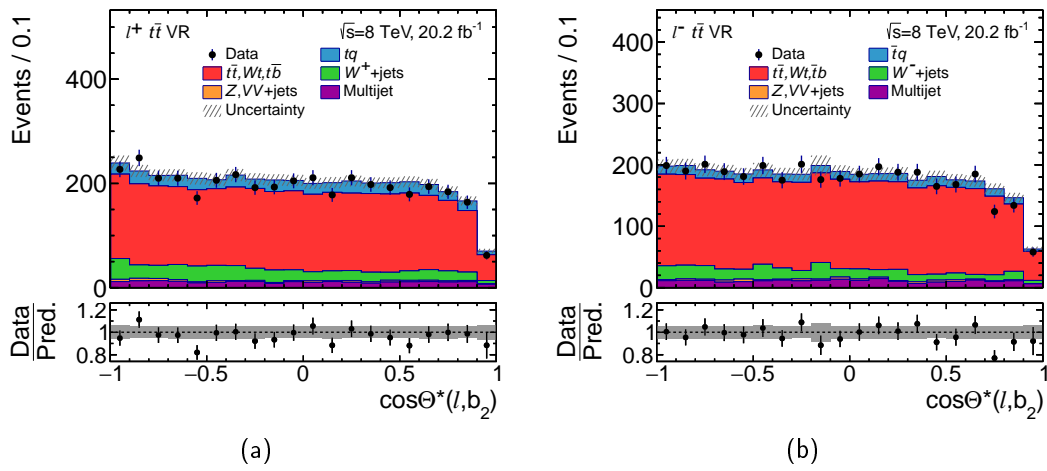
Figure 7.15.: Distributions of the neural network output: Distributions normalised to the number of expected events of the discriminating variables for the ℓ^+ channel (left) and ℓ^- channel (right) in the W+jets VR (top) and the $t\bar{t}$ VR (bottom). The hatched uncertainty band represents the uncertainty in the pre-fit process cross-sections and the bin-by-bin MC statistical uncertainty, added in quadrature. The ratio of observed to predicted (Pred.) number of events in each bin is shown in the lower panel.
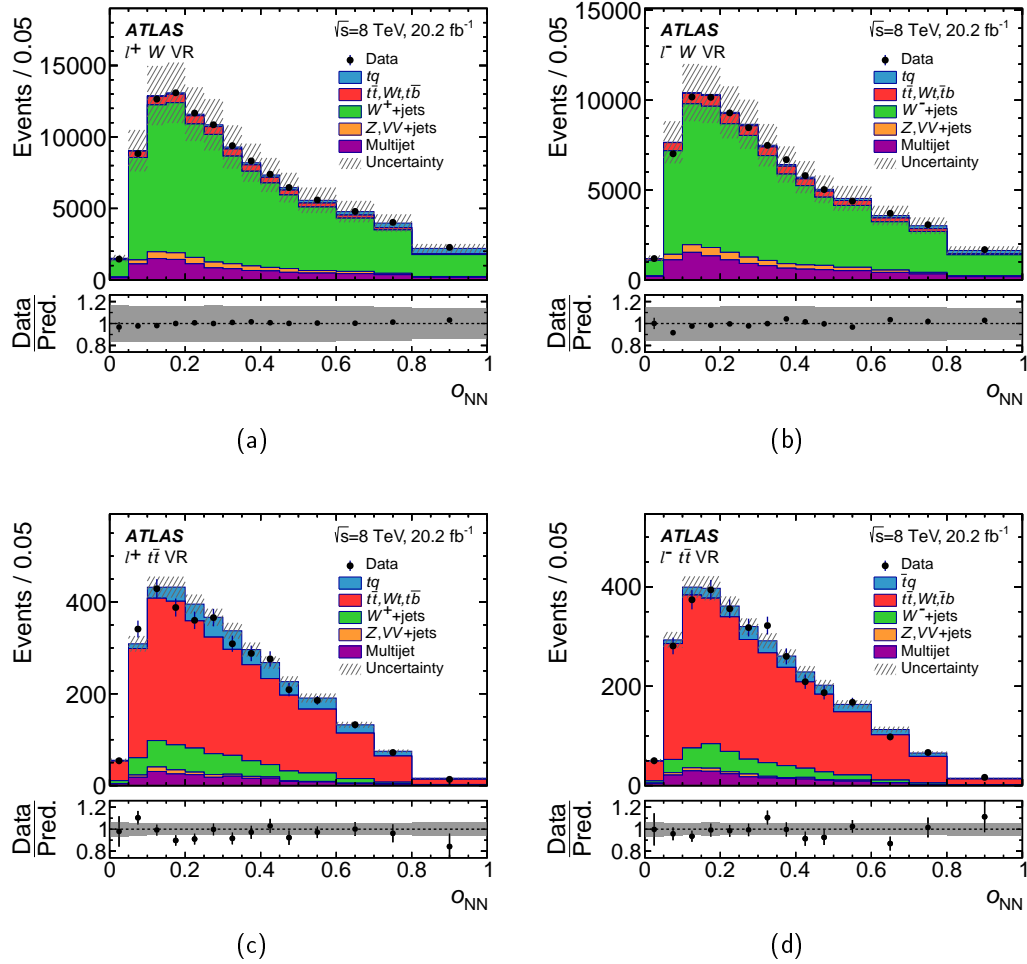
Measurement of t-channel single top-quark cross-sections

The cross-sections of the t-channel single top-quark and top anti-quark are extracted by performing a maximum-likelihood fit to the O_{NN} distributions in the ℓ^+ channel and ℓ^- channel simultaneously. By means of the ML-fit the quantities $\sigma_{\mathrm{fid}}(tq)$, $\sigma_{\mathrm{fid}}(\bar{t}q)$ are obtained which refer to the fiducial phase space. The total cross-sections are subsequently extrapolated to the full phase space, and their ratio R_t is determined. The CKM-matrix element $f_{\mathrm{LV}} \cdot |V_{tb}|$ is extracted using the total combined cross-section $\sigma_{\mathrm{tot}}(tq + \bar{t}q)$, which is the sum of $\sigma_{\mathrm{tot}}(tq)$ and $\sigma_{\mathrm{tot}}(\bar{t}q)$.

Due to the optimised separation of signal and background events in the NN, the O_{NN} discriminant provides a high sensitivity in obtaining the signal yield as well as the background normalisation.

This Chapter introduces the formulation of the ML fit and the estimation of the systematic uncertainties on the measurement. A detailed discussion of the systematic uncertainties, as well as the obtained results are part of this Chapter.

8.1. Statistical Methods

The likelihood function that is used in the ML as well as the uncertainty estimation are introduced briefly in this Section.

8.1.1. Binned Maximum-Likelihood Fit

The binned ML-fit that is employed to determine the signal and background contributions of the O_{NN} discriminant distributions is constructed of a product of the Poisson likelihood terms $\mathcal{P}$ and a Gaussian prior $\mathcal{G}$, shown in Equation 8.1. The Poisson term represents the number of events in each bin of the histogram and the Gaussian term encodes the uncertainty on the normalisation of the background processes. The Gaussian term can be interpreted as a penalty term, which reduces the value of the likelihood if the fit assumes normalisations of the background processes that deviate from the theory predictions. The strength of the penalty is inverse proportional to the relative uncertainty on the respective cross-section.

$$L\left(\beta_{tq}^s, \beta_{\bar{t}q}^s, \beta_j^b\right) = \prod_{k=1}^{M} \mathcal{P}\left(n_k; \mu_k\right) \ \cdot \ \prod_{j=1}^{B} \mathcal{G}\left(\beta_j^b; 1.0, \Delta_j\right) \tag{8.1}$$

The likelihood function has five parameters that are modified by the fitting procedure to maximise the likelihood function. The first two parameters, β_{tq}^s and $\beta_{\bar{t}q}^s$ are the scale factors of the signal processes, and β_j^b are the scale factors for all considered background processes B, where j is the index of each individual background process. The index k iterates over all bins of the O_{NN} discriminant histogram M. The Poisson function $\mathcal{P}\left(n_k; \mu_k\right)$ for bin k is given by

$$\mathcal{P}(n_k; \mu_k) = \frac{e^{-\mu_k} \cdot \mu_k^{n_k}}{n_k!}$$

where n_k denotes the number of observed events in collision data in bin k, and μ_k is the sum of the number of expected events of signal and background processes in bin k:

$$\mu_k = \mu_{tq,k}^s + \mu_{\bar{t}q,k}^s + \sum_{j=1}^{B} \mu_{jk}^b, \quad \mu_{t(\bar{t})q,k}^s = \beta_{t(\bar{t})q}^s \cdot \tilde{\nu}_{t(\bar{t})q}^s \cdot \alpha_{t(\bar{t})q,k}^s, \quad \text{and} \quad \mu_{jk}^b = \beta_j^b \cdot \tilde{\nu}_j \cdot \alpha_{jk}.$$

Where $\tilde{\nu}^s$ is the number of signal events predicted in the selected data set, and $\tilde{\nu}_j$ corresponds to the predicted number of background events of background j. The template fraction α_{jk} refers to the value of the normalised predicted template of process j in bin k. The normalisation condition of the template distributions is $\sum_{i=0}^{M} \alpha_k^{s,b} = 1$.

The second product of the likelihood function is the Gaussian prior $\mathcal{G}$, which is defined

as follows

$$\mathcal{G}(\beta_j^b; 1.0, \Delta_j) = \left(2\pi \cdot \Delta_j^2\right)^{-\frac{1}{2}} \cdot \exp\left(\frac{-\left(\beta_j^b - 1\right)^2}{2\Delta_j^2}\right)$$

where Δ_j corresponds to the relative theoretical uncertainty on each background process cross-section. Table 8.1 contains the cross-section uncertainties Δ_j, that are used in the ML fit.

Table 8.1.: Relative uncertainties on the background cross sections as applied as Gaussian constraints in the maximum likelihood fit.

Background process	Δ_j [%]
$W^+ + \text{jets}$	21
$W^- + \text{jets}$	21
$t\bar{t}, Wt, t\bar{b}$	6.6
$Z + \text{jets}, VV$	fixed
Multijet	fixed

The computation of the maximisation of the likelihood function is performed by using the negative logarithm of it, which improves numerical stability of the procedure. The minimisation is performed using the MINUIT minimisation package [149], by variation of the likelihood parameters. The fiducial cross-sections are calculated by using the estimators of the signal scale factors, called $\hat{\beta}_{tq}^s$ and $\hat{\beta}_{\bar{t}q}^s$. The estimated number of signal events is therefore determined $\hat{v}_{tq}^s = \hat{\beta}_{tq}^s \cdot \tilde{v}_{tq}^s$ and $\hat{v}_{\bar{t}q}^s = \hat{\beta}_{\bar{t}q}^s \cdot \tilde{v}_{\bar{t}q}^s$. Finally, the fiducial cross-sections are computed via Equation 6.4: $\sigma_{\text{fid}}(tq) = \frac{N_{\text{fid}}}{N_{\text{sel}}} \cdot \frac{\hat{v}_{tq}^s}{\mathcal{L}_{\text{int}}}$ and $\sigma_{\text{fid}}(\bar{t}q) = \frac{N_{\text{fid}}}{N_{\text{sel}}} \cdot \frac{\hat{v}_{\bar{t}q}^s}{\mathcal{L}_{\text{int}}}$.

Table 8.2 shows the result of the ML-fit for all processes and the ℓ^+ channel and ℓ^- channel.

8.1.2. Uncertainty Estimation in the Frequentist Approach

The uncertainty on the measured quantities is of paramount importance of this thesis, since it's comprehensive determination enables a correct interpretation of the results as well as an assessment of the achieved measurement precision.

Table 8.2.: Event yields for the different processes estimated with the fit to the NN distribution compared to the numbers of observed events. Only the statistical uncertainties are quoted. The Z + jets and VV contributions and the multijet background are fixed in the fit; therefore no uncertainty is quoted for these processes.

Process	$\hat{\nu}(\ell^+)$	$\hat{\nu}(\ell^-)$
tq	$11\,800 \pm 200$	17 ± 1
$\bar{t}q$	11 ± 1	6920 ± 170
$t\bar{t}, Wt, t\bar{b}/\bar{t}b$	$19\,300 \pm 740$	$18\,900 \pm 730$
$W^+ +$ jets	$18\,800 \pm 780$	48 ± 2
$W^- +$ jets	23 ± 1	$13\,100 \pm 740$
$Z, VV +$ jets	1290	1190
Multijet	4520	4520
Total estimated	$55\,800 \pm 1100$	$44\,700 \pm 1100$
Data	$55\,800$	$44\,687$

The employed frequentist formulation of the uncertainty estimation relies on the generation of pseudo experiments which reflect all possible measurements. The key idea of the generation of pseudo experiments is that only one realisation of the observed data was collected with the ATLAS experiment, and an infinitely large set of measurements would encompass all possible variations due to systematic uncertainties.

The pseudo experiments are generated to mimic many realisations of the observed data, accounting for uncertainties on the measured quantities i.e. jet p_T. For each pseudo experiment, the ML-fit is repeated, obtaining a set of $\hat{\beta}^s_{tq}$ and $\hat{\beta}^s_{\bar{t}q}$. The effect on $\hat{\nu}$ is decomposed into two orthogonal variations, the first is the relative acceptance-variation $\Delta\hat{\nu}/\hat{\nu}$ and the second is a variation of the template shape of the O_NN distribution. The relative variation of the template shape is given for bin k by α_k. For each systematic uncertainty a random number δ_i is introduced which is Gaussian-distributed, with mean zero and width one. A pseudo experiment is created with the given strength δ_i of systematic uncertainty i, which corresponds to its acceptance and template shape component, resulting in a 100 % correlated treatment of the individual uncertainty components.

In addition a systematic uncertainty Δ_j on the cross-section prediction for all background processes is considered, c.f. Table 8.1. A variation of $\tilde{\nu}_j$ is introduced to all pseudo experiments, where the variation corresponds to a log-normal distribution, which ensures a physically valid, positive background prediction. The limited size of the samples of MC simulated events is accounted for by variation of the template shape α_k according to a Gaussian distribution using the RMS of the statistical uncertainty in each bin k.
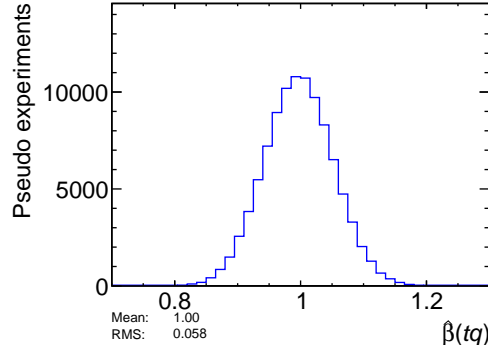
Figure 8.1.: Distribution of $\hat{\beta}^s_{tq}$ for 100000 pseudo experiments considering all sources of systematic uncertainties. The RMS of the distribution corresponds to the relative total systematic uncertainty of the $\sigma_{\text{fid}}(tq)$ measurement.

More details can be found in Ref. [147, 150, 151].

Figure 8.1 shows the distribution of $\hat{\beta}^s_{tq}$ for all generated pseudo experiments. For this analysis 100000 pseudo experiments have been generated, which corresponds to a residual statistical uncertainty of 0.3 %. The RMS refers to the relative total systematic-uncertainty on $\sigma_{\text{fid}}(tq)$.

Figure 8.2 shows the correlation of the $t\bar{t} + Wt + t\bar{b}$ and W + jets processes for the ℓ^+ channel (a) and ℓ^- channel (b). A correlation coefficient of $\rho = -0.91$ is determined. The high correlation of both processes in the O_{NN} discriminant distribution originates in the similar contribution to the event yield. In the training process, both backgrounds are considered of nearly equal importance to be distinguished from the signal, leading to a similar O_{NN} shape for both background processes. There is no consequence for the determination of the signal yield, but the individual estimates for either $t\bar{t} + Wt + t\bar{b}$ or W + jets processes are not reliable.
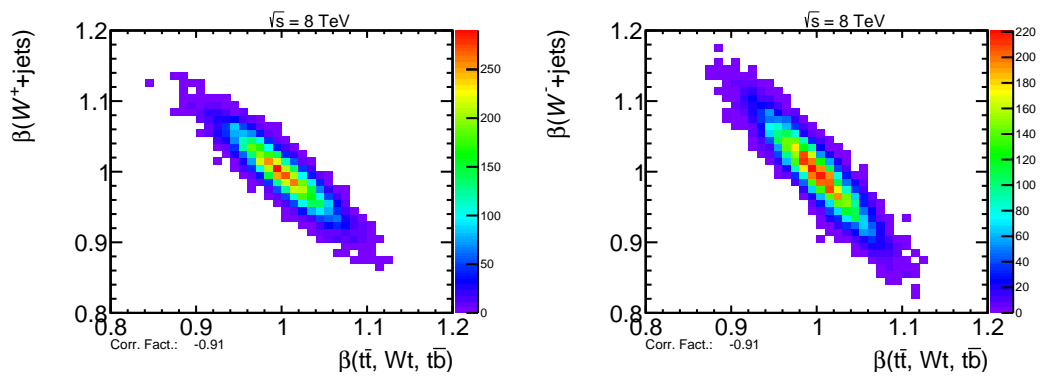
Figure 8.2.: Correlation of the W + jets and $t\bar{t} + Wt + t\bar{b}$ background processes in the ℓ^+ channel in (a) and the ℓ^- channel in (b).

8.1.3. Post-fit Distributions

After the ML-fit to the O_{NN} discriminant is performed, the observed O_{NN} discriminant distribution in collision data is compared to the compound model of signal and background processes in Figure 8.3. The individual contributions are scaled to the fit result, and the uncertainty is given by the post-fit acceptance uncertainty on all considered processes. In case of the Z + jets and multijet contributions, the pre-fit normalisation uncertainty is used, given in Table 8.7. The agreement of collision data and the compound model is very good over the entire range of the O_{NN} distribution for the ℓ^+ channel and ℓ^- channel.

In addition, Figure 8.4 to 8.6 show the distributions of all input variables used in the NN training, where the processes are scaled to the individual fit result.

A very good agreement of the MC prediction to collision data in all input variable distributions is observed in both the ℓ^+ channel and the ℓ^- channel, with the exception of the high $m_{\text{T}}(\ell\nu)$-tail in Figures 8.5(a) and 8.5(b). The reason for this disagreement was studied in detail and revealed a normalisation discrepancy of the $t\bar{t} + Wt + t\bar{b}$ processes. The high $m_{\text{T}}(\ell\nu)$-tail is the most pure $t\bar{t} + Wt + t\bar{b}$ process region of all input variable distribution, which therefore is highly sensitive to the accuracy of the normalisation of the $t\bar{t} + Wt + t\bar{b}$ process in the fit. As stated in Section 8.1.2, the high correlation of both $t\bar{t} + Wt + t\bar{b}$ and W + jets processes do not enable to extract the individual normalisations reliable, which is demonstrated in the high $m_{\text{T}}(\ell\nu)$-tail. The discrepancy was also removed, requiring $m_{\text{T}}(\ell\nu) < 120\,\text{GeV}$, to study the impact on the O_{NN} distribution and subsequently the agreement of collision data and the compound model. The impact of the additional $m_{\text{T}}(\ell\nu)$ requirement is found to be negligible, hence, events with $m_{\text{T}}(\ell\nu) > 120\,\text{GeV}$ are included in the final event selection.
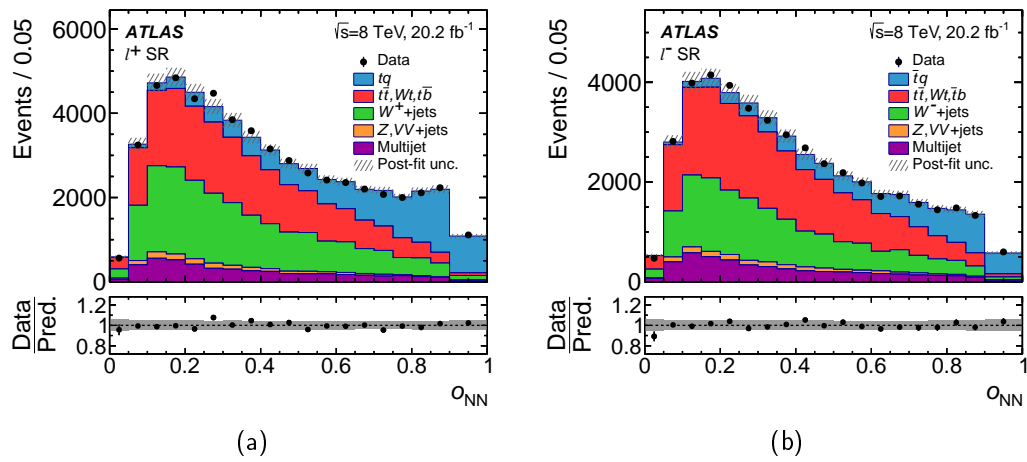
Figure 8.3.: Distributions of the neural network output: The observed distribution in the signal region of (a) the ℓ^+ channel channel and (b) the ℓ^- channel channel is compared to the distribution of simulated signal and background events normalised to the number of fitted events. The ratio of observed and expected number of events in each bin is shown in the lower panel. The uncertainty band contains the post-fit rate uncertainties for all processes and the MC statistical uncertainty.
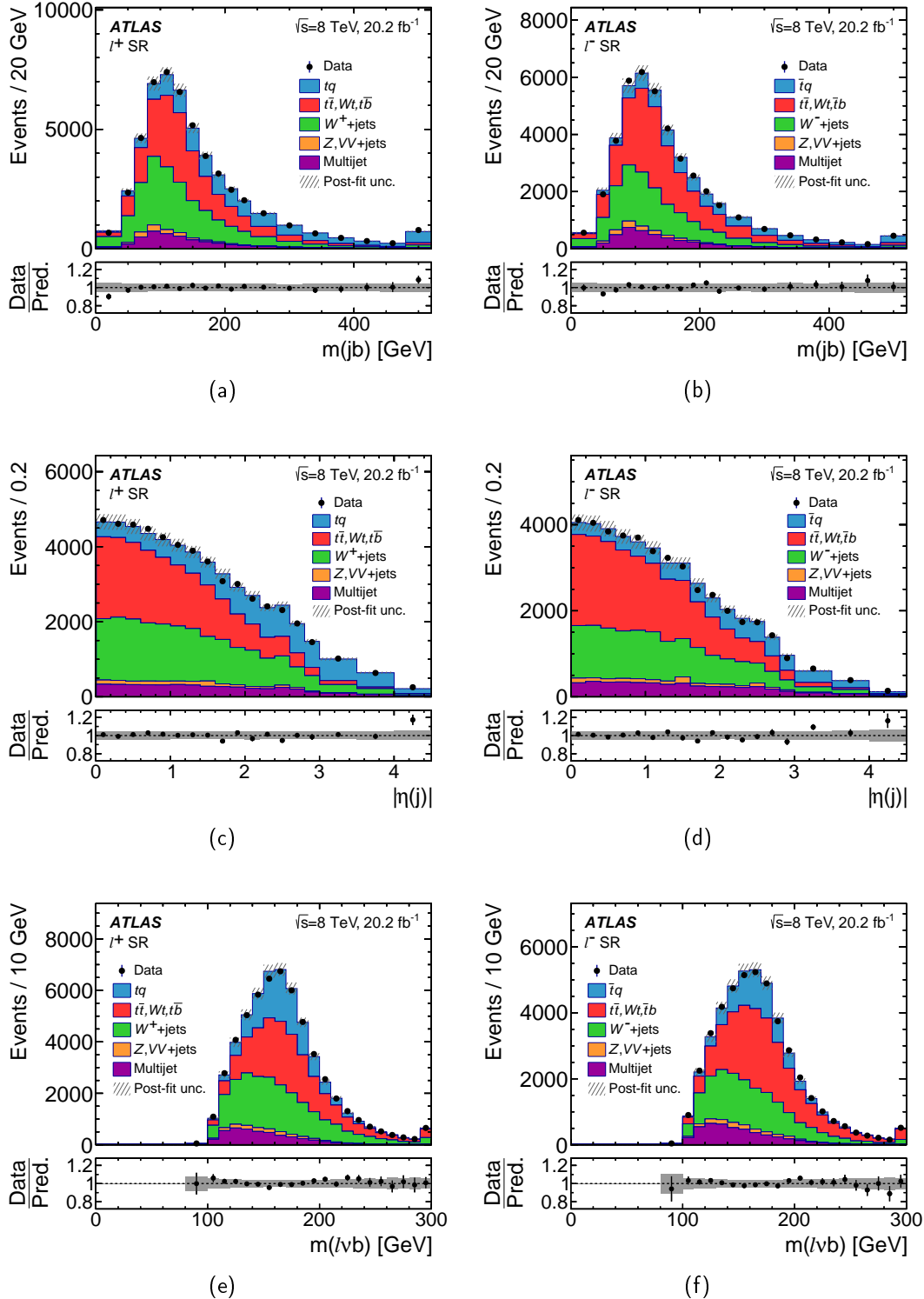
Figure 8.4.: The observed distribution of the three most discriminating input variables in the signal region of (left) the ℓ^+ channel channel and (right) the ℓ^- channel channel is compared to the distribution of simulated signal and background events normalised to the number of fitted events. The uncertainty band represents the post-fit normalisation uncertainty and the uncertainty due to limited sample size. The ratio between the observed and expected number of events in each bin is shown in the lower panel.
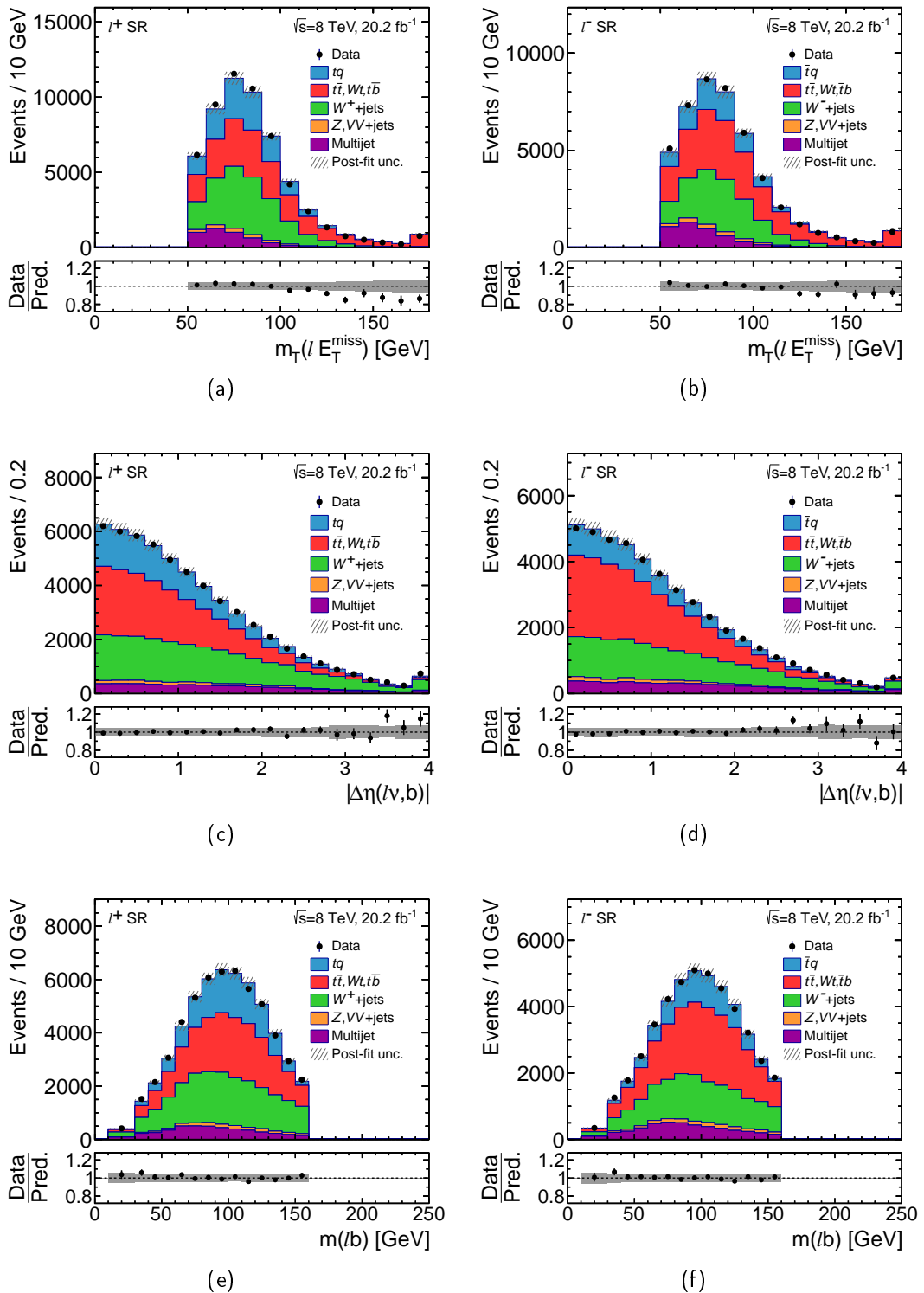
Figure 8.5.: The observed distribution of three input variables in the signal region of (left) the ℓ^+ channel channel and (right) the ℓ^- channel channel is compared to the distribution of simulated signal and background events normalised to the number of fitted events. The uncertainty band represents the post-fit normalisation uncertainty and the uncertainty due to limited sample size. The ratio between the observed and expected number of events in each bin is shown in the lower panel.
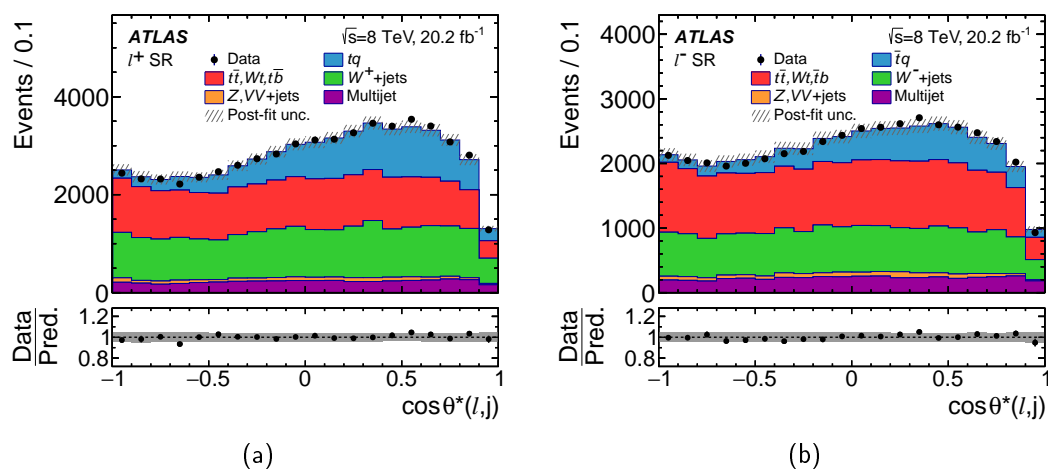
Figure 8.6.: The observed distribution of the $\cos\theta^*(\ell, j)$ input variable in the signal region of (a) the ℓ^+ channel channel and (b) the ℓ^- channel channel is compared to the distribution of simulated signal and background events normalised to the number of fitted events. The uncertainty band represents the post-fit normalisation uncertainty and the uncertainty due to limited sample size. The ratio between the observed and expected number of events in each bin is shown in the lower panel.

8.1.4. Post-fit Distributions in a Highly Enriched Signal Region

In addition to the distributions of the NN input observables normalised to the fit result, a closer inspection on the agreement of collision data and the simulated models of the signal and background processes can be performed. Only events which satisfy $O_{NN} >$ 0.8 are selected, which is the value of the evaluation of the neural network discriminant. The O_{NN} requirement is applied on top of the selection.

Figure 8.7 shows the three most discriminating input observables of the NN, normalised to the results of the ML fit. The uncertainty band represents the post-fit uncertainty on the individual processes and the uncertainty due to the limited sample size. A very good agreement of the simulated models to collision data is observed.

Figure 8.7.: The observed distribution of the three most discriminating input variables in the signal region+$O_{NN} > 0.8$ of (left) the ℓ^+ channel channel and (right) the ℓ^- channel channel is compared to the distribution of simulated signal and background events normalised to the number of fitted events. The uncertainty band represents the post-fit normalisation uncertainty and the uncertainty due to limited sample size. The ratio between the observed and expected number of events in each bin is shown in the lower panel.
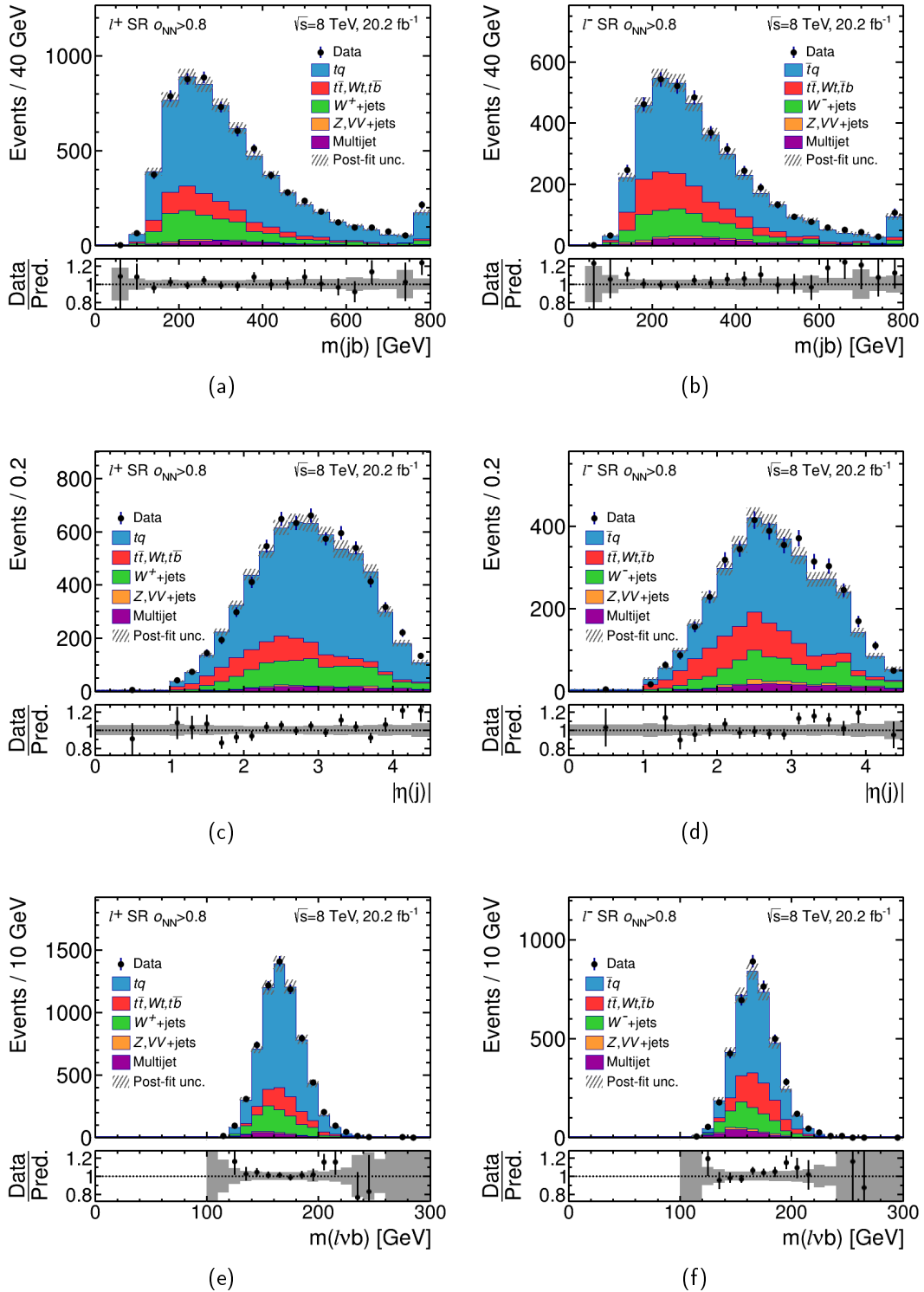
8.2. Estimation of Systematic Uncertainties

The cross-section measurements consider an extensive list of systematic uncertainties which encompass several different categories.

The considered categories include detector-related uncertainties, theoretical modeling and PDF uncertainties. In addition, the uncertainties due to the limited sample size, theoretical cross-sections and luminosity are evaluated.

8.2.1. Object Energy Scale/Resolution and Efficiencies

The uncertainties on objects, defined in Chapter 4, are derived from the residual difference of the MC model description and the reconstructed objects from observed data. The calibration of the energy of electrons, muons, jets and E_T^{miss} corrects the acceptance difference of MC simulation to the observed spectra. The correction-factor uncertainties are propagated to the event yields and observables.

Lepton reconstruction:

The mis-modeling of both electron and muon trigger, reconstruction and selection efficiencies are corrected in simulated events by scale factors to the observed lepton kinematics in collision data. The scale factors are mostly derived from leptonic Z boson and J/Ψ decays as functions of the lepton kinematics, as are the corresponding uncertainties on the scale factors, c.f. Section 4.

Lepton momentum scale and resolution:

The lepton momentum scale and resolution of simulated events are corrected to match the observed kinematic distributions in collision data. The associated uncertainty on the correction scale-factors correspond to variations in selection criteria, which are propagated through the analysis. To estimate the effect of the lepton momentum resolution uncertainty, the lepton momentum is smeared in simulation to match the resolution in data [152]. Table 8.3 shows the magnitude of the systematic uncertainties on the fiducial cross-sections and R_t, related to the lepton reconstruction.

Table 8.3.: Breakdown of the systematic uncertainties associated to the lepton reconstruction on the observed values for the fiducial cross sections as well as for R_t.

Source	$\frac{\Delta\sigma_{\mathrm{fid}}(t)}{\sigma_{\mathrm{fid}}(t)}$ [%]	$\frac{\Delta\sigma_{\mathrm{fid}}(\bar{t})}{\sigma_{\mathrm{fid}}(\bar{t})}$ [%]	$\frac{\Delta R_{\mathrm{t,fid}}}{R_{\mathrm{t,fid}}}$ [%]
Muon momentum resolution (ID)	± 0.0	± 0.2	± 0.3
Muon momentum scale	± 0.1	± 0.1	± 0.2
Muon momentum resolution	± 0.1	± 0.1	± 0.3
Electron energy resolution	± 0.2	± 0.1	± 0.3
Electron energy scale	± 0.3	± 0.2	± 0.2
Lepton trigger scalefactor	± 1.4	± 1.4	± 0.1
Lepton ID scalefactor	± 1.3	± 1.4	± 0.2
Lepton Reco scalefactor	± 0.3	± 0.1	± 0.1
Electron Charge ID	± 0.1	± 0.2	± 0.2

Jet energy scale:

The jet energy scale (JES) of reconstructed jets is obtained from collision data and simulation. The JES uncertainty comprises 22 components each corresponding to an orthogonal source. The uncertainty components originate from the calibration method, the calorimeter response, the detector simulation, and the employed physics model in simulation and are grouped into categories accordingly.

- Detector: Uncertainties related to the detector description, e.g. electron resolution and energy scale.

- Pile-up: Uncertainties associated to pile-up corrections as outlined in Ref. [153].

- Statistical: Uncertainties due to the limited size of samples of MC simulated events and datasets.

- Physics modeling: Uncertainties associated to the choice of modeling techniques, e.g. MC generator choice and radiation modeling.

- η inter-calibration modeling: Uncertainties associated to the calibration of forward jets.

- Flavour: Uncertainty on the flavour composition.

- Mixed detector and modeling: Uncertainties that cannot be fully distinguished between detector effect and physics modeling uncertainty.

- Single hadron response: Uncertainty due to high-p_{T} objects are defined.

- Punch-through: Uncertainty on jets which are not fully contained by the calorimeter system.

The full parametrisation of the uncertainty components is explained in Ref. [154].

Figure 8.8 shows the fractional components of the JES as a function of p_T (a) and η (b) of the jet. For this comparison the jet flavour uncertainties are evaluated assuming 50 % gluon-initiated jets and 50 % uncertainty on the fraction of gluon-initiated jets. This assumption is alleviated as described in the following paragraph.

(a) Total JES as a function of p_T at $\eta = 0$

(b) Total JES as a function of η for jets with $p_T = 40\,\text{GeV}$
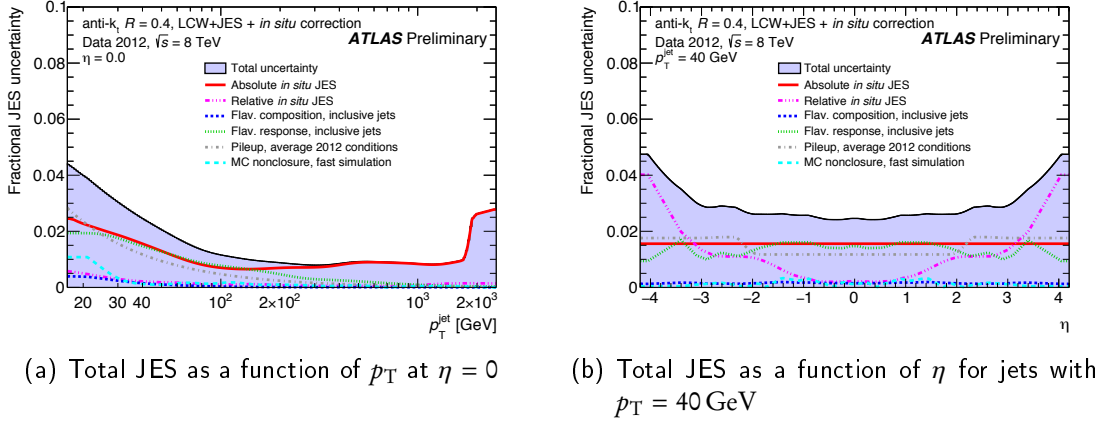
Figure 8.8.: Total JES as a function of p_T in (a) and η in (b). The individual contributions are added in quadrature. The contribution of the jet-flavour uncertainty corresponds to a gluon-jet fraction of 50 % and an uncertainty in this fraction of 50 % [155].

Jet flavour uncertainties:

Two components of the JES uncertainty correspond to the uncertainty in the fraction of gluon-initiated jets over quark-initiated jets. The JES flavour-composition and JES flavour-response uncertainties rely on the fraction of gluon-initiated jets due to ambiguities in the calibration. The ATLAS calibration of the JES flavour-uncertainties is parametrised in the two-dimensional plane of p_T and η of the jets. Due to the fact that a positive b-tag is strong evidence for a jet stemming from a quark, b-tagged jets are excluded from the determination of the gluon-jet fraction.

The flavour of the jets is accessed via the MC record, where the quarks or gluons in the event are associated to the jets using ΔR-matching.

The uncertainty on the gluon-jet fraction is estimated by comparing Powheg-Box + Pythia 6 with Powheg-Box + Herwig, MadGraph 5_aMC@NLO + Herwig with Powheg-Box + Herwig as well as scale variations using Powheg-Box + Pythia 6. The combined uncertainty is calculated by adding the deviation to the nominal case of all generators in quadrature.

Figure 8.9(a) shows the gluon-jet fraction in the η–p_T plane, which is around 10 % gluon initiated jets in average. The uncertainty is around 10 % to 20 % absolute, displayed in Figure 8.9(b)

JES η inter-calibration modeling:

The η inter-calibration modeling component of the JES uncertainty reflects the rising uncertainty on the JES calibration at high pseudorapidities. The JES calibration is performed using the p_T-balance technique [156], which essentially is a tag-and-probe method to select dijet events, where one centrally produced jet is balanced against a more forward jet. The probability of additional radiation being present in the event rising with the pseudorapidity difference of the central and forward jet. Therefore this technique is very sensitive to the modeling of radiation effects in the MC event simulation, in particular for very forward jets.

The radiation modeling uncertainty is estimated by the comparison of Sherpa and Powheg-Box + Pythia 8. The differences of these MC generators contribute the largest part of this JES uncertainty component, as seen in Figure 8.10, referred to as MC modeling uncertainty. Figure 8.11 displays the corresponding effect on the template distribution of the signal processes in the O_NN distribution. The impact of the JES η inter-calibration modeling enters via the high dependence of the NN on the $|\eta(j)|$ variable.

Table 8.4 shows the magnitude of the systematic uncertainties on the fiducial cross-sections and R_t, related to the jet reconstruction.

(a) Gluon-jet fraction   (b) Gluon-jet-fraction uncertainty
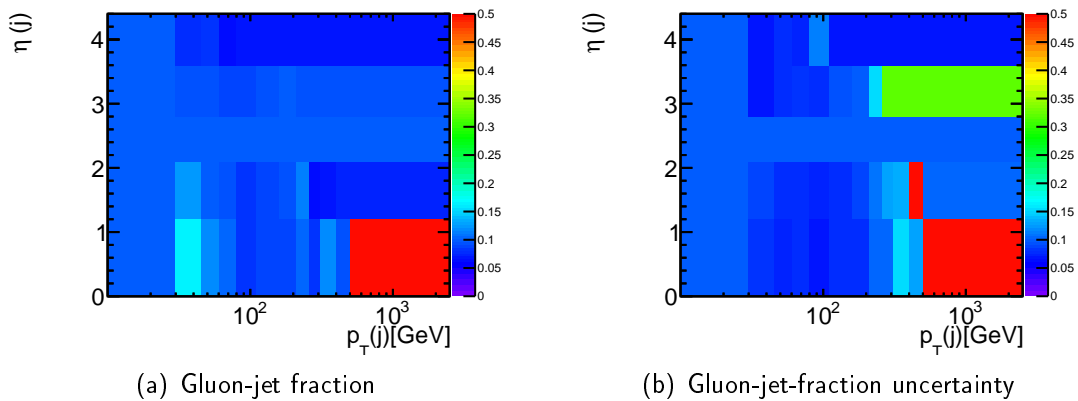
Figure 8.9.: Gluon fraction of non *b*-jets (a) and the corresponding uncertainty (b).

Jet energy resolution:

The finite detector resolution leads to a related uncertainty on the jet energy measurement. The effect is estimated by smearing the jet energy in MC simulated events according to previous measurements of the jet energy resolution.

Jet reconstruction efficiency:

The reconstruction efficiency of jets is estimated in minimum bias events. As shown in Ref. [157], given the analysis jet p_T threshold of 30 GeV, no significant effect is expected, since the jet reconstruction is fully efficient.
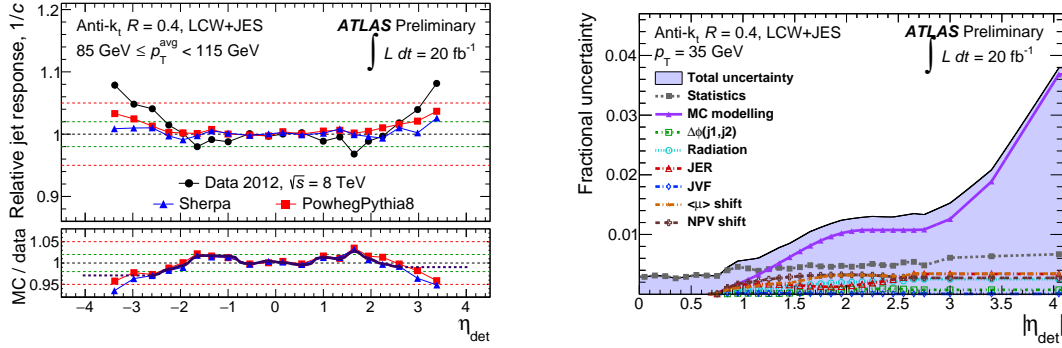
(a) Relative jet response for collision data and two MC simulation models

(b) Summary of uncertainties contributing to the η-inter-calibration uncertainty

Figure 8.10.: Relative jet response for the SHERPA and POWHEG-BOX + PYTHIA 8 MC generators compared to data in (a) and the summary of contributions to the η-inter-calibration uncertainty (b). The individual contributions are added in quadrature. [156].
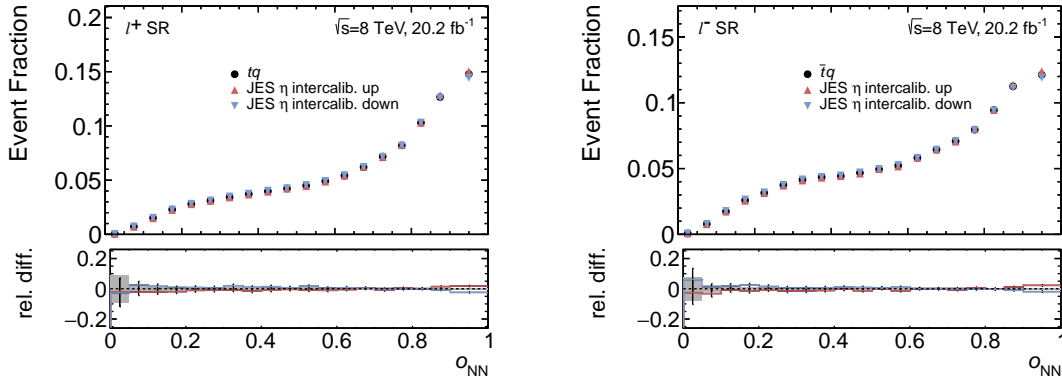
(a) O_{NN} shape uncertainty for the JES η-inter-calibration uncertainty in the ℓ^+ channel

(b) O_{NN} shape uncertainty for the JES η-inter-calibration uncertainty in the ℓ^- channel

Figure 8.11.: Template shape uncertainty of the JES η-inter-calibration uncertainty in the ℓ^+ channel (a) and the ℓ^- channel (b).

Table 8.4.: Breakdown of the JES related systematic uncertainties on the observed values for the fiducial cross sections as well as for R_t.

Source	$\frac{\Delta\sigma_{\mathrm{fid}}(t)}{\sigma_{\mathrm{fid}}(t)}$ [%]	$\frac{\Delta\sigma_{\mathrm{fid}}(\bar{t})}{\sigma_{\mathrm{fid}}(\bar{t})}$ [%]	$\frac{\Delta R_{\mathrm{t,fid}}}{R_{\mathrm{t,fid}}}$ [%]
b-jet energyscale	$\pm$ 0.1	$\pm$ 0.2	$\pm$ 0.1
JES single particle	$\pm$ 0.1	$\pm$ 0.2	$\pm$ 0.1
JES punch through	$\pm$ 0.1	$\pm$ 0.2	$\pm$ 0.1
JES pile-up μ	$\pm$ 0.1	$\pm$ 0.1	$\pm$ 0.2
JES pile-up n_{vtx}	$\pm$ 0.1	$\pm$ 0.1	$\pm$ 0.0
JES pile-up p_{T}	$\pm$ 0.2	$\pm$ 0.1	$\pm$ 0.1
JES pile-up ρ	$\pm$ 0.1	$\pm$ 0.3	$\pm$ 0.3
JES flavour composition	$\pm$ 0.0	$\pm$ 0.1	$\pm$ 0.1
JES flavour response	$\pm$ 0.1	$\pm$ 0.1	$\pm$ 0.1
Jet vertex fraction	$\pm$ 0.0	$\pm$ 0.2	$\pm$ 0.1
JES η intercalibration model	$\pm$ 2.7	$\pm$ 3.0	$\pm$ 0.3
JES η intercal. statistical	$\pm$ 0.1	$\pm$ 0.1	$\pm$ 0.2
JES detector 1	$\pm$ 0.1	$\pm$ 0.2	$\pm$ 0.1
JES detector 2	$\pm$ 0.1	$\pm$ 0.1	$\pm$ 0.2
JES detector 3	$\pm$ 0.1	$\pm$ 0.1	$\pm$ 0.2
JES mixed detector and modeling 1	$\pm$ 0.1	$\pm$ 0.1	$\pm$ 0.2
JES mixed detector and modeling 2	$\pm$ 0.1	$\pm$ 0.2	$\pm$ 0.2
JES mixed detector and modeling 3	$\pm$ 0.1	$\pm$ 0.0	$\pm$ 0.2
JES mixed detector and modeling 4	$\pm$ 0.1	$\pm$ 0.2	$\pm$ 0.3
JES physics modeling 1	$\pm$ 1.3	$\pm$ 1.4	$\pm$ 0.1
JES physics modeling 2	$\pm$ 0.1	$\pm$ 0.2	$\pm$ 0.1
JES physics modeling 3	$\pm$ 0.1	$\pm$ 0.2	$\pm$ 0.1
JES physics modeling 4	$\pm$ 0.1	$\pm$ 0.1	$\pm$ 0.2
JES statistical 1	$\pm$ 0.1	$\pm$ 0.2	$\pm$ 0.2
JES statistical 2	$\pm$ 0.1	$\pm$ 0.1	$\pm$ 0.1
JES statistical 3	$\pm$ 0.2	$\pm$ 0.2	$\pm$ 0.1
JES statistical 4	$\pm$ 0.1	$\pm$ 0.2	$\pm$ 0.2

Missing transverse energy:

Since the measurement of missing transverse energy directly depends on the precision with which leptons and jets are determined, the scale and resolution uncertainty on those objects are propagated to the uncertainty calculation on the E_T^{miss}. Two additional uncertainties, that are inherent to the E_T^{miss} determination, are considered. The contributions of calorimeter cells that are not associated to jets are considered and called `CellOut` term. The other contribution which is taken into account are soft jets with $7\,\mathrm{GeV} < p_T^{jet} < 20\,\mathrm{GeV}$. These soft jets originate mainly from pile-up.

Flavour-tagging efficiency:

The uncertainty on the b/c-tagging efficiency and the mis-tag rate are considered for this analysis. The flavour-tagging performance for the specific MV1c b-tagging algorithm in MC simulated events is corrected to match the performance in collision data. The calibration results are obtained by a combination of two methods, `system8` and $t\bar{t}$ combinatorial-likelihood. One method (`system8`) is based on a sophisticated tag-and-probe technique and the second method uses a combinatorial likelihood approach which is applied to dileptonic $t\bar{t}$ events, as introduced in Section 4.1.6. The uncertainties on the scale factors of b/c-tagged jets as well as mis-tagged jets are propagated independently through the analysis.

The scale factors are obtained in bins of p_T, which correspond to individual components of each flavour-tagging uncertainty. Since the measured cross-sections are charge exclusive the distinct difference in acceptance between b-quark and $\bar{b}$-quark initiated jets needs to be taken into account. The $b - \bar{b}$ acceptance uncertainty is determined by comparing the b-tagging efficiency of tq and $\bar{t}q$ MC simulated events. Table 8.5 contains the impact on each systematic variation on the measured cross-sections, and their ratio R_t.

Table 8.5.: Breakdown of the b-tagging related systematic uncertainties on the observed values for the fiducial cross sections as well as for R_t.

Source	$\frac{\Delta\sigma_{\mathrm{fid}}(t)}{\sigma_{\mathrm{fid}}(t)}$ [%]	$\frac{\Delta\sigma_{\mathrm{fid}}(\bar{t})}{\sigma_{\mathrm{fid}}(\bar{t})}$ [%]	$\frac{\Delta R_{\mathrm{t,fid}}}{R_{\mathrm{t,fid}}}$ [%]
b-tag scalefactor C0	± 0.1	± 0.1	± 0.2
b-tag scalefactor C1	± 0.1	± 0.0	± 0.1
b-tag scalefactor C2	± 0.1	± 0.1	± 0.2
b-tag scalefactor C3	± 0.1	± 0.2	± 0.1
b-tag scalefactor C4	± 0.1	± 0.1	± 0.2
b-tag scalefactor C5	± 0.3	± 0.2	± 0.2
b-tag scalefactor C6	± 0.4	± 0.2	± 0.1
b-tag scalefactor C7	± 0.9	± 0.9	± 0.2
b-tag scalefactor C8	± 0.1	± 0.1	± 0.2
c-tag scalefactor C0	± 0.1	± 0.2	± 0.1
c-tag scalefactor C1	± 0.1	± 0.2	± 0.2
c-tag scalefactor C2	± 0.1	± 0.1	± 0.1
c-tag scalefactor C3	± 0.1	± 0.1	± 0.2
mis-tag scalefactor C0	± 0.1	± 0.2	± 0.3
mis-tag scalefactor C1	± 0.1	± 0.1	± 0.1
mis-tag scalefactor C2	± 0.0	± 0.2	± 0.2
mis-tag scalefactor C3	± 0.1	± 0.2	± 0.3
mis-tag scalefactor C4	± 0.1	± 0.3	± 0.3
mis-tag scalefactor C5	± 0.1	± 0.1	± 0.2
mis-tag scalefactor C6	± 0.1	± 0.2	± 0.2
mis-tag scalefactor C7	± 0.1	± 0.1	± 0.2
mis-tag scalefactor C8	± 0.0	± 0.2	± 0.1
mis-tag scalefactor C9	± 0.1	± 0.1	± 0.1
mis-tag scalefactor C10	± 0.0	± 0.2	± 0.1
mis-tag scalefactor C11	± 0.1	± 0.2	± 0.2

8.2.2. Monte Carlo Generators and Parton Densities

The uncertainties on the modeling of the MC simulated events are estimated by different MC event generators introduced in Chapter 3. The employed models introduce certain parametrisations and methodology to which systematic uncertainties are assigned to estimate the level of confidence in the modeling. As introduced in Section 1.3, several PDF sets have been developed to provide the parton densities employed to perform the MC simulation. In order to estimate the systematic uncertainty on the choice of PDF set, the PDF4LHC15 prescriptions [158] of the authors of the main PDF sets are being followed.

Choice of parton shower:

In order to estimate the level of uncertainty due to the choice of parton-shower simulation, Powheg-Box + Pythia 6 is compared with Powheg-Box + Herwig. The effects of hadronisation and parton shower are compared. In case of the $t\bar{b}$ process contribution, no sample of MC events generated with Powheg-Box + Herwig is available. Therefore, the choice of parton-shower systematic uncertainty only considers the $t\bar{t}$ and Wt processes. Figures 8.12(a) and 8.12(b) show the impact of the parton-shower uncertainty on the O_{NN} distribution in the ℓ^+ channel for the tq and $t\bar{t} + Wt + t\bar{b}$ processes, respectively and the ℓ^- channel in Figures 8.13(a) and 8.13(b).

Scale choice:

An uncertainty on the choice of factorisation and renormalisation scale in the matrix element computation is assigned by variation of both μ_{f} and μ_{r} scales independently. MC simulated events using the nominal MC event generator Powheg-Box + Pythia 6, are produced with varied μ_{f} and μ_{r} by a factor of 0.5 and 2.0 simultaneously. In addition, a corresponding shower MC tune of Pythia 6, with modified α_s, is chosen to match the scale variation in the ME, as explained in Section 3.3.1. A detailed list of modified parameters of the shower tune is given in Ref. [101]. Figures 8.12(c) and 8.12(d) show the impact of the scale uncertainty on the O_{NN} distribution in the ℓ^+ channel for the tq and $t\bar{t} + Wt + t\bar{b}$ processes, respectively and the ℓ^- channel in Figures 8.13(c) and 8.13(d).

NLO-matching method:

The uncertainty due to the NLO-matching method is estimated by the comparison of MC@NLO and Powheg-Box, interfaced with Herwig, in case of $t\bar{t}$ production, $t\bar{b}$ and Wt single top-quark production. In case of the signal processes tq and $\bar{t}q$ production, MadGraph 5_aMC@NLO + Herwig is compared to Powheg-Box + Herwig. The difference in acceptance and O_{NN} shape is extrapolated to cover the $\pm 1\sigma$ uncertainty around the nominal sample of simulated events using Powheg-Box + Pythia 6. Figures 8.12(e) and 8.12(f) show the impact of the NLO-matching method uncertainty on the O_{NN} distribution in the ℓ^+ channel for the tq and $t\bar{t} + Wt + t\bar{b}$ processes, respectively and the ℓ^- channel in Figures 8.13(e) and 8.13(f). The particularly large impact
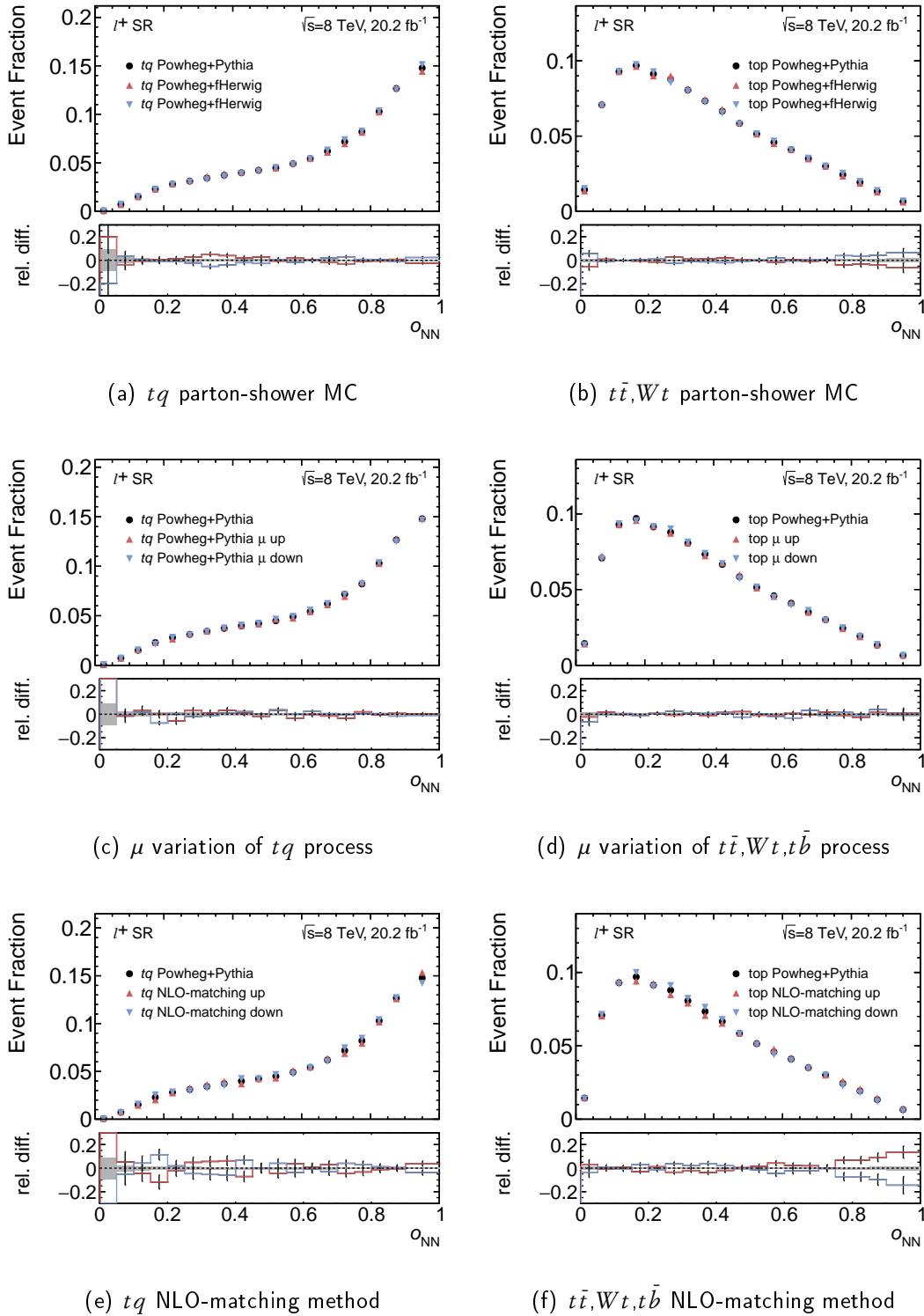
that can be observed at high values of O_{NN} is emerging from the dependence on the NN of the highly significant input variable $|\eta(j)|$. The uncertainty exploits specific differences in the modeling of forward jets in the compared MC event generators. The difference originates in the description of additional gluon radiation in MC@NLO and Powheg-Box. The effect is enhanced in the selected phase-space leading to a 10-20 % deviation between the predictions of $|\eta(j)|$.

Figure 8.14 shows the $|\eta(j)|$ distribution of the untagged jet for three different MC generators in the SR after applying a cut on the O_{NN} distribution, defined in Section 8.1.4. By requiring $O_{\mathrm{NN}} > 0.8$ for the selection of the highly enriched signal region, the impact of systematic uncertainties on the template shape can be studied in detail. In Figure 8.14(a), the $|\eta(j)|$ distribution is shown for three t-channel single top-quark MC generators. The nominal Powheg-Box + Pythia 6 MC generator is compared to Powheg-Box + Herwig and MadGraph 5_aMC@NLO + Herwig, which are used to define the uncertainty in the NLO-matching method and choice of parton shower uncertainties. The difference in the signal modeling at high values of $|\eta(j)|$ is approaching 20 %, and mainly leads to the final systematic uncertainty. Figure 8.14(b) also shows the $|\eta(j)|$ distribution but in case of the $t\bar{t} + Wt + t\bar{b}$ processes. The conclusion on the final systematic uncertainties is similar as for the signal process, while the differences at high values of $|\eta(j)|$ are even larger.

(a) tq parton-shower MC

(b) $t\bar{t}, Wt$ parton-shower MC

(c) μ variation of tq process

(d) μ variation of $t\bar{t}, Wt, t\bar{b}$ process

(e) tq NLO-matching method

(f) $t\bar{t}, Wt, t\bar{b}$ NLO-matching method

Figure 8.12.: The template shape components of the signal-modeling (left) and top-background modeling (right) uncertainties in the ℓ^+ channel.

(a) $\bar{t}q$ parton-shower MC

(b) $t\bar{t}$,Wt parton-shower MC

(c) μ variation of $\bar{t}q$ process

(d) μ variation of $t\bar{t}$,Wt,$t\bar{b}$ process

(e) $\bar{t}q$ NLO-matching method

(f) $t\bar{t}$,Wt,$t\bar{b}$ NLO-matching method
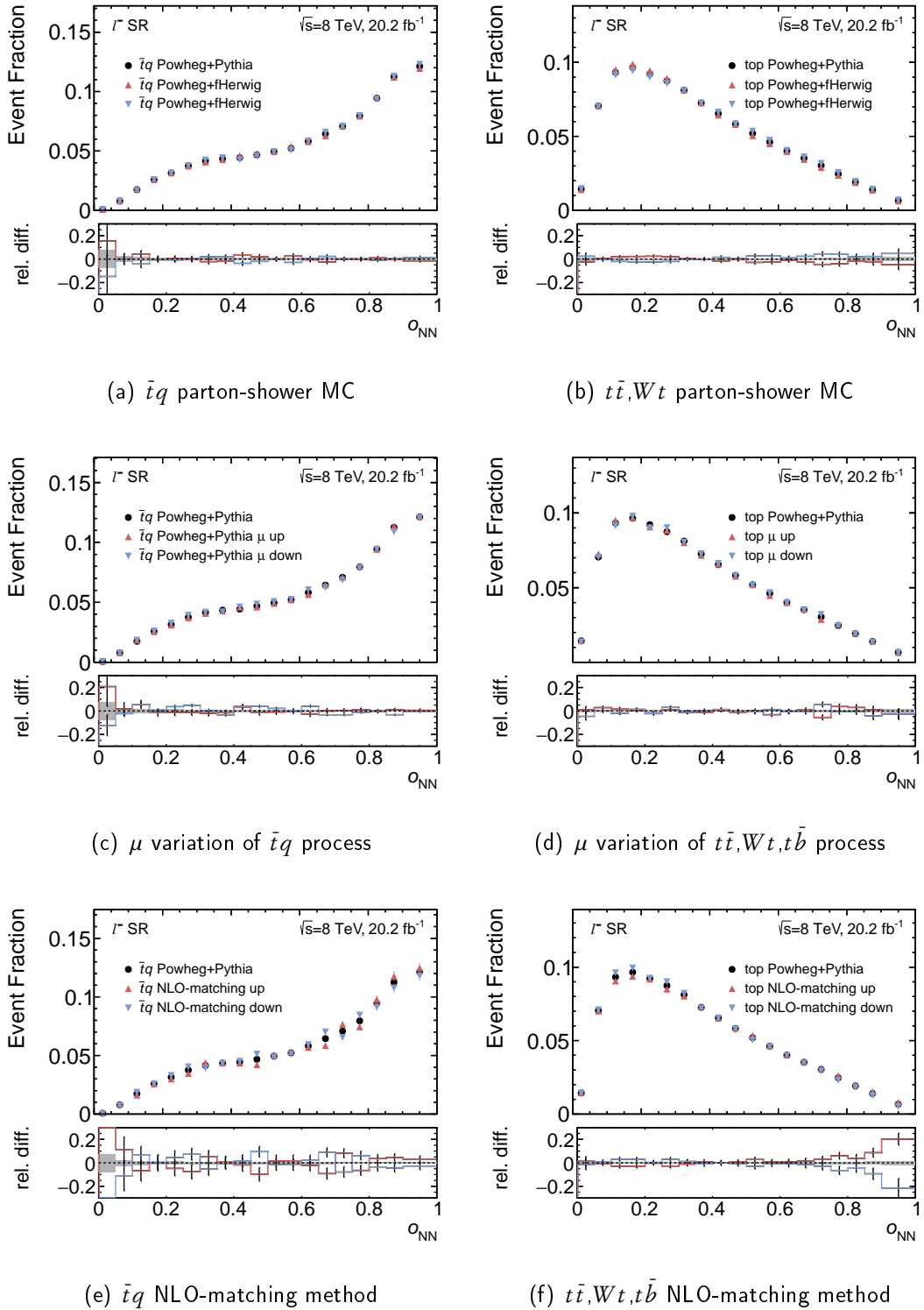
Figure 8.13.: The template shape components of the signal-modeling (left) and top-background modeling (right) uncertainties in the ℓ^- channel.

(a)   (b)
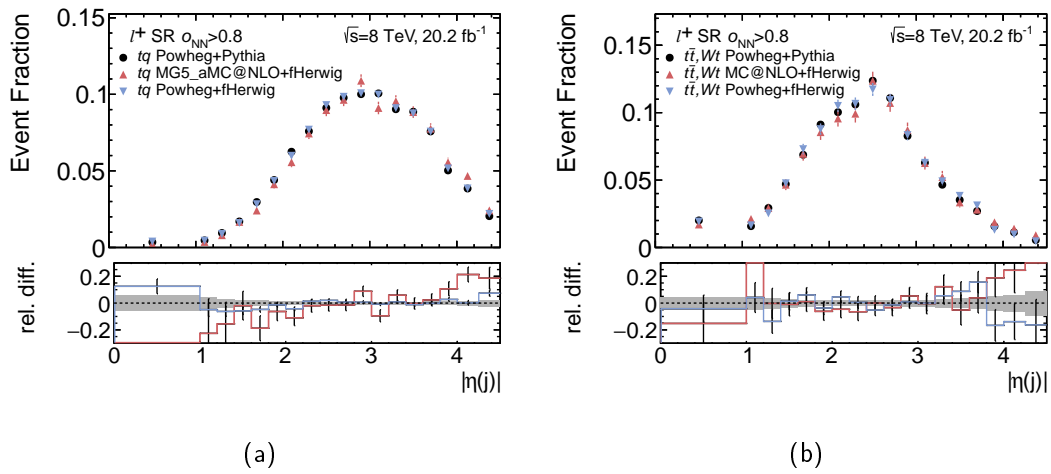
Figure 8.14.: Distribution of $|\eta(j)|$ in the SR+O_{NN} > 0.8 region, for the signal process in (a) and for the $t\bar{t}$ +Wt processes in (b). The nominal Powheg-Box + Pythia 6 MC generator is compared to Powheg-Box + Herwig and Mad-Graph 5_aMC@NLO + Herwig.

PDF sets:

The uncertainty on the PDF set is estimated by means of the PDF4LHC15 recommendation. A special PDF set, called PDF4LHC15, has been devised by the PDF groups, to provide the uncertainty estimate for the main PDF sets, CT14, MMHT14 and NNPDF 3.0. The PDF4LHC15 PDF set provides different modes, which are suited for different analysis types. It is recommended to evaluate the mode that provides 30 eigenvectors (n_{eig} = 30), that are orthogonal components, for this type of analysis. All eigenvectors are evaluated to extract the full coverage in terms of acceptance and O_{NN}-shape uncertainty. The eigenvectors comprise a so-called Hessian PDF-set, which are combined following the Hessian approach, given in Equation 8.2, where $F(S_k^+)$ and $F(S_k^-)$ are the predictions for the k − th eigenvector of a PDF set. The term ΔF corresponds to the total symmetric uncertainty.

$$\Delta F = \frac{1}{2}\sqrt{\sum_{k=0}^{n_{\mathrm{eig}}}\left[\left(F(S_k^+) - F(S_k^-)\right)\right]^2} \tag{8.2}$$

Equation 8.2 is adapted to approximate the shift of $\frac{N_{\mathrm{sel}}}{N_{\mathrm{fid}}}$:

$$\Delta\frac{N_{\mathrm{sel}}}{N_{\mathrm{fid}}} = \frac{1}{2}\sqrt{\sum_{k=0}^{n_{\mathrm{eig}}}\left[\left(\frac{N_{\mathrm{sel}}^{k,+}}{N_{\mathrm{fid}}^{k,+}} - \frac{N_{\mathrm{sel}}^{k,-}}{N_{\mathrm{fid}}^{k,-}}\right)\right]^2} \tag{8.3}$$

Figures 8.15(a) and 8.15(b) show the ratio $\frac{N_{\mathrm{sel}}}{N_{\mathrm{fid}}}$ for all eigenvectors of the PDF4LHC PDF set for tq production and $\bar{t}q$ production, respectively. The acceptance uncertainty considered on the fiducial cross-section corresponds to $\Delta\frac{N_{\mathrm{sel}}}{N_{\mathrm{fid}}}$. The PDF uncertainty on the fiducial acceptance is also obtained corresponding to the ΔA_{fid} variations for all eigenvector variations. The PDF uncertainty estimated on A_{fid} are shown in Figures 8.15(c) and 8.15(d). The estimation on the PDF uncertainty on the extrapolated total cross-section is done correlated and summarised in Figures 8.15(e) and 8.15(f).

An additional uncertainty is assigned to the comparison of the central value of PDF4LHC15 and CT10, since the CT10 PDF-set is not included in the determination of the PDF4LHC15 PDF-set. The resulting uncertainty yields 0.2 % in the ℓ^+ channel and 0.4 % in the ℓ^- channel.

Table 8.6 shows the relative contributions of the PDF uncertainties obtained on the W + jets and $t\bar{t}+Wt+t\bar{b}$ background processes. The relative PDF uncertainty is weighted with the individual template fraction. The PDF uncertainty on the $t\bar{t} + Wt + t\bar{b}$ processes is 1.5 %, and 1.0 % for the W + jets processes in the ℓ^+ channel, and 1.5 % in the ℓ^- channel.
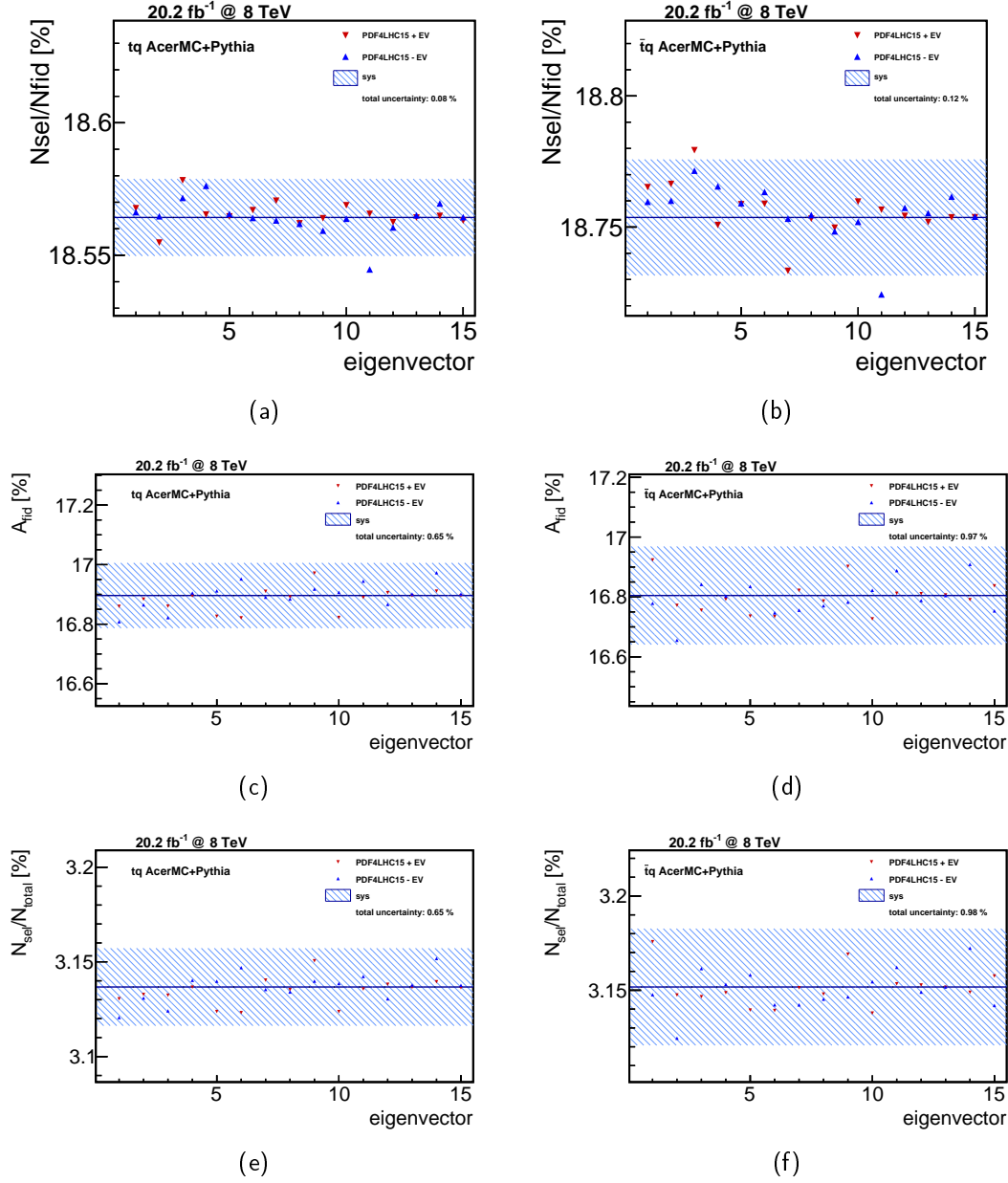
Figure 8.15.: Central value (solid line) and eigenvectors (triangles) as well as the corresponding uncertainty (hatched area) of the PDF4LHC PDF set for tq production (left) and for $\bar{t}q$ production (right). Figures (a) and (b) show the PDF uncertainty on the ratio $\frac{N_{sel}}{N_{fid}}$, while Figures (c) and (d) show the PDF uncertainty on A_{fid}. Figures (e) and (f) show the PDF uncertainty on the extrapolated total cross-section.

Table 8.6.: PDF acceptance uncertainties obtained with the PDF4LHC15 PDF set.

Process	Relative PDF uncertainty	Template fraction	Template
$t\bar{b}$	1.0%	3%	$t\bar{t}, Wt, t\bar{b}$
$t\bar{t}$	1.4%	85%	$t\bar{t}, Wt, t\bar{b}$
Wt	2.4%	12%	$t\bar{t}, Wt, t\bar{b}$
$W^+ +$light jets	0.8%	6%	$W^+ +$jets
$W^- +$light jets	0.8%	7%	$W^- +$jets
$W^+ + bb$ jets	0.6%	56%	$W^+ +$jets
$W^- + bb$ jets	0.9%	49%	$W^- +$jets
$W^+ + c(c)$ jets	1.7%	38%	$W^+ +$jets
$W^- + c(c)$ jets	2.2%	44%	$W^- +$jets

W + jets modeling:

In contrast to the top-quark processes, the modeling uncertainty on the W + jets process is estimated entirely by intrinsic parameter variation of the Sherpa MC event generator. As the appropriate parameter variations were not available with the Sherpa version used to produce all W + jets MC simulated samples, a separate set of samples of MC simulated events have been generated. The additional samples only provide MC-generator-level information since it was not feasible to perform the full ATLAS detector simulation for them. In Sherpa the `FSFRSF` parameter simultaneously modifies the $\mu_{r,f}$ scales, resummation scale, underlying event activity as well as the CKKW matching parameter. The `FSFRSF` parameter variations are separated in one up and one down variation, which are treated individually. A detailed study on the impact on the various parameters has been performed in Ref. [159], showing that mainly the variation of the $\mu_{r,f}$ scales impact the predicted results.

In order to estimate the modeling uncertainty due to the `FSFRSF` parameter variations, a loose selection is applied, requiring at least one jet in the event. The p_T spectrum of the W boson is reweighted to match the spectra obtained with the parameter variations for the inclusive W + jets MC sample. The p_T spectrum of the W boson is chosen to be reweighted, since it is sensitive to the recoil of the W boson against additional radiation in the event. The two reweighting functions are subsequently applied on the nominal W + jets MC sample such that the p_T spectrum of the W boson matches either `FSFRSF` parameter varied MC sample. Figure 8.16(a) shows the $p_T(W)$-distribution for the inclusive W + jets MC sample as well as the `FSFRSF` up and `FSFRSF` down parameter variations. Figure 8.16(b), 8.16(c) shows the weights assigned to each bin in the $p_T(W)$-distribution.

As apparent on inspection of Figures 8.16(d) and 8.16(e), the effective impact on the shape of the O_{NN} is insignificant. Therefore the W + jets modeling uncertainty can be dismissed in the statistical analysis.

Z + jets heavy-flavour normalisation:

An uncertainty on the Z + jets heavy-flavour normalisation is assigned to the Z + jets process, due to the b-tagging requirement within the event selection. The b-tagging requirement enriches the heavy-flavour fraction of the jets in selected Z + jets events. Therefore, the uncertainty in the heavy-flavour fraction in Z + jets events is particularly important. A relative uncertainty of 50 % on the Z + jets normalisation is considered.

Multijet estimate:

A uncertainty assigned to the estimated number of multijet events, as well as the O_{NN} shape of the multijet process is taken into account. In order to estimate the multijet uncertainty, the nominal assessment is compared to the Matrix Method normalisation and O_{NN} shape prediction. As a result, a normalisation uncertainty of 15 % is considered in the statistical analysis.

(a) $p_T(W)$-distribution

(b) FSFRSF up reweighting
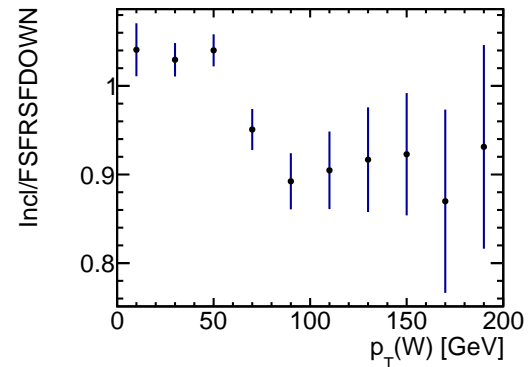
(c) FSFRSF down reweighting
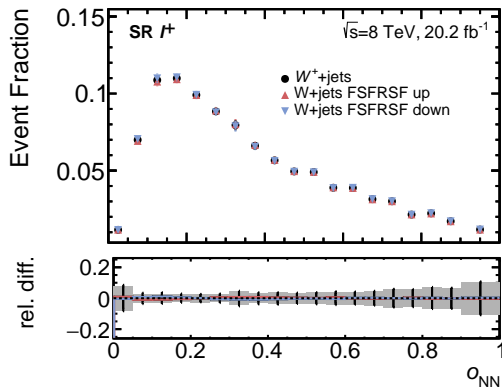
(d) W^++jets FSFRSF shape
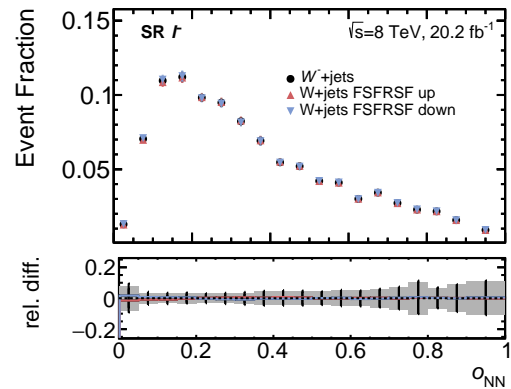
(e) W^-+jets FSFRSF shape

Figure 8.16.: Figure (a) shows the $p_T(W)$-distribution for all three MC samples. A reweighting is derived by scaling the inclusive W+jets MC sample to the FSFRSF up and down variation. Figures (b) and (c) show th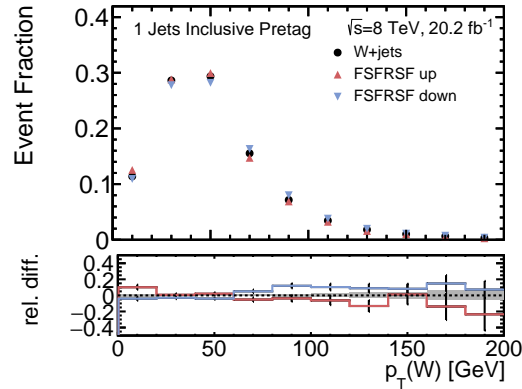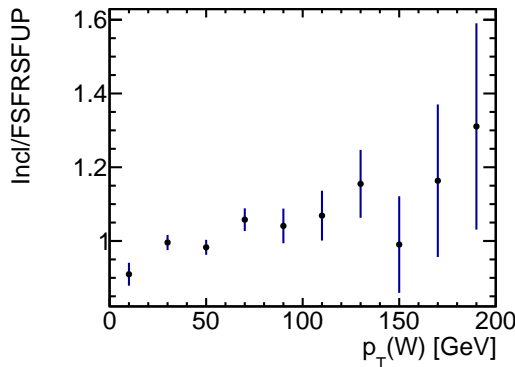e weights assigned to each bin in the $p_T(W)$-distribution. The reweighting is applied on the nominal Sherpa W+jets MC samples, yielding the shape uncertainty templates for the O_{NN} distribution, see Figures (d) and (e).

Cross section:

In order to propagate the theoretical uncertainty on the cross-sections that are used as the nominal reference normalisation, a corresponding cross-section uncertainty is considered in the statistical analysis for all background processes. Table 8.7 summarises the considered cross-section uncertainties.

Table 8.7.: Uncertainties on the normalisation of all background processes.

Process	ℓ^+-channel	ℓ^--channel
$t\bar{t}$ / Wt / $t\bar{b}$	6.6 %	6.6 %
W^+ + jets	21 %	21 %
W^- + jets	21 %	21 %
Z + jets, VV	21 %	21 %
Multijet	15.7 %	14.5 %

Monte Carlo statistics:

To account for the uncertainty on the limited size of samples of MC simulated events, a dedicated uncertainty is assigned.

Luminosity: The absolute luminosity scale is derived from beam-separation scans performed in November 2012. The uncertainty in the integrated luminosity is 1.9 % [160].

8.3. Evaluation of Systematic Uncertainties

The evaluation of the impact of the systematic uncertainties on the cross-section measurement is determined from pseudo experiments, introduced in Section 8.1.2. An ensemble of 100000 pseudo experiments is generated for each systematic uncertainty and one ensemble corresponding to the envelope of all considered systematic uncertainties.

As described in Section 8.1.2, systematic uncertainties are decomposed into an acceptance and a template shape component. While the acceptance uncertainty for all sources of systematic uncertainties are considered, several shape template components are neglected in the statistical analysis. Tables 8.8 and 8.9 contain a list of the considered systematics and whether the respective template shape uncertainty is considered in the statistical analysis. The decision if a shape uncertainty is not negligible is performed as follows. A median filter is employed to dampen statistical fluctuations in the shape template of a given process. The median filter uses a window of three neighboring bins, where all bins are considered. The selected bin is in the middle of the window, and its content is replaced by the median value of all three bins. The content of the first and last bin of the template shape histogram remain unchanged. Finally, a bin-by-bin comparison of the deviation between the nominal shape template distribution and the systematic variation w.r.t. the magnitude of the statistical uncertainty is performed. The statistical uncertainty refers to the uncertainty due to the limited size of the sample of MC simulated events. A systematic shape template variation is considered significant, if any bin exceeds the statistical uncertainty in the given bin, after the median filter is applied. The procedure is performed for all systematic variations and processes. If at least one significant variation is found for a process, the systematic shape template is considered for all processes.

Table 8.10 contains the impact of the considered systematic uncertainties on the $\sigma_{\mathrm{fid}}(tq)$ and $\sigma_{\mathrm{fid}}(\bar{t}q)$. The dominating uncertainties correspond to the jet energy scale, $tq/\bar{t}q$ scale variations and the NLO matching of the $t\bar{t}+Wt+t\bar{b}$ background processes.

The obtained relative total systematic uncertainty on $\sigma_{\mathrm{fid}}(tq)$ is ±5.8 % and in case of $\sigma_{\mathrm{fid}}(\bar{t}q)$ an uncertainty of ±7.8 % is deduced. The systematic uncertainty on the cross-section ratio is determined by correlating each uncertainty source for $\hat{\beta}^s_{tq}$ and $\hat{\beta}^s_{\bar{t}q}$. The relative total systematic-uncertainty on the cross-section ratio R_t is determined to be ±5.0 %.

Table 8.11 contains the post-fit normalisation uncertainties on the W + jets and $t\bar{t}$ + $Wt + t\bar{b}$ processes, and the cross-section uncertainties on the Z + jets and multijet processes. The post-fit normalisation uncertainties are obtained from pseudo experiments and the correlation of W + jets and $t\bar{t} + Wt + t\bar{b}$ processes in the fit is taken into account.

Appendix A contains a complete list of the acceptance uncertainties considered in the statistical analysis.

Table 8.8.: Considered shape uncertainties for the statistical analysis.

Systematic Uncertainty	Considered for statistical analysis
Flavour tagging	No
b-jet energy scale	No
JES single particle	No
JES pile-up μ	No
JES pile-up n_{vtx}	No
JES pile-up Pt	No
JES pile-up ρ	No
JES PunchThrough	No
JES flavour composition	No
JES flavour response	No
Jet vertex fraction	No
JES η intercal. statistical	No
JES η intercalibration	Yes
JES detector 1	No
JES detector 2	No
JES detector 3	No
JES mixed detector and modeling 1	No
JES mixed detector and modeling 2	No
JES mixed detector and modeling 3	No
JES mixed detector and modeling 4	No
JES physics modeling 1	Yes
JES physics modeling 2	No
JES physics modeling 3	No
JES physics modeling 4	No
JES statistical 1	No
JES statistical 2	No
JES statistical 3	No
JES statistical 4	No

Table 8.9.: Considered shape uncertainties for the statistical analysis.

Systematic Uncertainty	Considered for statistical analysis
JER	Yes
Flavour-tagging efficiency	No
Jet efficiency	No
Muon momentum resolution (ID)	No
Muon momentum scale	No
Muon momentum resolution	No
Electron energy resolution	No
Electron energy scale	No
Lepton trigger scalefactor	No
Lepton ID scalefactor	No
Lepton Reco scalefactor	No
Electron Charge ID	Yes
E_T^{miss} CellOut + SoftJet Resolution	Yes
E_T^{miss} CellOut + SoftJet Scale	Yes
Multijet model	Yes
$b\bar{b}$ tagging efficiency	No
Z+jets heavy flavour norm.	No
tq ($\bar{t}q$) NLO matching	Yes
tq ($\bar{t}q$) parton shower	Yes
$t\bar{t},Wt,t\bar{b}$ NLO matching	Yes
$t\bar{t},Wt$ parton shower	Yes
μ variation of $t\bar{t},Wt,t\bar{b}$ process	Yes
μ variation of tq process	Yes
PDF background	Yes
PDF tq	No
PDF tq CT10 to PDF4LHC15	No

Table 8.10.: Detailed list of the contribution of each source of uncertainty to the total uncertainty on the measured values of $\sigma_{\mathrm{fid}}(tq)$ and $\sigma_{\mathrm{fid}}(\bar{t}q)$. The evaluation of the systematic uncertainties has a statistical uncertainty of 0.3 %. Uncertainties contributing less than 0.5 % are marked with '< 0.5'.

Source	$\Delta\sigma_{\mathrm{fid}}(tq) \,/\, \sigma_{\mathrm{fid}}(tq)$ [%]	$\Delta\sigma_{\mathrm{fid}}(\bar{t}q) \,/\, \sigma_{\mathrm{fid}}(\bar{t}q)$ [%]
Data statistics	± 1.7	± 2.5
Monte Carlo statistics	± 1.0	± 1.4
Background normalisation	< 0.5	< 0.5
Background modelling	± 1.0	± 1.6
Lepton reconstruction	± 2.1	± 2.5
Jet reconstruction	± 1.2	± 1.5
Jet energy scale	± 3.1	± 3.6
Flavour tagging	± 1.5	± 1.8
$E_{\mathrm{T}}^{\mathrm{miss}}$ modelling	± 1.1	± 1.6
$b/\bar{b}$ tagging efficiency	± 0.9	± 0.9
PDF	± 1.3	± 2.2
tq ($\bar{t}q$) NLO matching	± 0.5	< 0.5
tq ($\bar{t}q$) parton shower	± 1.1	± 0.8
tq ($\bar{t}q$) scale variations	± 2.0	± 1.7
$t\bar{t}$ NLO matching	± 2.1	± 4.3
$t\bar{t}$ parton shower	± 0.8	± 2.5
$t\bar{t}$ scale variations	< 0.5	< 0.5
Luminosity	± 1.9	± 1.9
Total systematic	± 5.6	± 7.3
Total (stat. + syst.)	± 5.8	± 7.8

Table 8.11.: Uncertainties in the normalisations of the different backgrounds for all processes, as derived from pseudo experiments, the correlation of W + jets and $t\bar{t}$ + $Wt + t\bar{b}$ is taken into account.

Process	$\Delta N/N$
$t\bar{t} + Wt + t\bar{b}$	7.5 %
W^{+} + jets	7.1 %
W^{-} + jets	7.3 %
Z, VV + jets	not fitted process
Multijet	not fitted process

8.4. Measurement Results

The main results are obtained by means of an ML fit to the O_{NN} discriminant distributions in the ℓ^+ channel and ℓ^- channel channels of the SR. The attained yields of $\hat{\nu}(tq)$ and $\hat{\nu}(\bar{t}q)$ relate to the fiducial cross-sections via Equation 6.4.

8.4.1. Fiducial Cross-Section Measurements

The fiducial cross-sections are calculated via Equation 6.4 yielding:

$$\sigma_{\mathrm{fid}}(tq) = 9.78 \pm 0.16 \,(\text{stat.}) \pm 0.52 \,(\text{syst.}) \pm 0.19 \,(\text{lumi.}) \text{ pb} \tag{8.4}$$
$$= 9.78 \pm 0.57 \text{ pb}$$

and

$$\sigma_{\mathrm{fid}}(\bar{t}q) = 5.77 \pm 0.14 \,(\text{stat.}) \pm 0.41 \,(\text{syst.}) \pm 0.11 \,(\text{lumi.}) \text{ pb} \tag{8.5}$$
$$= 5.77 \pm 0.45 \text{ pb}.$$

The uncertainties are introduced in Section 8.2 and their effect on $\hat{\nu}(tq)$ and $\hat{\nu}(\bar{t}q)$ is propagated to the measured fiducial cross-sections. The uncertainties are evaluated using pseudo experiments for each systematic source, as well as the complete set.

Two sources of uncertainties are generally differentiated, acceptance uncertainties and O_{NN}-shape uncertainties. The acceptance uncertainties hereby refer to the ratio $N_{\mathrm{sel}}/N_{\mathrm{fid}}$. As described in Section 6.1, the impact of certain systematic uncertainties is reduced w.r.t. the uncertainty on the respective total cross-section. The reduction of the PDF, signal MC generator and PS uncertainties accounts for about 1 percentage point each. In case of the scale choice of the signal generator and the NLO-matching method, this reduction increases to about 2 percentage points each. The relative combined uncertainties, including the statistical and systematic uncertainties, are $\pm 5.8\,\%$ for $\sigma_{\mathrm{fid}}(tq)$ and $\pm 7.8\,\%$ for $\sigma_{\mathrm{fid}}(\bar{t}q)$.

Table 8.10 shows the relative uncertainties on $\sigma_{\mathrm{fid}}(tq)$ and $\sigma_{\mathrm{fid}}(\bar{t}q)$, for each uncertainty category and the total effect. The total uncertainty is dominated by the jet-energy-scale calibration uncertainty and the uncertainty in the $tq/\bar{t}q$ scale variations. The $t\bar{t}$ NLO-matching contribution is the largest background modelling uncertainty, especially on $\sigma_{\mathrm{fid}}(\bar{t}q)$. The difference in impact of the $t\bar{t}$ NLO-matching uncertainty between $\sigma_{\mathrm{fid}}(tq)$ and $\sigma_{\mathrm{fid}}(\bar{t}q)$, can be explained by the smaller S/B ratio in the ℓ^- channel, which leads to a larger impact of the $t\bar{t}$ modelling.

Predictions on the fiducial cross-sections are derived by using the predicted total cross-section of a given MC event generator and the corresponding fiducial acceptance A_{fid} in Equation 6.5. Figure 8.17 displays $\sigma_{\mathrm{fid}}(tq)$ in (a) and $\sigma_{\mathrm{fid}}(\bar{t}q)$ in (b). The predictions of several combinations of ME event generators, PS generators and fixed-number-flavour-schemes are included. The ME generators POWHEG-BOX and MADGRAPH 5_aMC@NLO are combined with the PS programs PYTHIA 6, PYTHIA 8, HERWIG and HERWIG 7. The four-flavour scheme (4 FS) and five-flavour scheme (5 FS) are compared, see also the discussion in 1.5.2. All ME generators are using the CT10 PDF set, and the intra-PDF uncertainties of CT10 are evaluated as PDF uncertainty. The scale uncertainties are determined by the method of independent restricted scale-variations as introduced in Section 3.3.1. The uncertainties on the measurement include the statistical, and the squared-sum of statistical and systematic uncertainty in yellow and green, respectively. The uncertainties on the predictions are distinguished for the PDF uncertainty in orange and the squared-sum of PDF and scale uncertainty in grey. The correlation of the PDF and scale uncertainties between the predicted total cross-section and A_{fid} is accounted for. The overall agreement of all predictions to the measured cross-section is very good, and only slightly deviates for POWHEG-BOX + HERWIG 7 in the 4 FS.

An interesting effect is visible in comparing the magnitude of the scale uncertainties of all 4 FS predictions compared to the 5 FS ones, which are substantially larger for the 4 FS predictions. This is due to the fact that, already at LO, an additional term in α_s is introduced to the 4 FS by including the initial gluon splitting in the ME. This is explained in Ref. [56]. Due to the smaller scale uncertainty the 5 FS results are generally considered to be more appropriate to estimate the total cross-section.
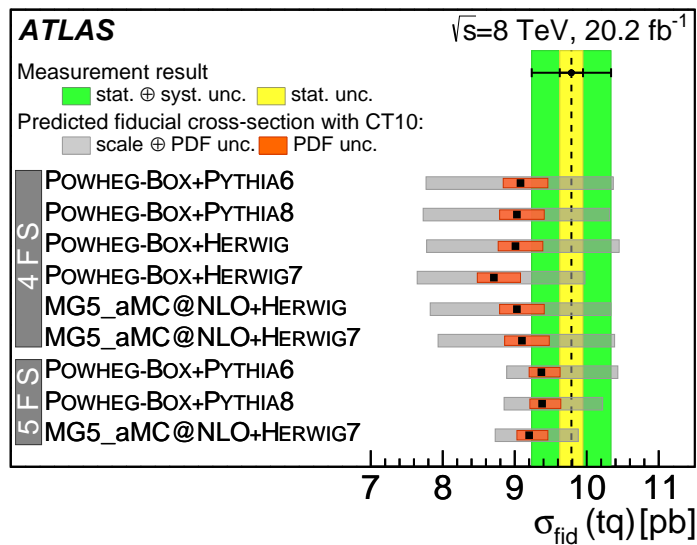
(a)
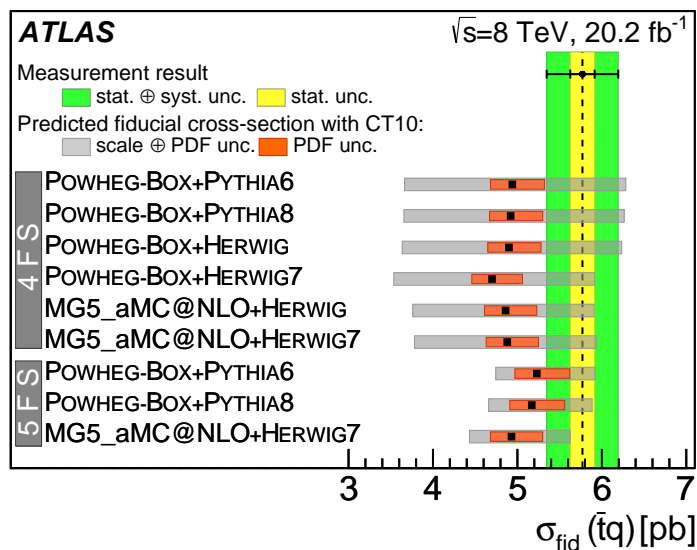
(b)

Figure 8.17.: Measured *t*-channel single top-quark (a) and top-antiquark (b) fiducial cross-sections compared to predictions by the NLO MC generators POWHEG-BOX and MADGRAPH5_aMC@NLO in the four-flavour scheme (4 FS) and five-flavour scheme (5 FS) combined with different PS models. The uncertainties on the predictions include the uncertainty on the scale choice using the method of independent restricted scale variations and the intra-PDF uncertainty on the CT10 PDF set.

8.4.2. Total Cross-Section Measurements

The total cross-sections, $\sigma_{\text{tot}}(tq)$ and $\sigma_{\text{tot}}(\bar{t}q)$ are extrapolated to the full phase-space using the result on the fiducial cross-sections as well as the fiducial acceptance A_{fid}. The result of the total cross-section can be obtained by any given MC generator. Using A_{fid} obtained with Powheg-Box + Pythia 6 in the 4 FS yields:

$$\sigma_{\text{tot}}(tq) = 56.7 \pm 0.9 \, (\text{stat.}) \pm 2.7 \, (\text{exp.}) \, {}^{+2.7}_{-1.7} \, (\text{scale}) \pm 0.4 \, (\text{PDF}) \tag{8.6}$$
$$\pm 1.0 \, (\text{NLO-matching method}) \pm 1.1 \, (\text{PS}) \pm 1.1 \, (\text{lumi.}) \, \text{pb}$$
$$= 56.7^{+4.3}_{-3.8} \, \text{pb}$$

and

$$\sigma_{\text{tot}}(\bar{t}q) = 32.9 \pm 0.8 \, (\text{stat.}) \pm 2.3 \, (\text{exp.}) \, {}^{+1.4}_{-0.8} \, (\text{scale}) \pm 0.3 \, (\text{PDF}) \tag{8.7}$$
$$ {}^{+0.7}_{-0.6} \, (\text{NLO-matching method}) \pm 0.6 \, (\text{PS}) \pm 0.6 \, (\text{lumi.}) \, \text{pb}$$
$$= 32.9^{+3.0}_{-2.7} \, \text{pb} \, .$$

The uncertainties on the fiducial cross-sections are treated as correlated to the respective ones on A_{fid}. The ME generators are using CT10 as input PDF set. The PDF uncertainty on A_{fid} is estimated using the PDF4LHC15 recommendation and AcerMC + Pythia 6 as MC event generator. The scale uncertainty is estimated following the restricted independent scale variation procedure. For cases where an evaluation of the scale uncertainty was not possible the result of Powheg-Box + Pythia 6 is adopted. Tables 6.3 and 6.4 contain the fiducial acceptances for the used MC generators.

Figure 8.18 displays the extrapolated total-cross sections using various MC generator combinations. The ME generators Powheg-Box and MadGraph 5_aMC@NLO are combined with the PS programs Pythia 6, Pythia 8, Herwig and Herwig 7. The upper combinations are evaluated in the 4 FS and the lower ones in the 5 FS. Since MC generators are compared, the NLO-matching method and PS uncertainties are not included in these figures. Three fixed-order calculations in perturbative QCD are included [141, 57, 161, 162]. The NLO, NLO+NNLL and NNLO calculation as well as their PDF and scale⊕PDF uncertainties are shown. In case of the NNLO calculation no PDF uncertainty estimate is available. Thus the PDF⊕α_s uncertainty is taken from the NLO calculation to improve the comparability of the calculations to the measurements and the other predictions.

Table 8.12 and 8.13 show the impact on the cross-section extrapolation for both uncertainties.

Table 8.12.: Correlated uncertainty consideration on the cross-section extrapolation for $\sigma(tq)$.

Uncertainty	$\sigma_{\text{fid}}(tq) + \Delta_{\text{unc.}}$ [pb]	$A_{\text{fid}} + \Delta_{\text{unc.}}$	$\sigma_{\text{tot}}(tq)$ [pb]	$\Delta\sigma(tq)$ [pb]	$\frac{\Delta\sigma(tq)}{\sigma(tq)}$
Nominal	9.79	0.1726	56.71	—	—
scale unc. up	9.98	0.168	59.38	2.7	4.5%
scale unc. down	9.59	0.174	55.01	-1.7	-3.1%
NLO-matching unc. up	9.84	0.1704	57.71	1.0	1.7%
NLO-matching unc. down	9.84	0.1747	55.73	-1.0	-1.8%
PS unc. up	9.89	0.171	57.77	1.1	1.8%
PS unc. down	9.68	0.174	57.77	1.1	1.8%

Table 8.13.: Correlated uncertainty consideration on the cross-section extrapolation for $\sigma(\bar{t}q)$.

Uncertainty	$\sigma_{\text{fid}}(\bar{t}q) + \Delta_{\text{unc.}}$ [pb]	$A_{\text{fid}} + \Delta_{\text{unc.}}$	$\sigma_{\text{tot}}(\bar{t}q)$ [pb]	$\Delta\sigma(\bar{t}q)$ [pb]	$\frac{\Delta\sigma(\bar{t}q)}{\sigma(\bar{t}q)}$
Nominal	5.77	0.1752	32.93	—	—
scale unc. up	5.87	0.1711	34.31	1.38	4.0%
scale unc. down	5.67	0.1763	32.17	-0.76	-2.4%
NLO-matching unc. up	5.79	0.1723	33.59	0.66	2.0%
NLO-matching unc. down	5.79	0.1782	32.29	-0.64	-2.0%
PS unc. up	5.82	0.1736	33.50	0.57	1.7%
PS unc. down	5.72	0.1769	33.50	0.57	1.7%
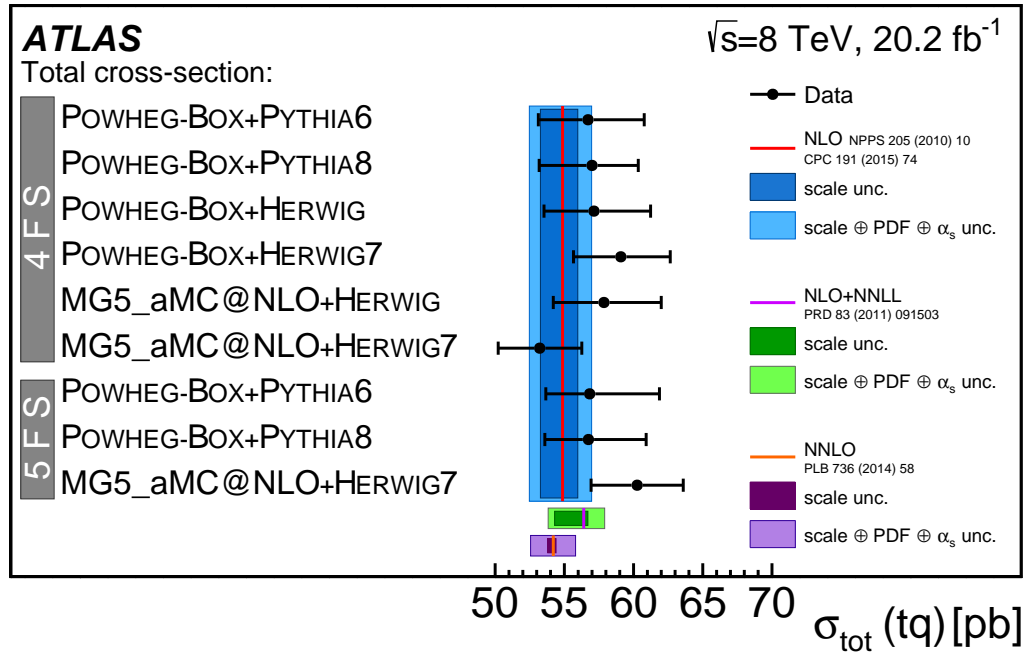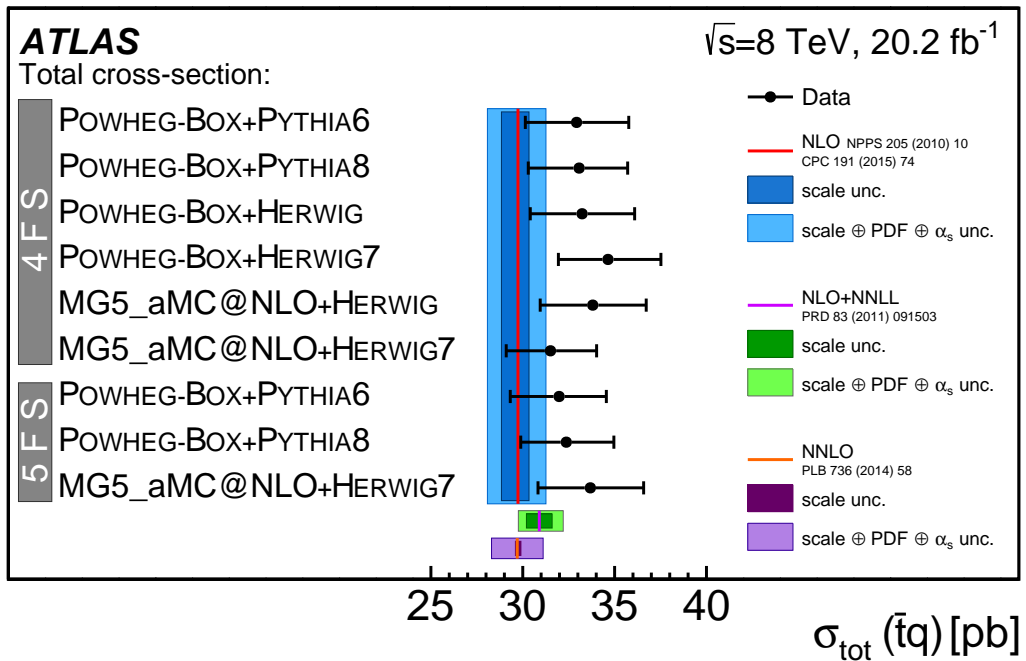
Figure 8.18.: Extrapolated t-channel single top-quark (a) and top-antiquark (b) production cross-sections for different MC-generators compared to fixed-order calculations. For the three calculations, the uncertainty on the μ_r and μ_f scales are indicated in darker shading, and the total uncertainties, including the PDF+α_s uncertainties, are indicated in lighter shading. In case of the NNLO prediction, only the μ_r and μ_f scale uncertainty is provided in Ref. [162]. For comparison, the PDF+α_s uncertainties from the NLO prediction [141] are added to the NNLO μ_r and μ_f scale uncertainty reflected in the lighter shaded uncertainty band. For this comparison, the uncertainty on the extrapolation does not include the contribution from the NLO-matching method and from the choice of the PS model.

Table 8.14.: Extrapolated total t-channel single top-quark cross-sections for different MC generators.

ME Generator	Shower MC	method	$\sigma_{\mathrm{tot}}(tq)$ [pb]	total unc. up [pb]	total unc. down [pb]
MG 5_aMC@NLO	Herwig	4FS(NLO)	57.9	+4.1	-3.7
MG 5_aMC@NLO	Herwig++	4FS(NLO)	63.0	+4.5	-4.0
MG 5_aMC@NLO	Herwig 7	4FS(NLO)	53.2	+3.0	-3.0
Powheg-Box	Pythia 6	4FS(NLO)	56.7	+4.1	-3.6
Powheg-Box	Pythia 8	4FS(NLO)	57.0	+3.3	-3.8
Powheg-Box	Herwig	4FS(NLO)	57.1	+4.1	-3.6
Powheg-Box	Herwig++	4FS(NLO)	62.5	+4.0	-3.9
Powheg-Box	Herwig 7	4FS(NLO)	59.1	+3.6	-3.4
AcerMC	Pythia 6	matched(LO)	62.4	+4.5	-4.0
MG 5_aMC@NLO	Herwig++	5FS(NLO)	60.9	+3.4	-3.4
MG 5_aMC@NLO	Herwig 7	5FS(NLO)	60.3	+3.4	-3.4
Powheg-Box	Pythia 6	5FS(NLO)	56.8	+5.0	-3.2
Powheg-Box	Pythia 8	5FS(NLO)	56.7	+4.2	-3.2

Table 8.15.: Extrapolated total *t*-channel single top-antiquark cross-sections for different MC generators.

ME Generator	Shower MC	method	$\sigma_{\text{tot}}(\bar{t}q)$ [pb]	total unc. up [pb]	total unc. down [pb]
MG 5_aMC@NLO	Herwig	4FS(NLO)	33.8	+2.9	-2.9
MG 5_aMC@NLO	Herwig++	4FS(NLO)	35.5	+3.0	-3.0
MG 5_aMC@NLO	Herwig 7	4FS(NLO)	31.5	+2.5	-2.4
Powheg-Box	Pythia 6	4FS(NLO)	32.9	+2.8	-2.8
Powheg-Box	Pythia 8	4FS(NLO)	33.1	+2.6	-2.8
Powheg-Box	Herwig	4FS(NLO)	33.2	+2.9	-2.8
Powheg-Box	Herwig++	4FS(NLO)	36.4	+3.2	-2.9
Powheg-Box	Herwig 7	4FS(NLO)	36.4	+3.2	-2.9
AcerMC	Pythia 6	matched(LO)	35.5	+3.1	-2.8
MG 5_aMC@NLO	Herwig++	5FS(NLO)	35.5	+2.8	-2.7
MG 5_aMC@NLO	Herwig 7	5FS(NLO)	33.7	+2.9	-2.9
Powheg-Box	Pythia 6	5FS(NLO)	32.0	+2.6	-2.7
Powheg-Box	Pythia 8	5FS(NLO)	32.4	+2.6	-2.5

8.4.3. Measurement of Cross-Section Ratio R_t

The cross-section ratio of the extrapolated total cross-sections $\sigma_{\text{tot}}(tq)$ and $\sigma_{\text{tot}}(\bar{t}q)$ is determined to be

$$R_t = \frac{\sigma_{\text{tot}}(tq)}{\sigma_{\text{tot}}(\bar{t}q)} = 1.72 \pm 0.05\,(\text{stat.})\ \pm 0.07\,(\text{exp.}) = 1.72 \pm 0.09. \qquad (8.8)$$

The individual uncertainties on $\sigma_{\text{tot}}(tq)$ and $\sigma_{\text{tot}}(\bar{t}q)$ are treated as correlated in the pseudo experiments, which leads to the cancellation of many uncertainties which are similar in magnitude for both signal processes. Significant contributions to the uncertainty on R_t are shown in Table 8.16, excluding those which account for less than 0.5 %. The main sources of uncertainty are the $t\bar{t}$ NLO matching and the statistical uncertainties. The large dependence on the $t\bar{t}$ modelling uncertainty, as mentioned, lies in the difference of the S/B ratios in the ℓ^+ channel and ℓ^- channel channels.

Table 8.16.: Significant contributions to the total relative uncertainty on the measured value of R_t. The evaluation of the systematic uncertainties has a statistical uncertainty of 0.3 %. Uncertainties contributing less than 0.5 % are not shown.

Source	$\Delta R_t / R_t$ [%]
Data statistics	± 3.0
Monte Carlo statistics	± 1.8
Background modelling	± 0.7
Jet reconstruction	± 0.5
$E_{\text{T}}^{\text{miss}}$ modelling	± 0.6
tq ($\bar{t}q$) NLO matching	± 0.5
tq ($\bar{t}q$) scale variations	± 0.7
$t\bar{t}$ NLO matching	± 2.3
$t\bar{t}$ PS	± 1.7
PDF	± 0.7
Total systematic	± 3.9
Total (stat. + syst.)	± 5.0

Figure 8.19 shows the measured cross-section ratio R_t compared to predictions of R_t by several PDF sets. The uncertainty on the measured value of R_t does not contain the PDF uncertainty since it is compared to other PDF set predictions. All cross-sections and the corresponding ratios are evaluated in the 5 FS and the uncertainties on renormalisation and factorisation scales as well as the intra-PDF and α_s uncertainties are considered. The agreement of the PDF set predictions to the measured R_t

is on the level on 1σ, while all predictions are higher than the measured one. The largest deviation of 2.5 σ is observed to the ABM PDF-set. The ABM PDF-set has two main differences with regard to the other PDF sets, for one the $\alpha_s(m_Z)$ is at a value of 0.109, considerably smaller than that of NNPDF 3.0 at 0.118. The second difference is the treatment of the b-quark PDF in contrast to the other compared PDF sets [33].
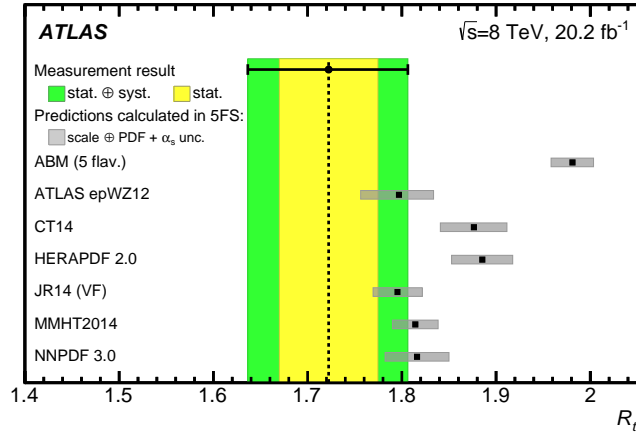
Figure 8.19.: Predicted values of $R_t = \sigma_{\text{tot}}(tq)/\sigma_{\text{tot}}(\bar{t}q)$ calculated with HATHOR [141] at NLO precision in QCD [57] in the 5 FS using different NLO PDF sets [33, 163, 31, 39, 32, 35, 37] compared to the measured value. The error bars on the predictions include the uncertainty on the renormalisation and factorisation scales and the combined internal PDF and α_s uncertainty. The dashed black line indicates the central value of the measured R_t value. The combined statistical and systematic uncertainty of the measurement is shown in green, while the statistical uncertainty is represented by the yellow error band. The uncertainty on the measured R_t value does not include the PDF components for this comparison.

8.4.4. Estimation of the Top-Quark Mass Dependence

The measurement of t-channel single top-quark cross-sections refer to a top-quark mass of $m_t = 172.5\,\text{GeV}$, whereas the uncertainty on the top-quark mass is not considered as an systematic uncertainty, but the dependence of the measurement is determined. To assess the magnitude of the cross-section dependence on the top-quark mass, the measurements are repeated with dedicated samples of MC simulated events which are produced with a modified top-quark mass. The modified values of m_t are $165, 167.5, 170, 175, 177.5$ and $180\,\text{GeV}$. As the measurement is repeated for a given value of m_t, the nominal acceptances and O_{NN} shapes of tq, $\bar{t}q$ and $t\bar{t}, Wt, t\bar{b}$ are substituted with the modified ones. The dependence of $\sigma_{\text{fid}}(tq)$, $\sigma_{\text{fid}}(\bar{t}q)$, $\sigma_{\text{tot}}(tq)$, $\sigma_{\text{tot}}(\bar{t}q)$, $\sigma_{\text{tot}}(tq + \bar{t}q)$ and R_t are evaluated. The resulting cross-section values of all quantities are separately fitted using the parametrisation:

$$\sigma(m_t) = \sigma(172.5\,\text{GeV}) + a \cdot \Delta m [\text{GeV}], \qquad (8.9)$$

where $\Delta m = m_t - 172.5\,\text{GeV}$ is with respect to the nominal top-quark mass.

Table 8.17 shows the results of the fit for the individual quantities. Figure 8.20 displays the measured cross-section as a function of Δm w.r.t. the nominal top-quark mass. A detailed study of the top-quark mass dependence was conducted in Ref. [164], using the same selection as this analysis. The study found that the sizable cross-section dependence on the top-quark mass is mainly due to the p_T requirement on the charged lepton.

Table 8.17.: Parametrisation factor for the cross sections $\sigma_{\text{fid}}(tq)$, $\sigma_{\text{fid}}(\bar{t}q)$, $\sigma_{\text{tot}}(tq)$, $\sigma_{\text{tot}}(\bar{t}q)$, $\sigma_{\text{tot}}(tq + \bar{t}q)$ and R_t.

Measurement	$a \left[\frac{\text{pb}}{\text{GeV}}\right]$
$\sigma_{\text{fid}}(tq)$	-0.06 ± 0.01
$\sigma_{\text{fid}}(\bar{t}q)$	-0.04 ± 0.01
$\sigma_{\text{tot}}(tq)$	-0.59 ± 0.08
$\sigma_{\text{tot}}(\bar{t}q)$	-0.37 ± 0.06
$\sigma_{\text{tot}}(tq + \bar{t}q)$	-0.96 ± 0.13
R_t	$+0.001 \pm 0.002$
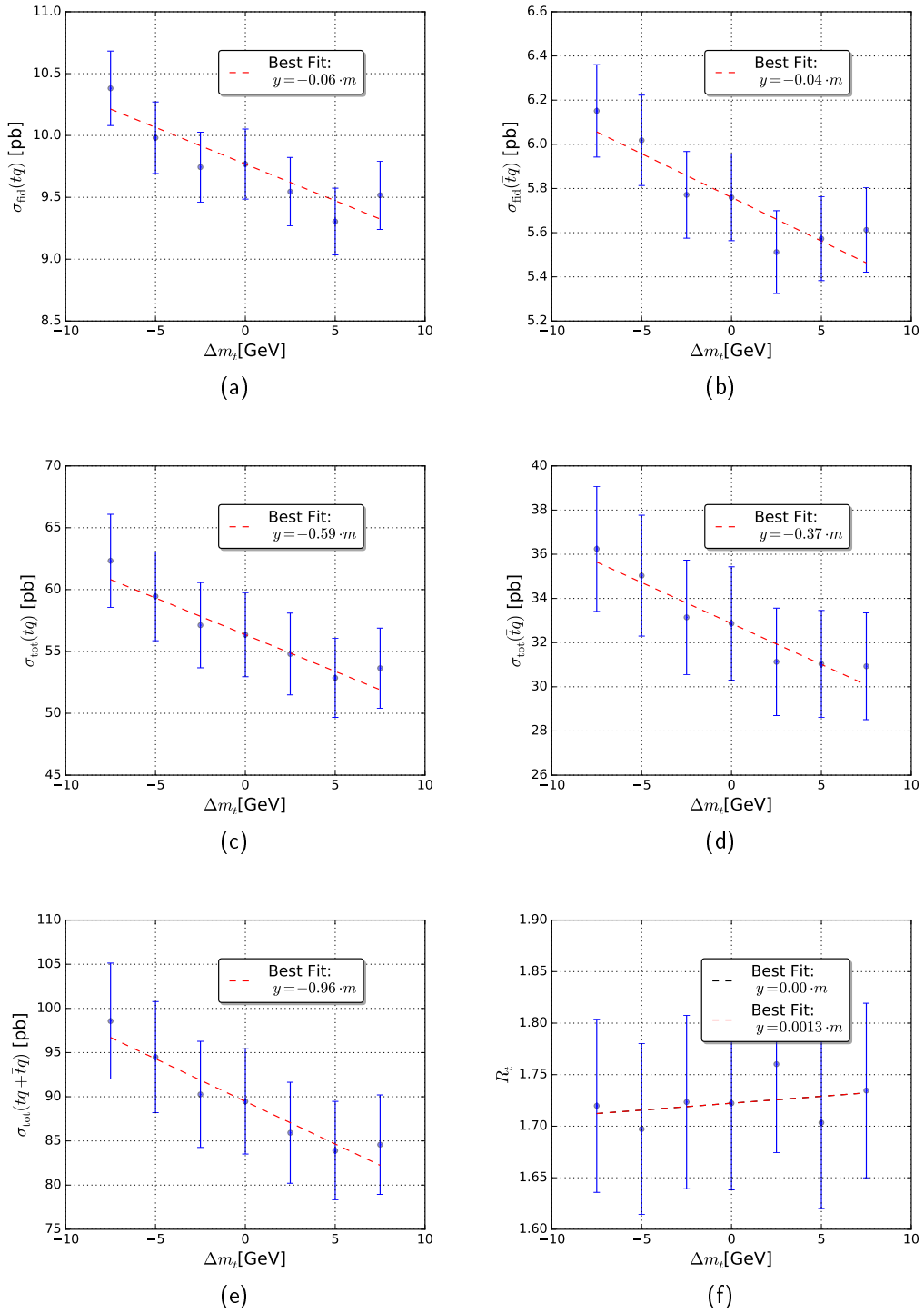
Figure 8.20.: Single top-quark t-channel cross-section dependence of the top-quark mass.

8.4.5. $|V_{tb}|$ Extraction

The CKM matrix-element, $|V_{tb}|$, can be determined from the measured total cross-section of t-channel single top-quark production due to the fact that the production proceeds via the Wtb vertex and the production cross-section is proportional to $f_{\mathrm{LV}}^2 \cdot |V_{tb}|^2$.

The value of $|V_{tb}|$ indirectly predicted by the SM is approximately one and the value of the left-handed form factor f_{LV} is predicted to be exactly one. The form factor is used to parametrise new-physics contributions to the Wtb vertex.

Two assumptions that are required to perform the extraction of $f_{\mathrm{LV}} \cdot |V_{tb}|$. The first assumption is that $|V_{tb}| \gg |V_{td}|, |V_{ts}|$ and the second is that the Wtb interaction is an SM-like left-handed weak coupling.

In order to determine $f_{\mathrm{LV}} \cdot |V_{tb}|$, the relation

$$f_{\mathrm{LV}} \cdot |V_{tb}| = \sqrt{\frac{\sigma_{\mathrm{tot}}^{\mathrm{meas}}(tq + \bar{t}q)}{\sigma_{\mathrm{tot}}^{\mathrm{NLO}}(tq + \bar{t}q)}} \tag{8.10}$$

is calculated using the total combined cross-section defined as the sum of the individual measured cross-sections $\sigma_{\mathrm{tot}}(tq + \bar{t}q) = \sigma_{\mathrm{tot}}(tq) + \sigma_{\mathrm{tot}}(\bar{t}q)$. The total combined cross-section yields:

$$
\begin{aligned}
\sigma_{\mathrm{tot}}(tq + \bar{t}q) &= 89.6 \pm 1.2\,(\text{stat.}) \pm 5.1\,(\text{exp.})\,{}^{+4.1}_{-2.5}\,(\text{scale}) \pm 0.7\,(\text{PDF}) \\
&\quad {}^{+1.7}_{-1.6}\,(\text{NLO-matching method}) \pm 1.6\,(\text{PS}) \\
&\quad \pm 1.7\,(\text{lumi.})\,\mathrm{pb} \\
&= 89.6^{+7.1}_{-6.3}\,\mathrm{pb}
\end{aligned} \tag{8.11}
$$

The individual systematic uncertainties are assumed to be 100 % correlated between $\sigma_{\mathrm{tot}}(tq)$ and $\sigma_{\mathrm{tot}}(\bar{t}q)$, except for the MC statistical uncertainty. Thus the linear addition of all uncertainty components individually yields the uncertainty on the total combined cross-section. The statistical uncertainties on data and MC samples are added in quadrature, as they are independent. The systematic uncertainty on the fiducial cross-section measurement denoted (exp.) is reduced by the magnitude of the scale, PDF, NLO-matching method and PS components, for they are given separately.

In addition to the cross-section uncertainty, the top-quark mass uncertainty, which was determined in Section 8.4.4, and the theoretical uncertainty are added in quadrature. The considered m_t uncertainty corresponds to a $\Delta m_t = \pm 1\,\mathrm{GeV}$. The determination of $f_{\mathrm{LV}} \cdot |V_{tb}|$ yields:

$$f_{\text{LV}} \cdot |V_{tb}| = 1.029 \pm 0.007 \, (\text{stat.}) \pm 0.029 \, (\text{exp.}) \, {}^{+0.023}_{-0.014} \, (\text{scale}) \pm 0.004 \, (\text{PDF})$$
$$\pm 0.010 \, (\text{NLO-matching method}) \pm 0.009 \, (\text{PS}) \pm 0.010 \, (\text{lumi.}) \quad (8.12)$$
$$\pm 0.005 \, (m_t) \pm 0.024 \, (\text{theor.})$$
$$= 1.029 \pm 0.048 \,.$$

The uncertainty components correspond to the ones provided for the total combined cross-section as well as the m_t and theoretical uncertainty on the cross-section calculation. The resulting value for $f_{\text{LV}} \cdot |V_{tb}|$ is in full agreement with the SM prediction. If the range of $|V_{tb}|$ is restricted to the interval $[0, 1]$ and assuming $f_{\text{LV}} = 1$, according to the SM a lower limit on $|V_{tb}|$ is obtained: $|V_{tb}| > 0.92$ at 95 % confidence level.

Figure 8.21 indicates the posterior probability density function of $|V_{tb}|^2$. The blue area corresponds to the 95 % confidence level.
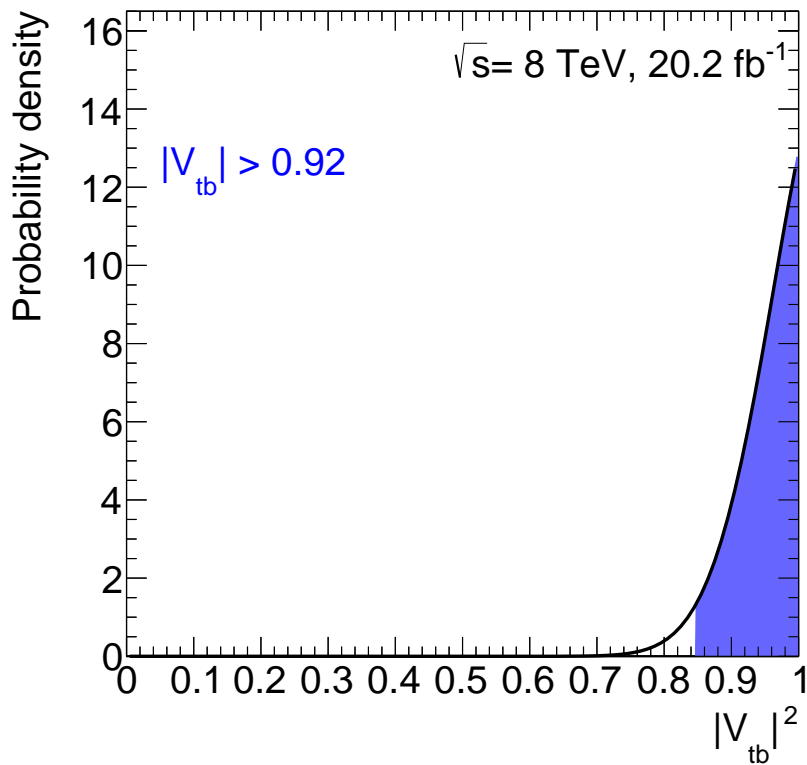
Figure 8.21.: Probability density function of the squared CKM matrix-element $|V_{tb}|$, assuming $|V_{tb}| < 1$. A lower limit on the value of $|V_{tb}|^2$ is extracted at 95 % confidence level (blue area) to be $|V_{tb}|^2 > 0.85$, which corresponds to a lower limit of $|V_{tb}| > 0.92$.

Conclusions

The measurement of the total and fiducial t-channel single top-quark cross-sections was performed in the presented analysis using pp-collision data collected by the ATLAS experiment at $\sqrt{s} = 8\,\text{TeV}$ at the LHC. The analysed data set corresponds to an integrated luminosity of $20.2\,\text{fb}^{-1}$. The t-channel single top-quark production is characterised by two jets and an isolated lepton in the detector. One of the jets is a b-jet, which originates from the decay of the top quark. The b-jet can be identified in the detector by b-tagging algorithms. The additional jet stems from an initial quark, which is typically scattered in the forward region of the detector. The isolated lepton in the final state originates from the leptonic decay of the W boson, which itself stems from the top-quark decay. The lepton can be either an electron or a muon, while decay modes via the tau-lepton, e.g. $W \rightarrow \tau \rightarrow e^- + \bar{\nu}_e + \nu_\tau$ are also considered. While the W boson can also decay via hadronic decay modes, in this analysis these decay modes are not considered. The signal region is separated into positively charged leptons and negatively charged leptons depending on the charge of the selected lepton, in order to determine the t-channel single top-quark production for top quarks and top antiquarks separately.

A neural network is employed to improve the sensitivity to the signal process and mitigate systematic uncertainties on the template shape compared to the use of a single kinematic variable. A study on the required complexity of the neural network in terms of number of input observables was performed and yielded seven highly sensitive input observables which are combined to the neural network discriminant.

The cross-section measurement is performed with a binned maximum-likelihood fit in the ℓ^+ channel and the ℓ^- channel simultaneously. The fit uses Gaussian constraints on
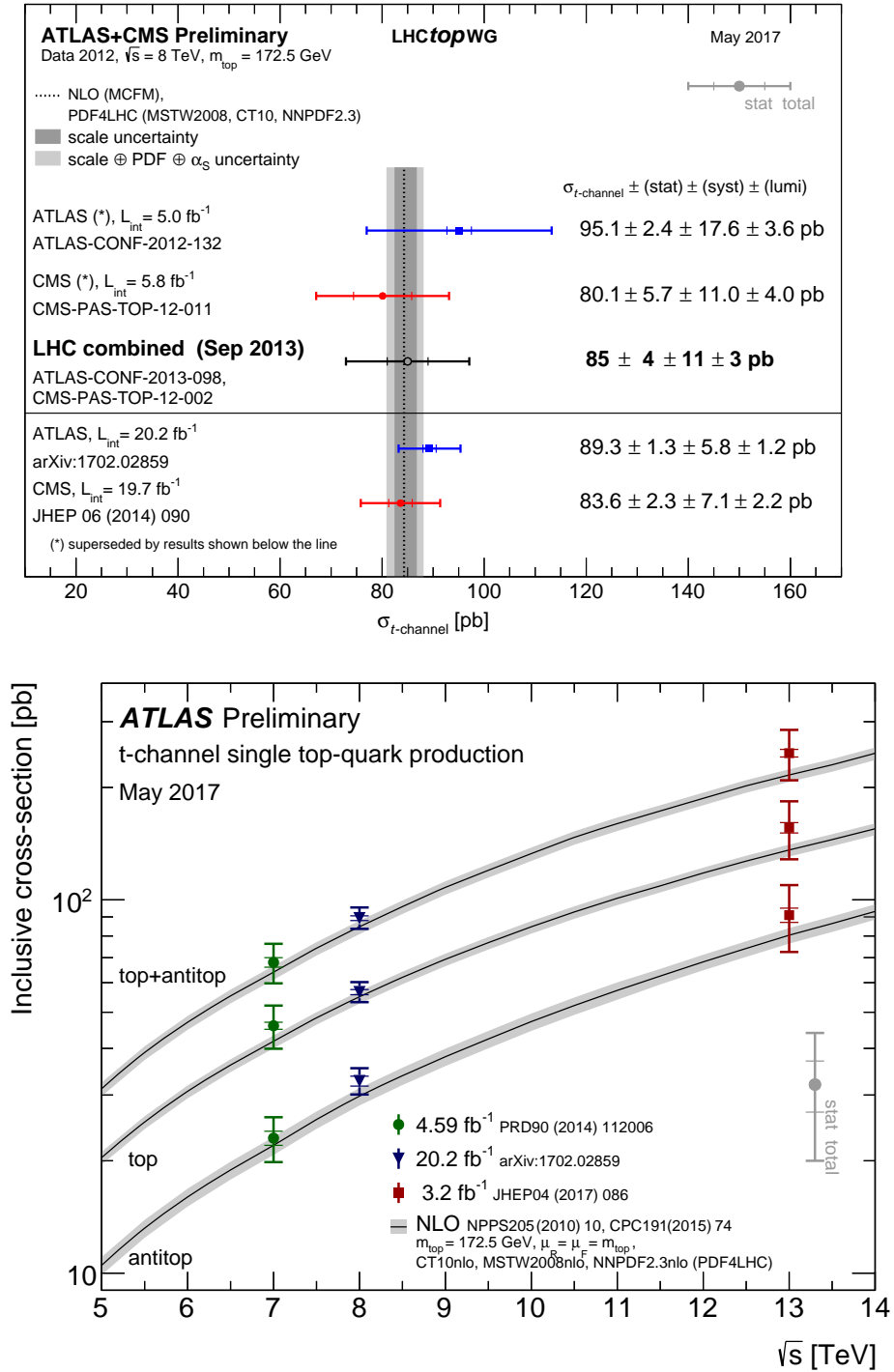
Figure 9.1.: Summary of the t-channel single top-quark measurements performed at $\sqrt{s} = 8\,\text{TeV}$ with the ATLAS and CMS experiments in (a) and ATLAS measurements for 7, 8 and 13 TeV center-of-mass energies [165] in (b).

the expected normalisation of the background processes. The systematic uncertainties are derived from an ensemble of pseudo experiments which probe the possible configurations of the uncertainty space. The systematic uncertainties that are considered include the prescriptions of the ATLAS collaboration and the TopLHC-working-group. In total, 76 sources of systematic uncertainties are considered and their impact on the measurement is evaluated. A criterion on the significance of shape template uncertainties has been developed to reduce the statistical fluctuations in the uncertainty determination.

The fiducial cross-sections are measured to be

$$\sigma_{\text{fid}}(tq) = 9.78 \pm 0.57 \text{ pb}$$
$$\sigma_{\text{fid}}(\bar{t}q) = 5.77 \pm 0.45 \text{ pb,} \tag{9.1}$$

which is in agreement with several MC event-generator predictions. The relative combined uncertainties are $\pm 5.8\,\%$ for $\sigma_{\text{fid}}(tq)$ and $\pm 7.8\,\%$ for $\sigma_{\text{fid}}(\bar{t}q)$. The systematic uncertainties on the fiducial cross-sections are dominated by the JES as well as signal- and background modelling. The importance of the JES arises from the characteristic forward jet of t-channel single top-quark events, which rely on a forward-jet JES calibration. The calibration method involves a jet-balancing method which is sensitive to modelling differences of MC event generators. The signal modelling uncertainties include the parton-shower MC, NLO-matching method and scale uncertainties.

The total cross-sections, $\sigma_{\text{tot}}(tq)$ and $\sigma_{\text{tot}}(\bar{t}q)$ are extrapolated to the full phase space using the result on the fiducial cross-sections, and the fiducial acceptance of the POWHEG-BOX + PYTHIA 6 MC generator.

$$\sigma_{\text{tot}}(tq) = 56.7^{+4.3}_{-3.8} \text{ pb}$$
$$\sigma_{\text{tot}}(\bar{t}q) = 32.9^{+3.0}_{-2.7} \text{ pb}$$
$$\sigma_{\text{tot}}(tq + \bar{t}q) = 89.6^{+7.1}_{-6.3} \text{ pb} \,.$$

Both total cross-sections are consistent with three fixed-order perturbative QCD calculations, and have relative uncertainties of $^{+7.6}_{-6.7}\,\%$ for $\sigma_{\text{tot}}(tq)$ and $^{+9.1}_{-8.2}\,\%$ for $\sigma_{\text{tot}}(\bar{t}q)$. These uncertainties are an improvement of about $50\,\%$ compared to the uncertainty on previous ATLAS analyses. The uncertainties on the total cross-sections are dominated by the signal scale-choice, which enters in the cross-section extrapolation. The extrapolation of the total cross-sections was performed for several MC generators, which yield excellent agreement with the nominal POWHEG-BOX + PYTHIA 6 MC generator.

The measured total cross-section is compared to other measurements performed us-

ing collision data at $\sqrt{s} = 8\,\text{TeV}$ in Figure 9.1(a) at ATLAS and CMS. Figure 9.1(b) shows only ATLAS measurements but includes the measurements performed at center-of-mass energies of 7 TeV and 13 TeV. All measurements are compared to a SM prediction calculated at NLO perturbative QCD. Both figures show the excellent agreement of the measurement results with the SM predictions and highlight the achieved precision of this analysis, which exceeds all other previous measurements, either ATLAS or CMS.

The ratio of the measured total cross-sections of the t-channel single top-quark and top-antiquark yields

$$R_t = 1.72 \pm 0.09\,.$$

The uncertainty consideration includes the correlation of $\sigma_{\text{tot}}(tq)$ and $\sigma_{\text{tot}}(\bar{t}q)$. The dominating uncertainties are the $t\bar{t}$ modelling and the statistical uncertainties. The R_t measurement has a precision of 5.0 %, which is the best result achieved so far.

The measured cross-section ratio R_t is compared to two R_t measurements at 7 TeV and 13 TeV, in Figure 9.2, which exhibit good agreement to predictions obtained with several PDF sets. The presented result of R_t exceeds the previous measurements in terms of precision and shows a slight tendency to a lower value than predicted. While the main PDF sets agree with the measured value of R_t within 1 σ, the comparison to the ABM PDF-set exhibits a 2 σ disagreement. Different assumptions used in the ABM PDF-set, e.g. the low value of $\alpha_s(m_Z)$ and treatment of b-quark PDF, can account for the observed deviation, but no definitive conclusion can be drawn.

Using the measurement of $\sigma_{\text{tot}}(tq + \bar{t}q)$, the CKM matrix-element $|V_{tb}|$ is calculated using $f_{\text{LV}} \cdot |V_{tb}| = \sqrt{\frac{\sigma_{\text{meas}}}{\sigma_{\text{NLO}}}}$. The resulting value of

$$f_{\text{LV}} \cdot |V_{tb}| = 1.029 \pm 0.048$$

is in full agreement with the SM prediction. If the range of $|V_{tb}|$ is constrained to the interval $[0, 1]$ and $f_{\text{LV}} = 1$ is assumed, a lower limit on $|V_{tb}|$ is obtained: $|V_{tb}| > 0.92$ at 95 % confidence level.

In Figure 9 the comparison of measurements of $|V_{tb}|$ are shown. All obtained values of $|V_{tb}|$ are in agreement with the SM and the most precise determination of a single analysis is achieved with this result, while it is slightly exceeded by the 7 + 8 TeV combination performed by CMS [166].

In future measurements, the limitation of the sensitivity is driven by the systematic uncertainties on the t-channel single top-quark process. In particular the signal modelling by MC event generators is most important. An improved understanding of the effects of hadronisation, shower and NLO-matching effects can significantly improve the precision. As the cross-section measurement using data at 13 TeV center-of-mass energy, has been performed recently, the signal modelling uncertainties are already limiting the sensitivity. A more aggressive strategy towards the constraining of the signal modelling
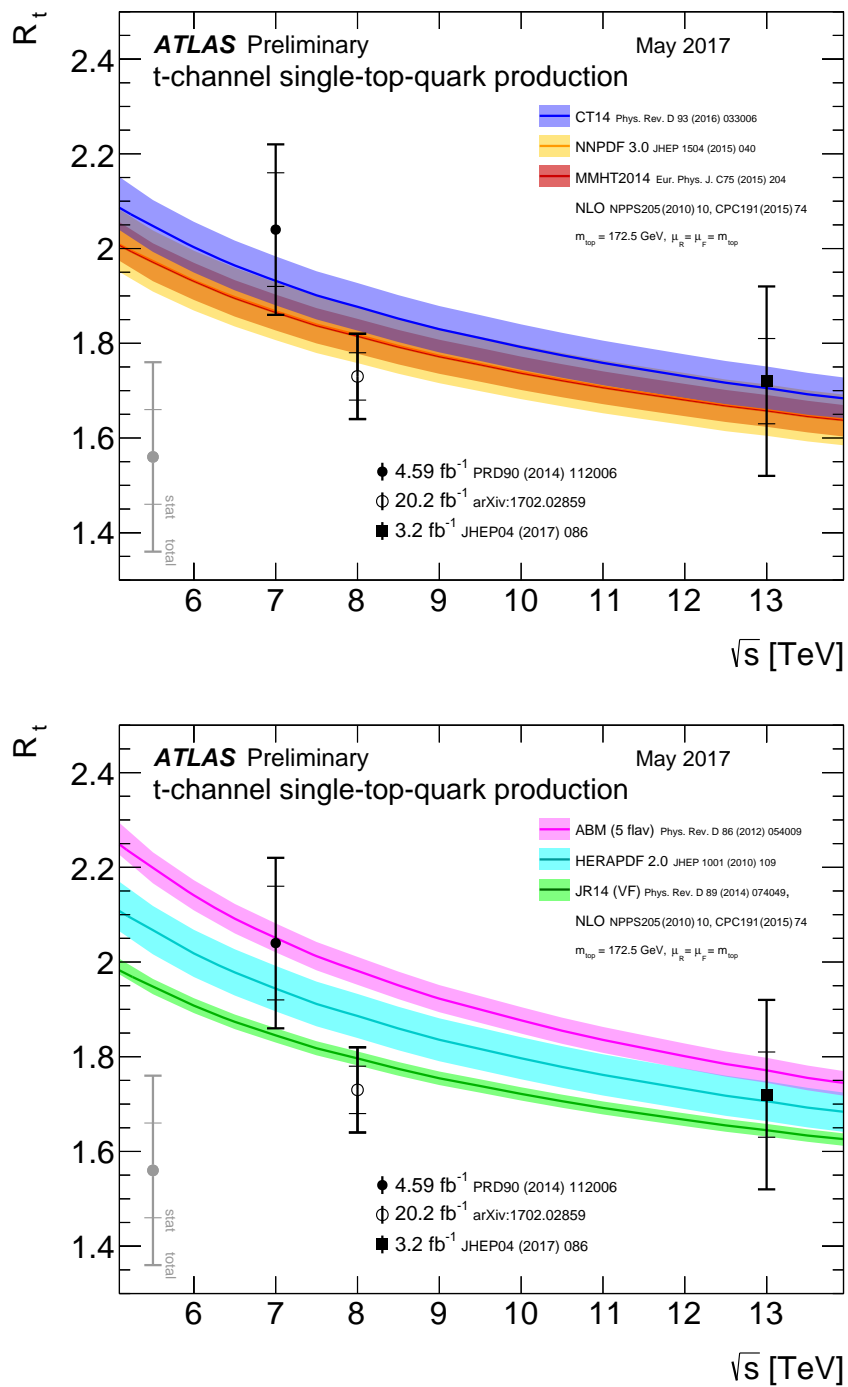
Figure 9.2.: The measured cross-section ratios at 7 and 13 TeV [165] are compared to this result. In (a) the measurements are compared to the main PDF-sets and to additional PDF sets in (b).

and JES uncertainties in additional selection regions can be adopted, which was not pursued in this thesis. The strategy of optimising the number of input observables for the NN training could be improved to account for individual observables which are highly dependent on distinct systematic uncertainties.
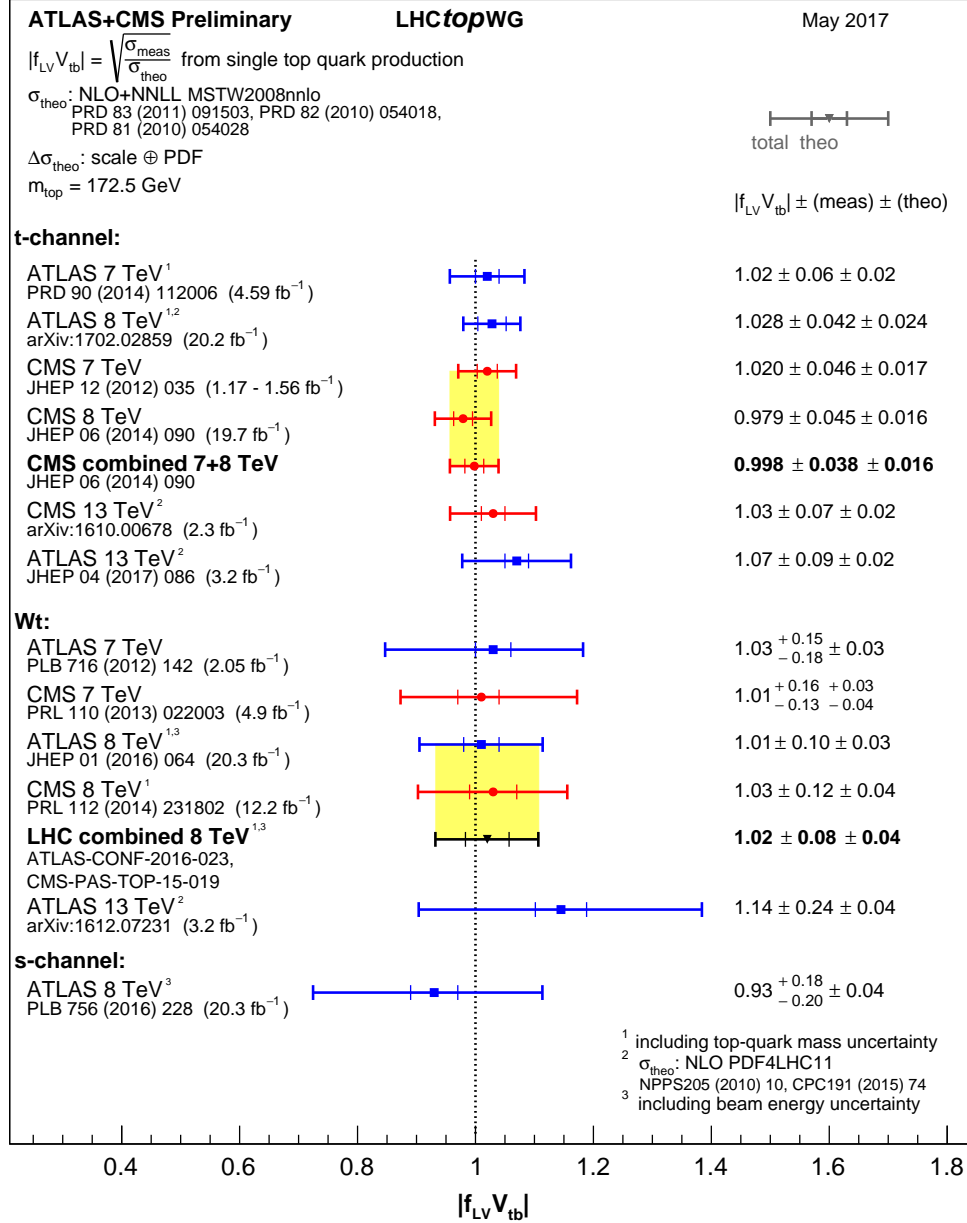
Figure 9.3.: Summary of measurements of the CKM matrix-element $f_{LV} \cdot |V_{tb}|$ performed by ATLAS and CMS for all three single top-quark production modes and for 7,8 and 13 TeV center-of-mass energies [165].

Bibliography

[1] Lyndon Evans and Philip Bryant. 'LHC Machine'. In: *Journal of Instrumentation* 3.08 (2008), S08001. URL: http://stacks.iop.org/1748-0221/3/i=08/a=S08001 (cit. on pp. I, 22).

[2] ATLAS Collaboration. 'The ATLAS Experiment at the CERN Large Hadron Collider'. In: *JINST* 3 (2008), S08003. DOI: 10.1088/1748-0221/3/08/S08003 (cit. on pp. I, 24, 29).

[3] F. Abe et al. 'Observation of top quark production in $\bar{p}p$ collisions'. In: *Phys. Rev. Lett.* 74 (1995), pp. 2626–2631. DOI: 10.1103/PhysRevLett.74.2626. arXiv: hep-ex/9503002 [hep-ex] (cit. on p. I).

[4] S. Abachi et al. 'Observation of the Top Quark'. In: *Phys. Rev. Lett.* 74 (14 Apr. 1995), pp. 2632–2637. DOI: 10.1103/PhysRevLett.74.2632. URL: http://link.aps.org/doi/10.1103/PhysRevLett.74.2632 (cit. on p. I).

[5] *First combination of Tevatron and LHC measurements of the top-quark mass*. Tech. rep. arXiv:1403.4427. ATLAS-CONF-2014-008. CDF-NOTE-11071. CMS-PAS-TOP-13-014. D0-NOTE-6416. Comments: 34 pages, 7 figures. Geneva: CERN, Mar. 2014. URL: https://cds.cern.ch/record/1669819 (cit. on p. I).

[6] Georges Aad et al. 'Measurement of the t-channel single top-quark production cross section in pp collisions at $\sqrt{s} = 7$ TeV with the ATLAS detector'. In: *Phys. Lett.* B717 (2012), pp. 330–350. DOI: 10.1016/j.physletb.2012.09.031. arXiv: 1205.3130 [hep-ex] (cit. on pp. II, 69).

[7] Georges Aad et al. 'Comprehensive measurements of t-channel single top-quark production cross sections at $\sqrt{s} = 7$ TeV with the ATLAS detector'. In: *Phys. Rev.* D90.11 (2014), p. 112006. DOI: 10.1103/PhysRevD.90.112006. arXiv: 1406.7844 [hep-ex] (cit. on pp. II, III, 69).

[8] ATLAS Collaboration. *Measurement of the Inclusive and Fiducial Cross-Section of Single Top-Quark t-Channel Events in pp Collisions at $\sqrt{s} = 8$ TeV*. ATLAS-CONF-2014-007. 2014. URL: http://cdsweb.cern.ch/record/1668960 (cit. on pp. II, III, 39).

[9]   Morad Aaboud et al. 'Fiducial, total and differential cross-section measurements of t-channel single top-quark production in pp collisions at 8 TeV using data collected by the ATLAS detector'. In: *Eur. Phys. J.* C77.8 (2017), p. 531. DOI: 10.1140/epjc/s10052-017-5061-9. arXiv: 1702.02859 [hep-ex] (cit. on p. II).

[10]   ATLAS Collaboration. *Measurement of t-Channel Single Top-Quark Production in pp Collisions at $\sqrt{s}$ = 8 TeV with the ATLAS detector.* ATLAS-CONF-2012-132. 2012. URL: http://cdsweb.cern.ch/record/1478371 (cit. on p. III).

[11]   David J Griffiths. *Introduction to elementary particles; 2nd rev. version.* Physics textbook. New York, NY: Wiley, 2008. URL: https://cds.cern.ch/record/111880 (cit. on p. 1).

[12]   The Free Encyclopedia website Wikipedia. June 2007. URL: https://upload.wikimedia.org/wikipedia/commons/0/00/Standard_Model_of_Elementary_Particles.svg#/media/File:Standard_Model_of_Elementary_Particles.svg (cit. on p. 2).

[13]   C. Patrignani et al. 'Review of Particle Physics'. In: *Chin. Phys.* C40.10 (2016), p. 100001. DOI: 10.1088/1674-1137/40/10/100001 (cit. on p. 2).

[14]   J. Beringer et al. 'Review of Particle Physics*'. In: *Phys. Rev. D* 86 (1 July 2012), p. 010001. DOI: 10.1103/PhysRevD.86.010001. URL: http://link.aps.org/doi/10.1103/PhysRevD.86.010001 (cit. on pp. 4, 6).

[15]   M. Gell-Mann. 'A schematic model of baryons and mesons'. In: *Physics Letters* 8.3 (1964), pp. 214–215. ISSN: 0031-9163. DOI: http://dx.doi.org/10.1016/S0031-9163(64)92001-3. URL: http://www.sciencedirect.com/science/article/pii/S0031916364920013 (cit. on p. 5).

[16]   G Zweig. 'An SU_3 model for strong interaction symmetry and its breaking; Version 2'. In: CERN-TH-412 (Feb. 1964). Version 1 is CERN preprint 8182/TH.401, Jan. 17, 1964, 80 p. URL: http://cds.cern.ch/record/570209 (cit. on p. 5).

[17]   R. Aaij et al. 'Observation of $J/\psi p$ Resonances Consistent with Pentaquark States in $\Lambda_b^0 \to J/\psi K^- p$ Decays'. In: *Phys. Rev. Lett.* 115 (7 Aug. 2015), p. 072001. DOI: 10.1103/PhysRevLett.115.072001. URL: http://link.aps.org/doi/10.1103/PhysRevLett.115.072001 (cit. on pp. 5, 21).

[18]   Dr. Eric Drexler website. Apr. 2014. URL: https://commons.wikimedia.org/wiki/File:Elementary_particle_interactions_in_the_Standard_Model.png#/media/File:Elementary_particle_interactions_in_the_Standard_Model.png (cit. on p. 5).

[19]   Sheldon L. Glashow. 'Partial-symmetries of weak interactions'. In: *Nuclear Physics* 22.4 (1961), pp. 579–588. ISSN: 0029-5582. DOI: http://dx.doi.org/10.1016/0029-5582(61)90469-2. URL: http://www.sciencedirect.com/science/article/pii/0029558261904692 (cit. on p. 5).

[20]   P.W. Higgs. 'Broken symmetries, massless particles and gauge fields'. In: *Physics Letters* 12.2 (1964), pp. 132–133. ISSN: 0031-9163. DOI: http://dx.doi.org/10.1016/0031-9163(64)91136-9. URL: http://www.sciencedirect.com/science/article/pii/0031916364911369 (cit. on p. 6).

[21]   Peter W. Higgs. 'Broken Symmetries and the Masses of Gauge Bosons'. In: *Phys. Rev. Lett.* 13 (16 Oct. 1964), pp. 508–509. DOI: 10.1103/PhysRevLett.13.508. URL: http://link.aps.org/doi/10.1103/PhysRevLett.13.508 (cit. on p. 6).

[22]   F. Englert and R. Brout. 'Broken Symmetry and the Mass of Gauge Vector Mesons'. In: *Phys. Rev. Lett.* 13 (9 Aug. 1964), pp. 321–323. DOI: 10.1103/PhysRevLett.13.321. URL: http://link.aps.org/doi/10.1103/PhysRevLett.13.321 (cit. on p. 6).

[23]   Georges Aad et al. 'Observation of a new particle in the search for the Standard Model Higgs boson with the ATLAS detector at the LHC'. In: *Phys. Lett.* B716 (2012), pp. 1–29. DOI: 10.1016/j.physletb.2012.08.020. arXiv: 1207.7214 [hep-ex] (cit. on p. 6).

[24]   Serguei Chatrchyan et al. 'Observation of a new boson at a mass of 125 GeV with the CMS experiment at the LHC'. In: *Phys. Lett.* B716 (2012), pp. 30–61. DOI: 10.1016/j.physletb.2012.08.021. arXiv: 1207.7235 [hep-ex] (cit. on p. 6).

[25]   Michael E Peskin and Daniel V Schroeder. *An Introduction to Quantum Field Theory; 1995 ed.* Includes exercises. Boulder, CO: Westview, 1995. URL: https://cds.cern.ch/record/257493 (cit. on p. 6).

[26]   Makoto Kobayashi and Toshihide Maskawa. 'CP-Violation in the Renormalizable Theory of Weak Interaction'. In: *Progress of Theoretical Physics* 49.2 (1973), pp. 652–657. DOI: 10.1143/PTP.49.652. eprint: http://ptp.oxfordjournals.org/content/49/2/652.full.pdf+html. URL: http://ptp.oxfordjournals.org/content/49/2/652.abstract (cit. on p. 6).

[27]   K. A. Olive et al. 'Review of Particle Physics'. In: *Chin. Phys.* C38 (2014), p. 090001. DOI: 10.1088/1674-1137/38/9/090001 (cit. on pp. 7, 13, 54).

[28]   V.N. Gribov and L.N. Lipatov. 'Deep inelastic electron scattering in perturbation theory'. In: *Physics Letters B* 37.1 (1971), pp. 78–80. ISSN: 0370-2693. DOI: http://dx.doi.org/10.1016/0370-2693(71)90576-4. URL: http://www.sciencedirect.com/science/article/pii/0370269371905764 (cit. on p. 7).

[29]   G. Altarelli and G. Parisi. 'Asymptotic freedom in parton language'. In: *Nuclear Physics B* 126.2 (1977), pp. 298–318. ISSN: 0550-3213. DOI: http://dx.doi.org/10.1016/0550-3213(77)90384-4. URL: http://www.sciencedirect.com/science/article/pii/0550321377903844 (cit. on p. 7).

[30]   Hung-Liang Lai et al. 'New parton distributions for collider physics'. In: *Phys. Rev. D* 82 (2010), p. 074024. DOI: 10.1103/PhysRevD.82.074024. arXiv: 1007.2241 [hep-ph] (cit. on pp. 8, 37).

[31]   Sayipjamal Dulat et al. 'New parton distribution functions from a global analysis of quantum chromodynamics'. In: *Phys. Rev. D* 93.3 (2016), p. 033006. DOI: 10.1103/PhysRevD.93.033006. arXiv: 1506.07443 [hep-ph] (cit. on pp. 8, 174).

[32]   Pedro Jimenez-Delgado and Ewald Reya. 'Delineating parton distributions and the strong coupling'. In: *Phys. Rev. D* 89.7 (2014), p. 074049. DOI: 10.1103/PhysRevD.89.074049. arXiv: 1403.1852 [hep-ph] (cit. on pp. 8, 174).

[33]   S. Alekhin, J. Blumlein and S. Moch. 'Parton Distribution Functions and Benchmark Cross Sections at NNLO'. In: *Phys. Rev. D* 86 (2012), p. 054009. DOI: 10.1103/PhysRevD.86.054009. arXiv: 1202.2281 [hep-ph] (cit. on pp. 8, 174).

[34]   A. D. Martin et al. 'Parton distributions for the LHC'. In: *Eur. Phys. J. C* 63 (2009), pp. 189–285. DOI: 10.1140/epjc/s10052-009-1072-5. arXiv: 0901.0002 [hep-ph] (cit. on p. 8).

[35]   L.A. Harland-Lang et al. 'Parton distributions in the LHC era: MMHT 2014 PDFs'. In: *Eur. Phys. J. C* 75.5 (2015), p. 204. DOI: 10.1140/epjc/s10052-015-3397-6. arXiv: 1412.3989 [hep-ph] (cit. on pp. 8, 174).

[36]   Richard D. Ball et al. 'Impact of Heavy Quark Masses on Parton Distributions and LHC Phenomenology'. In: *Nucl. Phys. B* 849 (2011), pp. 296–363. DOI: 10.1016/j.nuclphysb.2011.03.021. arXiv: 1101.1300 (cit. on p. 8).

[37]   Richard D. Ball et al. 'Parton distributions for the LHC Run II'. In: *JHEP* 04 (2015), p. 040. DOI: 10.1007/JHEP04(2015)040. arXiv: 1410.8849 [hep-ph] (cit. on pp. 8, 174).

[38]   H1 and ZEUS Collaborations, F. Aaron et al. 'Combined Measurement and QCD Analysis of the Inclusive $e^{\pm}p$ Scattering Cross Sections at HERA'. In: *JHEP* 1001 (2010), p. 109. DOI: 10.1007/JHEP01(2010)109 (cit. on p. 8).

[39]   H. Abramowicz et al. 'Combination of measurements of inclusive deep inelastic $e^{\pm}p$ scattering cross sections and QCD analysis of HERA data'. In: *Eur. Phys. J. C* 75.12 (2015), p. 580. DOI: 10.1140/epjc/s10052-015-3710-4. arXiv: 1506.06042 [hep-ex] (cit. on pp. 8, 174).

[40]   John C. Collins, Davison E. Soper and George F. Sterman. 'Factorization of Hard Processes in QCD'. In: *Adv. Ser. Direct. High Energy Phys.* 5 (1989), pp. 1–91. DOI: 10.1142/9789814503266_0001. arXiv: hep-ph/0409313 [hep-ph] (cit. on pp. 11, 34).

[41] David J. Gross and Frank Wilczek. 'Asymptotically Free Gauge Theories. I'. In: *Phys. Rev. D* 8 (10 Nov. 1973), pp. 3633–3652. DOI: 10.1103/PhysRevD.8.3633. URL: http://link.aps.org/doi/10.1103/PhysRevD.8.3633 (cit. on p. 11).

[42] Andy Buckley et al. 'General-purpose event generators for LHC physics'. In: *Phys. Rept.* 504 (2011), pp. 145–233. DOI: 10.1016/j.physrep.2011.03.005. arXiv: 1101.2599 [hep-ph] (cit. on pp. 11, 34, 35).

[43] Michal Czakon, Paul Fiedler and Alexander Mitov. 'Total Top-Quark Pair-Production Cross Section at Hadron Colliders Through $O(\alpha_S^4)$'. In: *Phys. Rev. Lett.* 110 (2013), p. 252004. DOI: 10.1103/PhysRevLett.110.252004. arXiv: 1303.6254 [hep-ph] (cit. on p. 11).

[44] Matteo Cacciari et al. 'Top-pair production at hadron colliders with next-to-next-to-leading logarithmic soft-gluon resummation'. In: *Phys. Lett.* B710 (2012), pp. 612–622. DOI: 10.1016/j.physletb.2012.03.013. arXiv: 1111.5869 [hep-ph] (cit. on p. 11).

[45] Roberto Bonciani et al. 'NLL resummation of the heavy quark hadroproduction cross-section'. In: *Nucl. Phys.* B529 (1998). [Erratum: Nucl. Phys.B803,234(2008)], pp. 424–450. DOI: 10.1016/j.nuclphysb.2008.06.006,10.1016/S0550-3213(98)00335-6. arXiv: hep-ph/9801375 [hep-ph] (cit. on p. 11).

[46] Wolfgang Wagner. 'Top quark physics in hadron collisions'. In: *Rept. Prog. Phys.* 68 (2005), pp. 2409–2494. DOI: 10.1088/0034-4885/68/10/R03. arXiv: hep-ph/0507207 [hep-ph] (cit. on p. 13).

[47] Ikaros I. Y. Bigi et al. 'Production and Decay Properties of Ultraheavy Quarks'. In: *Phys. Lett.* B181 (1986), pp. 157–163. DOI: 10.1016/0370-2693(86)91275-X (cit. on p. 13).

[48] Michal Czakon and Alexander Mitov. 'Top++: A Program for the Calculation of the Top-Pair Cross-Section at Hadron Colliders'. In: *Comput. Phys. Commun.* 185 (2014), p. 2930. DOI: 10.1016/j.cpc.2014.06.021. arXiv: 1112.5675 [hep-ph] (cit. on p. 13).

[49] T. Aaltonen et al. 'Observation of Electroweak Single Top-Quark Production'. In: *Phys. Rev. Lett.* 103 (9 Aug. 2009), p. 092002. DOI: 10.1103/PhysRevLett.103.092002. URL: http://link.aps.org/doi/10.1103/PhysRevLett.103.092002 (cit. on p. 15).

[50] V. M. Abazov et al. 'Observation of Single Top Quark Production'. In: *Phys. Rev. Lett.* 103 (2009), p. 092001. DOI: 10.1103/PhysRevLett.103.092001. arXiv: 0903.0850 [hep-ex] (cit. on p. 15).

[51]   ATLAS Collaboration. 'Measurement of the t-channel single top-quark produc-
       tion cross section in pp collisions at $\sqrt{s}$ = 7 TeV with the ATLAS detector'. In:
       Phys. Lett. B 717 (2012), p. 330. DOI: 10.1016/j.physletb.2012.09.031.
       arXiv: 1205.3130 [hep-ex] (cit. on p. 15).

[52]   ATLAS Collaboration. 'Comprehensive measurements of t-channel single top-
       quark production cross sections at $\sqrt{s}$ = 7 TeV with the ATLAS detector'. In:
       Phys. Rev. D 90 (2014), p. 112006. DOI: 10.1103/PhysRevD.90.112006. arXiv:
       1406.7844 [hep-ex] (cit. on p. 15).

[53]   CMS Collaboration. 'Measurement of the single-top-quark t-channel cross sec-
       tion in pp collisions at $\sqrt{s}$ = 7 TeV'. In: *JHEP* 1212 (2012), p. 035. DOI: 10.
       1007/JHEP12(2012)035. arXiv: 1209.4533 [hep-ex] (cit. on p. 15).

[54]   CMS Collaboration. 'Measurement of the t-channel single-top-quark produc-
       tion cross section and of the $|V_{tb}|$ CKM matrix element in pp collisions at
       $\sqrt{s}$ = 8 TeV'. In: *JHEP* 1406 (2014), p. 090. DOI: 10.1007/JHEP06(2014)090.
       arXiv: 1403.7366 [hep-ex] (cit. on p. 15).

[55]   S. Alekhin, J. Blumlein and S. Moch. 'PDF fit in the fixed-flavor-number scheme'.
       In: *Nucl. Phys. Proc. Suppl.* 222-224 (2012), pp. 41–51. DOI: 10.1016/j.nuclphysbps.
       2012.03.006. arXiv: 1202.4642 [hep-ph] (cit. on p. 15).

[56]   Rikkert Frederix, Emanuele Re and Paolo Torrielli. 'Single-top t-channel had-
       roproduction in the four-flavour scheme with POWHEG and aMC@NLO'. In:
       JHEP 09 (2012), p. 130. DOI: 10.1007/JHEP09(2012)130. arXiv: 1207.5391
       [hep-ph] (cit. on pp. 17, 35, 37, 166).

[57]   John M. Campbell et al. 'Next-to-Leading-Order Predictions for t-Channel Single-
       Top Production at Hadron Colliders'. In: *Phys. Rev. Lett.* 102 (2009), p. 182003.
       DOI: 10.1103/PhysRevLett.102.182003. arXiv: 0903.0005 [hep-ph] (cit.
       on pp. 17, 168, 174).

[58]   Fabio Maltoni, Giovanni Ridolfi and Maria Ubiali. 'b-initiated processes at the
       LHC: a reappraisal'. In: *JHEP* 07 (2012). [Erratum: JHEP04,095(2013)], p. 022.
       DOI: 10.1007/JHEP04(2013)095,10.1007/JHEP07(2012)022. arXiv: 1203.
       6393 [hep-ph] (cit. on p. 17).

[59]   Christiane Lefèvre. 'The CERN accelerator complex. Complexe des accèlèrat-
       eurs du CERN'. Dec. 2008. URL: http://cds.cern.ch/record/1260465
       (cit. on p. 20).

[60]   Georges Aad et al. 'Observation of a new particle in the search for the Standard
       Model Higgs boson with the ATLAS detector at the LHC'. In: *Phys. Lett.* B716
       (2012), pp. 1–29. DOI: 10.1016/j.physletb.2012.08.020. arXiv: 1207.7214
       [hep-ex] (cit. on p. 20).

[61]   CMS Collaboration. 'The CMS experiment at the CERN LHC'. In: *JINST* 3
       (2008), S08004. DOI: 10.1088/1748-0221/3/08/S08004 (cit. on p. 20).

[62] Serguei Chatrchyan et al. 'Observation of a new boson at a mass of 125 GeV with the CMS experiment at the LHC'. In: *Phys. Lett.* B716 (2012), pp. 30–61. DOI: 10.1016/j.physletb.2012.08.021. arXiv: 1207.7235 [hep-ex] (cit. on p. 21).

[63] K. Aamodt et al. 'The ALICE experiment at the CERN LHC'. In: *JINST* 3 (2008), S08002. DOI: 10.1088/1748-0221/3/08/S08002 (cit. on p. 21).

[64] A. Augusto Alves Jr. et al. 'The LHCb Detector at the LHC'. In: *JINST* 3 (2008), S08005. DOI: 10.1088/1748-0221/3/08/S08005 (cit. on p. 21).

[65] O. Adriani et al. 'The LHCf detector at the CERN Large Hadron Collider'. In: *JINST* 3 (2008), S08006. DOI: 10.1088/1748-0221/3/08/S08006 (cit. on p. 21).

[66] G. Anelli et al. 'The TOTEM experiment at the CERN Large Hadron Collider'. In: *JINST* 3 (2008), S08007. DOI: 10.1088/1748-0221/3/08/S08007 (cit. on p. 21).

[67] James Pinfold et al. 'Technical Design Report of the MoEDAL Experiment'. In: (2009) (cit. on p. 21).

[68] Mike Lamont. 'Status of the LHC'. In: *Journal of Physics: Conference Series* 455.1 (2013), p. 012001. URL: http://stacks.iop.org/1742-6596/455/i=1/a=012001 (cit. on p. 22).

[69] ATLAS Collaboration. 'The ATLAS Inner Detector commissioning and calibration'. In: *Eur. Phys. J. C* 70 (2010), p. 787. DOI: 10.1140/epjc/s10052-010-1366-7. arXiv: 1004.5293 [hep-ex] (cit. on p. 24).

[70] ATLAS Collaboration. 'Operation and performance of the ATLAS semiconductor tracker'. In: *JINST* 9 (2014), P08009. DOI: 10.1088/1748-0221/9/08/P08009. arXiv: 1404.7473 [hep-ex] (cit. on p. 25).

[71] The ATLAS TRT collaboration. 'The ATLAS Transition Radiation Tracker (TRT) proportional drift tube: design and performance'. In: *Journal of Instrumentation* 3.02 (2008), P02013. URL: http://stacks.iop.org/1748-0221/3/i=02/a=P02013 (cit. on p. 25).

[72] V Lacuesta. 'Track and vertex reconstruction in the ATLAS experiment'. In: *Journal of Instrumentation* 8.02 (2013), p. C02035. URL: http://stacks.iop.org/1748-0221/8/i=02/a=C02035 (cit. on p. 25).

[73] ATLAS Collaboration. *Alignment of the ATLAS Inner Detector and its Performance in 2012*. ATLAS-CONF-2014-047. 2014. URL: http://cdsweb.cern.ch/record/1741021 (cit. on p. 26).

[74] A. Airapetian et al. 'ATLAS calorimeter performance Technical Design Report'. In: (1996) (cit. on p. 27).

[75] 'ATLAS muon spectrometer: Technical design report'. In: (1997) (cit. on p. 28).

[76] C. Bini. 'Study of the performance of the ATLAS Muon Spectrometer'. In: *Proceedings, 2011 IEEE Nuclear Science Symposium and Medical Imaging Conference (NSS/MIC 2011): Valencia, Spain, October 23-29, 2011*. CERN. Geneva: CERN, 2011, pp. 1265–1268. DOI: 10.1109/NSSMIC.2011.6154323. URL: http://cdsweb.cern.ch/record/1398553/files/ATL-MUON-PROC-2011-008.pdf (cit. on p. 29).

[77] ATLAS Collaboration. 'Performance of the ATLAS muon trigger in pp collisions at $\sqrt{s}$ = 8 TeV'. In: *Eur. Phys. J. C* 75 (2015), p. 120. DOI: 10.1140/epjc/s10052-015-3325-9. arXiv: 1408.3179 [hep-ex] (cit. on pp. 29, 32).

[78] ATLAS Collaboration. 'Identification and energy calibration of hadronically decaying tau leptons with the ATLAS experiment in pp collisions at $\sqrt{s}$ = 8 TeV'. In: *Eur. Phys. J. C* 75 (2015), p. 303. DOI: 10.1140/epjc/s10052-015-3500-z. arXiv: 1412.7086 [hep-ex] (cit. on p. 29).

[79] Georges Aad et al. 'The performance of the jet trigger for the ATLAS detector during 2011 data taking'. In: *Eur. Phys. J.* C76.10 (2016), p. 526. DOI: 10.1140/epjc/s10052-016-4325-0. arXiv: 1606.07759 [hep-ex] (cit. on p. 30).

[80] ATLAS Collaboration. 'Improved luminosity determination in pp collisions at $\sqrt{s}$ = 7 TeV using the ATLAS detector at the LHC'. In: *Eur. Phys. J. C* 73 (2013), p. 2518. DOI: 10.1140/epjc/s10052-013-2518-3. arXiv: 1302.4393 [hep-ex] (cit. on p. 31).

[81] Luminosity Public Results website. Apr. 2016. URL: https://twiki.cern.ch/twiki/bin/view/AtlasPublic/LuminosityPublicResults (cit. on p. 32).

[82] ATLAS Collaboration. *Performance of the ATLAS Electron and Photon Trigger in pp Collisions at $\sqrt{s}$ = 7 TeV in 2011*. ATLAS-CONF-2012-048. 2012. URL: http://cdsweb.cern.ch/record/1450089 (cit. on p. 32).

[83] Stefan Hoeche. 'Introduction to parton-shower event generators'. In: *Theoretical Advanced Study Institute in Elementary Particle Physics: Journeys Through the Precision Frontier: Amplitudes for Colliders (TASI 2014) Boulder, Colorado, June 2-27, 2014*. 2014. arXiv: 1411.4085 [hep-ph]. URL: https://inspirehep.net/record/1328513/files/arXiv:1411.4085.pdf (cit. on p. 33).

[84] ATLAS Collaboration. 'The ATLAS Simulation Infrastructure'. In: *Eur. Phys. J. C* 70 (2010), p. 823. DOI: 10.1140/epjc/s10052-010-1429-9. arXiv: 1005.4568 [hep-ex] (cit. on p. 34).

[85] S. Agostinelli et al. 'GEANT4: A Simulation Toolkit'. In: *Nucl. Instrum. Meth. A* 506 (2003), pp. 250–303. DOI: 10.1016/S0168-9002(03)01368-8 (cit. on p. 34).

[86]   Paolo Nason and Bryan Webber. 'Next-to-Leading-Order Event Generators'. In: *Ann. Rev. Nucl. Part. Sci.* 62 (2012), pp. 187–213. DOI: 10.1146/annurev-nucl-102711-094928. arXiv: 1202.1251 [hep-ph] (cit. on p. 35).

[87]   Stefan Hoeche et al. 'QCD matrix elements and truncated showers'. In: *JHEP* 05 (2009), p. 053. DOI: 10.1088/1126-6708/2009/05/053. arXiv: 0903.1219 [hep-ph] (cit. on pp. 35, 36, 42).

[88]   Valentin Hirschi et al. 'Automation of one-loop QCD corrections'. In: *JHEP* 05 (2011), p. 044. DOI: 10.1007/JHEP05(2011)044. arXiv: 1103.0621 [hep-ph] (cit. on p. 35).

[89]   Steffen Schumann and Frank Krauss. 'A Parton shower algorithm based on Catani-Seymour dipole factorisation'. In: *JHEP* 03 (2008), p. 038. DOI: 10.1088/1126-6708/2008/03/038. arXiv: 0709.1027 [hep-ph] (cit. on p. 36).

[90]   Borut Paul Kersevan and Elzbieta Richter-Was. 'The Monte Carlo event generator AcerMC versions 2.0 to 3.8 with interfaces to {PYTHIA} 6.4, {HERWIG} 6.5 and {ARIADNE} 4.1'. In: *Computer Physics Communications* 184.3 (2013), pp. 919–985. ISSN: 0010-4655. DOI: http://dx.doi.org/10.1016/j.cpc.2012.10.032. URL: http://www.sciencedirect.com/science/article/pii/S001046551200375X (cit. on p. 36).

[91]   Borut Paul Kersevan and Ian Hinchliffe. 'A consistent prescription for the production involving massive quarks in hadron collisions'. In: *Journal of High Energy Physics* 2006.09 (2006), p. 033 (cit. on p. 36).

[92]   Torbjörn Sjöstrand, Stephen Mrenna and Peter Z. Skands. 'PYTHIA 6.4 Physics and Manual'. In: *JHEP* 05 (2006), p. 026. DOI: 10.1088/1126-6708/2006/05/026. arXiv: hep-ph/0603175 [hep-ph] (cit. on p. 36).

[93]   Torbjörn Sjöstrand et al. 'An Introduction to PYTHIA 8.2'. In: *Comput. Phys. Commun.* 191 (2015), pp. 159–177. DOI: 10.1016/j.cpc.2015.01.024. arXiv: 1410.3012 [hep-ph] (cit. on p. 36).

[94]   B. Andersson et al. 'Parton fragmentation and string dynamics'. In: *Physics Reports* 97.2 (1983), pp. 31–145. ISSN: 0370-1573. DOI: http://dx.doi.org/10.1016/0370-1573(83)90080-7. URL: http://www.sciencedirect.com/science/article/pii/0370157383900807 (cit. on p. 36).

[95]   T. Sjostrand and Peter Z. Skands. 'Transverse-momentum-ordered showers and interleaved multiple interactions'. In: *Eur. Phys. J.* C39 (2005), pp. 129–154. DOI: 10.1140/epjc/s2004-02084-y. arXiv: hep-ph/0408302 [hep-ph] (cit. on p. 36).

[96]   G. Corcella et al. 'HERWIG 6: An Event generator for hadron emission reactions with interfering gluons (including supersymmetric processes)'. In: *JHEP* 01 (2001), p. 010. DOI: 10.1088/1126-6708/2001/01/010. arXiv: hep-ph/0011363 (cit. on pp. 36, 37).

[97]   M. Bahr et al. 'Herwig++ Physics and Manual'. In: *Eur. Phys. J. C* 58 (2008), pp. 639–707. DOI: 10.1140/epjc/s10052-008-0798-9. arXiv: 0803.0883 [hep-ph] (cit. on p. 36).

[98]   Johannes Bellm et al. 'Herwig 7.0/Herwig++ 3.0 release note'. In: *Eur. Phys. J.* C76.4 (2016), p. 196. DOI: 10.1140/epjc/s10052-016-4018-8. arXiv: 1512.01178 [hep-ph] (cit. on p. 36).

[99]   D. Amati and G. Veneziano. 'Preconfinement as a property of perturbative QCD'. In: *Physics Letters B* 83.1 (1979), pp. 87–92. ISSN: 0370-2693. DOI: http://dx.doi.org/10.1016/0370-2693(79)90896-7. URL: http://www.sciencedirect.com/science/article/pii/0370269379908967 (cit. on p. 36).

[100] Pierre Artoisenet et al. 'Automatic spin-entangled decays of heavy resonances in Monte Carlo simulations'. In: *JHEP* 03 (2013), p. 015. DOI: 10.1007/JHEP03(2013)015. arXiv: 1212.3460 [hep-ph] (cit. on p. 37).

[101] Peter Zeiler Skands. 'Tuning Monte Carlo Generators: The Perugia Tunes'. In: *Phys. Rev. D* 82 (2010), p. 074018. DOI: 10.1103/PhysRevD.82.074018. arXiv: 1005.3457 [hep-ph] (cit. on pp. 37, 38, 149).

[102] J. Alwall et al. 'The automated computation of tree-level and next-to-leading order differential cross sections, and their matching to parton shower simulations'. In: *JHEP* 07 (2014), p. 079. DOI: 10.1007/JHEP07(2014)079. arXiv: 1405.0301 [hep-ph] (cit. on p. 37).

[103] J. M. Butterworth, Jeffrey R. Forshaw and M. H. Seymour. 'Multiparton Interactions in Photoproduction at HERA'. In: *Z. Phys.* C 72 (1996), pp. 637–646. DOI: 10.1007/s002880050286. arXiv: hep-ph/9601371 (cit. on p. 37).

[104] ATLAS Collaboration. *New ATLAS event generator tunes to 2010 data*. ATL-PHYS-PUB-2011-008. 2011. URL: http://cds.cern.ch/record/1345343 (cit. on pp. 37, 38).

[105] Michael H. Seymour and Andrzej Siodmok. 'Constraining MPI models using σ_{eff} and recent Tevatron and LHC Underlying Event data'. In: *JHEP* 10 (2013), p. 113. DOI: 10.1007/JHEP10(2013)113. arXiv: 1307.5015 [hep-ph] (cit. on p. 38).

[106] ATLAS Collaboration. *ATLAS Pythia 8 tunes to 7 TeV data*. ATL-PHYS-PUB-2014-021. 2014. URL: http://cdsweb.cern.ch/record/1966419 (cit. on p. 38).

[107] Simone Alioli et al. 'A general framework for implementing NLO calculations in shower Monte Carlo programs: the POWHEG BOX'. In: *JHEP* 06 (2010), p. 043. DOI: 10.1007/JHEP06(2010)043. arXiv: 1002.2581 [hep-ph] (cit. on p. 41).

[108] Emanuele Re. 'Single-top Wt-channel production matched with parton showers using the POWHEG method'. In: *Eur. Phys. J. C* 71 (2011), p. 1547. DOI: 10.1140/epjc/s10052-011-1547-z. arXiv: 1009.2450 [hep-ph] (cit. on p. 41).

[109] Simone Alioli et al. 'NLO single-top production matched with shower in POWHEG: *s*- and *t*-channel contributions'. In: *JHEP* 09 (2009). [Erratum: JHEP **02** (2010) 011], p. 111. DOI: 10.1007/JHEP02(2010)011, 10.1088/1126-6708/2009/09/111. arXiv: 0907.4076 [hep-ph] (cit. on p. 41).

[110] Stefano Frixione, Paolo Nason and Giovanni Ridolfi. 'A positive-weight next-to-leading-order Monte Carlo for heavy flavour hadroproduction'. In: *JHEP* 09 (2007), p. 126. DOI: 10.1088/1126-6708/2007/09/126. arXiv: 0707.3088 [hep-ph] (cit. on p. 41).

[111] T. Gleisberg et al. 'Event generation with SHERPA 1.1'. In: *JHEP* 02 (2009), p. 007. DOI: 10.1088/1126-6708/2009/02/007. arXiv: 0811.4622 [hep-ph] (cit. on p. 41).

[112] Thomas Kittelmann et al. 'The Virtual Point 1 event display for the ATLAS experiment'. In: *Journal of Physics: Conference Series* 219.3 (2010), p. 032012. URL: http://stacks.iop.org/1742-6596/219/i=3/a=032012 (cit. on p. 48).

[113] T. Cornelissen et al. 'Concepts, Design and Implementation of the ATLAS New Tracking (NEWT)'. In: (2007). Ed. by A. Salzburger (cit. on p. 49).

[114] R. Fruehwirth. 'Application of Kalman filtering to track and vertex fitting'. In: *Nuclear Instruments and Methods in Physics Research Section A: Accelerators, Spectrometers, Detectors and Associated Equipment* 262.2 (1987), pp. 444–450. ISSN: 0168-9002. DOI: http://dx.doi.org/10.1016/0168-9002(87)90887-4. URL: http://www.sciencedirect.com/science/article/pii/0168900287908874 (cit. on p. 49).

[115] Morad Aaboud et al. 'Reconstruction of primary vertices at the ATLAS experiment in Run 1 proton-proton collisions at the LHC'. In: (2016). arXiv: 1611.10235 [physics.ins-det] (cit. on p. 49).

[116] W Lampl et al. *Calorimeter Clustering Algorithms: Description and Performance.* Tech. rep. ATL-LARG-PUB-2008-002. ATL-COM-LARG-2008-003. Geneva: CERN, Apr. 2008. URL: http://cds.cern.ch/record/1099735 (cit. on pp. 49, 53).

[117] ATLAS Collaboration. 'Electron performance measurements with the ATLAS detector using the 2010 LHC proton–proton collision data'. In: *Eur. Phys. J. C* 72 (2012), p. 1909. DOI: 10.1140/epjc/s10052-012-1909-1. arXiv: 1110.3174 [hep-ex] (cit. on pp. 50, 51).

[118]   ATLAS Collaboration. 'Electron reconstruction and identification efficiency measurements with the ATLAS detector using the 2011 LHC proton–proton collision data'. In: *Eur. Phys. J. C* 74 (2014), p. 2941. DOI: 10.1140/epjc/s10052-014-2941-0. arXiv: 1404.2240 [hep-ex] (cit. on p. 50).

[119]   ATLAS Collaboration. *Electron efficiency measurements with the ATLAS detector using the 2012 LHC proton–proton collision data*. ATLAS-CONF-2014-032. 2014. URL: http://cdsweb.cern.ch/record/1706245 (cit. on pp. 50, 51).

[120]   ATLAS Collaboration. *Expected electron performance in the ATLAS experiment*. ATL-PHYS-PUB-2011-006. 2011. URL: http://cdsweb.cern.ch/record/1345327 (cit. on p. 51).

[121]   ATLAS Collaboration. 'Measurement of the muon reconstruction performance of the ATLAS detector using 2011 and 2012 LHC proton–proton collision data'. In: *Eur. Phys. J. C* 74 (2014), p. 3130. DOI: 10.1140/epjc/s10052-014-3130-x. arXiv: 1407.3935 [hep-ex] (cit. on p. 51).

[122]   Keith Rehermann and Brock Tweedie. 'Efficient Identification of Boosted Semileptonic Top Quarks at the LHC'. In: *JHEP* 03 (2011), p. 059. DOI: 10.1007/JHEP03(2011)059. arXiv: 1007.2221 [hep-ph] (cit. on p. 52).

[123]   ATLAS Collaboration. *Preliminary results on the muon reconstruction efficiency, momentum resolution, and momentum scale in ATLAS 2012 pp collision data*. ATLAS-CONF-2013-088. 2013. URL: http://cdsweb.cern.ch/record/1580207 (cit. on p. 52).

[124]   Georges Aad et al. 'Muon reconstruction efficiency and momentum resolution of the ATLAS experiment in proton-proton collisions at $\sqrt{s}$ = 7 TeV in 2010'. In: *Eur. Phys. J.* C74.9 (2014), p. 3034. DOI: 10.1140/epjc/s10052-014-3034-9. arXiv: 1404.4562 [hep-ex] (cit. on p. 52).

[125]   Georges Aad et al. 'Measurement of the muon reconstruction performance of the ATLAS detector using 2011 and 2012 LHC protonproton collision data'. In: *Eur. Phys. J.* C74.11 (2014), p. 3130. DOI: 10.1140/epjc/s10052-014-3130-x. arXiv: 1407.3935 [hep-ex] (cit. on p. 52).

[126]   ATLAS Collaboration. 'Topological cell clustering in the ATLAS calorimeters and its performance in LHC Run 1'. In: (2016). arXiv: 1603.02934 [hep-ex] (cit. on p. 53).

[127]   Matteo Cacciari, Gavin P. Salam and Gregory Soyez. 'The anti-k_t jet clustering algorithm'. In: *JHEP* 04 (2008), p. 063. DOI: 10.1088/1126-6708/2008/04/063. arXiv: 0802.1189 [hep-ph]. URL: http://fastjet.fr (cit. on p. 53).

[128] T Barillari et al. *Local Hadronic Calibration*. Tech. rep. ATL-LARG-PUB-2009-001-2. ATL-COM-LARG-2008-006. ATL-LARG-PUB-2009-001. Due to a report-number conflict with another document, the report-number ATL-LARG-PUB-2009-001-2 has been assigned. Geneva: CERN, June 2008. URL: https://cds.cern.ch/record/1112035 (cit. on p. 53).

[129] ATLAS Collaboration. *Data-Quality Requirements and Event Cleaning for Jets and Missing Transverse Energy Reconstruction with the ATLAS Detector in Proton–Proton Collisions at a Center-of-Mass Energy of $\sqrt{s}$ = 7 TeV*. ATLAS-CONF-2010-038. 2010. URL: http://cdsweb.cern.ch/record/1277678 (cit. on p. 53).

[130] ATLAS Collaboration. 'Performance of pile-up mitigation techniques for jets in pp collisions at $\sqrt{s}$ = 8 TeV using the ATLAS detector'. In: (2015). arXiv: 1510.03823 [hep-ex] (cit. on p. 54).

[131] Morad Aaboud et al. 'Performance of algorithms that reconstruct missing transverse momentum in $\sqrt{s}$ = 8 TeV proton–proton collisions in the ATLAS detector'. In: *Eur. Phys. J. C* 77.CERN-EP-2016-134. 4 (Sept. 2016). 69 pages in total, author list starting page 53, 26 figures, 6 tables, published version, all figures including auxiliary figures are available at https://atlas.web.cern.ch/Atlas/GROUPS/PHYSIC 2014-04/, 241. 68 p. URL: http://cds.cern.ch/record/2220441 (cit. on p. 54).

[132] ATLAS Collaboration. 'Performance of b -jet identification in the ATLAS experiment'. In: *Journal of Instrumentation* 11.04 (2016), P04008. URL: http://stacks.iop.org/1748-0221/11/i=04/a=P04008 (cit. on p. 55).

[133] Georges Aad et al. 'Performance of b-Jet Identification in the ATLAS Experiment'. In: *JINST* 11.04 (2016), P04008. DOI: 10.1088/1748-0221/11/04/P04008. arXiv: 1512.01094 [hep-ex] (cit. on p. 55).

[134] ATLAS Collaboration. *Performance of Impact Parameter-Based b-tagging Algorithms with the ATLAS Detector using Proton–Proton Collisions at $\sqrt{s}$ = 7 TeV*. ATLAS-CONF-2010-091. 2010. URL: http://cdsweb.cern.ch/record/1299106 (cit. on p. 55).

[135] G. Aad et al. 'Expected Performance of the ATLAS Experiment - Detector, Trigger and Physics'. In: (2009). arXiv: 0901.0512 [hep-ex] (cit. on p. 55).

[136] G Piacquadio and C Weiser. 'A new inclusive secondary vertex algorithm for b-jet tagging in ATLAS'. In: *Journal of Physics: Conference Series* 119.3 (2008), p. 032032. URL: http://stacks.iop.org/1742-6596/119/i=3/a=032032 (cit. on p. 55).

[137] ATLAS Collaboration. *b-tagging in dense environments*. ATL-PHYS-PUB-2014-014. 2014. URL: https://atlas.web.cern.ch/Atlas/GROUPS/PHYSICS/PUBNOTES/ATL-PHYS-PUB-2014-014 (cit. on p. 56).

[138]   Matteo Cacciari, Gavin P. Salam and Gregory Soyez. 'FastJet User Manual'. In: *Eur. Phys. J.* C72 (2012), p. 1896. DOI: 10.1140/epjc/s10052-012-1896-2. arXiv: 1111.6097 [hep-ph] (cit. on p. 59).

[139]   R. Frederix et al. 'Off-shell single-top production at NLO matched to parton showers'. In: *Journal of High Energy Physics* 2016.6 (2016), p. 27. ISSN: 1029-8479. DOI: 10.1007/JHEP06(2016)027. URL: http://dx.doi.org/10.1007/JHEP06(2016)027 (cit. on p. 62).

[140]   ATLAS Collaboration. *Estimation of non-prompt and fake lepton backgrounds in final states with top quarks produced in proton–proton collisions at $\sqrt{s} = 8$ TeV with the ATLAS Detector*. ATLAS-CONF-2014-058. 2014. URL: http://cdsweb.cern.ch/record/1951336 (cit. on pp. 67–69).

[141]   P. Kant et al. 'HatHor for single top-quark production: Updated predictions and uncertainty estimates for single top-quark production in hadronic collisions'. In: *Comput. Phys. Commun.* 191 (2015), pp. 74–89. DOI: 10.1016/j.cpc.2015.02.001. arXiv: 1406.4403 [hep-ph] (cit. on pp. 100, 168, 170, 174).

[142]   Andy Buckley et al. 'LHAPDF6: parton density access in the LHC precision era'. In: *Eur. Phys. J. C* 75.3 (2015), p. 132. DOI: 10.1140/epjc/s10052-015-3318-8. arXiv: 1412.7420 [hep-ph] (cit. on p. 100).

[143]   Nikolaos Kidonakis. 'Differential and total cross sections for top pair and single top production'. In: *Proceedings, 20th International Workshop on Deep-Inelastic Scattering and Related Subjects (DIS 2012)*. 2012, pp. 831–834. DOI: 10.3204/DESY-PROC-2012-02/251. arXiv: 1205.3453 [hep-ph]. URL: http://inspirehep.net/record/1114754/files/arXiv:1205.3453.pdf (cit. on p. 100).

[144]   *Talk in TOPLHCWG meeting 20.05.2015.* https://indico.cern.ch/event/375429/session/2/contribution/12/attachments/748041/1026252/TopWG_caola.pdf (cit. on p. 100).

[145]   Michael Feindt. *A Neural Bayesian Estimator for Conditional Probability Densities.* 2004. arXiv: 0402093v1 (cit. on p. 105).

[146]   M. Feindt and U. Kerzel. 'The NeuroBayes neural network package'. In: *Nucl. Instrum. Meth. A* 559 (2006), pp. 190–194. DOI: 10.1016/j.nima.2005.11.166 (cit. on p. 105).

[147]   Philipp Sturm. *Studies for the Measurement of Single-Top-Quark-Events with the CMS-Experiment. oai:cds.cern.ch:1311220.* Karlsruhe, 2008 (cit. on pp. 106, 131).

[148]   Thorsten Chwalek. *Measurement of the W boson helicity in top-antitop quark events with the CDF II experiment.* FERMILAB-MASTERS-2006-04. 2006 (cit. on p. 106).

[149]   F. James and M. Roos. 'Minuit - a system for function minimization and ana-
        lysis of the parameter errors and correlations'. In: *Computer Physics Communic-
        ations* 10.6 (1975), pp. 343–367. ISSN: 0010-4655. DOI: http://dx.doi.org/
        10.1016/0010-4655(75)90039-9. URL: http://www.sciencedirect.com/
        science/article/pii/0010465575900399 (cit. on p. 129).

[150]   Georg Sartisohn and W Wagner. 'Higgs Boson Search in the $H \rightarrow WW^{(*)} \rightarrow$
        $\ell\nu\ell\nu$ Channel using Neural Networks with the ATLAS Detector at 7 TeV'.
        Presented 08 May 2012. PhD thesis. Wuppertal U., Mar. 2012. URL: http://
        cds.cern.ch/record/1456081 (cit. on p. 131).

[151]   Kathrin Becker and Wolfgang Wagner. 'Inclusive and Differential Cross-Section
        Measurements of t-channel single top-quark production at $\sqrt{s} = 7$ TeV with the
        ATLAS detector'. Presented 16 Jan 2015. PhD thesis. Wuppertal, Germany:
        Wuppertal U., Mar. 2015. URL: http://cds.cern.ch/record/2056713 (cit.
        on p. 131).

[152]   ATLAS Collaboration. 'Electron and photon energy calibration with the AT-
        LAS detector using LHC Run 1 data'. In: *Eur. Phys. J. C* 74 (2014), p. 3071. DOI:
        10.1140/epjc/s10052-014-3071-4. arXiv: 1407.5063 [hep-ex] (cit. on
        p. 141).

[153]   ATLAS Collaboration. *Pile-up subtraction and suppression for jets in ATLAS.*
        ATLAS-CONF-2013-083. 2013. URL: http://cdsweb.cern.ch/record/
        1570994 (cit. on p. 142).

[154]   ATLAS Collaboration. *Jet energy scale and its systematic uncertainty in proton–
        proton collisions at $\sqrt{s} = 7$ TeV with ATLAS 2011 data.* ATLAS-CONF-2013-
        004. 2013. URL: http://cdsweb.cern.ch/record/1509552 (cit. on p. 142).

[155]   ATLAS Collaboration. *Monte Carlo Calibration and Combination of In-situ Meas-
        urements of Jet Energy Scale, Jet Energy Resolution and Jet Mass in ATLAS.* ATLAS-
        CONF-2015-037. 2015. URL: http://cdsweb.cern.ch/record/2044941 (cit.
        on p. 143).

[156]   ATLAS Collaboration. *Data-driven determination of the energy scale and resolu-
        tion of jets reconstructed in the ATLAS calorimeters using dijet and multijet events
        at $\sqrt{s} = 8$ TeV.* ATLAS-CONF-2015-017. 2015. URL: http://cdsweb.cern.
        ch/record/2008678 (cit. on pp. 144, 145).

[157]   ATLAS Collaboration. *Jet Energy Resolution and Selection Efficiency Relative to
        Track Jets from In-situ Techniques with the ATLAS Detector Using Proton–Proton
        Collisions at a Center of Mass Energy $\sqrt{s} = 7$ TeV.* ATLAS-CONF-2010-054.
        2010. URL: http://cdsweb.cern.ch/record/1281311 (cit. on p. 144).

[158]   Jon Butterworth et al. *PDF4LHC recommendations for LHC Run II.* 2015. arXiv:
        1510.03865 [hep-ph] (cit. on p. 149).

[159] Andy Buckley et al. 'Rivet user manual'. In: *Comput. Phys. Commun.* 184 (2013), pp. 2803–2819. DOI: `10.1016/j.cpc.2013.05.021`. arXiv: `1003.0694 [hep-ph]` (cit. on p. 157).

[160] ATLAS Collaboration. *Luminosity determination in pp collisions at $\sqrt{s} = 8$ TeV using the ATLAS detector at the LHC.* to be submitted to Eur. Phys. J. C. 2016 (cit. on p. 159).

[161] Nikolaos Kidonakis. 'Next-to-next-to-leading-order collinear and soft gluon corrections for t-channel single top quark production'. In: *Phys. Rev. D* 83 (2011), p. 091503. DOI: `10.1103/PhysRevD.83.091503`. arXiv: `1103.2792 [hep-ph]` (cit. on p. 168).

[162] Mathias Brucherseifer, Fabrizio Caola and Kirill Melnikov. 'On the NNLO QCD corrections to single-top production at the LHC'. In: *Phys. Lett. B* 736 (2014), pp. 58–63. DOI: `10.1016/j.physletb.2014.06.075`. arXiv: `1404.7116 [hep-ph]` (cit. on pp. 168, 170).

[163] ATLAS Collaboration. 'Determination of the Strange-Quark Density of the Proton from ATLAS Measurements of the $W \rightarrow \ell\nu$ and $Z \rightarrow \ell\ell$ Cross Sections'. In: *Phys. Rev. Lett.* 109 (2012), p. 012001. DOI: `10.1103/PhysRevLett.109.012001`. arXiv: `1203.4051 [hep-ex]` (cit. on p. 174).

[164] Michael Schuh and Wolfgang Wagner. 'Determination of the top-quark pole mass using single top-quark production cross-sections'. Presented 07 Nov 2016. Nov. 2016. URL: `https://cds.cern.ch/record/2233142` (cit. on p. 175).

[165] ATLAS Top Group Summary Plots website. Sept. 2016. URL: `https://atlas.web.cern.ch/Atlas/GROUPS/PHYSICS/CombinedSummaryPlots/TOP/` (cit. on pp. 182, 185, 186).

[166] Vardan Khachatryan et al. 'Measurement of the t-channel single-top-quark production cross section and of the $| V_{tb} |$ CKM matrix element in pp collisions at $\sqrt{s} = 8$ TeV'. In: *JHEP* 06 (2014), p. 090. DOI: `10.1007/JHEP06(2014)090`. arXiv: `1403.7366 [hep-ex]` (cit. on p. 184).

Appendix

Acceptance Uncertainties Considered in the Statistical Analysis

In this appendix all acceptance uncertainties included in the statistical analysis are presented.

A.1. Acceptance Uncertainties in the ℓ^+ channel

Table A.1.: Rate uncertainties of all considered systematic uncertainties.

	tq	$t\bar{t}/Wt/t\bar{b}$	W^++jets	Z+jets,VV
b-tag scalefactor C0	0.1% / -0.1%	0.0% / -0.0%	0.0% / -0.0%	0.0% / -0.0%
b-tag scalefactor C1	0.0% / -0.0%	0.0% / -0.0%	0.0% / -0.0%	0.0% / -0.0%
b-tag scalefactor C2	0.0% / -0.0%	-0.0% / -0.0%	0.0% / -0.0%	-0.0% / 0.0%
b-tag scalefactor C3	0.1% / -0.1%	0.1% / -0.1%	0.1% / -0.1%	0.1% / -0.1%
b-tag scalefactor C4	-0.2% / 0.2%	-0.2% / 0.1%	-0.0% / 0.0%	-0.1% / 0.1%
b-tag scalefactor C5	-0.3% / 0.3%	-0.2% / 0.2%	-0.1% / 0.1%	-0.2% / 0.2%
b-tag scalefactor C6	0.3% / -0.3%	0.3% / -0.3%	0.5% / -0.5%	0.6% / -0.6%
b-tag scalefactor C7	-0.9% / 0.9%	-0.6% / 0.6%	-0.3% / 0.3%	-0.4% / 0.4%
b-tag scalefactor C8	0.0% / -0.0%	0.0% / -0.0%	0.1% / -0.1%	0.1% / -0.1%
c-tag scalefactor C0	0.0% / -0.0%	0.0% / -0.0%	3.1% / -3.1%	2.1% / -2.2%
c-tag scalefactor C1	0.0% / -0.0%	0.0% / -0.0%	3.0% / -3.0%	1.5% / -1.5%
c-tag scalefactor C2	-0.0% / 0.0%	-0.0% / 0.0%	-1.8% / 1.8%	-0.9% / 0.9%
c-tag scalefactor C3	-0.0% / 0.0%	-0.0% / 0.0%	1.1% / -1.1%	0.5% / -0.5%
mis-tag scalefactor C0	0.0% / -0.0%	-0.0% / -0.0%	0.0% / -0.0%	-0.0% / 0.0%
mis-tag scalefactor C1	-0.0% / 0.0%	-0.0% / -0.0%	-0.0% / 0.0%	-0.0% / 0.0%
mis-tag scalefactor C2	0.0% / -0.0%	-0.0% / -0.0%	0.0% / -0.0%	0.0% / -0.0%
mis-tag scalefactor C3	-0.0% / 0.0%	-0.0% / -0.0%	-0.0% / 0.0%	-0.0% / -0.0%
mis-tag scalefactor C4	0.0% / -0.0%	-0.0% / 0.0%	0.0% / -0.0%	0.0% / -0.0%
mis-tag scalefactor C5	0.0% / -0.0%	-0.0% / 0.0%	-0.0% / 0.0%	0.1% / -0.1%
mis-tag scalefactor C6	-0.0% / 0.0%	-0.0% / -0.0%	-0.1% / 0.1%	-0.1% / 0.1%
mis-tag scalefactor C7	-0.0% / 0.0%	-0.0% / 0.0%	-0.6% / 0.6%	-0.6% / 0.6%
mis-tag scalefactor C8	-0.0% / 0.0%	-0.0% / 0.0%	-0.4% / 0.4%	-0.4% / 0.4%
mis-tag scalefactor C9	0.0% / -0.0%	0.0% / -0.0%	0.9% / -0.9%	0.9% / -0.9%
mis-tag scalefactor C10	-0.0% / 0.0%	-0.0% / 0.0%	-1.3% / 1.3%	-1.3% / 1.3%
mis-tag scalefactor C11	-0.0% / 0.0%	-0.0% / -0.0%	-0.1% / 0.1%	-0.2% / 0.2%

Table A.2.: Rate uncertainties of all considered systematic uncertainties.

	tq	$t\bar{t}$ / Wt / $t\bar{b}$	W^++jets	Z+jets,VV
b-jet energyscale	0.0% / -0.1%	-0.5% / 0.4%	0.7% / -0.7%	1.0% / -0.4%
JES single particle	—	—	—	—
JES pile-up μ	-0.0% / 0.0%	0.4% / -0.4%	-0.1% / 0.2%	-0.6% / 0.2%
JES pile-up n_{vtx}	-0.0% / -0.0%	0.7% / -0.8%	0.1% / 0.1%	-0.7% / -0.1%
JES pile-up Pt	0.0% / 0.0%	-0.1% / 0.0%	0.2% / -0.1%	-0.0% / 0.0%
JES pile-up ρ	0.1% / -0.1%	-2.3% / 2.3%	1.5% / -1.4%	1.4% / -2.1%
JES PunchThrough	-0.0% / 0.0%	-0.0% / 0.0%	0.0% / -0.0%	-0.0% / 0.0%
JES flavour composition	0.0% / -0.0%	-3.3% / 3.2%	1.4% / -1.4%	0.2% / -2.4%
JES flavour response	-0.0% / 0.0%	2.3% / -2.3%	-1.0% / 0.9%	-1.6% / 0.4%
Jet vertex fraction	-0.0% / -0.0%	0.6% / -0.0%	-0.6% / -0.0%	-0.5% / 0.0%
JES η intercal. statistical	0.0% / -0.1%	-0.8% / 0.8%	0.4% / -0.5%	0.3% / -0.6%
JES η intercalibration	0.3% / -0.3%	-1.1% / 1.1%	0.4% / -0.6%	0.3% / -0.7%
JES detector 1	-0.0% / -0.0%	-0.4% / 0.4%	0.2% / -0.2%	-0.0% / -0.1%
JES detector 2	-0.0% / -0.0%	-0.3% / 0.3%	0.2% / -0.4%	0.1% / -0.1%
JES detector 3	0.0% / 0.0%	-0.1% / 0.1%	0.0% / -0.1%	-0.0% / -0.1%
JES mixed detector and modeling 1	0.0% / -0.0%	-0.6% / 0.5%	0.3% / -0.3%	0.1% / -0.2%
JES mixed detector and modeling 2	-0.0% / 0.0%	0.5% / -0.5%	-0.4% / 0.4%	-0.3% / 0.3%
JES mixed detector and modeling 3	0.0% / 0.0%	-0.1% / 0.1%	0.1% / -0.2%	0.1% / -0.2%
JES mixed detector and modeling 4	0.0% / -0.0%	-0.0% / 0.0%	-0.0% / -0.0%	-0.0% / -0.0%
JES physics modeling 1	0.1% / -0.3%	-3.4% / 3.4%	2.2% / -2.2%	1.8% / -2.4%
JES physics modeling 2	0.0% / 0.0%	0.1% / -0.1%	-0.1% / 0.1%	-0.1% / 0.1%
JES physics modeling 3	-0.0% / 0.0%	0.0% / -0.1%	0.0% / -0.1%	0.1% / -0.2%
JES physics modeling 4	0.0% / -0.0%	-0.1% / 0.1%	0.1% / -0.1%	0.0% / -0.0%
JES statistical 1	0.0% / -0.1%	-1.1% / 1.1%	0.7% / -0.8%	0.6% / -1.4%
JES statistical 2	-0.0% / 0.0%	0.1% / -0.1%	-0.1% / 0.1%	-0.1% / 0.1%
JES statistical 3	-0.0% / 0.0%	0.3% / -0.3%	-0.2% / 0.2%	-0.1% / -0.0%
JES statistical 4	0.0% / -0.0%	-0.3% / 0.2%	0.2% / -0.2%	-0.0% / -0.2%
Jet energy resolution	-0.7% / 0.7%	-0.4% / 0.4%	0.3% / -0.3%	0.6% / -0.6%
Jet efficiency	-0.0% / 0.0%	0.0% / -0.0%	0.0% / -0.0%	-0.0% / 0.0%

Table A.3.: Rate uncertainties of all considered systematic uncertainties.

	tq	$t\bar{t}$ / Wt / $t\bar{b}$	W^++jets	Z+jets,VV
Muon momentum resolution (ID)	0.0% / -0.0%	-0.0% / 0.0% 0.0% / 0.0% -0.0% / 0.0%	-0.0% / 0.0%	-0.1% / 0.1%
Muon momentum scale	-0.0% / 0.0%	-0.0% / 0.0% 0.0% / 0.0% -0.1% / 0.1%	-0.1% / 0.1%	-0.0% / 0.0%
Muon momentum resolution	0.1% / -0.1%	0.0% / -0.0% 0.0% / -0.0% 0.1% / -0.2%	0.1% / -0.2%	0.0% / -0.1%
Electron energy resolution	-0.1% / 0.1%	-0.0% / 0.0% 0.0% / -0.1% 0.1% / 0.1%	0.1% / 0.1%	0.1% / 0.2%
Electron energy scale	0.2% / -0.2%	0.1% / -0.1% 1.3% / -0.1% 0.3% / -0.1%	0.3% / -0.1%	0.1% / -0.1%
Lepton TriggerSF	1.4% / -1.4%	1.3% / -1.3% 1.4% / -1.4% 1.3% / -1.3%	1.4% / -1.4%	1.4% / -1.4%
Lepton ID SF	1.3% / -1.3%	1.3% / -1.3% 1.3% / -1.3% 1.3% / -1.3%	1.3% / -1.3%	1.3% / -1.3%
Lepton Reco SF	0.3% / -0.3%	0.3% / -0.3% 0.3% / -0.3% 0.3% / -0.3%	0.3% / -0.3%	0.3% / -0.3%
Electron Charge ID	-0.1% / 0.1%	0.0% / 5.0% -0.0% / 0.1% 0.0% / -0.1%	-0.1% / 0.2%	-0.4% / -25.5%
E_T^{miss} CellOut + SoftJet Resolution	-0.0% / -0.0%	-0.0% / 0.1% 0.1% / 0.1% 0.1% / 0.1%	0.1% / 0.1%	0.2% / -0.4%
E_T^{miss} CellOut + SoftJet Scale	0.0% / -0.1%	0.0% / -0.1% 0.1% / 0.1% 0.1% / -0.1%	0.1% / -0.1%	0.9% / -1.0%
$b\bar{b}$ tagging efficiency	0.9% / -0.9%	—	—	—
Z+jets heavy flavour norm.	—	—	—	50.0% / -50.0%
tq NLO matching method	-0.2% / 0.2%	—	—	—
tq Parton-Shower model	0.0% / 0.0%	—	—	—
$t\bar{t}$,Wt,$t\bar{b}$ NLO matching method	—	3.1% / -3.1%	—	—
$t\bar{t}$,Wt Parton-Shower model	—	0.2% / -0.2%	—	—
μ variation of $t\bar{t}$,Wt,$t\bar{b}$ process	—	-1.5% / -1.7%	—	—
PDF $t\bar{t}$,Wt,$t\bar{b}$,W+jets	—	5.9% / -5.9%	1.4% / -1.4%	—
tq CT10 PDF4LHC	0.2% / -0.2%	—	—	—
tq PDF	0.1% / -0.1%	—	—	—
μ variation of tq process	-2.0% / 2.6%	—	—	—

A.2. Acceptance Uncertainties in the ℓ^- channel

Table A.4.: Rate uncertainties of all considered systematic uncertainties.

	$t\bar{q}$	$t\bar{t}$ / Wt / $t\bar{b}$	W^-+jets	Z+jets,VV
b-tag scalefactor C0	0.1% / -0.1%	0.0% / -0.0%	0.0% / -0.0%	0.0% / -0.0%
b-tag scalefactor C1	0.0% / -0.0%	0.0% / -0.0%	0.0% / -0.0%	0.0% / -0.0%
b-tag scalefactor C2	0.0% / -0.0%	-0.0% / -0.0%	-0.0% / 0.0%	-0.0% / 0.0%
b-tag scalefactor C3	0.1% / -0.1%	0.1% / -0.1%	0.0% / -0.0%	0.1% / -0.1%
b-tag scalefactor C4	-0.2% / 0.2%	-0.2% / 0.1%	-0.0% / 0.0%	-0.1% / 0.1%
b-tag scalefactor C5	-0.3% / 0.3%	-0.2% / 0.2%	-0.1% / 0.1%	-0.2% / 0.2%
b-tag scalefactor C6	0.3% / -0.3%	0.3% / -0.3%	0.4% / -0.4%	0.6% / -0.6%
b-tag scalefactor C7	-0.9% / 0.9%	-0.6% / 0.6%	-0.3% / 0.3%	-0.4% / 0.4%
b-tag scalefactor C8	0.0% / -0.0%	0.0% / -0.0%	0.1% / -0.1%	0.1% / -0.1%
c-tag scalefactor C0	0.0% / -0.0%	0.0% / -0.0%	3.5% / -3.5%	2.2% / -2.2%
c-tag scalefactor C1	-0.0% / 0.0%	0.0% / -0.0%	3.5% / -3.5%	1.9% / -1.9%
c-tag scalefactor C2	0.0% / -0.0%	-0.0% / 0.0%	-2.1% / 2.1%	-1.2% / 1.2%
c-tag scalefactor C3	-0.0% / 0.0%	-0.0% / 0.0%	1.2% / -1.2%	0.6% / -0.6%
mis-tag scalefactor C0	-0.0% / 0.0%	-0.0% / -0.0%	0.0% / -0.0%	-0.0% / -0.0%
mis-tag scalefactor C1	-0.0% / 0.0%	-0.0% / -0.0%	-0.0% / 0.0%	-0.0% / 0.0%
mis-tag scalefactor C2	0.0% / -0.0%	-0.0% / -0.0%	-0.0% / 0.0%	0.0% / -0.0%
mis-tag scalefactor C3	-0.0% / 0.0%	-0.0% / -0.0%	-0.0% / 0.0%	-0.0% / 0.0%
mis-tag scalefactor C4	0.0% / -0.0%	-0.0% / 0.0%	0.0% / -0.0%	0.0% / -0.0%
mis-tag scalefactor C5	0.0% / -0.0%	-0.0% / 0.0%	-0.1% / 0.1%	-0.1% / 0.1%
mis-tag scalefactor C6	-0.0% / 0.0%	-0.0% / -0.0%	-0.2% / 0.2%	-0.1% / 0.1%
mis-tag scalefactor C7	-0.0% / 0.0%	-0.0% / 0.0%	-0.6% / 0.6%	-0.4% / 0.4%
mis-tag scalefactor C8	-0.0% / 0.0%	-0.0% / 0.0%	-0.4% / 0.4%	-0.2% / 0.2%
mis-tag scalefactor C9	0.0% / -0.0%	0.0% / -0.0%	1.1% / -1.1%	0.7% / -0.7%
mis-tag scalefactor C10	-0.0% / 0.0%	-0.0% / 0.0%	-1.4% / 1.4%	-0.9% / 0.9%
mis-tag scalefactor C11	-0.0% / 0.0%	-0.0% / -0.0%	-0.1% / 0.1%	-0.1% / 0.1%

Table A.5.: Rate uncertainties of all considered systematic uncertainties.

	$\bar{t}q$	$t\bar{t}/Wt/t\bar{b}$	W^-+jets	Z+jets,VV
b-jet energyscale	0.1% / -0.1%	-0.4% / 0.5%	0.7% / -0.6%	0.2% / -0.8%
JES single particle	—	—	—	—
JES pile-up μ	-0.1% / 0.1%	0.4% / -0.3%	-0.4% / 0.2%	0.0% / -0.3%
JES pile-up n_{vtx}	-0.1% / 0.2%	0.7% / -0.7%	-0.2% / 0.0%	-0.8% / -0.7%
JES pile-up Pt	0.0% / 0.0%	-0.0% / 0.1%	-0.1% / -0.1%	-0.2% / -0.1%
JES pile-up ρ	0.3% / -0.3%	-2.3% / 2.4%	1.6% / -1.8%	1.1% / -2.7%
JES PunchThrough	-0.0% / 0.0%	-0.0% / 0.0%	0.0% / 0.0%	0.0% / -0.0%
JES flavour composition	0.0% / -0.0%	-3.3% / 3.4%	1.2% / -1.9%	1.8% / -3.3%
JES flavour response	-0.0% / 0.0%	2.3% / -2.3%	-1.4% / 1.1%	-2.2% / 1.3%
Jet vertex fraction	-0.1% / -0.0%	0.6% / -0.0%	-0.3% / -0.0%	-0.3% / 0.0%
JES η intercal. statistical	0.1% / -0.1%	-0.8% / 0.8%	0.5% / -0.7%	0.5% / -0.6%
JES η intercalibration	0.3% / -0.3%	-1.1% / 1.2%	0.6% / -1.0%	0.6% / -0.7%
JES detector 1	0.1% / -0.0%	-0.4% / 0.4%	0.1% / -0.2%	0.1% / 0.0%
JES detector 2	0.0% / -0.0%	-0.3% / 0.3%	0.2% / -0.2%	0.2% / -0.1%
JES detector 3	0.0% / -0.0%	-0.1% / 0.1%	0.0% / -0.0%	-0.1% / -0.1%
JES mixed detector and modeling 1	0.1% / -0.1%	-0.5% / 0.6%	0.3% / -0.3%	-0.1% / -0.1%
JES mixed detector and modeling 2	-0.1% / 0.1%	0.5% / -0.5%	-0.4% / 0.4%	-0.3% / 0.1%
JES mixed detector and modeling 3	0.0% / 0.0%	-0.1% / 0.1%	0.1% / -0.1%	0.1% / -0.1%
JES mixed detector and modeling 4	0.0% / 0.0%	-0.0% / 0.0%	-0.0% / 0.0%	0.0% / 0.0%
JES physics modeling 1	0.5% / -0.4%	-3.4% / 3.6%	2.0% / -2.6%	1.5% / -3.8%
JES physics modeling 2	0.0% / 0.0%	0.1% / -0.1%	-0.0% / 0.1%	-0.0% / -0.0%
JES physics modeling 3	0.0% / 0.0%	0.1% / -0.0%	0.1% / -0.1%	0.0% / -0.2%
JES physics modeling 4	0.0% / -0.0%	-0.1% / 0.1%	0.1% / -0.0%	-0.0% / -0.0%
JES statistical 1	0.2% / -0.1%	-1.1% / 1.2%	1.0% / -1.0%	0.4% / -0.9%
JES statistical 2	0.0% / 0.0%	0.1% / -0.1%	-0.1% / 0.1%	-0.0% / -0.0%
JES statistical 3	-0.0% / 0.1%	0.3% / -0.3%	-0.1% / 0.1%	0.1% / -0.1%
JES statistical 4	0.1% / -0.0%	-0.2% / 0.2%	0.2% / -0.2%	0.1% / 0.0%
Jet energy resolution	-0.6% / 0.6%	-0.4% / 0.4%	-0.0% / 0.0%	1.9% / -1.9%
Jet efficiency	0.0% / -0.0%	0.0% / -0.0%	-0.0% / 0.0%	0.0% / -0.0%

Table A.6.: Rate uncertainties of all considered systematic uncertainties.

	$\bar{t}q$	$t\bar{t}/Wt/t\bar{b}$	W^-+jets	Z+jets,VV
Muon momentum resolution (ID)	0.0% / -0.0%	0.0% / -0.0%	-0.0% / 0.0%	0.0% / -0.0%
Muon momentum scale	0.0% / -0.0%	0.0% / -0.0%	-0.0% / 0.0%	0.1% / -0.1%
Muon momentum resolution	0.1% / -0.0%	0.0% / -0.0%	0.0% / -0.1%	0.1% / -0.1%
Electron energy resolution	-0.1% / 0.1%	-0.0% / 0.0%	-0.1% / 0.1%	0.5% / 0.1%
Electron energy scale	0.2% / -0.3%	0.1% / -0.1%	0.1% / -0.1%	-0.0% / -0.0%
Lepton TriggerSF	1.3% / -1.3%	1.3% / -1.3%	1.4% / -1.4%	1.4% / -1.4%
Lepton ID SF	1.3% / -1.3%	1.3% / -1.3%	1.3% / -1.3%	1.4% / -1.4%
Lepton Reco SF	0.3% / -0.3%	0.3% / -0.3%	0.3% / -0.3%	0.3% / -0.3%
Electron Charge ID	-0.1% / 0.1%	-0.0% / -2.3%	-0.0% / 0.1%	0.7% / 56.8%
E_T^{miss} CellOut + SoftJet Resolution	0.1% / 0.1%	0.0% / 0.0%	-0.2% / 0.0%	0.3% / -0.1%
E_T^{miss} CellOut + SoftJet Scale	0.0% / -0.0%	0.0% / -0.0%	0.2% / -0.4%	0.6% / -0.8%
$b\bar{b}$ tagging efficiency	0.9% / -0.9%	—	—	—
Z+jets heavy flavour norm.				50.0% /-50.0%
tq NLO matching method	-2.1% / 2.1%	—	—	—
tq Parton-Shower model	-0.2% / 0.2%	—	—	—
$t\bar{t},Wt,t\bar{b}$ NLO matching method		3.8% / -3.8%	—	—
$t\bar{t},Wt$ Parton-Shower model		0.7% / -0.7%	—	—
μ variation of $t\bar{t},Wt,t\bar{b}$ process		-0.9% / -1.1%	—	—
PDF $t\bar{t},Wt,t\bar{b},W$+jets		5.9% / -5.9%	1.6% / -1.6%	—
tq CT10 PDF4LHC	0.5% / -0.5%	—	—	—
tq PDF	0.1% / -0.1%	—	—	—
μ variation of tq process	-2.9% / 2.4%	—	—	—

Danksagung